Experimental measurement and numerical modelling of velocity, density and turbulence profiles of a gravity current

by

George Gerber

Dissertation presented for the degree of Doctor of Philosophy (Engineering) at the University of Stellenbosch

Promoters:

Internal:	External:
Prof G.R. Basson	Dr. G. Diedericks
Civil Engineering	CSIR
Stellenbosch University	Stellenbosch

March 2008

Declaration

I, the undersigned, hereby declare that the work contained in this dissertation is my own original work and that I have not previously in its entirety or in part submitted it at any university for a degree.

Signature: .....
G. Gerber

Date: .....

Abstract

The velocity, density and turbulence profiles of a horizontal, saline gravity current were measured experimentally. Stable stratification damped the turbulence and prevented the gravity current from becoming self-similar. The velocity and density profiles were measured simultaneously and non-intrusively with particle image velocimetry scalar (PIV-S) technology. The application of the PIV-S technology had to be extended in order to measure the continuously stratified gravity current. Measurement of the Reynolds fluxes and Reynolds stresses revealed the anisotropic turbulent transport of mass and momentum within the gravity current body. These measurements also allowed the interaction between turbulence and stratification to be studied. The measured profiles were used to evaluate the accuracy of a gravity current model which did not assume self-similarity. The gravity current model was based on a Reynolds-averaged Navier-Stokes (RANS) multispecies mixture model.

The Reynolds flux and Reynolds stress profiles did not show self-similarity with increasing downstream distance. Comparison of the vertical and horizontal Reynolds fluxes showed that gravity strongly damped the vertical flux. At a downstream location, where the bulk Richardson number was supercritical, the shear production profile had a positive inner (near bed) peak and a positive outer peak, while the buoyancy production profile had a negative outer peak. Further downstream, where the bulk Richardson number was near-critical, the outer shear and buoyancy production peaks disappeared, due to the continuous damping of the turbulence intensities by the stable stratification. However, near bed shearing allowed the inner shear production peak to remain. Sensitivity analyses of different turbulence models for the gravity current model showed that the standard $k-\epsilon$ turbulence model, as well as the Renormalization Group theory (RNG) $k-\epsilon$ turbulence model, generally underpredicted the mean streamwise velocity profile and overpredicted the excess density profile. The flux-gradient hypothesis, used to provide closure for the Reynolds fluxes, modelled the vertical Reynolds flux reasonably, but not the horizontal flux. This did not compromise the results, since the horizontal gravity current had the characteristics of a boundary-layer flow, where

the horizontal flux does not contribute significantly to the flow structure. It was shown that the gravity current model, implementing the standard $k-\epsilon$ turbulence model with a constant turbulent Schmidt number of $\sigma_t = 1{,}3$, produced profiles which were within $10\% - 20\%$ of the measured profiles.

Opsomming

Die snelheid, digtheid en turbulensie profiele van 'n soutoplossing digtheidstroom was gemeet. Die turbulensie van die digtheidstroom was gedemp deur die stabiele stratifikasie. Dit het veroorsaak dat die digtheidstroom nie gelykvormig kon word nie. Snelheid- en digtheids-profiele was gelyktydig gemeet met die nie-indringende partikel beeld snelheidsmeting skalaar (PIV-S) tegnologie. Hierdie tegnologie moes egter uitgebrei word om die kontinu gestratifiseerde digtheidstroom te kon meet. Die Reynolds stromings en Reynolds spannings metings het aangedui dat die turbulente vervoer van massa en momentum anisotropies was binne die digtheidstroom se lyf. Die interaksie tussen turbulensie en stratifikasie was ook bestudeer met behulp van hierdie metings. Die gemete profiele was ook gebruik om die akkuraatheid van 'n digtheidstroom model te evalueer wat nie gebaseer is op die aanname van gelykvormigheid nie. Die digtheidstroom model was gebaseer op 'n Reynolds-gemiddelde Navier-Stokes, meervoudige spesie model.

Reynolds stromings en Reynolds spannings-profiele het aangedui dat die digtheidstroom nie gelykvormigheid handhaaf met afstand nie. Die Reynolds stromings-profiele het verder aangedui dat gravitasie die vertikale Reynolds stromings komponent kragtig demp. Die skuifproduksie-profiel het 'n positiewe binne (bodem nabye) piek en 'n positiewe buite piek getoon vir 'n stroomaf posisie waarvan die grootmaat Richardson getal superkrities was. By hierdie posisie het die dryfkrag-profiel slegs 'n negatiewe buite piek getoon. Nog verder stroomaf, waar die grootmaat Richardson getal naby aan krities was, het die buitepieke van skuifproduksie en dryfkragproduksie verdwyn, as gevolg van die aanhoudende demping van stratifikasie op die turbulente fluktuasies. Skuifvervorming naby die bodem het egter verhoed dat die binne piek van die skuifproduksie-profiel verdwyn. Sensitiwiteits analises op verskillende turbulensie modelle het aangedui dat die standaard $k-\epsilon$ turbulensie model, sowel as die hernormaliserings groep teorie (RNG) $k-\epsilon$ turbulensie model, oor die algemeen die stroomwaartse snelheid onderskat en die oormaat digtheids-profiel oorskat. Die stromings-gradient hipotese, wat gebruik word om die Reynolds strominge te bereken, kon slegs die vertikale Reynolds stroming akkuraat

bereken. Die resultate was egter nie nadelig beïnvloed nie, omdat die digtheidstroom die eienskappe van 'n grenslaag vloei besit het. Die horisontale komponent dra nie noemenswaardig by tot die ontwikkeling van 'n grenslaag vloei nie. Die digtheidstroom model (met 'n standaard $k - \epsilon$ turbulensie model en 'n konstante turbulente Schmidt getal van $\sigma_t = 1.3$) het profiele gelewer, wat binne $10\% - 20\%$ van die gemete profiele was.

Acknowledgements

I would like to express my gratitude to my promotors Prof G.R. Basson (internal, Stellenbosch University) and Dr. G. Diedericks (external, CSIR) for their guidance. I would also like to thank the following people for their support and help:

Dr. C.M. Steenkamp (laser research institute, Stellenbosch University) and Mr. U.G.K. Deutschlander (laser research institute, Stellenbosch University) for demonstrating how to use the helium-neon laser safely. Susan Roux and Ian Snyman, two B.Eng students, who helped with preliminary experiments. Anita van der Spuy who checked the language and spelling of this dissertation.

Finally, a warm thanks to my friends at Stellenbosch, especially Wernich de Villiers, for their support and encouragement.

Dedications

To my parents
George and Lynette

Contents

Declaration i

Abstract ii

Opsomming iv

Acknowledgements vi

Dedications vii

Contents viii

List of Figures xi

List of Tables xviii

Nomenclature xix

Glossary xxvi

1 Introduction 1
- 1.1 Mechanisms of gravity current flow . . . 3
- 1.2 Historical experimental studies of gravity current flow . . . 10
- 1.3 Historical numerical studies of gravity current flow . . . 12
- 1.4 Motivation of present research . . . 16
- 1.5 Research aims . . . 17
- 1.6 Research methodology . . . 18
- 1.7 Outline of this dissertation . . . 19

2 Experimental setup and measurement techniques 20
- 2.1 Hydraulic setup . . . 21
- 2.2 Particle image velocimetry scalar setup . . . 24
- 2.3 Velocity measurement by PIV . . . 28

2.4 Density measurement techniques . . . 32
2.5 Excess density measurement by PIV-S . . . 34
2.6 Velocity and density signal processing . . . 44
2.7 Summary . . . 54

3 Experimental results **56**
3.1 Inlet flow conditions . . . 57
3.2 Gravity current profiles: 0,9 m from the inlet . . . 64
3.3 Gravity current profiles: 2,4 m from the inlet . . . 88
3.4 Summary . . . 106

4 Numerical model and results **110**
4.1 Computational Fluid Dynamics software . . . 111
4.2 Governing equations for a multispecies mixture . . . 113
4.3 Turbulence Model . . . 123
4.4 Grid, boundary conditions and initial conditions . . . 132
4.5 Solution technique . . . 142
4.6 Sensitivity analysis of turbulence models . . . 156
4.7 Sensitivity analysis of inlet conditions . . . 161
4.8 Evaluation of model accuracy . . . 171
4.9 Summary . . . 180

5 Conclusions and Recommendations **183**
5.1 Conclusions . . . 183
5.2 Recommendations . . . 186

List of References **189**

Appendices **194**

A Tables of depth-averaged differences and errors **195**

B FLUENT User Defined Functions **200**
B.1 Mixture density . . . 200
B.2 Molecular mixture viscosity . . . 201
B.3 Effective diffusivity of $NaCl$ species . . . 201

C Tensor integral theorems **202**
C.1 Gauss divergence theorem . . . 202
C.2 Integration by parts . . . 202
C.3 Differentiation of a volume integral (Leibniz formula) . . . 203

D Original contributions **204**

D.1 Contributions by George Gerber 204
D.2 Contributions not by George Gerber 207
D.3 Location where research was conducted 207

List of Figures

1 Outer length and velocity scales for a gravity current (same as fig. 3.3) xxx

1.1 Gravity currents formed by opening the door between a warm and cool room . . . 2
1.2 Possible flow routes of a gravity current entering a reservoir . . . 3
1.3 Different levels of turbulent mass and momentum transport for a saline gravity current (Simpson, 1997) . . . 5
(a) 0° slope . . . 5
(b) 5° slope . . . 5
(c) 20° slope . . . 5
1.4 Water entrainment as a function stratification: historical data (Bournet *et al.*, 1999) . . . 8

2.1 Layout of mixture tank, inlet, flume and damping tank . . . 22
2.2 Photographs of mixture tank, inlet, flume and damping tank . . . 23
(a) Mixture tank . . . 23
(b) Damping tank . . . 23
(c) Flow conditioning inlet and perspex flume . . . 23
2.3 Photographs of pink dyed gravity current (present research) . . . 25
(a) Siphons with gravity current entering the flume . . . 25
(b) Gravity current body . . . 25
(c) Siphons and lightsheet with passing gravity current head . . . 25
2.4 Laser, lightsheet lenses and mirror . . . 26
2.5 Microscope photograph of 20 micron polyamid particles. Particles on ruler with 1mm markings. . . . 27
2.6 Digital camera, camera lens and laptop . . . 28
2.7 Camera timing sequence . . . 29
2.8 A typical PIV image pair, near the bed of the flume. Flow direction is downwards. (images rotated 90° clockwise) . . . 29
(a) First image . . . 29
(b) Second image . . . 29

2.9 One-dimensional, frequency based, energy spectrum of the gravity current: 0,9 m downstream from inlet and 24 mm above the bed 32
2.10 Displacement histograms of the gravity current: 2,4 m from inlet and 40 mm above the bed 33
(a) X-displacement histogram 33
(b) Y-displacement histogram 33
2.11 Fluid density as functions of NaCl mass fraction and temperature (CRC handbook of chemistry and physics, pg. 8-73, 6-3) 35
(a) NaCl mass fraction 35
(b) Temperature 35
2.12 Threshold sensitivity analysis on spatially-averaged intensity profiles . . 38
(a) Mean spatially averaged intensity 38
(b) Variance of spatially averaged intensity 38
2.13 Threshold sensitivity analysis on excess density profiles 39
(a) Mean excess density 39
(b) Variance of excess density 39
2.14 Background noise removal by pixel intensity thresholding 40
(a) No thresholding 40
(b) Threshold value of 150 40
2.15 Window size sensitivity analysis on spatially-averaged intensity profiles 41
(a) Mean spatially averaged intensity 41
(b) Variance of spatially averaged intensity 41
2.16 Test cases on spatially-averaged intensity profiles: No flow, clear-water flow and gravity current flow 43
(a) Mean spatially-averaged intensity 43
(b) Variance of spatially-averaged intensity 43
2.17 Polynomial degree sensitivity analysis: 0,9 m from the inlet 45
(a) Mean excess density as a function of mean spatially averaged intensity 45
(b) Excess density variance profile 45
2.18 Polynomial degree sensitivity analysis: 2,4 m from the inlet 46
(a) Mean excess density as a function of mean spatially averaged intensity 46
(b) Excess density variance profile 46
2.19 v-velocity time series for a point 2,4 m from inlet and 40 mm above the bed, sampled at 6 Hz 47
2.20 Measured sample autocorrelation coefficients for a point 2.4m from inlet and 40mm above the bed (present research) 51
(a) Sample autocorrelation coefficient of u-velocity 51
(b) Sample autocorrelation coefficient of v-velocity 51

3.1 Inlet flow profiles: plan view 61

(a) Mean velocity 61
(b) Turbulence intensity 61
3.2 One dimensional, wavenumber-based, energy spectrum at centre of inlet: present research and Pope (2001, pg. 235) 63
3.3 Outer length and velocity scales for a gravity current 66
3.4 Mean streamwise velocity: present research 69
(a) outer scaling 69
(b) inner scaling 69
3.5 Mean cross-stream velocity: present research 70
3.6 Mean excess density: present research 70
3.7 Mean velocity gradients: present research 71
3.8 Gradient Richardson number: present research 71
3.9 Gravity current Reynolds stress profiles: present research 75
(a) outer scaling 75
(b) inner scaling 75
3.10 Wall-jet Reynolds stress profiles (outer scaling): Eriksson *et al.* (1998) . 76
(a) 76
(b) 76
(c) 76
3.11 Gravity current Reynolds stress profiles (outer scaling): Buckee *et al.* (2001) 77
3.12 Gravity current Reynolds flux profiles: present research 79
(a) outer scaling 79
(b) inner scaling 79
3.13 Wall-jet Reynolds flux profiles (outer scaling):Ahlman (2006) 80
(a) Streamwise flux (u-component) 80
(b) Cross-stream flux (v-component) 80
3.14 Profiles of gravity current excess density intensity and wall-jet scalar intensity (outer scaling) 81
(a) Gravity current excess density intensity: present research . . 81
(b) Wall-jet scalar intensity: Ahlman (2006) 81
3.15 Partial budget of turbulent kinetic energy: present research 83
(a) outer scaling 83
(b) inner scaling 83
3.16 Turbulent viscosity and diffusivity ratio profiles (outer scaling): present research 85
(a) Turbulent viscosity ratio 85
(b) Turbulent diffusivity ratio 85
3.17 Turbulent Schmidt number: present research 86
3.18 Energy spectra of u- and v-velocities at $y/y_{0.5} = 0.44$: present research 87
3.19 Mean streamwise velocity: present research 90
(a) outer scaling 90

(b) inner scaling 90
3.20 Mean cross-stream velocity: present research 91
3.21 Mean excess density: present research 91
3.22 Mean velocity gradients: present research 92
3.23 Gradient Richardson number: present research 92
3.24 Gravity current Reynolds stress profiles at 2,4 m: present research . . . 95
(a) outer scaling 95
(b) inner scaling 95
3.25 Reynolds stress profiles at 0,9 m and 2,4 m: present research 96
(a) $\langle u'u' \rangle$ 96
(b) $\langle v'v' \rangle$ 96
(a) $\langle u'v' \rangle$ Reynolds stress profiles at 0,9 m and 2,4 m: present research 97
(b) Gravity current Reynolds stresses (outer scaling): Buckee *et al.* (2001) 97
3.27 Gravity current Reynolds flux profiles at 2,4 m: present research 99
(a) outer scaling 99
(b) inner scaling 99
3.28 Gravity current Reynolds flux profiles at 0,9 m and 2,4 m (outer scaling): present research 100
(a) Streamwise Reynolds flux 100
(b) Cross-stream Reynolds flux 100
3.29 Profiles of gravity current excess density intensity and standard deviation (outer scaling) 101
(a) Gravity current excess density intensity at 0,9 m and 2,4 m: present research 101
(b) Gravity current excess density standard deviation: Buckee *et al.* (2001) 101
3.30 Partial budget of turbulent kinetic energy: present research 103
(a) outer scaling 103
(b) inner scaling 103
3.31 Turbulent viscosity ratio profiles: present research 104
(a) outer scaling (at 0,9 m and 2,4 m) 104
(b) inner scaling (at 2,4 m) 104
3.32 Turbulent diffusivity and Schmidt number profiles (outer scaling): present research 105
(a) Turbulent diffusivity (at 0,9 m and 2,4 m) 105
(b) Turbulent Schmidt number (at 2,4 m) 105
3.33 Energy spectra of u- and v-velocities at $y/y_{0.5} = 0.47$: present research 106

4.1 Dynamic viscosity dependence on $NaCl$ mass fraction (CRC handbook of chemistry and physics, pg. 8-73) 123

4.2 Overall grid and near-wall grid quality 133
(a) Computational grid and boundary conditions 133
(b) Cell centroid profile for bed adjacent cells ($k-\epsilon$ model) . . . 133
4.3 Simulated U-profiles for different initial values of ϵ, based on standard $k-\epsilon$ model: present research 143
(a) 0,9 m from the inlet 143
(b) 2,4 m from the inlet 143
4.4 Simulated $\langle\Delta\rho\rangle$-profiles for different initial values of ϵ, based on standard $k-\epsilon$ model: present research 144
(a) 0,9 m from the inlet 144
(b) 2,4 m from the inlet 144
4.5 Simulated U-profiles for different grid resolutions with standard $k-\epsilon$ model: present research 149
(a) 0,9 m from the inlet 149
(b) 2,4 m from the inlet 149
4.6 Simulated $\langle\Delta\rho\rangle$-profiles for different grid resolutions with standard $k-\epsilon$ model: present research 150
(a) 0,9 m from the inlet 150
(b) 2,4 m from the inlet 150
4.7 Simulated U-profiles for different scaled residuals R^{ϕ} with standard $k-\epsilon$ model: present research 151
(a) 0,9 m from the inlet 151
(b) 2,4 m from the inlet 151
4.8 Simulated $\langle\Delta\rho\rangle$-profiles for different scaled residuals R^{ϕ} with standard $k-\epsilon$ model: present research 152
(a) 0,9 m from the inlet 152
(b) 2,4 m from the inlet 152
4.9 Simulated U-profiles for different flume depths with standard $k-\epsilon$ model: present research 154
(a) 0,9 m from the inlet 154
(b) 2,4 m from the inlet 154
4.10 Simulated $\langle\Delta\rho\rangle$-profiles for different flume depths with standard $k-\epsilon$ model: present research 155
(a) 0,9 m from the inlet 155
(b) 2,4 m from the inlet 155
4.11 Simulated $\langle\Delta\rho\rangle$-profiles for different turbulence models and turbulent Schmidt numbers σ_t: present research 158
(a) 0,9 m from the inlet 158
(b) 2,4 m from the inlet 158
4.12 Simulated U-profiles for different turbulence models and turbulent Schmidt numbers σ_t: present research 159
(a) 0,9 m from the inlet 159

(b) 2,4 m from the inlet . . . 159
4.13 Simulated $\langle\Delta\rho\rangle$ contour time series: standard $k-\epsilon$ model with $\sigma_t = 1{,}3$: present research . . . 160
(a) t=8s . . . 160
(b) t=78s . . . 160
(c) t=148s . . . 160
(d) t=218s . . . 160
(e) t=288s . . . 160
4.14 Simulated $\langle\Delta\rho\rangle$ contour time series: RNG $k-\epsilon$ model: present research 160
(a) t=8s . . . 160
(b) t=78s . . . 160
(c) t=148s . . . 160
(d) t=218s . . . 160
(e) t=288s . . . 160
4.15 Simulated U-profiles for different inlet velocities with standard $k-\epsilon$ model: present research . . . 163
(a) 0,9 m from the inlet . . . 163
(b) 2,4 m from the inlet . . . 163
4.16 Simulated $\langle\Delta\rho\rangle$-profiles for different inlet velocities with standard $k-\epsilon$ model: present research . . . 164
(a) 0,9 m from the inlet . . . 164
(b) 2,4 m from the inlet . . . 164
4.17 Simulated U-profiles for different inlet $NaCl$ mass fractions with standard $k-\epsilon$ model: present research . . . 165
(a) 0,9 m from the inlet . . . 165
(b) 2,4 m from the inlet . . . 165
4.18 Simulated $\langle\Delta\rho\rangle$-profiles for different inlet $NaCl$ mass fractions with standard $k-\epsilon$ model: present research . . . 166
(a) 0,9 m from the inlet . . . 166
(b) 2,4 m from the inlet . . . 166
4.19 Simulated U-profiles for different inlet k values with standard $k-\epsilon$ model: present research . . . 167
(a) 0,9 m from the inlet . . . 167
(b) 2,4 m from the inlet . . . 167
4.20 Simulated $\langle\Delta\rho\rangle$-profiles for different inlet k values with standard $k-\epsilon$ model: present research . . . 168
(a) 0,9 m from the inlet . . . 168
(b) 2,4 m from the inlet . . . 168
4.21 Simulated U-profiles for different inlet ϵ values with standard $k-\epsilon$ model: present research . . . 169
(a) 0,9 m from the inlet . . . 169
(b) 2,4 m from the inlet . . . 169

4.22 Simulated $\langle\Delta\rho\rangle$-profiles for different inlet ϵ values with standard $k-\epsilon$ model: present research 170
(a) 0,9 m from the inlet 170
(b) 2,4 m from the inlet 170
4.23 Mean U-profiles: Simulated and PIV-S measurements: present research 174
(a) 0,9 m from the inlet 174
(b) 2,4 m from the inlet 174
4.24 Mean $\langle\Delta\rho\rangle$-profiles: Simulated and PIV-S measurements: present research 175
(a) 0,9 m from the inlet 175
(b) 2,4 m from the inlet 175
4.25 ν_t/ν-profiles: Simulated and PIV-S measurements: present research . . 176
(a) 0,9 m from the inlet 176
(b) 2,4 m from the inlet 176
4.26 $\langle\Delta\rho' v'\rangle$-profiles: Simulated and PIV-S measurements: present research 177
(a) 0,9 m from the inlet 177
(b) 2,4 m from the inlet 177
4.27 $\mathcal{P}$- and G_b-profiles: Simulated and PIV-S measurements: present research 178
(a) 0,9 m from the inlet 178
(b) 2,4 m from the inlet 178
4.28 Downstream development of gravity current: Simulated and PIV-S measurements: present research 179
(a) Outer lengthscale $y_{0.5}$ 179
(b) Maximum $NaCl$ mass fraction $\langle\omega\rangle_{max}$ 179
4.29 Downstream development of outer velocity scale U_{max}: Simulated and PIV-S measurements: present research 179

List of Tables

3.1 Inlet flow conditions 62
3.2 Gravity current flow conditions near the inlet 67
3.3 Gravity current flow conditions far from inlet 89

4.1 Definitions of multispecies mixture variables (Bird *et al.*, 2002) 114
4.2 Inlet boundary conditions 136
4.3 Initial conditions 142
4.4 Interpolation schemes for solution variables 147
4.5 Under-relaxation factors for solution variables 147

A.1 Depth-averaged differences: $\delta_d[U, \epsilon = 1{,}38 \times 10^{-5}, \text{alternative}]$ 195
A.2 Depth-averaged differences: $\delta_d[\langle\Delta\rho\rangle, \epsilon = 1{,}38 \times 10^{-5}, \text{alternative}]$ 195
A.3 Depth-averaged differences: $\delta_d[U, 16\text{x}660, \text{alternative}]$ 195
A.4 Depth-averaged differences: $\delta_d[\langle\Delta\rho\rangle, 16\text{x}660, \text{alternative}]$ 196
A.5 Depth-averaged differences: $\delta_d[U, R^\phi = 10^{-4}, \text{alternative}]$ 196
A.6 Depth-averaged differences: $\delta_d[\langle\Delta\rho\rangle, R^\phi = 10^{-4}, \text{alternative}]$ 196
A.7 Depth-averaged differences: $\delta_d[U, U = 0{,}079, \text{alternative}]$ 196
A.8 Depth-averaged differences: $\delta_d[\langle\Delta\rho\rangle, U = 0{,}079, \text{alternative}]$ 196
A.9 Depth-averaged differences: $\delta_d[U, \langle\omega\rangle = 0{,}002\,81, \text{alternative}]$ 197
A.10 Depth-averaged differences: $\delta_d[\langle\Delta\rho\rangle, \langle\omega\rangle = 0{,}002\,81, \text{alternative}]$ 197
A.11 Depth-averaged differences: $\delta_d[U, k = 6{,}875 \times 10^{-5}, \text{alternative}]$ 197
A.12 Depth-averaged differences: $\delta_d[\langle\Delta\rho\rangle, k = 6{,}875 \times 10^{-5}, \text{alternative}]$ . . . 197
A.13 Depth-averaged differences: $\delta_d[U, \epsilon = 1{,}38 \times 10^{-5}, \text{alternative}]$ 197
A.14 Depth-averaged differences: $\delta_d[\langle\Delta\rho\rangle, \epsilon = 1{,}38 \times 10^{-5}, \text{alternative}]$ 197
A.15 Depth-averaged errors: $\varepsilon_d[U, \text{PIV-S}, \text{alternative}]$ 198
A.16 Depth-averaged errors: $\varepsilon_d[\langle\Delta\rho\rangle, \text{PIV-S}, \text{alternative}]$ 198
A.17 Depth-averaged errors: $\varepsilon_d[\nu_t/\nu, \text{PIV-S}, \text{alternative}]$ 198
A.18 Depth-averaged errors: $\varepsilon_d[\langle\Delta\rho' v'\rangle, \text{PIV-S}, \text{alternative}]$ 198
A.19 Depth-averaged errors: $\varepsilon_d[\mathcal{P}, \text{PIV-S}, \text{alternative}]$ 199

Nomenclature

An excellent aid to the vector and tensor algebra used in this dissertation can be found in Appendix A of Bird *et al.* (2002).

Mathematical symbols

ϕ No bar: A scalar, such as instantaneous density ρ

$\bar{\phi}$ Single bar: A first order tensor, such as the instantaneous velocity vector

$$\bar{u} = \left\{ \begin{array}{c} u \\ v \end{array} \right\}$$

$\bar{\bar{\phi}}$ Double bar: A second order tensor, such as the instantaneous viscous stress tensor

$$\bar{\bar{\tau}} = \left[\begin{array}{cc} \tau_{xx} & \tau_{xy} \\ \tau_{yx} & \tau_{yy} \end{array} \right]$$

$\langle\phi\rangle$ Angular brackets: Mean value of ϕ. Furthermore, uppercase symbols are also used to denote mean values.

ϕ' Single prime: Fluctuation of ϕ from its mean value. Therefore, ϕ can be regarded as both the sum of a mean value $\langle\phi\rangle$ and a fluctuation ϕ'

$$\phi = \langle\phi\rangle + \phi'$$

$\Delta\phi$ Delta: Excess of ϕ with respect to a reference value. For example the excess density of a saline mixture having a density ρ with respect to the density of water ρ_w is given by

$$\Delta\rho = \rho - \rho_w$$

$\bar{\nabla}$ Nabla: In two-dimensional (2D) problems it is given by

$$\bar{\nabla} = \left\{ \begin{array}{c} \frac{\partial}{\partial x} \\ \frac{\partial}{\partial y} \end{array} \right\}$$

$\bar{\nabla}\phi$ Gradient of ϕ: In two-dimensional (2D) problems it is given by

$$\bar{\nabla}\phi = \left\{ \begin{array}{c} \frac{\partial \phi}{\partial x} \\ \frac{\partial \phi}{\partial y} \end{array} \right\}$$

$\bar{\phi} \cdot \bar{\theta}$ Single dot: Dot product of two single order tensors

$\bar{\bar{\phi}} : \bar{\bar{\theta}}$ Double dot: Double dot product of a second order tensor with a third order tensor

$\bar{\nabla} \cdot \bar{\phi}$ Divergence of $\bar{\phi}$: In two-dimensional (2D) problems it is given by

$$\bar{\nabla} \cdot \bar{\phi} = \frac{\partial \phi}{\partial x} + \frac{\partial \phi}{\partial y}$$

$\frac{D\,\phi}{D\,t}$ Total derivative, or Lagrangean time derivative, which can be written as

$$\frac{D\,\phi}{D\,t} = \frac{\partial \phi}{\partial t} + \bar{u} \cdot \bar{\nabla}\phi$$

Uppercase and lowercase symbols

Uppercase symbols denote mean values, for example $\bar{U}\ (= \langle \bar{u} \rangle)$
Lowercase symbols with a prime denote fluctuating values, for example $\bar{u}'$
Lowercase symbols without a prime denote instantaneous values, for example $\bar{u}$

Roman symbols

A	surface of material volume
$\bar{A}$	surface vector
$\bar{A}_f$	surface vector at cell face
a_{nb}	influence coefficient of neighbour cell
a_p	centre coefficient of discretized equation
ΔB	law-of-the-wall constant for bed roughness
b	inlet width
b	constant part of linearized source term
C_s	roughness constant
$C_{1\epsilon}$	first constant of ϵ equation
$C_{2\epsilon}$	second constant of ϵ equation
$C^*_{2\epsilon}$	second constant of ϵ equation in RNG $k-\epsilon$ model
$C_{3\epsilon}$	third constant of ϵ equation
C_μ	turbulent viscosity constant
C_ν	constant for effective viscosity in RNG $k-\epsilon$ model
D	inlet hydraulic diameter
d_p	particle diameter
E	empirical constant for law-of-the-wall
$E(\kappa)$	Three dimensional wavenumber based energy spectrum
$E_{uu}(\kappa_1)$	One dimensional wavenumber based energy spectrum of streamwise velocity
$E_{vv}(f)$	One dimensional frequency based energy spectrum of cross-stream velocity
$E_{vv}(\kappa_1)$	One dimensional wavenumber based energy spectrum of cross-stream velocity
f	frequency
f	empirical function relating density to spatially-averaged intensity
G_b	buoyancy production of turbulent kinetic energy
g	magnitude of gravitational acceleration
$\bar{g}$	gravitational acceleration vector
H_d	mean depth-averaged current height
h	inlet height
I_o	inlet turbulence intensity, based on streamwise velocity
$\bar{\bar{I}}$	identity tensor
$i_s(m_o, n_o)$	spatially-averaged intensity at centre of interrogation window
$\langle i_s \rangle$	mean spatially-averaged intensity
$\langle i'_s i'_s \rangle$	spatially-averaged intensity variance
$i_1(m, n)$	intensity at pixel position (m, n) in first image
$i_2(m+dm, n+dn)$	intensity at pixel position $(m+dm, n+dn)$ in second image
$\bar{j}_\alpha$	diffusive flux of specie α

k	turbulent kinetic energy
k_o	inlet turbulent kinetic energy
k_p	turbulent kinetic energy at wall adjacent node
k_s	roughness height
k_s^+	dimensionless roughness height
$\bar{n}$	normal vector of material volume surface
P	mean pressure
$\mathcal{P}$	shear production of turbulent kinetic energy
$\mathcal{P}_{cell}$	cell-averaged shear production of turbulent kinetic energy
p'	pressure fluctuation
p^*	instantaneous absolute pressure
p_r	reference pressure
Q	inlet flow rate
$R\left(dm, dn\right)$	cross-correlation value of displacement (dm, dn)
R^ϕ	scaled residual of scalar ϕ
R_λ	Taylor Reynolds number
$R_{vv}\left(s\right)$	autocorrelation function of cross-stream velocity
$R_{vv,i}[p]$	unbiased sample autocorrelation value for subsequence i
$R_{vv}[p]$	average unbiased sample autocorrelation value
Re_o	inlet Reynolds number
Re_D	inlet Reynolds number, based on hydraulic diameter
Ri	bulk Richardson number
Ri_f	flux Richardson number
Ri_g	gradient Richardson number
Ri_o	inlet bulk Richardson number
$\bar{\bar{S}}$	mean rate-of-strain tensor
s	time lag
$\bar{\bar{s}}$	rate-of-strain tensor
$\bar{\bar{s}}'$	rate-of-strain tensor fluctuation
S_ϕ	source term of scalar ϕ
St	Stokes number
T	integration time
T	transpose of a tensor
$\mathcal{T}$	integral timescale
$\mathcal{T}_{vv}$	integral timescale, based on cross-stream velocity
t	time
Δt	time-step size
U	mean streamwise velocity
$\bar{U}$	mean velocity vector
U^*	friction velocity
U^+	dimensionless velocity
$\bar{\nabla}\bar{U}$	gradient of mean velocity vector
U_{bulk}	mean cross-section averaged inlet velocity
U_d	mean depth-averaged streamwise current velocity

$\bar{U}_f$	mean velocity vector at cell face
U_{max}	maximum mean streamwise velocity. Outer velocity scale
$U_{o\,max}$	inlet maximum mean streamwise velocity
U_{ref}	reference velocity
$\langle u \rangle$	mean streamwise velocity
$\bar{u}$	velocity vector
$\bar{u}'$	fluctuation of velocity vector
u'	fluctuation of streamwise velocity
$\bar{u}_\alpha$	velocity of specie α
$\langle \bar{u}'\bar{u}' \rangle$	velocity variance tensor. Reynolds stress tensor
$\langle u'u' \rangle$	streamwise velocity variance. Normal Reynolds stress
$\langle u'u' \rangle_o$	inlet streamwise velocity variance. Normal Reynolds stress
$\langle u'v' \rangle$	covariance of streamwise and cross-stream velocity components. Shear Reynolds stress
$\langle u'v' \rangle_o$	inlet covariance of streamwise and cross-stream velocity components. Shear Reynolds stress
$\langle u'w' \rangle_o$	inlet covariance of streamwise and spanwise velocity components. Shear Reynolds stress
V	volume of material volume
V	volume of computational cell
V	mean cross-stream velocity component
v'	fluctuation of cross-stream velocity
$\langle v'v' \rangle$	cross-stream velocity variance. Normal Reynolds stress
$\langle v'v' \rangle_o$	inlet cross-stream velocity variance. Normal Reynolds stress
$\langle w'w' \rangle$	spanwise velocity variance. Normal Reynolds stress
$\langle w'w' \rangle_o$	inlet spanwise velocity variance. Normal Reynolds stress
x	streamwise coordinate
y	cross-stream coordinate or flow depth
y^+	dimensionless cross-stream coordinate
y_v	viscous sublayer thickness
y_n	height of wall adjacent cell
$y_{0.5}$	outer lengthscale. Halfwidth of gravity current

Greek symbols

α	specie index
β	constant of RNG $k-\epsilon$ model
γ	molecular diffusivity
γ_t	turbulent diffusivity
γ_ϕ	diffusivity of scalar ϕ
δ_d	depth-averaged difference
ϵ	dissipation rate of turbulent kinetic energy
ϵ_{cell}	cell-averaged dissipation rate of turbulent kinetic energy
ϵ_o	inlet dissipation rate of turbulent kinetic energy
ϵ_p	dissipation rate of turbulent kinetic energy at the wall adjacent cell
ϵ_u	estimated dissipation rate of turbulent kinetic energy, based on streamwise velocity
ϵ_v	estimated dissipation rate of turbulent kinetic energy, based on cross-stream velocity
ε_d	depth-averaged error
η	Kolmogorov lengthscale
η_0	constant for RNG $k-\epsilon$ model
θ	temperature
κ	von Karman constant
$\bar{\kappa}$	wavenumber vector
κ	wavenumber magnitude
κ_1	streamwise component of wavenumber vector
λ_{emit}	dye emittance wavelength
λ_{excite}	dye excitation wavelength
λ_g	Taylor microscale
λ_{lp}	cutoff wavelength of long-pass filter
μ	dynamic viscosity of fluid
ν	molecular kinematic viscosity
$\hat{\nu}$	ratio of effective kinematic viscosity to molecular kinematic viscosity
ν_{eff}	effective kinematic viscosity
ν_t	turbulent kinematic viscosity
ρ	mixture density
ρ_f	mixture density at cell face
ρ_p	particle density
$\rho_{vv}(s)$	autocorrelation coefficient of cross-stream velocity
$\rho_{vv}[p]$	sample autocorrelation coefficient
ρ_w	density of water
ρ_α	mass density of specie α
$\langle\rho\rangle$	mean density
$\langle\rho\rangle_d$	mean depth-averaged density

$\langle \rho' \bar{u}' \rangle$	covariance of excess density and velocity vector. Reynolds flux tensor
$\langle \Delta\rho \rangle$	mean excess density
$\Delta\rho$	excess density of mixture
$\Delta\rho'$	fluctuation of excess density
$\langle \Delta\rho \rangle_d$	mean depth-averaged excess density
$\langle \Delta\rho \rangle_{max}$	maximum mean excess density
$\langle \Delta\rho \rangle_o$	inlet mean excess density
$\langle \Delta\rho \rangle_{pivs}$	mean excess density measured by PIV-S
$\langle \Delta\rho \rangle_{siphon}$	mean excess density measured with siphons
$\langle \Delta\rho' u' \rangle$	covariance of excess density and streamwise velocity
$\langle \Delta\rho' v' \rangle$	covariance of excess density and cross-stream velocity
$\langle \Delta\rho' \Delta\rho' \rangle$	excess density variance
σ	molecular Schmidt number
σ_0	Prandtl number constant for RNG $k-\epsilon$ model
σ_k	Prandtl number for k
σ_t	turbulent Schmidt number
σ_ϵ	Prandtl number for ϵ
τ	total shear stress
$\bar{\bar{\tau}}$	viscous stress tensor
$\langle \bar{\bar{\tau}} \rangle$	mean viscous stress tensor
τ_k	Kolmogorov timescale
τ_p	particle response time
τ_t	turbulent shear stress
τ_w	wall shear stress
ϕ	scalar quantity
ϕ^{n-1}	scalar value at previous time level
ϕ^n	scalar value at present time level
ϕ^{n+1}	scalar value at next time level
ϕ_f	scalar value at cell face
ϕ_{nb}	discrete scalar value at centre of neighbour cell
ϕ_p	discrete scalar value at centre of cell p
ω	$NaCl$ mass fraction
$\langle \omega \rangle$	mean $NaCl$ mass fraction
$\langle \omega \rangle_o$	inlet mean $NaCl$ mass fraction
ω_α	mass fraction of specie α
$\langle \omega_\alpha \rangle$	mean mass fraction of specie α
ω'_α	mass fraction fluctuation of specie α
$\langle \omega' \bar{u}' \rangle$	covariance of $NaCl$ mass fraction and velocity vector. Reynolds flux vector
$\langle \omega' \omega' \rangle$	$NaCl$ mass fraction variance

Glossary

This list contains terminology used in this dissertation. The definitions are intended as an aid to reading.

Bulk Richardson number The bulk Richardson number is the ratio between buoyancy forces and inertia forces. It is defined as (Ellison and Turner, 1959)

$$Ri = \frac{g \langle \Delta\rho \rangle_d H_d}{\rho_w U_d^2} \tag{1}$$

with

$$\langle \Delta\rho \rangle_d = \langle \rho \rangle_d - \rho_w \tag{2}$$

where g is the magnitude of gravity acceleration, $\langle \Delta\rho \rangle_d$ is the mean depth-averaged excess density of the fluid, $\langle \rho \rangle_d$ is the mean depth-averaged density of the fluid, ρ_w is the density of water, while U_d and H_d are the mean depth-averaged current velocity and current height.

For $Ri < 1$, inertial forces dominate the buoyancy forces. Analogous to open-channel flow this is referred to as supercritical flow. A supercritical bulk Richardson number indicates a less stable interface between the gravity current and the ambient fluid. The reduced stability increases the amount of mixing across the interface, which in turn increases the entrainment of ambient fluid into the current (Ellison and Turner, 1959). In the limit of a zero bulk Richardson number, the gravity current becomes essentially a non-buoyant wall jet (Fernandez and Imberger, 2006).

For $Ri > 1$, buoyancy forces dominate inertial forces. This is referred to as subcritical flow. A subcritical Richardson number indicates a stable interface. A stable interface dampens the turbulence and hence reduces mixing. This results in a reduction in the entrainment of ambient fluid into the gravity current.

Coordinate system The coordinate system used in this dissertation is as follows: x denotes the streamwise coordinate and y the cross-stream coordinate. Furthermore, u denotes the streamwise velocity component, while v denotes the cross-stream velocity component. Hence for a horizontal flow, u denotes the horizontal velocity component and v the vertical velocity component. In the case of a vertical flow, u denotes the vertical velocity component and v the horizontal velocity component. This coordinate system is similar to the one used by Hossain and Rodi (1977).

Depth-averaged scales Historical experimental studies on gravity currents have found it useful to normalize velocity and density profiles with depth-averaged scales (Garcia, 1993), (Parker *et al.*, 1987). These depth-averaged scales include: the depth-averaged current velocity U_d, depth-averaged current height H_d and depth-averaged excess density $\langle \Delta\rho \rangle_d$. These scales are calculated from the following moments

$$U_d H_d = \int_0^\infty U \, dy \tag{3}$$

$$U_d^2 H_d = \int_0^\infty U^2 \, dy \tag{4}$$

$$U_d \langle \Delta\rho \rangle_d H_d = \int_0^\infty U \langle \Delta\rho \rangle \, dy \tag{5}$$

where U is the mean streamwise velocity, $\langle \Delta\rho \rangle$ is the mean excess density of the fluid and $y = \infty$ is height of the free surface. These scales are often used to calculate the depth-averaged Reynolds number and bulk Richardson number.

DNS Direct numerical simulation (DNS) is a simulation approach which solves the continuity, Navier-Stokes and scalar transport equations for the *whole* spectrum of length and timescales of turbulence. No modeling assumptions are required. However, the computational effort required to simulate the whole spectrum of length and timescales at even moderate Reynolds numbers makes DNS impractical for industrial use. DNS is primarily used for research.

Flux Richardson number The Flux Richardson number is the ratio between buoyancy and shear production of turbulent kinetic energy k (Tennekes and Lumley, 1973, pg. 98). It is defined as

$$Ri_f = -\frac{G_b}{\mathcal{P}} \tag{6}$$

with

$$G_b = \frac{\bar{g}}{\rho_w} \cdot \langle \Delta\rho' \bar{u}' \rangle \tag{7}$$

$$\mathcal{P} = -\langle \bar{u}' \bar{u}' \rangle : \bar{\bar{S}} \tag{8}$$

$$\bar{\bar{S}} = \frac{1}{2}\left(\bar{\nabla}\bar{U} + \bar{\nabla}\bar{U}^T\right) \tag{9}$$

where G_b is the production of k due to buoyancy, $\mathcal{P}$ is the production of k due to shearing, $\bar{g}$ is the gravity acceleration vector equal to 9,81 m/s^2 vertically downwards, $\Delta\rho'$ is the fluctuation of the excess density of the fluid, $\bar{u}'$ is the fluctuation of the velocity vector, $\langle \Delta\rho' \bar{u}' \rangle$ is the Reynolds flux vector, $\langle \bar{u}' \bar{u}' \rangle$ is the Reynolds stress tensor, $\bar{\bar{S}}$ is the mean rate-of-strain tensor, $\bar{\nabla}\bar{U}$ is the gradient of the mean velocity vector and T denotes the transpose of this tensor. $\mathcal{P}$ is usually positive, since $\langle \bar{u}' \bar{u}' \rangle$ and $\bar{\bar{S}}$ have, in general, opposite signs.

For $Ri_f < 0$ (unstable stratification) buoyancy converts potential energy to turbulent kinetic energy and conversely for $Ri_f > 0$ (stable stratification) buoyancy converts turbulent kinetic energy into potential energy. When buoyancy production becomes too large relative to shear production in a stably stratified flow, turbulence cannot be maintained unless an external energy source exists. Hossain and Rodi (1977) found that for heated water jets turbulence collapsed when $Ri_f > 0{,}4$.

Gradient Richardson number Unlike the bulk Richardson number, which is a depth-averaged quantity, the gradient Richardson number indicates whether a point in the flow is stably stratified or not. It is given by (Tennekes and Lumley, 1973, pg. 99):

$$Ri_g \equiv -\frac{g}{\rho_w} \frac{\frac{\partial \langle \rho \rangle}{\partial y}}{\left(\frac{\partial U}{\partial y}\right)^2} \tag{10}$$

where $\langle \rho \rangle$ is the mean density. According to Turner (1973, pg. 99) turbulence cannot be maintained in stably stratified flows when $Ri_g > 0{,}25$, unless an external energy source exists. Hence, in the absence of an external source, turbulence eventually collapses.

Homogeneous turbulence occurs when the fluctuating velocity field is statistically invariant to translations of the coordinate axes (Pope, 2001, pg. 76). This implies that the gradients of mean quantities, containing fluctuating velocities, are zero. For example

$$\frac{\partial}{\partial x}\left\langle u' \frac{\partial u'}{\partial x} \right\rangle = 0 \tag{11}$$

where x is the streamwise coordinate and u' is the streamwise velocity fluctuation.

Inner scales George *et al.* (2000) shows that a turbulent plane wall jet, which is related to a gravity current, can be divided into an inner region next to the bed and an outer region further away from the bed. The characteristic velocity and lengthscales of the inner region are U^* and ν/U^*. With the friction velocity U^* defined as

$$U^* \equiv \sqrt{\frac{\tau_w}{\rho}} \tag{12}$$

where ν is the kinematic viscosity, τ_w is the wall shear stress and ρ is the density of the fluid. From these scales the dimensionless velocity U^+ and dimensionless cross-stream coordinate y^+ are defined as

$$u^+ = \frac{U}{U^*} \tag{13}$$

$$y^+ = \frac{yU^*}{\nu} \tag{14}$$

where y is the cross-stream coordinate (distance from the wall).

Isotropic turbulence occurs when the fluctuating velocity field is statistically invariant of rotations and reflections of the coordinate axes (Pope, 2001, pg. 76). This means that

$$\langle u'u' \rangle = \langle v'v' \rangle \qquad \langle u'v' \rangle = 0 \tag{15}$$

where v' is the cross-stream velocity fluctuation.

Outer scales George *et al.* (2000) show that the characteristic velocity and lengthscales of the outer region of a wall jet, which is related to a gravity current, are U_{max} and $y_{0.5}$. Figure 1 presents the definition sketch of these outer scales (George *et al.*, 2000; Eriksson *et al.*, 1998).

Experiments (Eriksson *et al.*, 1998) have shown that the wall-jet is characterized by universal (or self-similar) velocity and turbulence profiles. Self-similar profiles are independent of downstream location. These profiles are derived by scaling the measured velocity and turbulence profiles by the outer scales of the flow.

Generally, self-similarity does not hold for horizontal gravity currents, since stable stratification reduces turbulence until it collapses (Hossain and Rodi, 1977). Despite this, gravity current research has found it useful to normalise velocity, density and turbulence profiles with the outer scales U_{max} and $y_{0.5}$ (Buckee *et al.*, 2001).

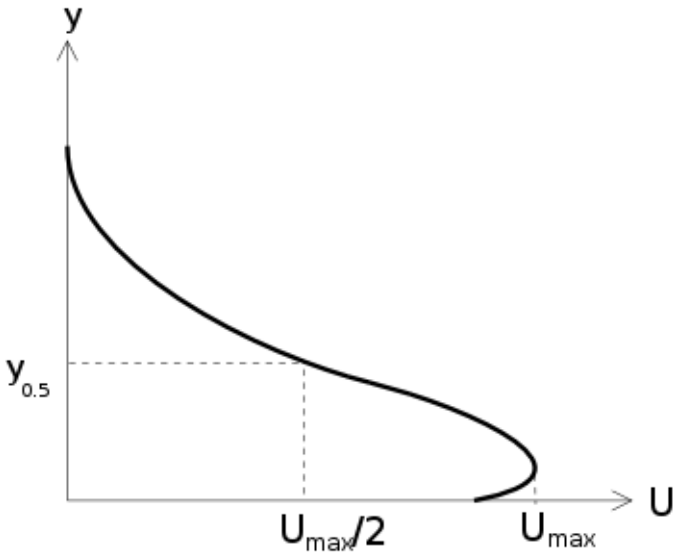

Figure 1: Outer length and velocity scales for a gravity current (same as fig. 3.3)

Particle Image Velocimetry (PIV) Particle image velocimetry (PIV) is a non-intrusive velocity measuring technique (Raffel *et al.*, 1998). The technique involves seeding a flow with small, reflective, neutrally-buoyant particles. A laser lightsheet illuminates the particles, which helps in visualizing the local flow velocity. A sequence of images is then recorded of the particles transported by the flow, using a digital camera. Local displacement estimates are then computed by cross-correlating two consecutive images of the image sequence with each other. The cross-correlation function is given by

$$R(dm, dn) = \sum_{m=-K}^{K} \sum_{n=-L}^{L} i_1(m, n) i_2(m + dm, n + dn) \tag{16}$$

where $R(dm, dn)$ is the cross-correlation value for displacement (dm, dn), $2K$ is the horizontal size of the interrogation window, $2L$ is the vertical size of the interrogation window, $i_1(m, n)$ is the intensity at pixel position (m, n) in the first image, $i_2(m + dm, n + dn)$ is the intensity at pixel $(m + dm, n + dn)$ in the second image. The displacement is associated with the largest $R(dm, dn)$ value, which is (dm, dn). Finally, local velocity estimates are computed by dividing the displacement estimates by the time elapsed between the recordings of the two consecutive images.

Particle Image Velocimetry-Scalar (PIV-S) Particle image velocimetry scalar (PIV-S) extends the PIV technique by measuring density non-intrusively

(Ramaprabhu and Andrews, 2003, 2004). The technique involves 'marking' fluids with different densities with different concentrations of tracer particles. A laser lightsheet illuminates the particles and helps in visualizing the spatial distribution of density. A sequence of grayscale images is then recorded of the flow. Since the spatially-averaged intensity (average color) in an image is dependent on the local particle concentration and since particle concentration is an indicator of density it follows that the spatially-averaged intensity is related to density.

$$\rho(x,y) = f\left(i_s(m_0,n_0)\right) \tag{17}$$

with

$$i_s(m_0,n_0) = \frac{\int_A i\,dA}{A} = \sum_{m=-K}^{K}\sum_{n=-L}^{L}\frac{i(m_0+m,n_0+n)}{4KL} \tag{18}$$

where $\rho(x,y)$ is the density estimate at laboratory coordinates (x,y), f is an empirical function relating density to spatially-averaged intensity, $i_s(m_0,n_0)$ is the spatially-averaged intensity at the center of the interrogation window, having pixel coordinates (m_0,n_0), A is the area of the interrogation window, $2K$ is the horizontal size of the interrogation window, $2L$ is the vertical size of the interrogation window and $i(m_0+m,n_0+n)$ is the pixel intensity at pixel coordinates (m_0+m,n_0+n).

Planar Laser Induced Fluorescence (PLIF) Planar laser induced fluorescence (PLIF) is based on the same concept as PIV-S (Fajardo *et al.*, 2006; Cowen *et al.*, 2001). That is, local densities are inferred from image color values. The spatial density distribution is visualized by exciting a fluorescent dye with a laser lightsheet. PLIF measurements have a very high spatial resolution (1x1 pixels), compared to PIV-S (for example 32x32 pixels).

RANS Reynolds-averaged Navier-Stokes models solve the Reynolds-averaged continuity, Navier-Stokes and scalar transport equations. These models avoid simulating the whole spectrum of length and timescales of turbulence by introducing assumptions regarding turbulence. Assumptions need to be made, since Reynolds-averaging introduces second order moments (Reynolds stresses and Reynolds fluxes) into the governing equations. These assumptions take the form of a turbulence model. RANS models can be accurate and their computational effort makes them practical for industrial use.

Schmidt number The Schmidt number is defined as the ratio between kinematic viscosity ν and molecular diffusivity γ

$$\sigma = \frac{\nu}{\gamma} \tag{19}$$

Eddy-viscosity turbulence models often use a turbulent Schmidt number σ_t, analogous to the Schmidt number σ defined above, to estimate turbulent diffusivity (Rodi, 1980, pg. 12), (Tennekes and Lumley, 1973, pg. 51)

$$\gamma_t = \frac{\nu_t}{\sigma_t} \tag{20}$$

where γ_t is the turbulent diffusivity and ν_t is the turbulent viscosity.

Shear flow occurs when at least one mean velocity gradient is non-zero (Tennekes and Lumley, 1973, pg. 34). For example

$$\frac{\partial \langle u \rangle}{\partial y} \neq 0 \tag{21}$$

where $\langle u \rangle$ is the mean streamwise velocity.

Stationary turbulence occurs when the fluctuating velocity field is statistically invariant to shifts in time (Pope, 2001, pg. 75). For example

$$\frac{\partial \langle u'u' \rangle}{\partial t} = 0 \tag{22}$$

where $\langle u'u' \rangle$ is the streamwise velocity variance and t is time.

Stokes number The Stokes number St is the ratio between the particle response time τ_p and the timescale of a fluctuating motion τ_x. It is given by

$$St = \frac{\tau_p}{\tau_x} \tag{23}$$

with the particle response time for Stokes flow given by

$$\tau_p = \frac{\rho_p d_p^2}{18 \rho_w \nu} \tag{24}$$

where ρ_p is the density of the particle, d_p is the diameter of the particle, ν is the kinematic viscosity of the fluid and τ_x can be the Kolmogorov timescale τ_k (Yang and Shy, 2005) or the integral timescale $\mathcal{T}$. The Stokes number St indicates the scale of fluctuating fluid motion that the particle is able to follow.

For $St \ll 1$ the particles will closely follow the fluctuating motion, while for $St \gg 1$ the particle motion will be indifferent to the fluctuating motion. For $St \approx 1$ the particles will only follow the largest scales of the fluctuating motion Poelma (2004, pg. 7, 17).

Stratification A stratified fluid has a density distribution which varies vertically, but remains uniform horizontally.

Unstable stratification occurs when denser fluid overlies less dense fluid $\partial \langle \Delta\rho \rangle / \partial y > 0$. It is unstable since small displacements of the interface between the two fluids will lead to increased displacements and consequent flow (Turner, 1973, pg. 4). A packet of fluid denser than its surroundings $\Delta\rho - \langle \Delta\rho \rangle > 0$ will form part of a downward flux $\langle \Delta\rho' v' \rangle < 0$, due to gravity. Hence, for unstable stratification (Tennekes and Lumley, 1973, pg. 98)

$$\frac{\partial \langle \Delta\rho \rangle}{\partial y} > 0 \qquad \langle \Delta\rho' v' \rangle < 0 \tag{25}$$

From eq. 7 it follows that $G_b > 0$ and hence $Ri_f < 0$. This indicates that potential energy is converted into turbulent kinetic energy.

Stable stratification occurs when denser fluid underlies less dense fluid. It is stable since small displacements of the density interface between the two fluids will create a restoring force, damping the displacement (Turner, 1973, pg. 4). For stable stratification (Tennekes and Lumley, 1973, pg. 98)

$$\frac{\partial \langle \Delta\rho \rangle}{\partial y} < 0 \qquad \langle \Delta\rho' v' \rangle > 0 \tag{26}$$

From eq. 7 it follows that $G_b < 0$ and hence $Ri_f > 0$. This indicates that turbulent kinetic energy is converted into potential energy.

Neutrally stable stratification occurs when there is no vertical variation in density distribution. For neutrally stable stratification (Tennekes and Lumley, 1973, pg. 99)

$$\frac{\partial \langle \Delta\rho \rangle}{\partial y} = 0 \qquad \langle \Delta\rho' v' \rangle = 0 \tag{27}$$

It follows that $Ri_f = 0$ and hence turbulence is only produced by the action of shearing.

Equations 25, 26 and 27 indicate that the Reynolds flux $\langle \Delta\rho' v' \rangle$ is opposite in sign to that of $\partial \langle \Delta\rho \rangle / \partial y$. This relationship leads to the flux-gradient hypothesis, which is often used by turbulence models to compute the Reynolds fluxes. The flux-gradient hypothesis is given by (Pope, 2001, pg. 93), (Rodi, 1980, pg. 12), (Tennekes and Lumley, 1973, pg. 51)

$$\langle \Delta\rho' \bar{u}' \rangle = -\frac{\nu_t}{\sigma_t} \bar{\nabla} \langle \Delta\rho \rangle \tag{28}$$

where ν_t is the turbulent viscosity and σ_t is the turbulent Schmidt number.

Timescale Turbulence is a three-dimensional, time-dependent motion, having a wide spectrum of lengthscales and corresponding timescales. Large eddies are associated with low frequency fluctuations, while small eddies are associated with high frequency fluctuations. The size of the large eddies is of the same order of magnitude as the flow domain and they transport most of the momentum and mass. The size of the smaller eddies is determined by the viscous forces. The influence of viscous forces decreases with increasing Reynolds number, which results in the smaller eddies decreasing in size. The integral timescale $\mathcal{T}$ is the largest timescale (lowest frequency) occurring in turbulent motion. The Kolmogorov timescale τ_k is the smallest timescale (highest frequency) occurring in turbulent motion (Bradshaw, 1971, pg. 17), (Rodi, 1980, pg. 9).

Chapter 1

Introduction

Gravity currents are flows caused by gravity acting on a difference in density between the current itself and its surroundings. The difference in density can be caused by temperature variations or variations in mixture composition. Since atmospheric and aquatic environments often contain non-isothermal or inhomogeneous regions, it follows that gravity current flow is common.

For instance, opening the door between a steaming bathroom and a cooler adjacent room forms two gravity currents. The warm, less dense air flows along the ceiling out of the bathroom and into the cooler adjacent room. At the same time cool, denser air flows along the floor from the cool adjacent room into the bathroom. Figure 1.1 illustrates these two gravity currents.

Another example of gravity current flow occurs when cold milk is gently poured into a hot cup of coffee. Gravity causes the cold, denser milk to sink below the hot, less dense coffee water. Stirring produces turbulence, which homogenizes the milk-coffee mixture and removes the density difference. Snow avalanches are examples of gravity currents, caused by variations in mixture composition (Simpson, 1997). The avalanche itself is a dense, multiphase suspension of air and snow particles. The atmosphere surrounding the avalanche is less dense, containing only air.

Rivers entering lakes and reservoirs can form gravity currents in a number of ways Alavian *et al.* (1992), Dallimore *et al.* (2001) and Fernandez and Imberger (2006). Differences in density can be caused by an inflow which is warmer or cooler, more saline or less saline, more turbid or less turbid than that of the reservoir. These continuous currents can be divided into two main parts: a head and a body. The head is the foremost part of the current, which sheds eddies behind it as it

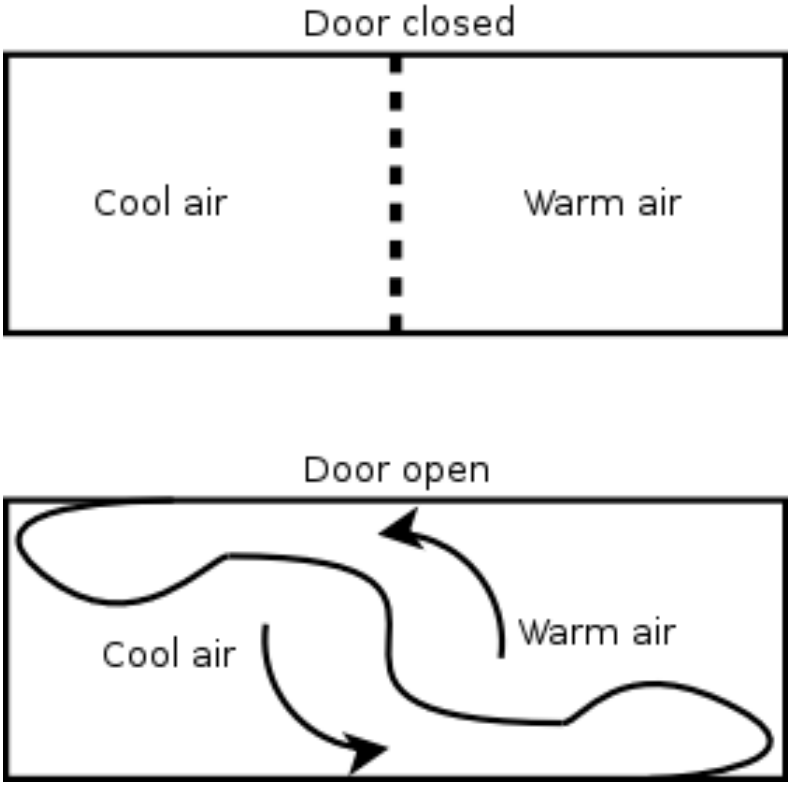

Figure 1.1: Gravity currents formed by opening the door between a warm and cool room

moves downstream. The body is the uniform, steady region behind the head. The motion of the head is inherently unsteady and non-uniform and it acts as a moving boundary condition for the body.

Depending on the stratification of the reservoir, the flow routes can be just as varied as the causes of density difference (Alavian *et al.*, 1992). For example, if the density of the inflow is greater than the density of the reservoir, an underflow will result. This underflow is a gravity current travelling underneath the ambient water along the bed. If an underflow reaches a depth within the reservoir where it becomes neutrally-buoyant, interflow will result. Interflow occurs where the underflow leaves the bed and travels along the region of similar density (usually horizontally). If the density of the inflow is less than the density of the reservoir, then an overflow results. An overflow is a gravity current traveling over the ambient water along the free surface. Figure 1.2 illustrates underflow, interflow and overflow.

The monograph of Simpson (1997) contains many other examples of natural and man-made gravity currents.

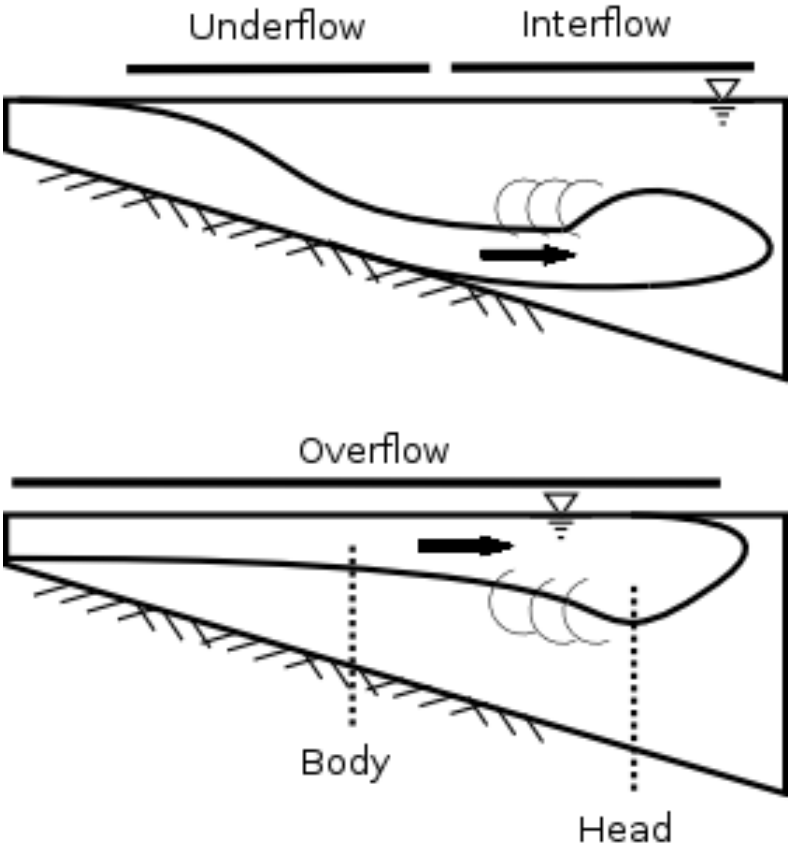

Figure 1.2: Possible flow routes of a gravity current entering a reservoir

1.1 Mechanisms of gravity current flow

Gravity currents are able to transport matter, such as pollutants, over vast distances (Simpson, 1997, pg. 2). This has motivated experimental and numerical investigations aimed at understanding their flow mechanics. Knowledge of their flow mechanics enables predictions to be made of their impact on the environment.

A number of mechanisms control gravity current flow: First and foremost is the interaction between turbulence and stratification. Turbulence plays a crucial role in the transport of mass, momentum and heat in fluids. It is a three-dimensional time-dependent motion having a wide spectrum of lengthscales and corresponding timescales. Turbulent flows are characterised by fluctuations in velocity and density. The greater the fluctuations, the greater the mixing of mass, momentum and heat. Increased levels of mixing result in increased dilution of the gravity current. Mixing reduces the gravity current's main driving force, the density difference.

The fluctuations are caused by eddies, which have a wide spectrum of length-scales. Large eddies are associated with low frequency fluctuations. The integral timescale $\mathcal{T}$ is the largest timescale (lowest frequency) occurring in turbulent motion. The lengthscale of the large eddies is of the same order of magnitude as the flow domain. Large eddies are responsible for most of the momentum, mass and heat transport.

Small eddies are associated with high frequency fluctuations. The Kolmogorov timescale τ_k is the smallest timescale (highest frequency) occurring in turbulent motion. The lengthscale of the smaller eddies is determined by the viscous forces. An increase in the Reynolds number results in a decrease in the lengthscale of the smallest eddies, due to the decrease in significance of the viscous forces (Bradshaw, 1971, pg. 17), (Rodi, 1980, pg. 9).

The turbulent kinetic energy k is a measure of the velocity variance of the flow and hence also of the degree of turbulent mixing. The turbulent kinetic energy is defined as

$$k = \frac{1}{2}\left(\langle u'u'\rangle + \langle v'v'\rangle + \langle w'w'\rangle\right) \tag{1.1.1}$$

where u' is the streamwise velocity fluctuation, v' is the cross-stream velocity fluctuation, w' is the spanwise velocity fluctuation, $\langle u'u'\rangle$ is the streamwise velocity variance (or streamwise normal Reynolds stress), $\langle v'v'\rangle$ is the cross-stream velocity variance and $\langle w'w'\rangle$ is the spanwise velocity variance. Turbulent kinetic energy is produced through shearing and buoyancy. Shear production $\mathcal{P}$ is given by

$$\mathcal{P} = -\langle \bar{u}'\bar{u}'\rangle : \bar{\bar{S}} \qquad \bar{\bar{S}} = \frac{1}{2}\left(\bar{\nabla}\bar{U} + \bar{\nabla}\bar{U}^T\right) \tag{1.1.2}$$

and buoyancy production G_b is given by

$$G_b = \frac{\bar{g}}{\rho_w} \cdot \langle \Delta\rho'\bar{u}'\rangle \tag{1.1.3}$$

where $\bar{u}'$ is the fluctuation of the velocity vector, $\langle \bar{u}'\bar{u}'\rangle$ is the velocity variance tensor (or Reynolds stress tensor), $\bar{\bar{S}}$ is the mean rate-of-strain tensor, $\bar{\nabla}\bar{U}$ is the gradient of the mean velocity vector and T denotes the transpose of this tensor, $\bar{g}$ is the gravity acceleration vector equal to $9{,}81\,\mathrm{m/s^2}$ vertically downwards, ρ_w is the density of water, $\Delta\rho'$ is the fluctuation of the excess density of the fluid and $\langle \Delta\rho'\bar{u}'\rangle$ is the covariance of excess density and velocity (or Reynolds flux vector).

In the case of underflows, shearing occurs at the bed as well as at the current interface. In these regions turbulent kinetic energy is produced, which drives the turbulent mixing of mass, momentum and heat. Turbulent mixing removes density inhomogeneities, leading to reduced stratification.

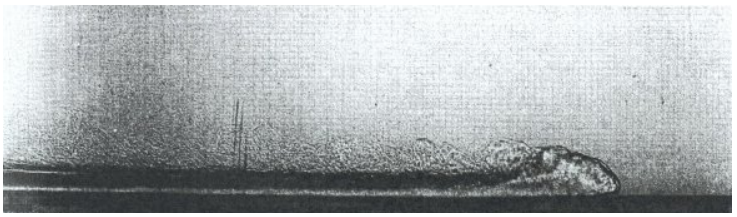

(a) 0° **slope**

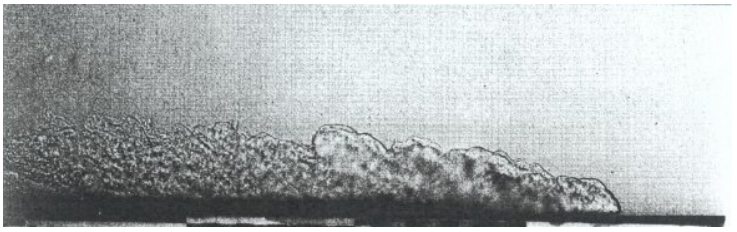

(b) 5° **slope**

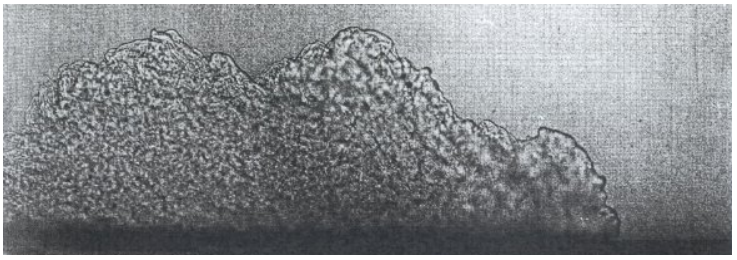

(c) 20° **slope**

Figure 1.3: Different levels of turbulent mass and momentum transport for a saline gravity current (Simpson, 1997)

Figure 1.3 illustrates different levels of mixing due to different levels of turbulent kinetic energy: By increasing the bed slope the streamwise component of the buoyancy body force is increased. This body force is balanced in part by increased shear stresses at the bed and at the current interface. The increased shearing produces more turbulent kinetic energy, which leads to higher levels of mixing.

Stratification, on the other hand, can increase or reduce turbulence. A body of fluid is stratified when its density distribution varies vertically, but remains uniform horizontally.

When more dense fluid overlies less dense fluid unstable stratification exists. This is given by

$$\frac{\partial \langle \Delta\rho \rangle}{\partial y} > 0 \tag{1.1.4}$$

where $\langle \Delta\rho \rangle$ is the mean (or time-average) of the fluid excess density and y is the

cross-stream coordinate, which is positive upwards. The stratification is unstable, since small displacements at the interface between the more dense and less dense fluid will lead to increased displacements and consequently penetrative convection. The potential energy of the more dense fluid is converted into turbulent kinetic energy, which leads to turbulent mixing. This buoyancy production of turbulent kinetic energy enhances turbulence.

When denser fluid underlies less dense fluid stable stratification exists. This is given by

$$\frac{\partial \langle \Delta\rho \rangle}{\partial y} < 0 \tag{1.1.5}$$

The stratification is stable, since a small displacement at the interface between the denser and less dense fluid will create a restoring force, which will damp the displacement. In this case negative buoyancy production removes turbulent kinetic energy from the flow, reducing the turbulence. At very high levels of stable stratification turbulence can be extinguished, eliminating mixing and hence maintaining inhomogeneous, stratified regions.

The flux Richardson number provides an indication of whether turbulence is increased or reduced. It is defined as

$$Ri_f = -\frac{G_b}{\mathcal{P}} \tag{1.1.6}$$

For unstable stratification $Ri_f < 0$ buoyancy enhances turbulence. For stable stratification $Ri_f > 0$ buoyancy reduces turbulence. When negative buoyancy production becomes too large relative to shear production, in a stably stratified flow, turbulence cannot be maintained unless an external energy source exists. Hossain and Rodi (1977) found that for heated water jets turbulence collapsed when $Ri_f > 0{,}4$.

The spreading rate of a shear flow also provides an indication of the level of turbulent mixing. For example a two-dimensional 2D plane jet has a spreading rate of 0,105. A wall jet on the other hand has a lower spreading rate of 0,075, due to the wall damping the fluctuations of the velocity component normal to the wall Ahlman (2006). Vertical buoyant plumes have a spreading rate of 0,135, which is greater than that of a plane 2D jet, because the unstable stratification enhances the turbulent mixing and entrainment into the plume Hossain and Rodi (1977). Horizontal gravity currents have a lower spreading rate than wall jets $< 0{,}075$, since stable stratification reduces turbulent mixing and the entrainment of ambient fluid into the current.

The bulk Richardson number provides another indication of the stability of the gravity current interface. It is defined as

$$Ri = \frac{g \langle \Delta\rho \rangle_d H_d}{\rho_w U_d^2} \tag{1.1.7}$$

with

$$\langle \Delta\rho \rangle_d = \langle \rho \rangle_d - \rho_w \tag{1.1.8}$$

where g is the magnitude of gravity acceleration, $\langle \Delta\rho \rangle_d$ is the mean depth-averaged excess density of the fluid, $\langle \rho \rangle_d$ is the mean depth-averaged density of the fluid, ρ_w is the density of water, while U_d and H_d are the mean depth-averaged current velocity and current height.

For $Ri < 1$, inertial forces dominate the buoyancy forces. Analogous to open-channel flow, this is referred to as supercritical flow. A supercritical bulk Richardson number indicates an unstable interface. The instability increases the amount of mixing across the interface, which in turn increases the entrainment of ambient fluid into the current (Ellison and Turner, 1959).

For $Ri > 1$, buoyancy forces dominate inertial forces. This is referred to as subcritical flow. A subcritical Richardson number indicates a stable interface. A stable interface dampens the turbulence and hence reduces mixing. This results in a reduction in the entrainment of ambient fluid into the current. Figure 1.4 shows how the entrainment coefficient, indicative of the spreading rate, decreases with increased bulk Richardson number. In other words, how the turbulent mixing decreases with increased stratification stability.

Anisotropy is another mechanism controlling the evolution of gravity currents. Isotropic turbulence occurs when the fluctuating velocity field is statistically invariant of rotations and reflections of the coordinate axes (Pope, 2001, pg. 76). This means that

$$\langle u'u' \rangle = \langle v'v' \rangle \qquad \langle u'v' \rangle = 0 \tag{1.1.9}$$

where $\langle u'v' \rangle$ is the covariance of the streamwise and cross-stream velocity components (shear Reynolds stress). Neutrally-buoyant boundary-layer type flows are characterised by one significant Reynolds stress (the shear Reynolds stress $\langle u'v' \rangle$) and one significant Reynolds flux (the cross-stream Reynolds flux $\langle \Delta\rho' v' \rangle$) (Pope, 2001, pg. 94).

Vertical plumes are also boundary layer-type flows but, in contrast to the non-buoyant case, both Reynolds fluxes are significant. The streamwise (vertical) Reynolds flux contributes to the production of turbulent kinetic energy, while the

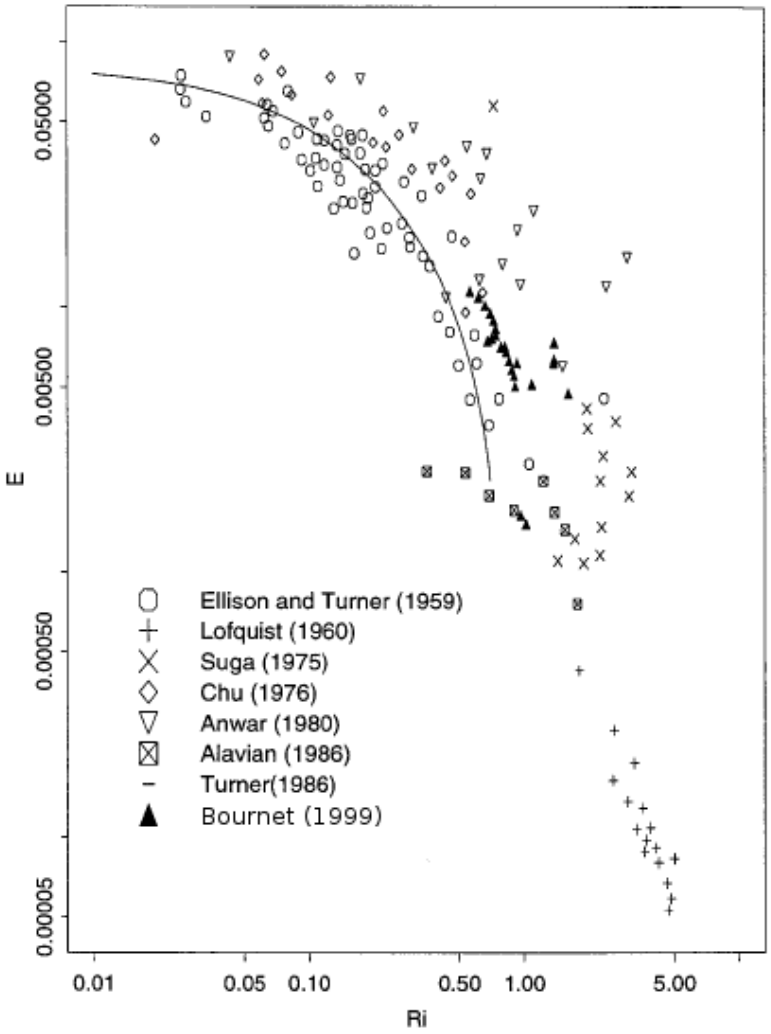

Figure 1.4: Water entrainment as a function stratification: historical data (Bournet *et al.*, 1999)

cross-stream (horizontal) Reynolds flux is responsible for the turbulent spreading of the plume.

Horizontal gravity currents are also boundary layer-type flows, having one significant Reynolds stress (the shear Reynolds stress $\langle u'v' \rangle$) and one significant Reynolds flux (the cross-stream Reynolds flux $\langle \Delta\rho' v' \rangle$). However, the cross-stream Reynolds flux fulfills a dual role: It removes turbulent kinetic energy by negative buoyancy production and it is responsible for the turbulent spreading of the current.

The causes of the density differences also play a very important role in gravity current mechanics. Density differences can be caused by thermal or mixture inhomogeneities. Mixtures can be composed of multiple phases, multiple species or a combination of both.

Multiphase mixtures may transport mass, momentum and heat across the interface separating the different phases. Turbidity currents are multiphase mixtures, composed of water (liquid, continuous phase) and sediments (solid, dispersed phase). Drag forces are responsible for the transport of momentum across the fluid-solid interface. The dispersed phase may be dynamically passive or active. The dispersed phase is dynamically active when it has a large volumetric concentration, as well as a density very different from that of the continuous phase. A dynamically active dispersed phase is able to influence the flow dynamics of the mixture. For example, the dispersed phase may increase the density and momentum of the mixture. The inertia of the dispersed phase may also increase or decrease the turbulence of the continuous phase. Furthermore, the buoyancy flux of the mixture may be conservative or non-conservative depending on the characteristics of the dispersed phase. Turbidity currents are non-conservative, since sediment deposition will decrease the buoyancy flux, while sediment entrainment will increase the buoyancy flux.

Multispecies mixtures may transport mass, momentum and heat from one species to another through chemical reactions. Saline gravity currents are unreactive multispecies mixtures, composed of sodium chloride ($NaCl$) and water (H_2O). Dissolved sodium chloride is miscible in water and produces a conservative buoyancy flux. Hence, the buoyancy flux of the mixture is invariant within the flow domain. Furthermore, if the $NaCl$ mass fraction is large enough it becomes a dynamically active tracer. The dissolved $NaCl$ can therefore influence the flow dynamics of the mixture. In the case of combustible gas mixtures, such as methane-air, chemical reactions may increase the mass of one species and decrease the mass of another. Density differences may also be increased or decreased, depending on whether the reactions are endothermic or exothermic.

1.2 Historical experimental studies of gravity current flow

A large amount of research has been done on gravity currents. Experimental studies have mainly used salinity, turbidity or temperature to create density differences. Most of this research has been steered towards providing empirical closures for depth-averaged models. For example, quantifying the turbulent entrainment of ambient fluid into a current experiencing a certain level of stable stratification. It is well known that an increase in stable stratification results in a decrease in the entrainment of ambient fluid.

Ellison and Turner (1959) presented a theory in which the turbulent entrainment is proportional to the product of the depth-averaged current velocity and a variable entrainment coefficient E. They also derived an empirical relationship between E and the bulk Richardson number Ri, which quantifies the level of stratification. From their experiments they observed that for a given slope a current quickly attained an equilibrium state where the streamwise gravity force is balanced by the bed and interfacial frictional forces. In this state the current spreads linearly, while its velocity and bulk Richardson number remains constant. Hence there exists a unique bulk Richardson number Ri_n for a given slope and drag coefficient.

The equilibrium state has been used extensively as a basis from which to derive other empirical relationships. For example, Parker *et al.* (1987) have measured approximately self-similar velocity and excess density profiles for near equilibrium turbidity currents. This allowed them to evaluate certain shape factors which were required by their depth-averaged numerical model (Parker *et al.*, 1986). Parker *et al.* (1987) also derived empirical relationships for water entrainment, bed sediment entrainment and near bed sediment concentration under these equilibrium conditions.

Garcia (1993) have also used the equilibrium conditions upstream and downstream of an internal hydraulic jump to investigate the amount of water entrained across the jump. Their results showed that the entrainment across a jump is small and that the approximate self-similar profiles of the subcritical and supercritical regions were different.

Approximate self-similar profiles under equilibrium conditions were also measured for excess density (Buckee *et al.*, 2001), sediment concentration (McCaffrey *et al.*, 2003; Choux *et al.*, 2005; Parker *et al.*, 1987), grain size (McCaffrey *et al.*, 2003), Choux *et al.* (2005) and temperature (Ramaprabhu and Andrews, 2003,

2004).

Ellison and Turner (1959) assumed that entrainment is simply a function of the bulk Richardson number at sufficiently high Reynolds numbers. From their experiments they concluded that negligible entrainment occurred when the bulk Richardson number exceeded 0,8. More recently, Fernandez and Imberger (2006) suggested from field observations that entrainment was possible at much higher bulk Richardson numbers. They proposed an empirical entrainment relation, which is a function of bulk Richardson number and bottom drag coefficient. Numerous investigations have been done on the entrainment relation and figure 1.4 from Bournet *et al.* (1999) presents a compilation of the data from some of these studies.

Improvements in measurement technology have also made a significant contribution to the overall depth of experimental studies. Early experiments were restricted to measuring the mean properties of gravity currents intrusively. For example, point measurements of mean velocity were done by micropropellors (Parker *et al.*, 1987; Garcia, 1993) and point measurements of excess density by siphons Parker *et al.* (1987); Lee and Yu (1997); Choux *et al.* (2005); McCaffrey *et al.* (2003).

Lately, mean and turbulence measurements can be done non-intrusively for regions (not only points) within the flow. For example Choux *et al.* (2005); McCaffrey *et al.* (2003) used ultrasonic doppler velocity profiling (UDVP) to measure profiles of streamwise mean velocity U and Reynolds stress $\langle u'u' \rangle$ for high density turbidity currents (5% and 14% volumetric concentration).

Kneller *et al.* (1999); Buckee *et al.* (2001) used laser doppler anemometry (LDA) to measure profiles of streamwise and cross-stream mean velocity U, V, as well as the Reynolds stresses $\langle u'u' \rangle$, $\langle v'v' \rangle$ and $\langle u'v' \rangle$ for a a saline gravity current. Kneller *et al.* (1999) found that for the gravity current head ambient fluid is entrained beneath the nose and at the back of the head in the wake region. Buckee *et al.* (2001) showed that the vertical gradient of downstream velocity had a large influence on the turbulence structure of gravity currents and that shear production was significant in subcritical and supercritical currents.

Thomas *et al.* (2003) used particle tracking velocimetry (PTV) to measure contours of streamwise and cross-stream mean velocity U, V, as well as Reynolds stresses $\langle u'u' \rangle$ and $\langle u'v' \rangle$ for a saline gravity current head of low excess density (0,07-7,0 $\mathrm{kg/m^3}$). Their results differed from those of Kneller *et al.* (1999) for the internal mean flow structure within the gravity current head. They observed that the flow of dense fluid from the centre of the head towards the leading edge forms two counter rotating eddies, whose positions depend on the Reynolds number.

As far as gravity current Reynolds flux measurements are concerned, only Dallimore *et al.* (2001) measured the vertical component of these fluxes for a saline underflow, in lake Ogawara, Japan. Their measurements were made using a portable flux profiler (PFP), which is a free-falling rising profiler equipped with thermistors, microconductivity sensors, a pressure transducer, inclinometers and a flux gate compass. They used their vertical Reynolds flux measurements to calculate the rate of entrainment at the interface of the underflow, which compared well with their proposed entrainment relation. This entrainment relation is a function of bulk Richardson number and bottom friction coefficient.

Another experimental study related to Reynolds flux measurements in a stratified environment is that of Ramaprabhu and Andrews (2003). They introduced the scalar velocimetry technique (PIV-S) to measure velocity and density fields of a turbulent Rayleigh-Taylor mixing layer. Their results included profiles of streamwise and cross-stream mean velocity U, V, Reynolds stress $\langle u'u' \rangle, \langle v'v' \rangle$ and Reynolds flux $\langle \Delta\rho' u' \rangle, \langle \Delta\rho' v' \rangle$.

Although recent advances in measurement technology have enabled simultaneous velocity and density measurements to be made, to the author's knowledge no experimental data have been published of the streamwise and cross-stream Reynolds flux profiles of a gravity current. This forms one of the research aims of this dissertation.

1.3 Historical numerical studies of gravity current flow

Experimental studies are restricted by the flow scales that can practically be attained in a laboratory. A numerical model does not have scale restrictions and is therefore a complementary tool by means of which to study gravity currents. Different mixture theories are required by a numerical gravity current model, depending on whether the density differences are caused by inhomogeneities in the mixture composition of multiple phases or multiple species. A numerical model also needs to account for the turbulent transport of mass, momentum and heat.

Multiphase mixture theory is required when density differences are caused by inhomogeneities in the mixture composition of different phases. This theory accounts for the transport of mass, momentum and heat across the interface separating the different phases. This theory is suitable for turbidity currents. A wide

variety of multiphase models exists. These models can be broadly divided into Euler-Euler models and Euler-Lagrange models (FLUENT 6.3, pg. 22-3,23-6), (Manninen and Taivassalo, 1996; Wörner, 2003). The Euler-Euler models treat the different phases as interpenetrating continua in an Eulerian manner, while the Euler-Lagrange model treats the continuous phase in an Eulerian manner and the dispersed phase in a Lagrangian manner. The Eulerian approach views the flow from a fixed control volume. Hence flow variables are functions of position and time. The Lagrangian approach views the flow from a moving control body. Hence flow variables are functions of time only.

Euler-Euler multiphase models can be further divided into mixture models or Eulerian models (full multiphase models). The mixture model assumes that the coupling between the different phases is strong, that is, the velocities of the phases reach a local equilibrium over short lengthscales (FLUENT 6.3, pg. 23-29), (Manninen and Taivassalo, 1996, pg. 10). The mixture model consists of a continuity and momentum differential equation for the mixture; a volume fraction transport differential equation for each dispersed phase and an algebraic momentum equation for each dispersed phase. The algebraic momentum equation for each dispersed phase is written in terms of the relative velocity between that phase and the mixture. Hence, the mixture model solves only the velocity of the mixture (by way of the mixture momentum differential equation), while the dispersed phase velocities are described relative to the mixture's velocity. This reduces computational effort, since the number of unknown velocities that actually need to be solved are kept to a minimum.

In contrast to the mixture model, the Eulerian model does not require that the coupling between the different phases be strong (Manninen and Taivassalo, 1996, pg. 10). The Eulerian model consists of volume fraction transport differential equations for each phase, as well as momentum differential equations for each phase. The computational effort of this model is therefore greater than that of the mixture model, since more unknown velocities need to be solved due to the additional differential momentum equations.

Multispecies mixture theory is required when density differences are caused by inhomogeneities in the mixture composition of different species. This theory accounts for the transfer of mass, momentum and heat from one species to another in the presence of chemical reactions. This theory can be applied to saline gravity currents, for the special case where chemical reactions are absent. Multispecies models usually consist of a continuity and momentum differential equation for the mixture and a mass fraction transport differential equation for each species (FLUENT 6.3, pg. 14-3).

A wide range of approaches also exists for modeling turbulence, varying in sophistication and computational effort. At the extreme end of computational effort is direct numerical simulation (DNS). DNS solves the continuity, Navier-Stokes and scalar transport equations for the *whole* spectrum of length and timescales of turbulence. The results are very accurate, since no modeling assumptions are used. However, the computational effort required to simulate the whole spectrum of length and timescales at even moderate Reynolds numbers makes DNS impractical for industrial use. Hartel *et al.* (2000) performed a 3D DNS on a gravity current head for a Reynolds number of 750. They investigated the internal flow structure within the current head, as well as the lobe-cleft instability at the front of the head. Ahlman (2006) performed a 3D DNS on a neutrally buoyant, compressible wall-jet for a Reynolds number of 2000. The total computational time used was 22 000 CPU hours. He investigated the dynamics and mixing occurring within the wall-jet.

At the lower end of computational effort are spatially-averaged models. These models are obtained by averaging the 3D continuity, Navier-Stokes and scalar transport equations in space. Spatially-averaged models can be derived by integrating over: the flow depth (2D horizontal), flow width (2D vertical), cross-section (1D) or entire reservoir (0D). Integration can be done analytically by assuming that the flow profiles are self-similar. Self-similarity means that the shape of the profiles does not change in the streamwise direction. This assumption works well for constant slopes where the flow has reached an equilibrium between the streamwise gravity force and the frictional forces at the bed and interface. Self-similarity does not hold when an underflow separates from the bed and becomes an interflow or when the bed slope suddenly changes. However, spatially-averaged models can be fairly robust and may be effectively used for conditions where the flow is not strictly self-similar. A problem with the spatial-averaging process is that residual terms are produced which need to be properly modeled. For gravity currents empirical equations are required for the water entrainment (at the interface) and shear velocity (at the bed).

Parker *et al.* (1986) used a depth-averaged multiphase mixture model to investigate the possibility of self-accelerating turbidity currents. Self-acceleration occurs when a turbidity current reaches a critical speed, whereon sediment entrainment increases, the concentration and density difference increases and subsequently the current velocity increases. A self-reinforcing of sediment entrainment and increased velocity develops. Their model predicted that self-acceleration was possible.

Winslow (2001) also used a depth-averaged multiphase mixture model to investigate the sensitivity of a turbidity current to initial conditions, channel properties, entrainment relationships and mixture composition. He found that initial conditions of current height H_d, current velocity U_d and concentration did not have a

long-term effect on the flow. Channel properties, such as slope and bed friction, and mixture composition, such as sediment size and mixture viscosity, did have a significant influence on gravity current evolution.

Midway between 3D DNS and spatially-averaged models are Reynolds-averaged Navier-Stokes (RANS) models. These models solve Reynolds-averaged continuity, Navier-Stokes and scalar transport equations. They do not assume self-similarity or use empirical entrainment relationships nor do they simulate the whole spectrum of turbulence length and timescales. They are therefore more general than spatially-averaged models and can be more accurate for flow situations where the streamwise gravity and frictional forces are not in equilibrium. Reynolds-averaging of the governing equations introduces second order moments (Reynolds stresses and Reynolds fluxes), which requires closure for the model to work. Closure is provided by introducing the Boussinesq and flux-gradient hypotheses, as well as a turbulence model. The computational effort required by RANS models makes them practical for industrial use.

The flux-gradient hypothesis, used by RANS models, requires specifying a turbulent Schmidt number in order to quantify the turbulent diffusion coefficient. Often a constant isotropic turbulent Schmidt number has been used (Huang *et al.*, 2005), (Farrell and Stefan, 1988). Rodi (1980, pg. 12,15), Rodi (1987) have suggested that this might be unrealistic and that the turbulent Schmidt number should be a function of the level of stratification. There is presently no generally accepted function for the turbulent Schmidt number.

Bournet *et al.* (1999) used a RANS model with a standard $k-\epsilon$ turbulence model, extended for buoyancy, to study the plunging and water entrainment of a temperature induced underflow in a reservoir. Their results compared well with empirical plunge depth and water entrainment relations. Similarly, Farrell and Stefan (1988) also used a RANS model to investigate the plunging of a temperature induced gravity current. They found that their model overpredicted the depth where plunging occurred. Hossain and Rodi (1977) also used a RANS model to study the entrainment of a stably stratified heated surface jet. They solved the Reynolds stresses and fluxes by simplifying the Reynolds stress/flux differential transport equations into algebraic equations. They found that their model realistically predicted the reduction of entrainment and collapse of turbulence due to stable stratification.

Huang *et al.* (2005) used a RANS multiphase mixture model with a standard $k-\epsilon$ turbulence model, extended for buoyancy, to model a turbidity current. Their model allowed the bed boundary condition to dynamically evolve due to sediment entrainment and deposition. Their results compared well with experimental data

when they used a turbulent Schmidt number of 1,3. Brørs and Eidsvik (1992) modeled turbidity current flow using a multiphase mixture model with a Reynolds stress turbulence model. They argued that $k-\epsilon$ turbulence models underpredicted the turbulent mass transport at the height of the velocity maximum. They showed that their Reynolds stress model gave higher estimates for k and turbulent mass transport at the velocity maximum.

1.4 Motivation of present research

The main motivation of the present research was to determine the accuracy of a Reynolds-averaged Navier-Stokes (RANS) multispecies gravity current model. Reynolds-averaging of the governing equations produces first-order moments (mean velocity, mean density and mean pressure), as well as second-order moments (variances and covariances or equivalently Reynolds stresses and Reynolds fluxes). These mean velocities, mean densities and turbulence quantities vary spatially within a gravity current and hence profiles are often used to represent their distribution.

Engineers are usually only interested in the mean values. However, the Reynolds stresses and Reynolds fluxes influence the mean velocities and densities of a gravity current. Turbulence models are required to quantify the Reynolds stresses and fluxes. The accuracy of these turbulence models therefore has a direct impact on the mean velocities and densities of the simulated gravity current. These turbulence models need to accurately account for the effects of stable stratification. Stable stratification continuously reduces the turbulence intensities of the flow, preventing the flow from becoming self-similar. Most experimental work has been conducted on approximately self-similar gravity currents. RANS models do not assume self-similarity, but little experimental data exist with which to validate this feature.

Inaccurate predictions of the Reynolds stresses and fluxes can produce different model outcomes. If the model is over-diffusive, too much turbulent mixing with the ambient water will be predicted. This would lead to too a large spreading rate of the current and too low a density difference. Low density differences would result in a smaller driving force and consequently a lower velocity and shorter run-out distance. A lower density difference would also lead to a less stable stratification and hence smaller negative buoyancy production. More turbulent kinetic energy would be available, leading to even more turbulent mixing.

If the model is under-diffusive, too little turbulent mixing with the ambient water would be predicted. This would lead to a too small spreading rate of the

current and a too high density difference. High density differences would result in a larger driving force and consequently a higher velocity and longer run-out distance. A greater density difference would also lead to a more stable stratification and hence increased negative buoyancy production. Less turbulent kinetic energy would be available, leading to even less turbulent mixing.

The second motivation was to increase the understanding of how turbulence transports mass and momentum within a gravity current. This requires profiles of Reynolds stresses and fluxes. Although much research has been conducted on gravity currents, very little is known about their Reynolds stresses and fluxes. Kneller *et al.* (1999) and Buckee *et al.* (2001) have presented profiles of measured Reynolds stresses within gravity currents. No measured Reynolds flux profiles are available. The third motivation was to extend the particle image velocimetry scalar (PIV-S) technology to continuously stratified flows, such as the body of a gravity current. The PIV-S as presented by Ramaprabhu and Andrews (2003) can measure Reynolds fluxes only in two-layer fluids. Future gravity current research could benefit from this technology if its application range included continuously stratified flows.

1.5 Research aims

This dissertation had three research aims: The first aim was to measure the spatial distribution of the Reynolds stresses and fluxes of a gravity current, whose turbulence structure was not self-similar. This was done by measuring the Reynolds flux $\langle \Delta\rho' \bar{u}' \rangle$ and Reynolds stress $\langle \bar{u}' \bar{u}' \rangle$ profiles.

The second aim was to measure how the turbulence of the gravity current was influenced by the stable stratification. This was done by measuring profiles of gradient Richardson number Ri_g, buoyancy and shear production of turbulent kinetic energy $G_b, \mathcal{P}$, turbulent viscosity ratio ν_t/ν, as well as turbulent diffusivity ratio γ_t/γ. The gradient Richardson profile quantifies the stability of the stratification. The buoyancy production profile indicates how much turbulent kinetic energy is removed due to stable statification, while the shear production profile indicates how much turbulent kinetic energy is produced through shearing of the mean flow. The turbulent viscosity ratio profile and turbulent diffusivity ratio profile indicate the distribution of the turbulent momentum and mass transport within the current.

The third aim was to evaluate the accuracy of a RANS multispecies model for a gravity current whose turbulence structure was not self-similar. This was done

by comparing the simulated profiles of mean velocity $\bar{U}$, mean excess density $\langle\Delta\rho\rangle$, turbulent viscosity ratio ν_t/ν, cross-stream Reynolds flux $\langle\Delta\rho' v'\rangle$, shear production $\mathcal{P}$ and buoyancy production G_b with the measured profiles of a gravity current along a section where the bulk Richardson number varied. Such an evaluation would reveal whether the model can correctly predict the mean velocity and density profiles of the flow, as well as the turbulence profiles.

1.6 Research methodology

The following methodology was used to attain the above research aims: A steady saline inflow was introduced into a flume filled with fresh water. The inflow developed into a saline gravity current which traveled along the flume bed. The saline inflow and fresh water were transparent and allowed optical measurement techniques to be used. Turbidity currents are opaque flows and cannot be used with such techniques. However, the behaviour of turbidity currents composed of very fine sediments will probably be very similar to saline gravity currents. The flume walls were parallel and constrained the saline gravity current so that it developed two-dimensionally in the vertical.

A time series of velocity and density profiles of the gravity current was simultaneously measured using particle image velocimetry scalar (PIV-S). Profiles were taken along a section where the bulk Richardson number varied. The time series of velocity profiles allowed the mean velocity $\bar{U}$ and velocity variance $\langle\bar{u}'\bar{u}'\rangle$ (Reynolds stress) profiles to be computed. The time series of velocity and excess density profiles allowed the mean excess density $\langle\Delta\rho\rangle$, excess density variance $\langle\Delta\rho'\Delta\rho'\rangle$, as well as velocity and excess density covariance $\langle\Delta\rho'\bar{u}'\rangle$ (Reynolds flux) profiles to be computed. The turbulent viscosity ratio ν_t/ν and turbulent diffusivity ratio γ_t/γ profiles were computed from the Reynolds stress and Reynolds flux profiles, using the Boussinesq and flux-gradient hypotheses. The gradient Richardson number Ri_g profile was computed from the measured mean velocity and mean excess density profiles.

A 2D vertical, multispecies RANS model was used to simulate the measured saline gravity current. The Reynolds stresses and fluxes, produced by the Reynolds-averaging, were approximated by the Boussinesq and flux-gradient hypotheses. The turbulent viscosity and diffusivity, required by the two hypotheses, were computed from $k-\epsilon$ turbulence models. The model equations were discretized with the finite volume method and solved as an unsteady flow.

The simulated mean velocity, mean excess density, turbulent viscosity ratio and cross-stream Reynolds flux, shear production and buoyancy production profiles were subtracted from the measured profiles. The resulting profiles gave the error between the simulated and measured profiles. These profiles were then integrated over the flow depth to obtain a depth-averaged error. This allowed the accuracy of the RANS multispecies model to be determined for a gravity current whose turbulence structure was not self-similar.

1.7 Outline of this dissertation

Chapter 2 presents the hydraulic setup used to generate the continuous saline gravity current. It also presents the particle image velocimetry scalar (PIV-S) setup by which time series of velocity and density profiles were simultaneously measured. The methodology used to obtain the velocity and density signals is discussed, as well as how these signals were processed to obtain means, variances, covariances, energy spectra and other turbulence quantities.

Measurements of a continuous saline gravity current is presented in chapter 3. The measurements of the gravity current include mean flow profiles, turbulence profiles and energy spectra.

The RANS multispecies gravity current model is presented in chapter 4. Sensitivity analyses are performed to show that the results are grid independent and fully converged. Sensitivity analyses are also performed on different initial conditions, flume depths, turbulence models and inlet boundary conditions. Furthermore, the accuracy of the numerical model is evaluated against the PIV-S measurements.

The summary and conclusions of this dissertation are presented in chapter 5.

Chapter 2

Experimental setup and measurement techniques

Historical experimental studies on gravity currents were restricted mainly to intrusive point measurements, for example, micropropellors and siphons. Recent improvements in digital imaging technology have made it possible to measure the mean and turbulence structure non-intrusively for whole regions within a gravity current. These measurements allow the interaction between turbulence and stratification to be studied, as well as the anisotropic turbulent transport of mass, momentum and energy.

These digital imaging technologies allow the simultaneous measurement of velocity and excess density profiles. They can be applied at high speed, allowing the compilation of a time series of profiles. The time series of velocity profiles allows profiles of mean velocity and velocity variance (Reynolds stress) to be computed. Furthermore, the time series of velocity and excess density profiles allows profiles of mean excess density, excess density variance, as well as velocity and excess density covariance (Reynolds flux) to be computed. These profiles allow the mean and turbulent structure within a gravity current to be studied.

However, gravity currents pose unique challenges to optical measurements. Optical methods such as particle image velocimetry scalar (PIV-S) are limited by visibility and refractive index effects. Multiphase turbidity currents of moderate volumetric concentration are opaque, making PIV-S impractical. Measurement of multispecies saline currents of moderate mass fraction is plagued by refractive index effects. Refractive index matching of the working fluids is required in order to use optical methods. These problems explain why the literature on gravity current

turbulence is still limited (Kneller *et al.*, 1997, 1999; Buckee *et al.*, 2001).

This chapter describes how a continuous gravity current was generated and how its mean and turbulence structures were measured. The chapter begins by describing the hydraulic setup used to generate continuous dilute gravity current flows. This is followed by a description of the PIV-S setup, which was used to measure instantaneous velocity and density profiles. Sensitivity analyses on important parameters of the PIV-S setup are also presented. The rest of the chapter shows how the various turbulence statistics were computed. These statistics include the mean velocity and excess density, as well as Reynolds stresses, Reynolds fluxes and energy spectra.

2.1 Hydraulic setup

The working materials used to generate the density current were salt $NaCl$ and water H_2O. These materials were chosen, because of their low cost and safety. Figures 2.1 and 2.2 show the setup used to generate a steady gravity current. The inlet volumetric flux was 0,59 l/s. The inlet and outlet conditions, as well as flow geometry, were designed so as to be simple to model numerically. The setup comprises four parts: A mixture tank, a flow conditioning inlet, a perspex flume and a damping tank.

A saline mixture, having an excess density of $2\,\mathrm{kg/m^3}$ with respect to water, was stored within the mixture tank (figure 2.2a). A submersible pump pumped the mixture upwards along a pipe, which overflowed at the top, creating a constant head. The capacity of the mixture tank allowed nine minutes of steady flow. A second, smaller pipe tapped flow at a constant head and fed it into the flow conditioning inlet (figure 2.2c). The inner dimensions of the inlet were 0,25 m wide by 0,03 m high and its bottom was aligned with that of the flume.

At the start of each experimental run the flume and damping tank contained only water. The filled flume was 5,3 m long, 0,25 m wide and 0,3 m deep. This gave an inlet height to flow depth ratio of 10. The flume width and depth were similar to that used by Choux *et al.* (2005) and McCaffrey *et al.* (2003) for turbidity currents. Upon entering the flume, the gravity current had the velocity profile of a wall jet (figure 2.3a). The gravity current travelled along the flume bottom (figure 2.3b) and exited it supercritically by spilling into the damping tank (figure 2.2b). The spilling created a hydraulic control, which prevented an internal hydraulic bore from traveling upstream in the flume. A weir at the downstream end of the damping

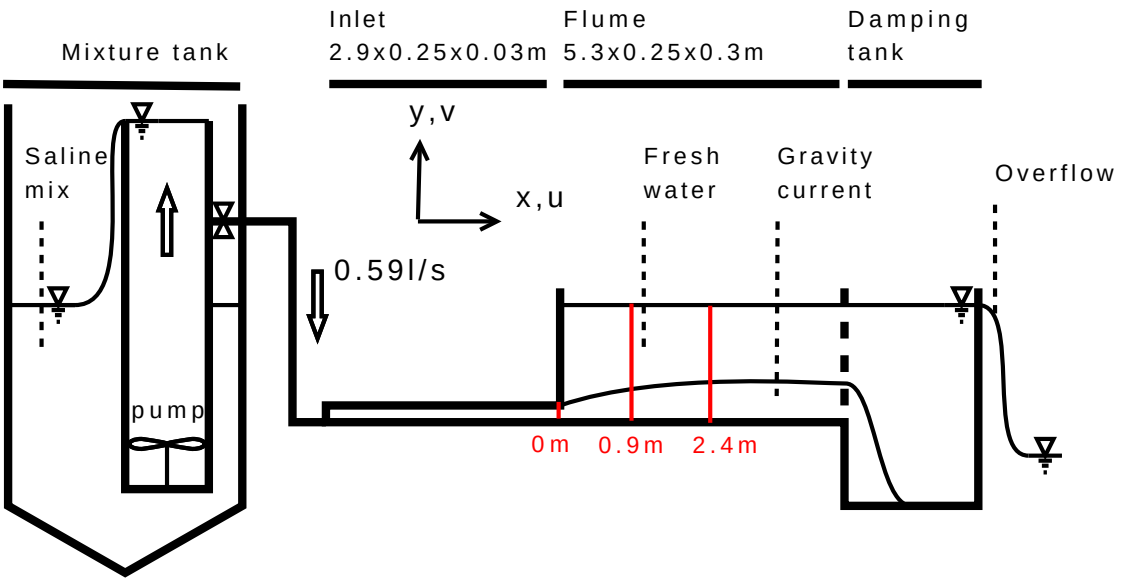

Figure 2.1: Layout of mixture tank, inlet, flume and damping tank

tank controlled the water level within the flume. The capacity of the damping tank allowed six minutes of steady gravity current flow, before drowning the hydraulic control.

Figure 2.3c shows the dyed head of the saline gravity current moving downstream in the flume. It also shows the siphons used to measure the time-averaged density profile. It should be noted that the lightsheet and siphons were never used during the same experimental run, in order to avoid introducing local flow disturbances.

It was originally planned to measure velocity and density profiles at approximately 1 m intervals, but scratches on the perspex flume at these locations prevented camera recordings from being made. Suitable recording locations were found at the inlet and at 0,9 m and 2,4 m downstream of the inlet.

Due to the size of the hydraulic setup no temperature regulation was used. Figure 2.11b shows how the density of water decreases with an increase in temperature. Equation 2.1.1 was obtained by a least-squares parabola fit to the data given in CRC handbook of chemistry and physics, pg. 6-3.

$$\rho = -0.005464\theta^2 + 0.02567\theta + 999.8891 \tag{2.1.1}$$

where θ is the temperature in degrees Celsius. Temperatures were measured at arbitrary locations on the flume bed and in the top quarter of the mixing tank. The

(a) Mixture tank

(b) Damping tank

(c) Flow conditioning inlet and perspex flume

Figure 2.2: Photographs of mixture tank, inlet, flume and damping tank

average temperature of the water was 17℃. The maximum temperature difference between the water in the flume and the saline inflow was 1℃. This temperature difference created a maximum excess density difference of about 0,166 kg/m^3. Therefore, if the inflow excess density due to dissolved salt is 2 kg/m^3, then the maximum contribution due to temperature differences was 8% of this. This was of the same order as the experiments of Parker *et al.* (1987) (7.6%).

2.2 Particle image velocimetry scalar setup

Figure 2.4 shows the laser lightsheet setup used for the PIV-S measurements. It consisted of a helium-neon laser (Spectra-Physics: 107S), three cylindrical lenses (Thorlabs: LJ1821L1-A, LJ1277L1-A, LJ1567L1-A) and a silver plated mirror (Thorlabs: ME2S-P01).

The laser output a continuous red beam 633 nm at 25 mW. The laser beam runs beneath the flume and is aligned with the centreline of the flume. The three cylindrical lenses changed the circular cross section of the beam into a 2 mmx20 mm elliptical lightsheet. A mirror reflected the lightsheet upwards and through the perspex bottom of the flume, illuminating the particles within the flow.

Figure 2.5 shows the tracer particles that were used to seed the flow (Dantec Dynamics: PSP-20). The datasheet indicated that the particles had a density of 1,03 g/cm^3, a size distribution of $5 - 35\,\mu$m and a refractive index of 1.5. The seeding concentration of the particles used in the experiments ranged from $10 - 20$ mg/l.

The Stokes number St indicates the scale of fluctuating fluid motion that the particles are able to follow. It is defined as

$$St = \frac{\tau_p}{\tau_k} \tag{2.2.1}$$

where τ_p is the particle response time and τ_k is the Kolmogorov timescale. The Kolmogorov timescale is the smallest timescale (highest frequency) appearing in turbulent flow. For $St \ll 1$ the particles will closely follow the fluctuating motion, while for $St \gg 1$ the particle motion will be indifferent to the fluctuating motion. For $St \approx 1$ the particles will follow only the largest scales of the fluctuating motion Poelma (2004, pg. 7, 17).

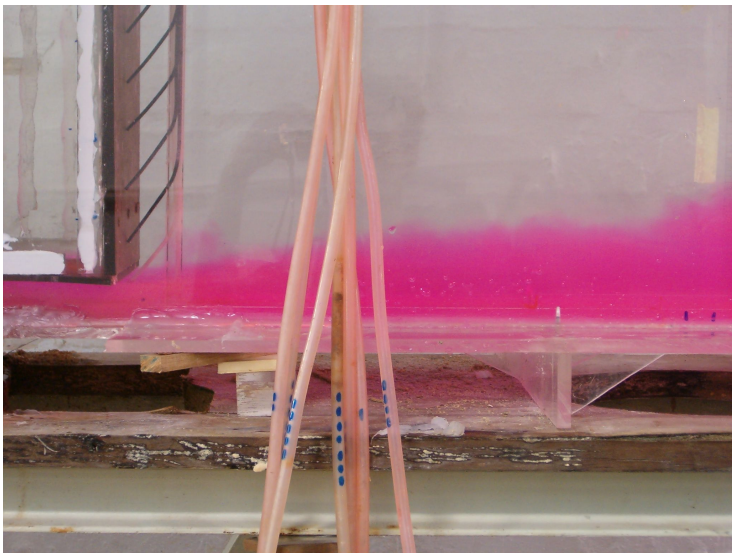

(a) Siphons with gravity current entering the flume

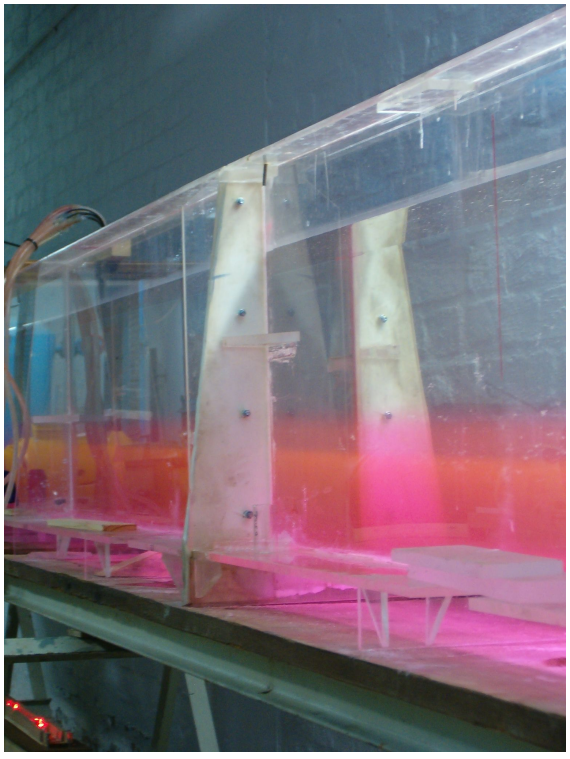

(b) Gravity current body

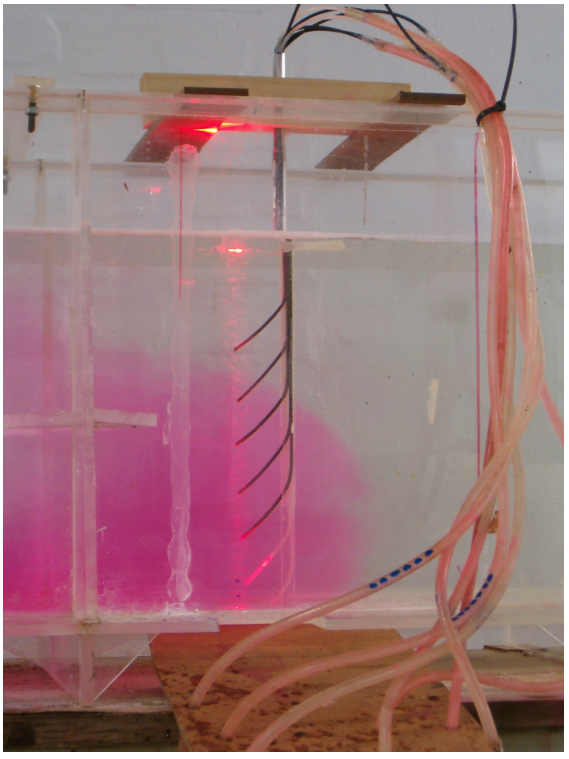

(c) Siphons and lightsheet with passing gravity current head

Figure 2.3: Photographs of pink dyed gravity current (present research)

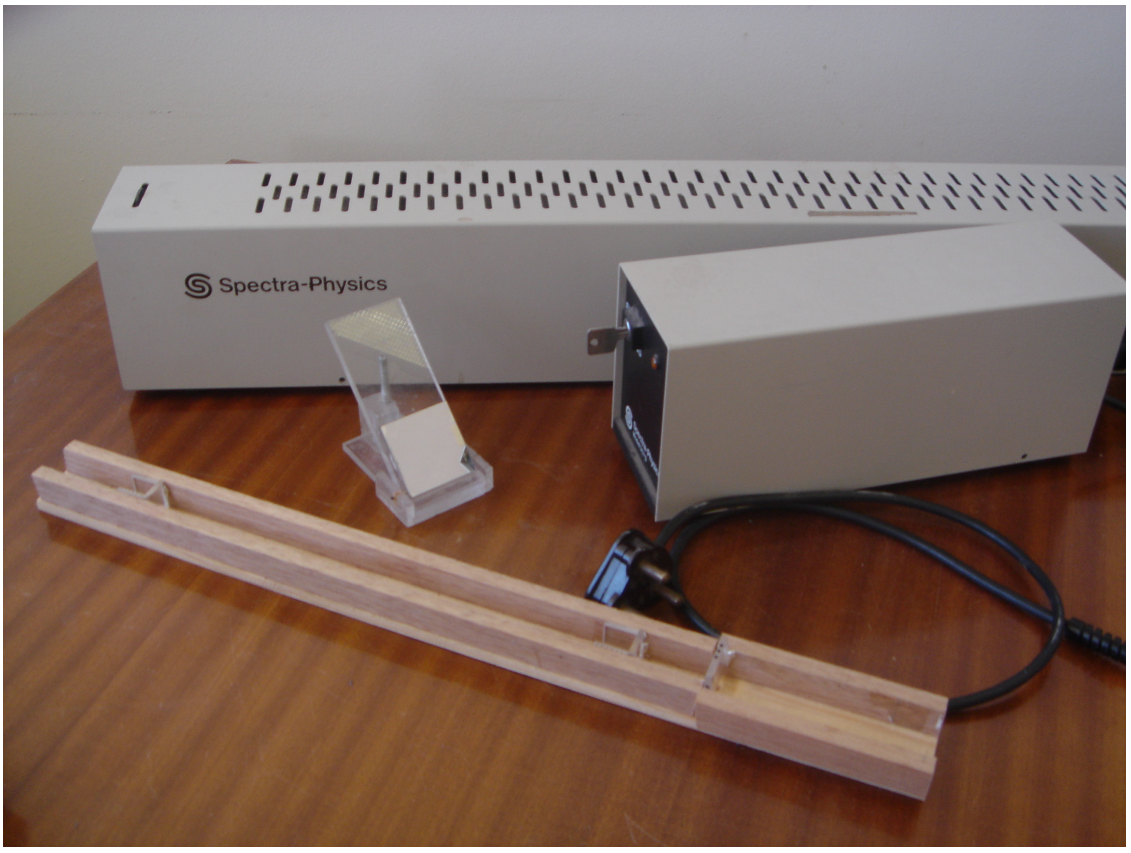

Figure 2.4: Laser, lightsheet lenses and mirror

For Stokes flow, the particle response time is

$$\tau_p = \frac{\rho_p d_p^2}{18\rho_w \nu} \approx 20\,\mu\text{s} \tag{2.2.2}$$

where ρ_p is the density of the particle, ρ_w is the density of water, d_p is the particle diameter and ν is the kinematic viscosity of water. Section 3.1 shows that the Kolmogorov timescale $\tau_k \approx 0{,}37\,\text{s}$ at the inlet. This gives a Stokes number of $5{,}4 \times 10^{-5}$. The very low Stokes number indicates that the particles closely followed the smallest motions of the turbulent flow.

The images were recorded by a grayscale charge-coupled device (CCD) camera (Matrix Vision: mvBlueFox), which was aligned normal to the lightsheet. The camera had a maximum frame rate of 60Hz for 640x480 pixel images. The image size used was 640x128 pixels, which allowed a maximum frame rate of 140Hz to be achieved. This 640x128 image size allowed 4000 images to be recorded with the available 1.5Gb of memory. Figure 2.6 shows the digital camera, camera lens (Fujinon: CF25HA-1) and laptop used to record the images.

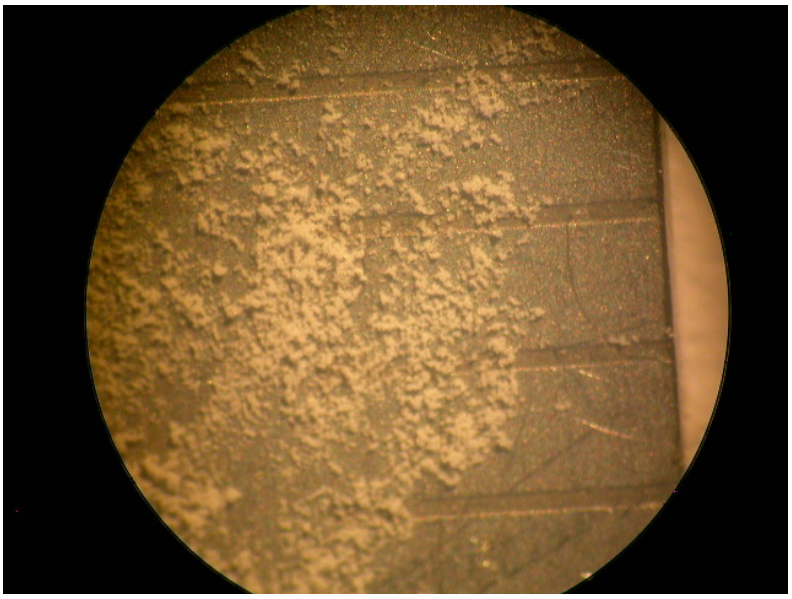

Figure 2.5: Microscope photograph of 20 micron polyamid particles. Particles on ruler with 1mm markings.

A single exposure, double frame recording technique was used (Raffel *et al.*, 1998, pg. 80): Every frame of the recording is exposed only once, with displacement estimates computed from two consecutive frames. This technique was necessary, since the helium-neon laser outputs only a continuous beam and not a pulsed beam. The electronic shutter of the camera was used to control the timing of the CCD exposure. Figure 2.7 gives the CCD exposure timing, as well as when during the image sequence the velocity and density samples were taken.

An image exposure duration of 2 ms produced well exposed images, without any particle streaks. PIV experiments usually have shorter exposure durations, but because gravity currents move quite slowly ($U < 0{,}1$ m/s), this duration was adequate. Figures 2.8a and 2.8b shows a typical PIV image pair of the gravity current flow.

The last aspect of the PIV-S setup is that of refractive index matching. Flows driven by large density differences often have large refractive index differences. These refractive index differences lead to distorted particle images and hence inaccurate displacement estimates. Daviero *et al.* (2001) show how to economically achieve refractive index matching for large-scale stratified flows. They recommend using salt $NaCl$ and ethanol solutions for stratified experiments. The present research measured gravity currents with low excess densities over short laser beam distances. Figure 2.8a shows that particle image distortion was minimal and hence

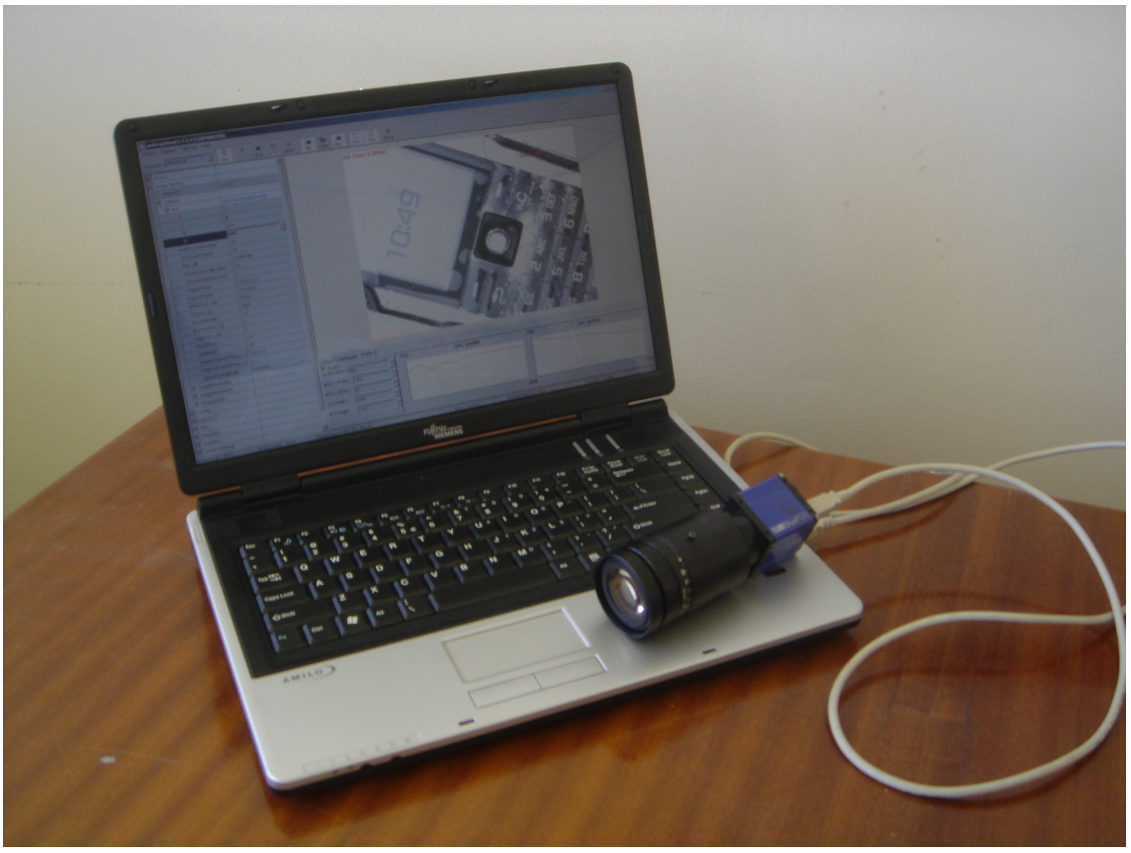

Figure 2.6: Digital camera, camera lens and laptop

refractive index matching was not required.

2.3 Velocity measurement by PIV

Particle image velocimetry (PIV) is a two-dimensional, non-intrusive velocity measuring technique. It involves seeding a flow with small, reflective, neutrally-buoyant particles. A laser lightsheet illuminates the particles, which helps in visualizing the local flow velocity. Using a digital camera, a sequence of images was then recorded of the particles transported by the flow. Local displacement estimates are then computed by cross-correlating two consecutive images of the image sequence, with each other. The cross-correlation function is given by

$$R(dm, dn) = \sum_{m=-K}^{K} \sum_{n=-L}^{L} i_1(m, n) i_2(m + dm, n + dn) \tag{2.3.1}$$

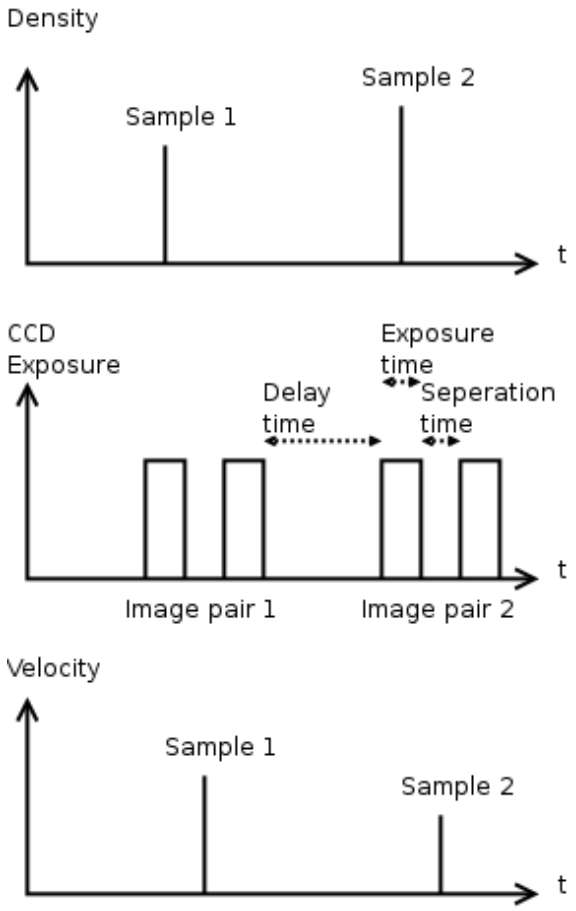

Figure 2.7: Camera timing sequence

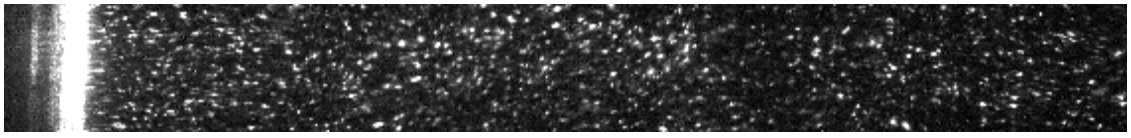

(a) First image

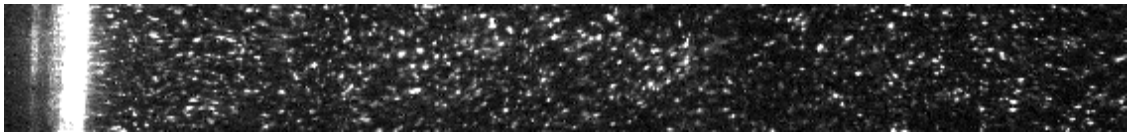

(b) Second image

Figure 2.8: A typical PIV image pair, near the bed of the flume. Flow direction is downwards. (images rotated 90° clockwise)

where $R(dm, dn)$ is the cross-correlation value for displacement (dm, dn), $2K$ is the horizontal size of the interrogation window, $2L$ is the vertical size of the interrogation window, $i_1(m, n)$ is the intensity at pixel position (m, n) in the first image, $i_2(m+dm, n+dn)$ is the intensity at pixel $(m+dm, n+dn)$ in the second image. The displacement is associated with the largest $R(dm, dn)$ value, which is (dm, dn). Finally, local velocity estimates are computed by dividing the displacement estimates by the time elapsed between two consecutive images.

The recorded sequence of images was analysed by the PIV software developed by van der Graaf (2007). The images were interrogated by a multi-pass cross correlation scheme as follows (Raffel *et al.*, 1998, pg. 127):

1. Large interrogation windows (64x64 with a 50% overlap) were used in order for each window to contain a sufficient number of particle images. The seeding concentration of the ambient flume water was kept low (10 mg/l) to maximise the visual contrast with the saline inflow, which had a higher seeding concentration (20 mg/l).

2. No initial pre-shifting was used because the maximum displacements were relatively small (≈ 5 pixels) compared to the large interrogation windows (64 pixels). However, pre-shifting was applied after each pass of the multi-pass scheme, using the displacement results of the previous pass.

3. The computed displacements of each pass were validated by the normalised median test as suggested by Westerweel and Scarano (2005). The threshold for maximum deviation of the tested vector and the median of its eight neighbours was chosen to be two pixels. Tested vectors failing the normalised median test (outliers) were replaced by the medians of their neighbours.

4. The multi-pass scheme continued until the convergence criterion was met. Convergence was declared when the sum of the differences between two successive passes, related to the number of grid-points, was less than 0.25 pixels.

Since the main focus of the experiments was to measure the vertical profiles of the gravity current, a fairly narrow image (640x128 pixels) sufficed. Applying a 64x64 interrogation window with 50% overlap on the narrow image produced a 19x3 data grid (19 vertical points by 3 horizontal points). Hence each image pair produced three vertical profiles.

To compute a velocity gradient at least two points are necessary. In the case of horizontal gradients three points were available from the 19x3 data grid. This

allowed a parabola to be fitted to the three points, from which an accurate estimate of the slope or horizontal gradient was computed at the image centre. Similar parabolic fits were applied to the 19 vertical points to compute the vertical gradients.

2.3.1 Optimisation of velocity measurements

Velocity variances (Reynolds stresses) are computed from measured velocity fluctuations. These fluctuations are usually an order of magnitude smaller than the mean velocity, emphasizing the importance of accurate velocity measurements.

The simplest way to improve the accuracy is to extend the separation time between two images in an image pair as long as possible so that the particle displacements become large (figure 2.7). However, the separation time cannot be too long, since then the two images will become uncorrelated, resulting in erroneous displacement estimates. At the inlet and at a position 0,9 m downstream the greatest displacements which maintained correlation between images was achieved with a separation time of 10 ms. This is the region where the gravity current moves relatively fast. At 2,4 m downstream from the inlet, where the gravity current had become slower, the separation time could be relaxed to 16 ms.

Energy spectra can be computed from velocity time series. The width of the measured spectra are determined by the sampling frequency (highest frequency), as well as the length of the time series (lowest frequency). The sampling frequency was controlled by the image delay and image separation times (figure 2.7).

The maximum sampling frequency is limited by the bandwidth of the digital camera (in this case 140 Hz with a Nyquist limit of 70 Hz), as well as the noise level of the PIV-S setup. Figure 2.9 shows the beginning of a plateau in the one-dimensional energy spectrum for frequencies ≥ 7 Hz, due to the 'white noise' energy level intrinsic to the PIV-S setup. This energy spectrum therefore suggests that it is unnecessary to sample at a frequency much greater than twice this limit, say 20 Hz, for the present PIV-S setup.

PIV measurements, sampled initially at 140 Hz, showed that the maximum attainable sampling frequency was 20 Hz at the inlet and 0,9 m downstream. At 2,4 m downstream from the inlet the maximum attainable sampling frequency was found to be 6 Hz.

Another aspect which influences the accuracy of the velocity measurements is

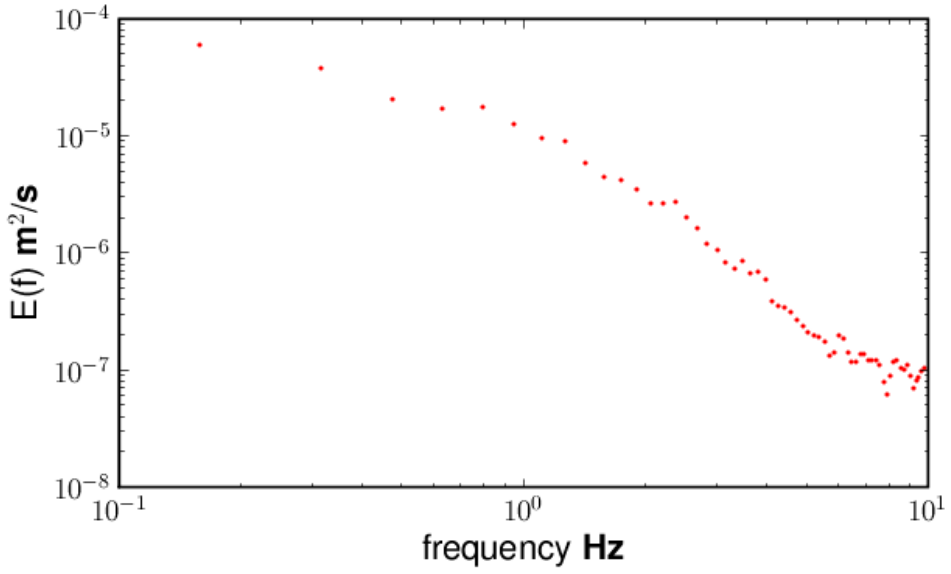

Figure 2.9: One-dimensional, frequency based, energy spectrum of the gravity current: 0,9 m **downstream from inlet and** 24 mm **above the bed**

peak-locking. Peak locking refers to a systematic bias toward integer displacement values, by the sub-pixel estimator on the the cross-correlation values $R(dm, dn)$. This bias is due to the loss of spatial information when the recorded particle image diameters become too small. Raffel *et al.* (1998, pg. 138) recommends that particle image diameters should not be less than two pixels to avoid peak-locking.

The PIV-S setup adhered to this restriction by limiting the distance between the camera and lightsheet. Peak-locking can often be identified by localised peaks at integer values in displacement histograms. Figures 2.10a and 2.10b show typical displacement histograms for the PIV-S setup. The figures do not show any localised peaks at integer values, hence peak-locking did not influence the results.

2.4 Density measurement techniques

There are a number of methods by which to measure the excess density within a gravity current. The first method involves taking samples of the flow at different depths with siphons. The $NaCl$ mass fraction is calculated by weighing the mixture and its dry mass. The density of the sample is calculated by using the empirical

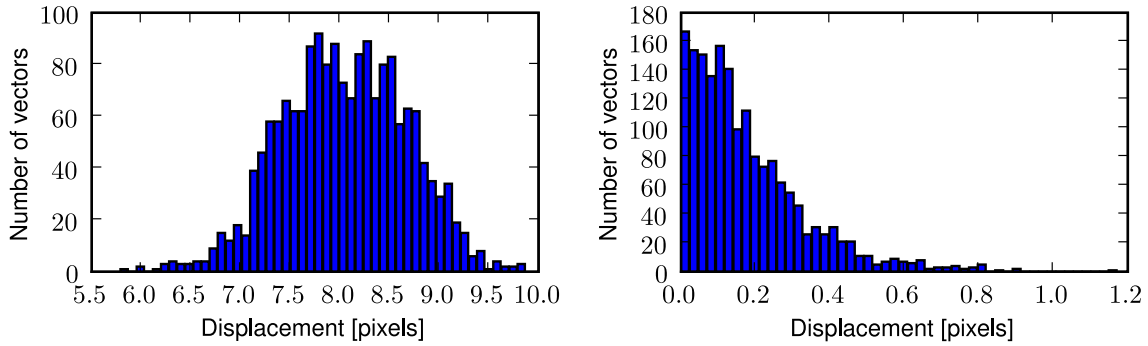

(a) X-displacement histogram **(b) Y-displacement histogram**

Figure 2.10: Displacement histograms of the gravity current: 2,4 m **from inlet and** 40 mm **above the bed**

equation

$$\rho = 711.8182\omega + 998.2364 \tag{2.4.1}$$

where ω is the NaCl mass fraction. Equation 2.4.1 was obtained by a least-squares line fit to the data given in CRC handbook of chemistry and physics, pg. 8-73 (figure 2.11a). A second density measurement method, which is also intrusive, measures the electrical conductivity of the fluid with a probe. The density is also calculated by using an empirical relationship between mixture density and electrical conductivity.

A third density measurement method, which is non-intrusive, measures the image intensity of a tracer entrained in the flow. This is the domain of optical methods such as planar laser induced fluorescence (PLIF) and particle image velocimetry scalar (PIV-S). PLIF and PIV-S are not restricted to point measurements, but allow profiles or contours of image intensity to be measured. The mixture density is calculated by using an empirical relationship between mixture density and image intensity.

Combined PIV-PLIF experiments are usually based on a single laser, double camera technique (Fajardo *et al.*, 2006) or a single camera, double laser technique (Cowen *et al.*, 2001). Both these techniques use different light wavelengths (colours) to discriminate between the image intensities caused by PIV tracers (required for velocity measurements) and PLIF dyes (required for density measurements).

For example, the single laser, double camera technique works as follows: The flow is seeded with PIV tracer particles and a PLIF dye. One camera records PIV images, while the other camera records PLIF images. A single pulsed laser

illuminates the flow at a wavelength λ_{excite}. The PIV camera records the illuminated PIV tracers at this wavelength.

Furthermore, the laser's wavelength excites the PLIF dye. The dye absorbs the light and emits light at a longer wavelength $\lambda_{emit}\,(> \lambda_{excite})$. In order for the PLIF camera to record only images of the dye and not of the PIV tracers a long-pass filter $\lambda_{lp}\,(> \lambda_{excite})$ is placed in front of the PLIF camera. This allows only the λ_{emit} wavelength to pass through to the PLIF camera and hence only images of the PLIF dye to be recorded.

Another example is the single camera, double laser technique, which works as follows: The flow is seeded with PIV tracer particles and a PLIF dye. A continuous laser illuminates the flow at a wavelength λ_{excite}, while a pulsed laser illuminates the flow at a wavelength $\lambda_{PIV}\,(> \lambda_{excite})$. The PLIF dye absorbs the light at the λ_{excite} wavelength and emits light at a longer wavelength $\lambda_{emit}\,(> \lambda_{excite})$. In order to remove the λ_{excite} light of the continuous laser a long-pass filter $\lambda_{lp}\,(> \lambda_{excite})$ is placed in front of the camera.

PIV images are recorded when the pulsed laser and continuous lasers are illuminating the flow simultaneously (i.e. both λ_{PIV} and λ_{emit} wavelengths are recorded). PLIF images are recorded when only the continuous laser is illuminating the flow at λ_{emit}.

PIV-S experiments are based on a single laser, single camera technique, which is described in detail in the following section. The present research measured excess density profiles intrusively with siphons and non-intrusively with PIV-S. The intrusive siphon samples provided a time-averaged excess density profile, while the PIV-S measurements provided instantaneous excess density profiles. The instantaneous excess density data allowed the the excess density variance and Reynolds flux profiles to be computed.

2.5 Excess density measurement by PIV-S

The PIV-S technique is based on the idea that fluids with different densities can be 'marked' with different concentrations of tracer particles (Ramaprabhu and Andrews, 2003, 2004). The spatial distribution of excess density can be visualized by seeding the ambient water in the flume with a low concentration of tracer particles and the saline inflow with a high concentration of tracer particles. The greater the difference in seeding concentration between the ambient water and the gravity

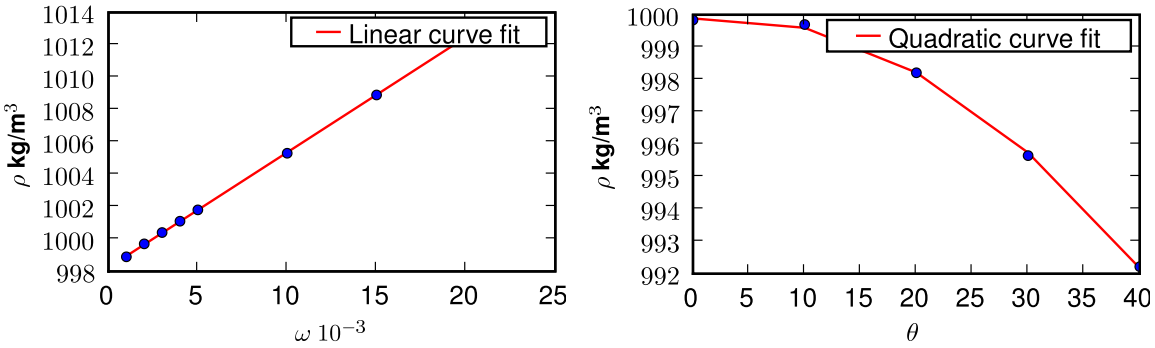

(a) NaCl mass fraction **(b) Temperature**

Figure 2.11: Fluid density as functions of NaCl mass fraction and temperature (CRC handbook of chemistry and physics, pg. 8-73, 6-3)

current, the greater their visual contrast. Ideally, the greatest contrast will be attained when the ambient water contains no tracer particles. However, the absence of tracer particles prevents displacements and velocities from being computed. The visual contrast, therefore, has to be compromised to a limited extent, in order to measure the flow velocity.

Once the ambient flume water and saline inflow are 'marked' the gravity current is recorded in a sequence of 8-bit grayscale images. These 8-bit images have an intensity palette of 256 shades of gray. This means that the intensity i of a pixel can range from 0 (black) to 255 (white), with intermediate values representing different shades of gray.

After the flow has been recorded, particle concentrations are estimated in each image. Ramaprabhu and Andrews (2003, 2004) suggested that the spatially-averaged intensity i_s of an interrogation window is related to its particle concentration. Since particle concentration is used as an indicator for excess density, Ramaprabhu and Andrews (2003, 2004) assumed that $\Delta\rho$ is a linear function of i_s.

The present research assumes that $\Delta\rho$ is a polynomial function of i_s

$$\Delta\rho\left(x,y\right) = f\left(i_s\left(m_0,n_0\right)\right) \tag{2.5.1}$$

with

$$i_s\left(m_0,n_0\right) = \frac{\int_A i\,dA}{A} = \sum_{m=-K}^{K}\sum_{n=-L}^{L}\frac{i\left(m_0+m,n_0+n\right)}{4KL} \tag{2.5.2}$$

where $\Delta\rho\left(x,y\right)$ is the instantaneous excess density estimate at laboratory coordinates (x,y), f is a polynomial function relating excess density to spatially-averaged

intensity, (m_0, n_0) are the pixel coordinates at the centre of the interrogation window, A is the area of the interrogation window, $2K$ is the horizontal size of the interrogation window, $2L$ is the vertical size of the interrogation window and $i\,(m_0 + m, n_0 + n)$ is the pixel intensity at pixel coordinates $(m_0 + m, n_0 + n)$.

Applying equation 2.5.1, with a 64x64 interrogation window and 50% overlap, to the 640x128 pixel images produced a 19x3 density signal grid. Furthermore, the density signals had the same sampling frequency as the velocity signals, since only the first image of each image pair in the image sequence was used (figure 2.7).

2.5.1 PIV-S sensitivity to intensity thresholding

A problem encountered with the PIV-S measurements was that concatenated profiles of mean spatially-averaged intensity $\langle i_s \rangle$ and spatially-averaged intensity variance $\langle i'_s i'_s \rangle$ were discontinuous. The line with an intensity threshold combination of [0,0,0] in figure 2.12a shows such a discontinuous, mean profile.

Profiles of mean excess density $\langle \Delta\rho \rangle$ and excess density variance $\langle \Delta\rho' \Delta\rho' \rangle$ are continuous. Furthermore, it is reasonable to assume that a continuous relation exists between $\Delta\rho$ and i_s (PLIF experiments often assume linear relationships Guillard *et al.* (1998); Cowen *et al.* (2001)). Hence, it follows that profiles of $\langle i_s \rangle$ and $\langle i'_s i'_s \rangle$ should also be continuous.

The discontinuous concatenated profiles may have been caused by a slight misalignment between the centreline of the lightsheet and the centreline of the field of view of the camera. Since the laser intensity of the lightsheet was not uniform, but gaussian (Raffel *et al.*, 1998, pg. 26), it follows that the misalignment caused the recordings to have different overall exposures. Hence each recording had different offsets of mean spatially-averaged intensity.

The problem of discontinuous concatenated $\langle i_s \rangle$ and $\langle i'_s i'_s \rangle$ profiles was solved by applying intensity thresholding to each image. Intensity thresholding is a method by which to discriminate between well-focused in-plane particle images (which have high pixel intensities) and unfocused out-of-plane particle images (which have low pixel intensities). Intensity thresholding reassigns a pixel's intensity to zero (black) if it falls below a specified minimum threshold value. Figures 2.14a and 2.14b show how an intensity threshold value of 150 removes the unfocused particle images (background noise). Reassigning low pixel intensities to zero not only decreases $\langle i_s \rangle$, but also $\langle i'_s i'_s \rangle$, since $\langle i'_s i'_s \rangle$ is sensitive to any background noise.

Intensity thresholding therefore allows $\langle i_s \rangle$ and $\langle i'_s i'_s \rangle$ profiles to be adjusted, so that their concatenated profiles become continuous. Figures 2.12a and 2.12b show how different threshold value combinations adjusted the concatenated profile. For example, the threshold combination [0,0,0] indicates that threshold values of 0 have been applied to the lower, middle and upper profiles (the first index refers to the lower profile, the second index to the middle profile and the third index to the upper profile).

The intensity threshold value should, however, be kept low, since figures 2.12b and 2.13b show that $\langle i'_s i'_s \rangle$ and $\langle \Delta\rho' \Delta\rho' \rangle$ become dependent on the threshold value if it becomes large. Figures 2.13a and 2.13b show that a threshold combination of [50,40,75] produced threshold independent, continuous concatenated profiles.

2.5.2 PIV-S sensitivity to window size

Ramaprabhu and Andrews (2003) notes that $\langle i'_s i'_s \rangle$ can be dependent on the size of the interrogation window. If the window is too small the estimate of $\langle i'_s i'_s \rangle$ will be unstable, since the number of particle image realizations will be too few. If the window is too large averaging may hide real gradients of i_s within the flow field.

Figure 2.15a shows that the $\langle i_s \rangle$ profiles are independent for window sizes greater than 16x16 pixels. Figure 2.15b shows that the $\langle i'_s i'_s \rangle$ profiles become independent for window sizes greater than 64x64 pixels. A window size of 64x64 pixels with a 50% overlap was therefore chosen as the default window size.

2.5.3 PIV-S test cases

The consistency of the PIV-S technology was verified against three test cases: (1) A quiescent flume, having a homogeneous distribution of tracer particles. (2) A clear water flow with a similar concentration of tracer particles, also homogeneously distributed. (3) A gravity current, where the ambient flume water was homogeneously seeded with the same concentration as in the quiescent case and the saline inflow homogeneously seeded with a higher concentration of tracer particles.

Figures 2.16a and 2.16b shows that the $\langle i_s \rangle$ and $\langle i'_s i'_s \rangle$ profiles for the quiescent and clear water test-cases are similar. This is due to the similar particle concentrations used. These profiles show that the PIV-S results are independent of fluid motion if the tracer particles are homogeneously distributed throughout the flow.

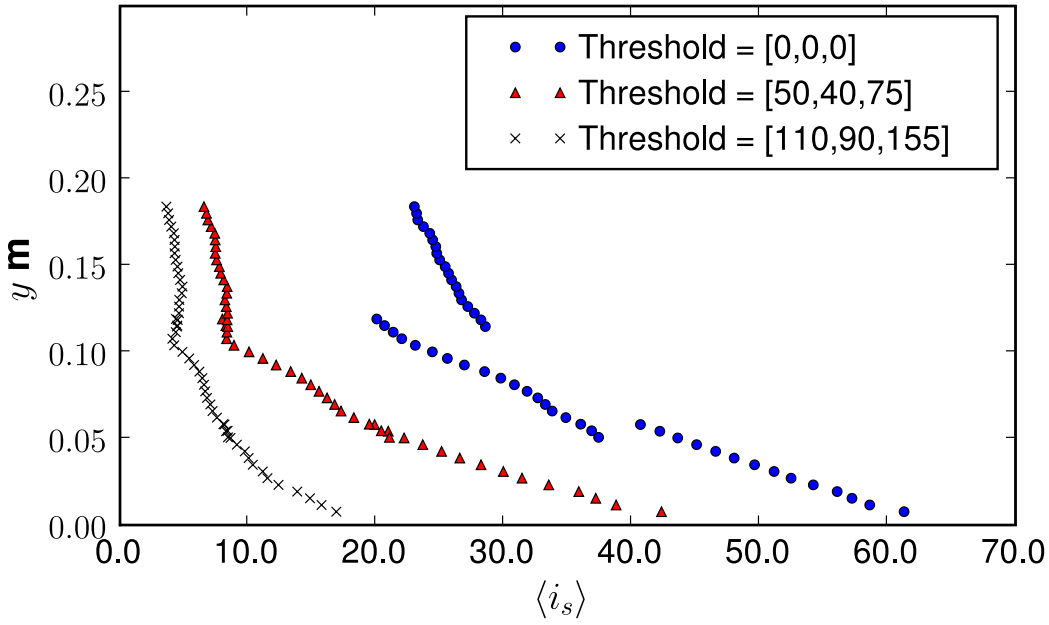

(a) Mean spatially averaged intensity

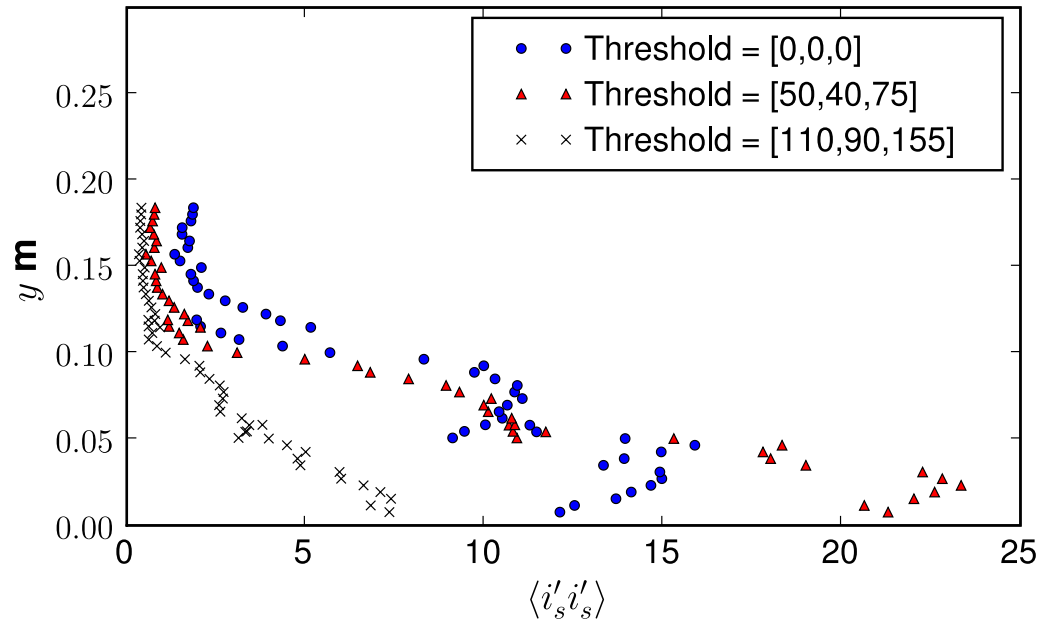

(b) Variance of spatially averaged intensity

Figure 2.12: Threshold sensitivity analysis on spatially-averaged intensity profiles

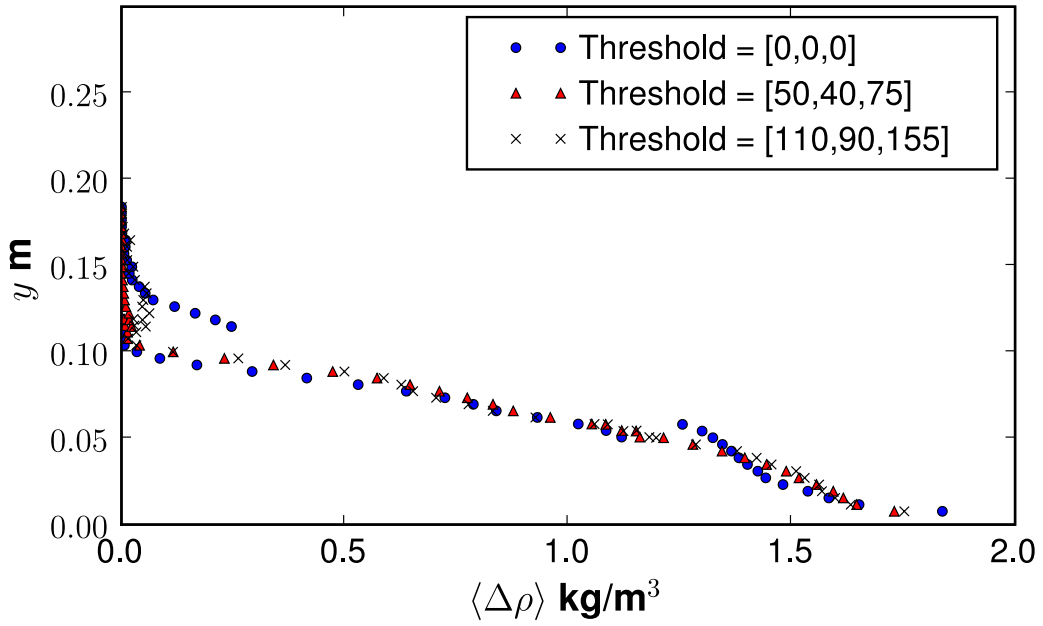

(a) Mean excess density

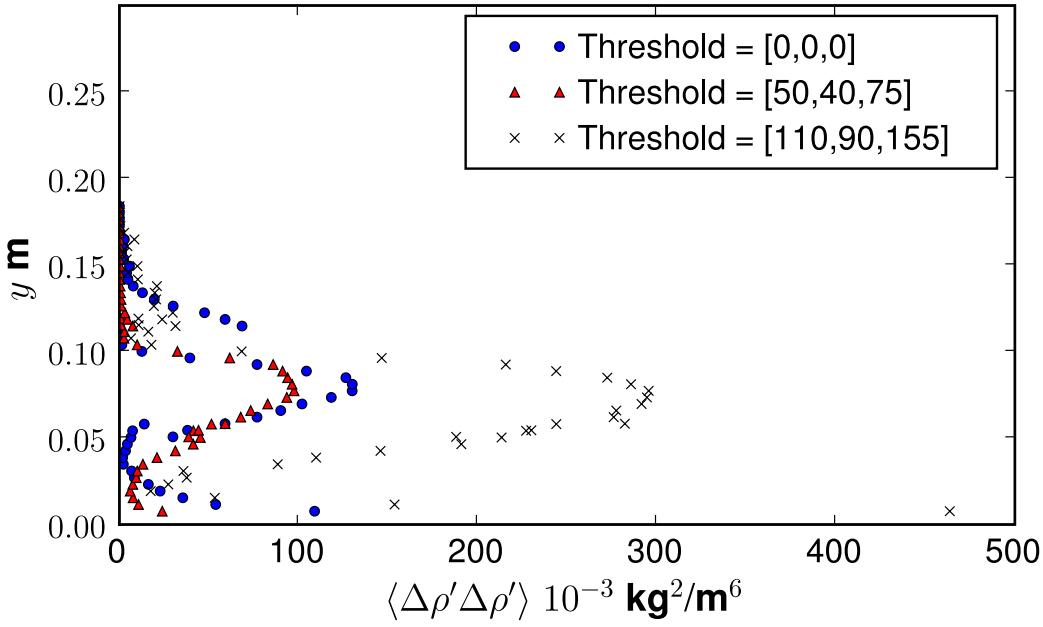

(b) Variance of excess density

Figure 2.13: Threshold sensitivity analysis on excess density profiles

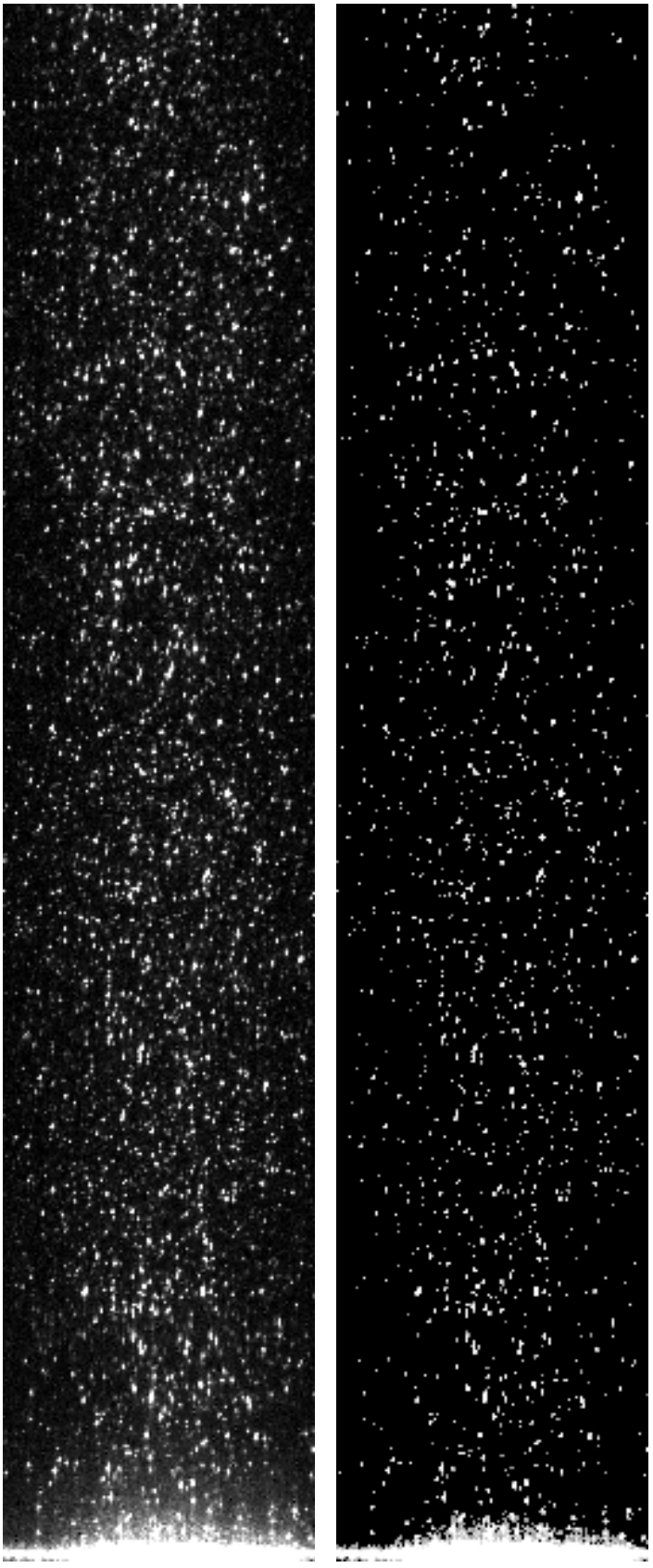

(a) No thresholding (b) Threshold value of 150

Figure 2.14: Background noise removal by pixel intensity thresholding

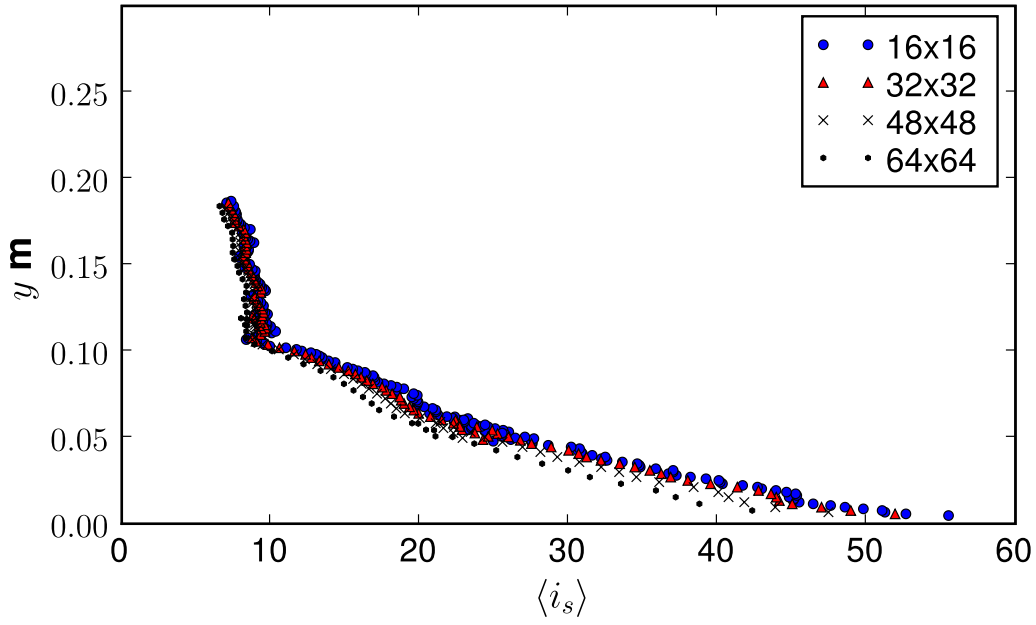

(a) Mean spatially averaged intensity

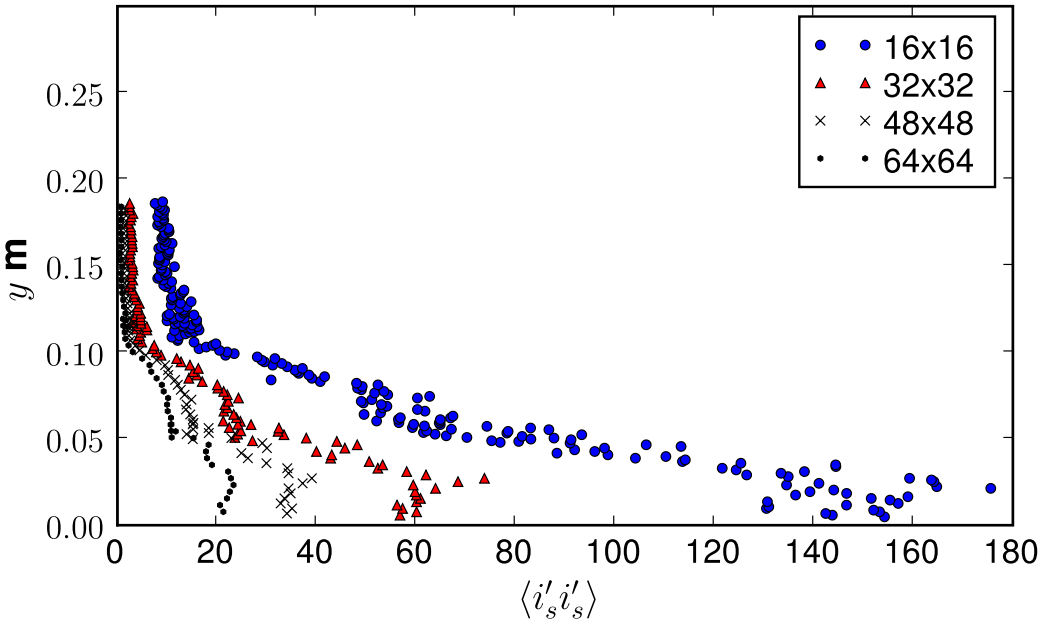

(b) Variance of spatially averaged intensity

Figure 2.15: Window size sensitivity analysis on spatially-averaged intensity profiles

Furthermore, the $\langle i_s \rangle$ profiles for the quiescent and clear water test cases should be independent of flow depth, due to the homogeneous distribution of tracer particles. Figure 2.16a, however, shows that there is a slight decrease in $\langle i_s \rangle$ with depth, due to lightsheet attenuation through the flow.

Figure 2.16b also shows that $\langle \acute{i_s}\acute{i_s} \rangle$ for the quiescent and clear water test-cases are small. This is due to the homogeneous distribution of particles, where $\acute{i_s}$ fluctuations from the mean $\langle i_s \rangle$ are small.

In contrast to the quiescent and clear water test-cases, the $\langle i_s \rangle$ and $\langle \acute{i_s}\acute{i_s} \rangle$ profiles of the gravity current near the bed have large values at 0,9 m. This increase in mean spatially-averaged intensity and variance is due to the mixing of the different particle concentrations between the ambient water and the gravity current. The interface between the ambient flume water and gravity current can be discerned by the slope discontinuity in the $\langle i_s \rangle$ and $\langle \acute{i_s}\acute{i_s} \rangle$ profiles.

The $\langle i_s \rangle$ profile of the gravity current at 2,4 m does not show a slope discontinuity, which indicates that the interface was above the field of view of the PIV-S measurements. Furthermore, the slope of the i_s profile at 2,4 m is similar to the near-bed gravity current i_s slope at 0,9 m. The $\langle i'_s i'_s \rangle$ profile slope of the gravity current at 2,4 m is similar to those of the quiescent and clear water flows, which indicates that little turbulent mixing of the particle concentrations occurred at 2,4 m.

2.5.4 PIV-S sensitivity to polynomial degree

The application of the PIV-S technology to a sequence of images produces a grid of velocity signals and spatially-averaged intensity signals. The spatially-averaged intensity signals are transformed into density signals by an empirical function such as equation 2.5.1.

PLIF experiments (Guillard *et al.*, 1998; Cowen *et al.*, 2001) convert individual pixel intensities into concentrations. Each pixel has its own empirical function, which is derived by fitting a straight line to the intensity and concentration calibration data for that pixel.

The present research used a different approach to obtain an empirical function since the volume of fluid, the number of experimental runs and the cost of the tracer particles made the approach of Guillard *et al.* (1998) expensive. Instead of assuming that $\Delta\rho$ is a linear function of i_s it is assumed that $\Delta\rho$ is a polynomial

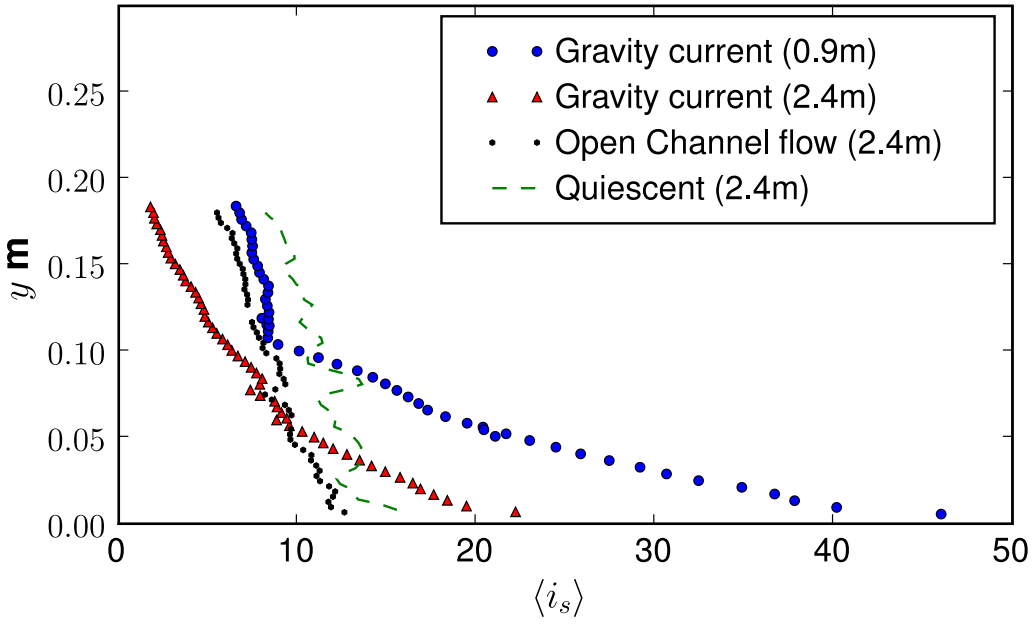

(a) Mean spatially-averaged intensity

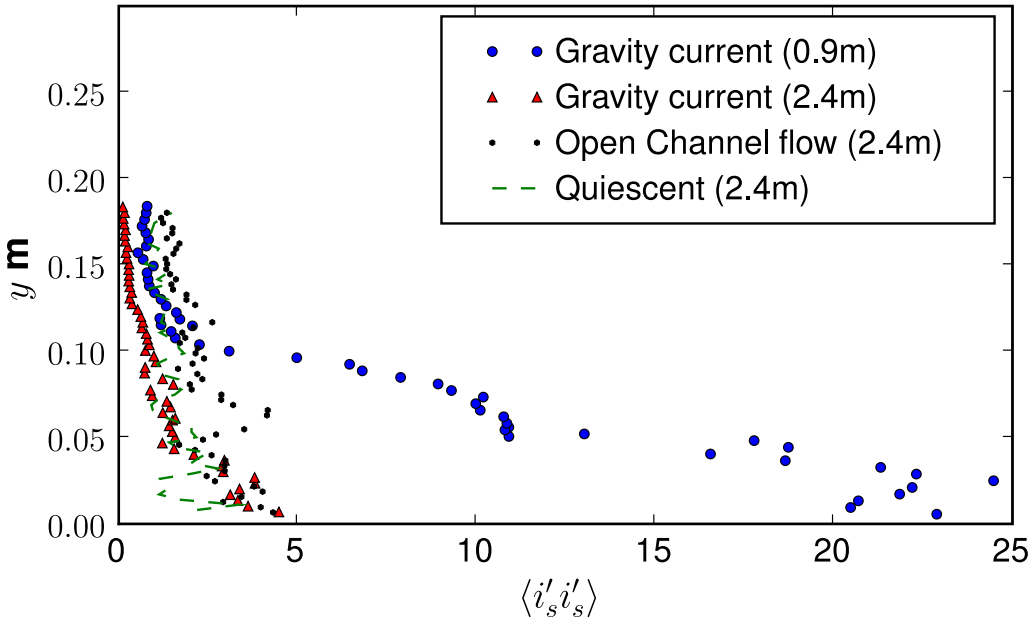

(b) Variance of spatially-averaged intensity

Figure 2.16: Test cases on spatially-averaged intensity profiles: No flow, clear-water flow and gravity current flow

function of i_s (eq. 2.5.1). The polynomial was determined as follows:

1. The time-averaged excess density $\langle\Delta\rho\rangle_{siphon}$ profiles of the gravity current were first measured using siphons.
2. The time series of i_s profiles was then computed.
3. The coefficients for the polynomial were guessed.
4. The polynomial was used to convert the time series of i_s profiles into a time series of $\Delta\rho$ profiles.
5. The mean excess density $\langle\Delta\rho\rangle_{pivs}$ profile was computed from the time series of $\Delta\rho$ profiles.
6. Steps 4 to 6 were repeated with adjusted coefficients until the $\langle\Delta\rho\rangle_{pivs}$ profile of the intensity measurements was the same as the $\langle\Delta\rho\rangle_{siphons}$ profile of the siphon measurements.
7. The optimised polynomial passing step 6 is returned.

Figure 2.17a plots $\langle\Delta\rho\rangle_{siphon}$ against the corresponding value of $\langle i_s\rangle$ for a particular flow depth. Some of the $\langle\Delta\rho\rangle_{siphon}$ values had to be interpolated along the flow depth to find a match for the high resolution profile of $\langle i_s\rangle$ values. Figure 2.17a also show the optimized empirical polynomials of different degrees.

Figure 2.17b shows that the $\langle\Delta\rho'\Delta\rho'\rangle$ profile is least sensitive to the polynomial degree for third and fourth degree polynomials. The optimised third degree polynomial was therefore used as the empirical transfer function. At a position 0,9 m the polynomial was

$$\Delta\rho = 7{,}9\times10^{-5}i_s^3 - 8{,}4\times10^{-3}i_s^2 + 3{,}1\times10^{-1}i_s - 2{,}3 \tag{2.5.3}$$

and at a position 2,4 m the polynomial was

$$\Delta\rho = 1{,}5\times10^{-6}i_s^3 - 6{,}2\times10^{-4}i_s^2 + 7{,}3\times10^{-2}i_s - 9{,}4\times10^{-1} \tag{2.5.4}$$

2.6 Velocity and density signal processing

The present PIV-S setup produced a 19x3 velocity and density signal grid for each field of view recorded. By using different fields of view, signal grids can be

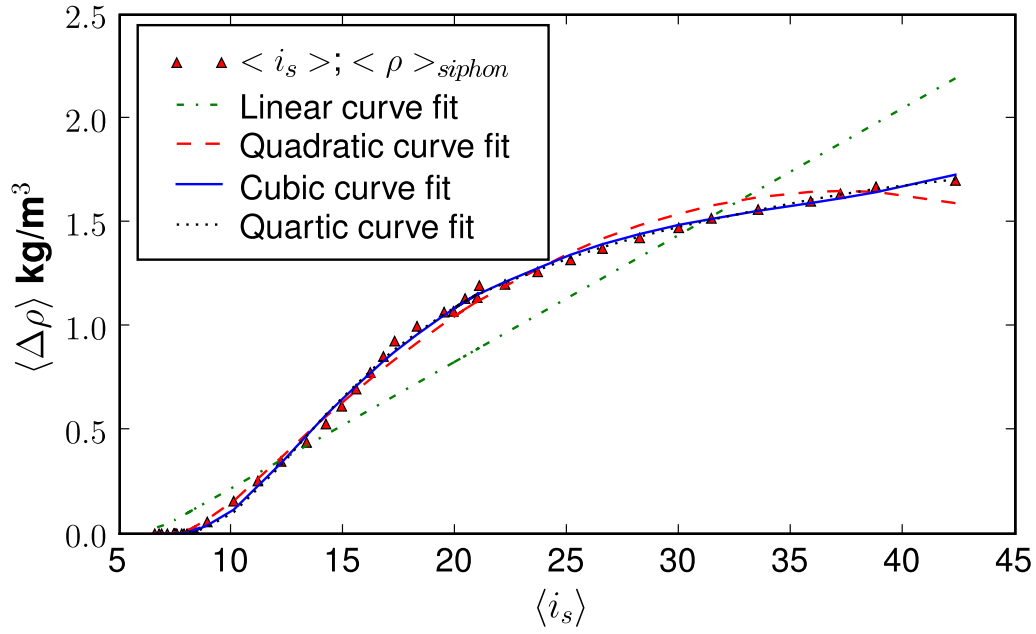

(a) Mean excess density as a function of mean spatially averaged intensity

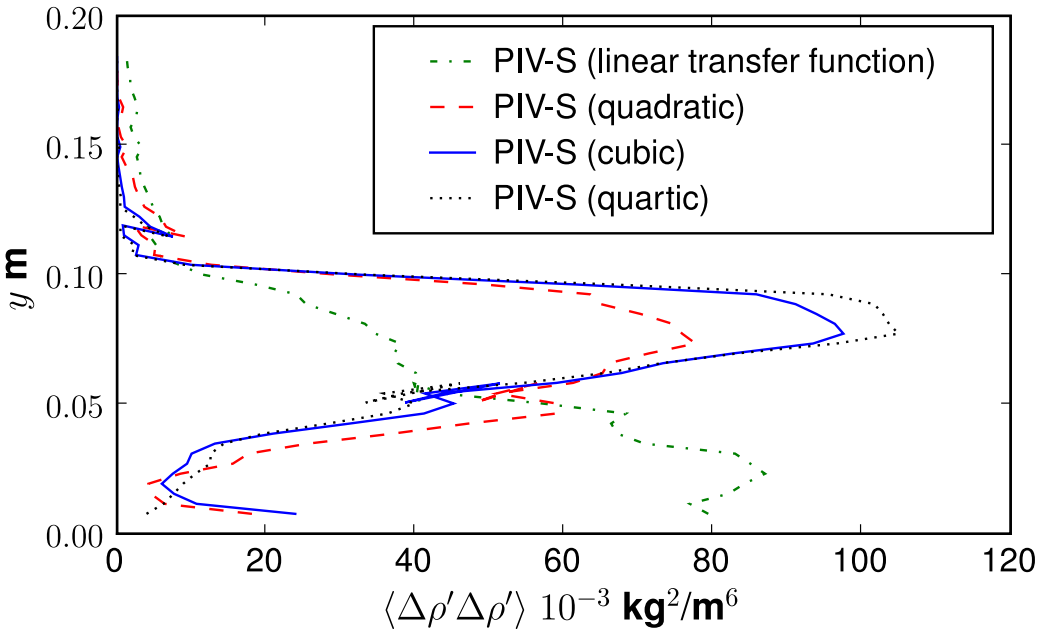

(b) Excess density variance profile

Figure 2.17: Polynomial degree sensitivity analysis: 0,9 m from the inlet

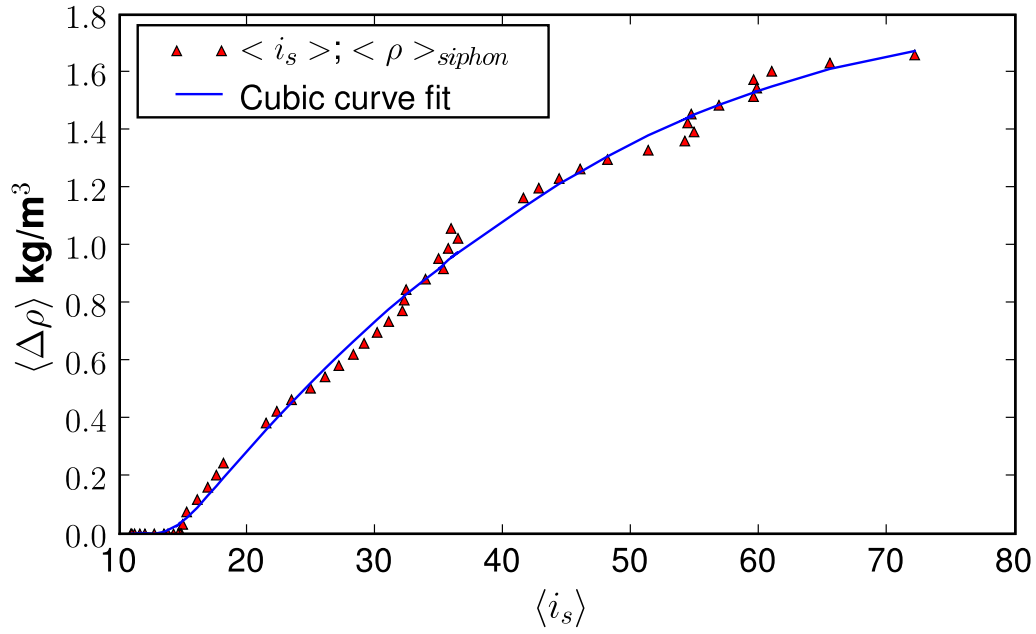

(a) Mean excess density as a function of mean spatially averaged intensity

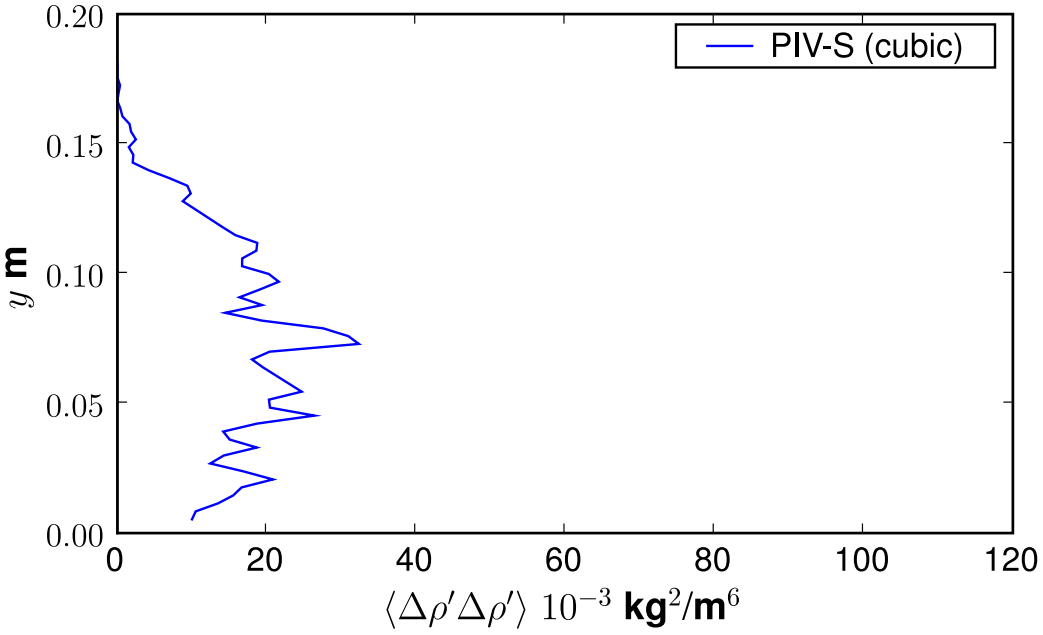

(b) Excess density variance profile

Figure 2.18: Polynomial degree sensitivity analysis: 2,4 m from the inlet

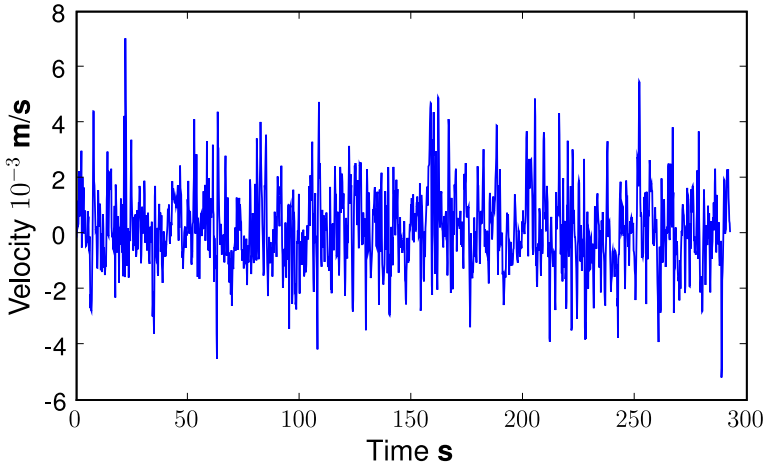

Figure 2.19: v-velocity time series for a point 2,4 m from inlet and 40 mm above the bed, sampled at 6 Hz

concatenated on top of one another, allowing profiles with more than 19 points in the vertical. Each element of these grids represents the velocity or density signal for a point within the flow (for example, figure 2.19 presents a typical v-velocity signal). This section shows how these signals were processed to produce profiles of mean velocity, mean excess density, excess density variance, Reynolds stresses, Reynolds fluxes and 1D energy spectra.

The paper of Benedict and Gould (1996) discusses methods of calculating the statistical uncertainty for various turbulence quantities. The present research follows their approach to compute the turbulence quantities, but does not attempt to calculate the uncertainty limits, due to the limited number of independent samples collected for 300 s of flow (approximately 300).

2.6.1 Calculation of means and covariances

The sample mean velocity U and excess density $\langle \Delta\rho \rangle$ for a data grid point is given by

$$U = \frac{1}{N}\sum_{i=1}^{N} u_i \tag{2.6.1}$$

$$\langle \Delta\rho \rangle = \frac{1}{N}\sum_{i=1}^{N} \Delta\rho_i \tag{2.6.2}$$

where N is the number of independent samples and u_i, $\Delta\rho_i$ are the instantaneous velocity and excess density samples for the the grid point.

The sample variances and covariances (which are estimates of the Reynolds stresses and fluxes) for a data grid point are given by

$$\langle u'u' \rangle = \frac{1}{N} \sum_{i=1}^{N} (u_i - U)^2 \tag{2.6.3}$$

$$\langle v'v' \rangle = \frac{1}{N} \sum_{i=1}^{N} (v_i - V)^2 \tag{2.6.4}$$

$$\langle \Delta\rho'\Delta\rho' \rangle = \frac{1}{N} \sum_{i=1}^{N} (\Delta\rho_i - \langle \Delta\rho \rangle)^2 \tag{2.6.5}$$

$$\langle u'v' \rangle = \frac{1}{N} \sum_{i=1}^{N} (u_i - U)(v_i - V) \tag{2.6.6}$$

$$\langle \Delta\rho'u' \rangle = \frac{1}{N} \sum_{i=1}^{N} (\Delta\rho_i - \langle \Delta\rho \rangle)(u_i - U) \tag{2.6.7}$$

$$\langle \Delta\rho'v' \rangle = \frac{1}{N} \sum_{i=1}^{N} (\Delta\rho_i - \langle \Delta\rho \rangle)(v_i - V) \tag{2.6.8}$$

2.6.2 Calculation of the temporal autocorrelation function

The autocorrelation function, or simply autocorrelation of a signal, is the starting point for calculating many turbulence quantities. For example, it is used to calculate the integral timescale $\mathcal{T}$, which provides an indication of the time lag between uncorrelated and independent samples. The autocorrelation function is also used to calculate the one-dimensional frequency-based energy spectrum of turbulence. The inertial subrange of this spectrum is used to test whether turbulence is locally isotropic, as well as to calculate the dissipation rate of turbulent kinetic energy ϵ (Tennekes and Lumley, 1973, pg. 254).

The autocorrelation of the v-velocity signal is defined as (Tennekes and Lumley, 1973, pg. 210)

$$R_{vv}(s) \equiv \langle v'(t)\, v'(t+s) \rangle \tag{2.6.9}$$

where $v'(t)$ is the v-velocity fluctuation at an arbitrary time t and s is the time lag. Furthermore, the autocorrelation coefficient is given by (Tennekes and Lumley,

1973, pg. 210)

$$\rho_{vv}(s) \equiv \frac{\langle v'(t)\, v'(t+s)\rangle}{\langle v'v'\rangle} \tag{2.6.10}$$

The unbiased sample autocorrelation for subsequence i of the velocity time series is given by (Matlab, 2006, pg. 3-4)

$$R_{vv,i}[p] = \frac{1}{N-p}\sum_{n=0}^{N-1-p} \acute{v}[n]\,\acute{v}[p+n] \qquad p = 0, 1, 2...N-1 \tag{2.6.11}$$

where p is the lag index, N is the number of samples and $\acute{v}[n]$ is the v-velocity fluctuation for sample n.

The *average* unbiased sample autocorrelation $R_{vv}[p]$ is computed as follows (Phillips and Parr, 1999, pg. 594)(Poelma, 2004, pg. 71):

1. The sample mean velocity V (equation 2.6.1) is subtracted from the v-velocity time series, giving the fluctuating velocity time series.
2. The fluctuating velocity series is divided into L overlapping subsequences each having a length of at least five integral timescales $5\mathcal{T}$. This ensures that each subsequence is long enough to provide a representative history of the measured velocity.

   Furthermore, the subsequences overlap each other to avoid data loss when the Hanning window function is applied to the autocorrelation function. The Hanning window function is used when computing the one-dimensional energy spectrum.
3. The unbiased sample autocorrelation for each subsequence $R_{vv,i}[p]$ is computed from equation 2.6.11.
4. The *average* unbiased sample autocorrelation $R_{vv}[p]$ is found by

$$R_{vv}[p] = \frac{1}{L}\sum_{i=1}^{L} R_{vv,i}[p] \tag{2.6.12}$$

Henceforth the *average* unbiased sample autocorrelation $R_{vv}[p]$ is simply referred to as the autocorrelation. Once the autocorrelation is known, the sample autocorrelation coefficient $\rho_{vv}[p]$ can be calculated by (Matlab, 2006, pg. 3-4)

$$\rho_{vv}[p] = \frac{R_{vv}[p]}{R_{vv}[0]} \qquad p = 0, 1, 2...N-1 \tag{2.6.13}$$

Figures 2.20a and 2.20b show the measured sample autocorrelation coefficients for a point in the gravity current flow. Note that the sample autocorrelation coefficient becomes less reliable for large lag times, since the length of the subsequence has to be finite and hence there are necessarily fewer large lag time data than short lag time data.

2.6.3 Selection of independent samples

The integral timescale $\mathcal{T}$ is an indication of how long a signal is correlated with itself. For time intervals larger than $\mathcal{T}$, the signal becomes increasingly uncorrelated and independent of itself. The integral timescale of the v-velocity signal is given by (Tennekes and Lumley, 1973, pg. 210)

$$\mathcal{T}_{vv} = \int_0^\infty \rho_{vv}(s)\, ds \tag{2.6.14}$$

The present research computed the integral timescale by numerically integrating equation 2.6.13 from $p = 0$ up to its first zero-crossing $\rho_{vv}[p] \geq 0$ (Wernersson and Tragardh, 2000). Following Tennekes and Lumley (1973, pg. 214) independent samples of a signal were obtained by sampling at intervals twice that of the integral timescale. Sampling at intervals of one integral timescale would theoretically also work but, to be conservative, sampling intervals are made twice as long as the integral timescale.

The PIV measurements revealed that the u-velocity based integral timescale $\mathcal{T}_{uu}$ was much larger than the v-velocity based integral timescale $\mathcal{T}_{vv}$, due to the anisotropy of the flow. It was decided not to use the u-velocity integral timescale, since it would have resulted in less than 30 independent samples for the flow record length of 300s. Instead $\mathcal{T}_{vv}$ was used as the integral timescale. $\mathcal{T}_{vv}$ was approximately 0,5 s, resulting in 300 independent samples for the record length of 300s.

Historical gravity current experiments used record lengths of 12 s Buckee *et al.* (2001), 4 s Kneller *et al.* (1999), while the experiments of Choux *et al.* (2005) had a constant inlet discharge for 21,5 s. These studies may have suffered from unconverged averages (unconverged means, variances and covariances), if one takes into account the large time lag required to obtain an independent sample in the present research (1 s) and the short record lengths used in those studies.

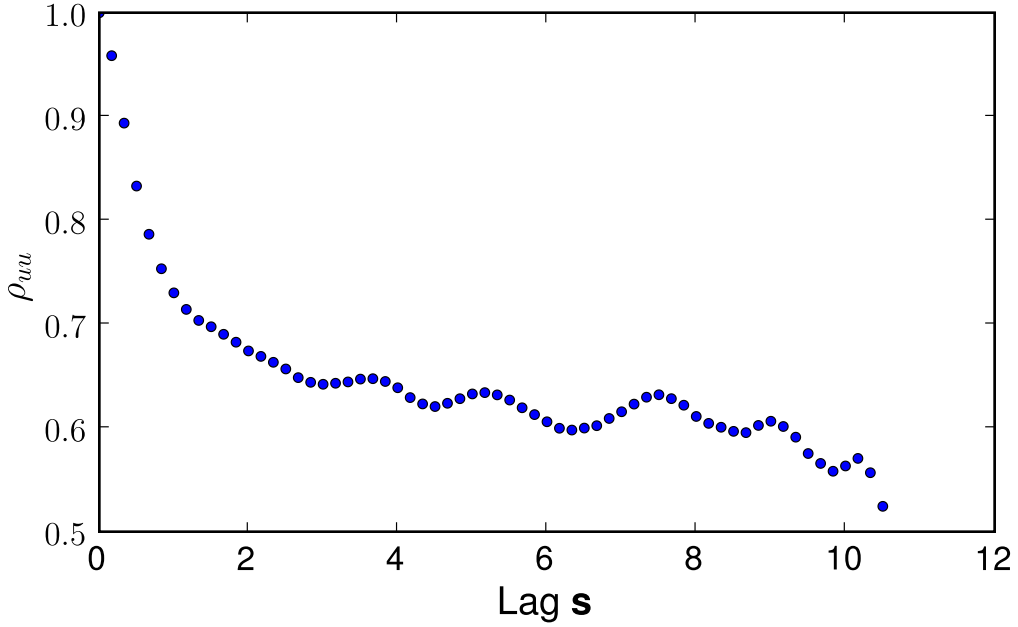

(a) Sample autocorrelation coefficient of u-velocity

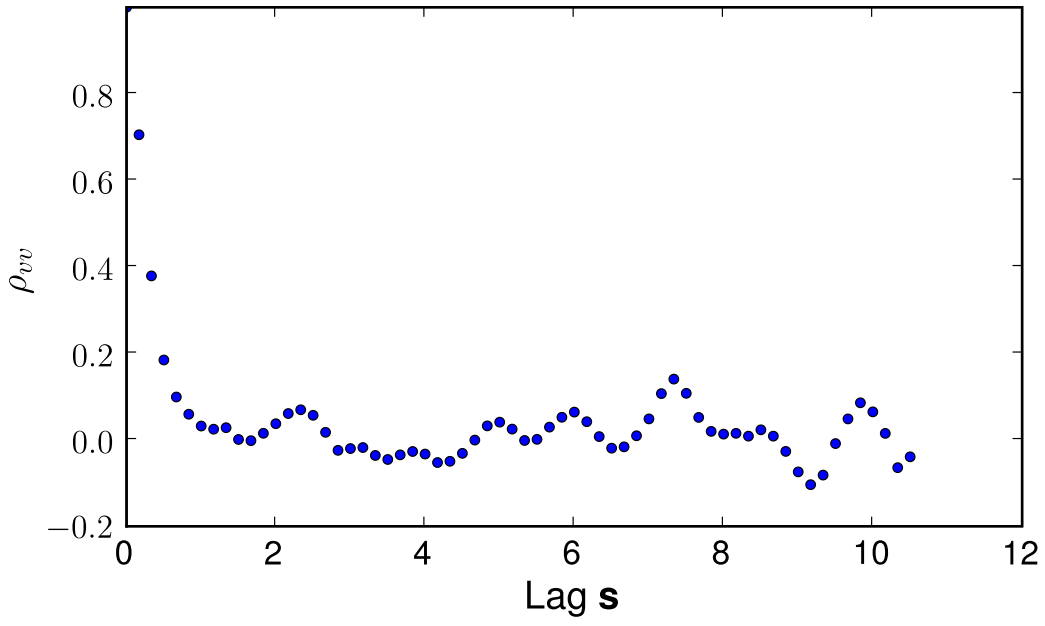

(b) Sample autocorrelation coefficient of v-velocity

Figure 2.20: Measured sample autocorrelation coefficients for a point 2.4m from inlet and 40mm above the bed (present research)

2.6.4 One-dimensional energy spectra

Turbulence is a three-dimensional time-dependent motion having a wide spectrum of lengthscales and corresponding timescales. The greater the Reynolds number of the flow, the wider this spectrum of lengthscales and timescales.

Turbulent flows are characterised by velocity and density fluctuations. These fluctuations are caused by eddies, which can have different lengthscales and timescales. Large eddies are associated with low frequency fluctuations, while small eddies are associated with high frequency fluctuations. For example, the integral timescale is the largest timescale (lowest frequency) occurring in turbulent motion and the Kolmogorov timescale is the smallest timescale (highest frequency).

The large eddies interact with the mean flow by converting the mean kinetic energy of the flow into turbulent kinetic energy. The turbulent kinetic energy is passed on to successively smaller eddies through vortex stretching. The turbulent kinetic energy is finally dissipated by the smallest eddies of the turbulence. This transfer of energy from the largest eddies to the smallest is known as the energy cascade (Rodi, 1980, pg. 9), (Bradshaw, 1971, pg. 17).

The energy cascade can be studied with the energy spectrum. The energy spectrum gives the mean energy for each frequency or wavelength. The one-dimensional frequency based energy spectrum $E_{vv}(f)$ is defined as twice the Fourier transform of the temporal velocity autocorrelation $R_{vv}(s)$ Pope (2001, pg. 225). This definition has the convenient property that its integral is equal to the variance of the signal

$$\int_0^\infty E_{vv}(f)\,df = \langle v'v' \rangle \tag{2.6.15}$$

where f is the frequency. In order to transform between the frequency domain and the wavenumber domain, the Taylor hypothesis is commonly used:

$$-\frac{\partial u_i}{\partial t} = U_{ref}\frac{\partial u_i}{\partial x_i} \tag{2.6.16}$$

where U_{ref} is a reference velocity of the local flow. This hypothesis states that a spatial velocity fluctuation passes an observation point so fast that it varies little in time during this passage. This is only true when the mean velocity is much greater than the turbulent velocity fluctuations $\sqrt{\langle u'u' \rangle}/U < 0{,}1$. In other words, the turbulent intensity should be low. Using the Taylor hypothesis, frequency based energy spectra $E_{vv}(f)$ can be transformed into wavenumber based energy spectra

$E_{vv}(\kappa)$ as follows:

$$\kappa = |\bar{\kappa}| = \frac{2\pi f}{U_{ref}} \tag{2.6.17}$$

$$E_{vv}(\kappa) = \frac{U_{ref}}{2\pi} E_{vv}(f) \tag{2.6.18}$$

where $\bar{\kappa}$ is the wavenumber vector and κ is the wavenumber magnitude. If the Reynolds number is large enough (i.e. the energy spectrum is sufficiently wide) the energy spectrum can be divided into three subranges: the production subrange, the inertial subrange and the viscous subrange. The production subrange contains the large eddies which interact with the mean flow and convert mean kinetic energy into turbulent kinetic energy. The dissipation subrange contains the small eddies which dissipate the turbulent kinetic energy into heat.

Between the production subrange and dissipation subrange lies the inertial subrange. The inertial subrange contains eddies that do not contribute to the production or the dissipation of turbulent kinetic energy. These eddies merely transfer the turbulent kinetic energy to successively smaller eddies. Within the inertial subrange Kolmogorov's -5/3 law holds Pope (2001, pg. 231)

$$E(\kappa) = C\epsilon^{2/3}\kappa^{-5/3} \tag{2.6.19}$$

where $E(\kappa)$ is the three-dimensional energy spectrum defined as the total energy contained in a wave with wavenumber magnitude κ, ϵ is the dissipation rate of turbulent kinetic energy and $C = 1{,}5$ was determined by experimental studies. Pope (2001, pg. 232) and Tennekes and Lumley (1973, pg. 254) show that for isotropic turbulence the following ratios hold in the inertial subrange:

$$\frac{E_{uu}(\kappa_1)}{1} = \frac{E_{vv}(\kappa_1)}{\frac{4}{3}} = \frac{E(\kappa)}{\frac{55}{18}} \tag{2.6.20}$$

where κ_1 is the component of the wavenumber vector in the streamwise direction. Equation 2.6.20 is often used to test whether turbulence is isotropic. If it is, then equation 2.6.20 can be used to convert the measured $E_{uu}(\kappa_1)$ or $E_{vv}(\kappa_1)$ into $E(\kappa)$. Equation 2.6.19 can then be used to estimate the dissipation rate of turbulent kinetic energy ϵ.

The dissipation rate ϵ is an important variable in turbulence models. So much so, that the transport equation for ϵ has often been blamed for the poor performance of turbulence models. Model verification by measured ϵ values can therefore be very useful.

2.7 Summary

This chapter has presented the hydraulic setup used to generate a continuous, dilute, saline gravity current. The current was dilute enough not to require refractive index matching. Particle image velocimetry scalar (PIV-S) was also introduced as a non-intrusive technology by which to measure a time series of velocity and density profiles. The components used for the PIV-S setup, such as laser, tracer particles and camera were described.

The methodology by which the velocity and density signals were computed from the raw images was presented. Sensitivity analyses were performed on the PIV-S interrogation window size and thresholding values. It was shown that pixel intensity thresholding was required when different, spatially-averaged intensity profiles were concatenated on top of one another. Thresholding removed the discontinuities in the concatenated mean and variance profiles of spatially-averaged intensity. The PIV-S technique was also validated against three test cases: A flume filled with water, clear water flow, as well as gravity current flow. The chapter concluded by presenting the equations used to compute the mean velocity, mean excess density, Reynolds stresses, Reynolds fluxes and energy spectra from measured velocity and excess density signals.

Ramaprabhu and Andrews (2003, 2004), who introduced the PIV-S technology, noted that it is unclear how to extend the technique to continuously stratified flows. The present research has demonstrated how this technology can be extended to continuously stratified flows. The main advantage of the PIV-S technology over combined PIV-PLIF technologies lies in its simplicity and low cost. It requires only one camera and laser and no fluorescent dyes. Furthermore, PIV-S works as well with a continuous laser as with a pulsed laser, provided the camera has an electronic shutter.

Further improvements to PIV-S might be possible. Firstly, only the first image of an image pair was used to compute the spatially-averaged intensities (figure 2.7). This resulted in using only half of the available images. Use of both images in an image pair might lead to better spatially-averaged intensity estimates. For example, blending the two images of an image pair into a single image might remove unnecessary background noise and hence increase the signal-to-noise ratio of the spatially-averaged intensities. To ensure that the particles are properly aligned in both images, before blending, the PIV displacement estimates might be used to shift one image to align it with the other.

Another possible improvement lies in spatially-averaged intensity validation and

replacement. The method reported in this dissertation did not make use of such a scheme where outliers were detected and removed. A similar scheme such as Westerweel and Scarano (2005) proposed for PIV measurements could be used for the spatially-averaged intensities. Lastly, similar image processing challenges are encountered in the astrophotography field. The PIV-S might benefit from using some of the image processing techniques from this field.

Chapter 3

Experimental results

Experiments are undertaken to enable the mechanisms controlling gravity currents to be studied. For example, measurements of buoyancy and shear production indicate where turbulent kinetic energy is being produced or removed within the gravity current. Measurements of Reynolds stresses and fluxes show the anisotropic transport of mass and momentum within the current, while measurements of gradient Richardson number show where the current is strongly stratified and where it is not.

Ellison and Turner (1959) noted that gravity currents which moved down an inclined slope quickly reached a self-similar state. In this state, the current thickness grew linearly with downstream distance, while the current velocity remained constant. Tennekes and Lumley (1973) and Hossain and Rodi (1977) show that self-similar, vertical, plane plumes also spread linearly with a constant centreline velocity. For both these self-similar flows the streamwise buoyancy force is responsible for the constant streamwise velocity. A flow is self-similar when only a single lengthscale, velocity scale and excess density scale is required to describe all mean quantities in terms of a single geometrical variable. Hence, the profile shapes of mean quantities remain similar with increasing downstream distance.

Depth-averaged gravity current models assume self-similarity. Empirical relations for water entrainment, bed sediment entrainment and near-bed sediment concentration are needed to provide closure for these depth-averaged models. Extensive experimental work has been done on approximately self-similar gravity currents to derive these empirical relationships. There are, however, many situations where self-similarity does not hold, for example, when an underflow becomes neutrally buoyant and separates from the bed to become an interflow. Another example is

acceleration or deceleration of a gravity current due to a change in bed property, such as slope or roughness.

Recent improvements in the computational capacity of computers have allowed more general gravity current models to be used. For instance, multispecies Reynolds-averaged Navier-Stokes models do not assume self-similarity. They do, however, make assumptions regarding the state of turbulence within the gravity current. Experimental data on the mean velocity, excess density and turbulence structure for non self-similar gravity currents is limited. The turbulence structure of gravity currents has only recently been investigated experimentally. These investigations have centred mostly on the Reynolds stresses and density variance (Buckee *et al.*, 2001), (Kneller *et al.*, 1999) and (Kneller *et al.*, 1997). To the author's knowledge, almost no data exists quantifying turbulent mass transport in terms of Reynolds fluxes. This is due to the difficulty in measuring density and velocity simultaneously within a gravity current.

This chapter presents velocity, density and turbulence measurements of a horizontal, saline gravity current. The chapter begins by presenting the inlet conditions used for the gravity current. The remainder of the chapter is divided into two parts: The first part presents the mean velocity, density and turbulence profiles 0,9 m downstream of the inlet, while the second part presents the mean velocity, density and turbulence profiles 2,4 m downstream of the inlet. The measured profiles are compared with historical gravity current and wall-jet data.

3.1 Inlet flow conditions

This section presents the results of the measurements taken at the inlet. The measured mean velocity, NaCl mass fraction, k and ϵ are used to define the inlet boundary condition for the numerical model in chapter 4.

Figure 3.1a presents the mean U- and W-velocity profiles (horizontal plane) at the inlet of the flume for the gravity current. Due to restricted optical access no velocity measurements could be made nearer than 0,02 m from one of the flume walls. The flume was 0,25 m wide.

The flume centreline is located at 0,125 m in figure 3.1a. The centreline of the U-velocity profile is located at approximately 0,1 m, giving a misalignment of 0,025 m between the two centrelines. However, the flume centreline falls within the region where the U-velocity profile has become uniform and therefore wall effects

are assumed to be negligible for vertical profiles taken on the flume centreline. It is assumed that the misalignment in the U-profile will become smaller further downstream, because of the flow development along the symmetric flume walls.

Figure 3.1b presents the turbulent intensity profile of the u-velocity component. The u-turbulence intensity I_o at the centre of the inlet is a moderate 6% to 8%, which is in agreement with the intensity estimate for fully-developed duct flow (FLUENT 6.3, pg. 7-15).

$$I_o = \frac{\sqrt{\langle u'u' \rangle}}{U_{bulk}} \tag{3.1.1}$$

$$= 0.16 Re_D^{-0.125} \tag{3.1.2}$$

$$= 0.067 \tag{3.1.3}$$

with

$$Re_D = \frac{U_{bulk} D}{\nu} \tag{3.1.4}$$

$$= 1048 \tag{3.1.5}$$

where Re_D is the Reynolds number based on the hydraulic diameter of the inlet, $U_{bulk} = 0{,}079\,\mathrm{m/s}$ is the cross-section averaged inlet velocity, $D = 0{,}0134\,\mathrm{m}$ the hydraulic diameter of the inlet and $\nu = 1{,}01 \times 10^{-6}\,\mathrm{m^2/s}$ the kinematic viscosity of the inflow.

The inlet turbulent kinetic energy k_o was calculated from

$$k_o = \frac{1}{2}\left[\langle u'u' \rangle_o + \langle v'v' \rangle_o + \langle w'w' \rangle_o\right] \tag{3.1.6}$$

$$= 64 \times 10^{-6}\,\mathrm{m^2/s^2} \tag{3.1.7}$$

where $\langle u'u' \rangle_o = 69 \times 10^{-6}\,\mathrm{m^2/s^2}$, $\langle v'v' \rangle_o = 24 \times 10^{-6}\,\mathrm{m^2/s^2}$ and $\langle w'w' \rangle_o = 34 \times 10^{-6}\,\mathrm{m^2/s^2}$ are the measured normal Reynolds stresses at the centre of the inlet. Although the normal Reynolds stresses are moderately anisotropic, k_o is of the same order of magnitude as its isotropic estimate (FLUENT 6.3, pg. 7-17)

$$k = \frac{3}{2}\left(U_{bulk} I_o\right)^2 \tag{3.1.8}$$

$$= 43 \times 10^{-6}\,\mathrm{m^2/s^2} \tag{3.1.9}$$

Figure 3.2 presents the one-dimensional wavenumber-based energy spectrum at the centre of the inlet. At the inlet the inertial subrange was locally isotropic, which allowed the inlet dissipation rate of turbulent kinetic energy ϵ_o to be measured from

the one-dimensional energy spectrum using equation 2.6.19. The measured inlet dissipation rate was $\epsilon_o = 8 \times 10^{-6}\,\mathrm{m^2/s^3}$. The inlet Kolmogorov timescale τ_k was computed from the measured dissipation rate as follows (Pope, 2001, pg. 129):

$$\tau_k = \sqrt{\frac{\nu}{\epsilon_o}} \tag{3.1.10}$$

$$= 0{,}37\,\mathrm{s} \tag{3.1.11}$$

Furthermore, the Kolmogorov lengthscale η was computed as follows (Pope, 2001, pg. 128):

$$\eta = \left(\frac{\nu^3}{\epsilon_o}\right)^{\frac{1}{4}} \tag{3.1.12}$$

$$= 0{,}6\,\mathrm{mm} \tag{3.1.13}$$

The measured energy spectrum had a Taylor Reynolds number of $R_\lambda = 98$, which was midway between the $R_\lambda = 72$ and $R_\lambda = 130$ energy spectra given by Pope (2001, pg. 235). The Taylor Reynolds number is defined as

$$R_\lambda = \frac{\sqrt{\langle u'u' \rangle_o}\lambda_g}{\nu} \tag{3.1.14}$$

with the isotropic estimate of the Taylor microscale λ_g given by

$$\lambda_g = \sqrt{15}\tau_k\sqrt{\langle u'u' \rangle_o} \tag{3.1.15}$$

The inlet turbulence can also be quantified by the turbulent viscosity ratio ν_t/ν. The turbulent viscosity ν_t can be estimated from the Kolomogorov-Prandtl expression as follows (Rodi, 1980, pg. 21,27)

$$\nu_t = C'_\mu\sqrt{k_o}l \tag{3.1.16}$$

where $\sqrt{k_o}$ and l are respectively the velocity and lengthscales of the large scale turbulent motions. From dimensional arguments

$$\epsilon_o = C_D\frac{k_o^{\frac{3}{2}}}{l} \tag{3.1.17}$$

Substitution of equation 3.1.17 into equation 3.1.16 gives

$$\nu_t = C_\mu\frac{k_o^2}{\epsilon_o} \tag{3.1.18}$$

$$= 46 \times 10^{-6}\,\mathrm{m^2/s} \tag{3.1.19}$$

where $C_\mu = 0{,}09$. The measured turbulent viscosity ratio was therefore $\nu_t/\nu = 46$, which indicated that the inlet turbulence was moderately low.

Table 3.1 summarizes the inlet conditions for the gravity current. The variables appearing in table 3.1, which have not previously been defined, are as follows: h is the inlet height, b is the inlet width, Q is the inlet bulk flow, $\langle\Delta\rho\rangle_o$ is the inlet excess density, $U_{o\,max}$ is the maximum inlet velocity, Re_o is the inlet Reynolds number, $\langle u'w'\rangle_o$ and $\langle u'v'\rangle_o$ are the shear Reynolds stresses at the centre of the inlet, Ri_o is the inlet bulk Richardson number and $\langle\Delta\rho\rangle_o h U_{bulk}$ is the inlet excess density flux. The inlet Reynolds number Re_o and inlet bulk Richardson number Ri_o appearing in table 3.1 are defined as:

$$Re_o = \frac{U_{bulk}h}{\nu} \tag{3.1.20}$$

$$Ri_o = \frac{g\langle\Delta\rho\rangle_o h}{\rho_w U_{bulk}^2} \tag{3.1.21}$$

where $\rho_w = 998{,}2364\,\mathrm{kg/m^3}$ is the density of water and g is the gravity acceleration constant.

The inlet Reynolds and bulk Richardson numbers indicate that the gravity current flow was weakly turbulent ($Re_o = 2300$) and highly supercritical ($Ri_o = 0{,}09 \ll 1$). A supercritical bulk Richardson number indicates a less stable interface between the current and the ambient fluid. The reduced stability increases the amount of mixing across the interface which, in turn, increases the entrainment of low momentum fluid into the density current.

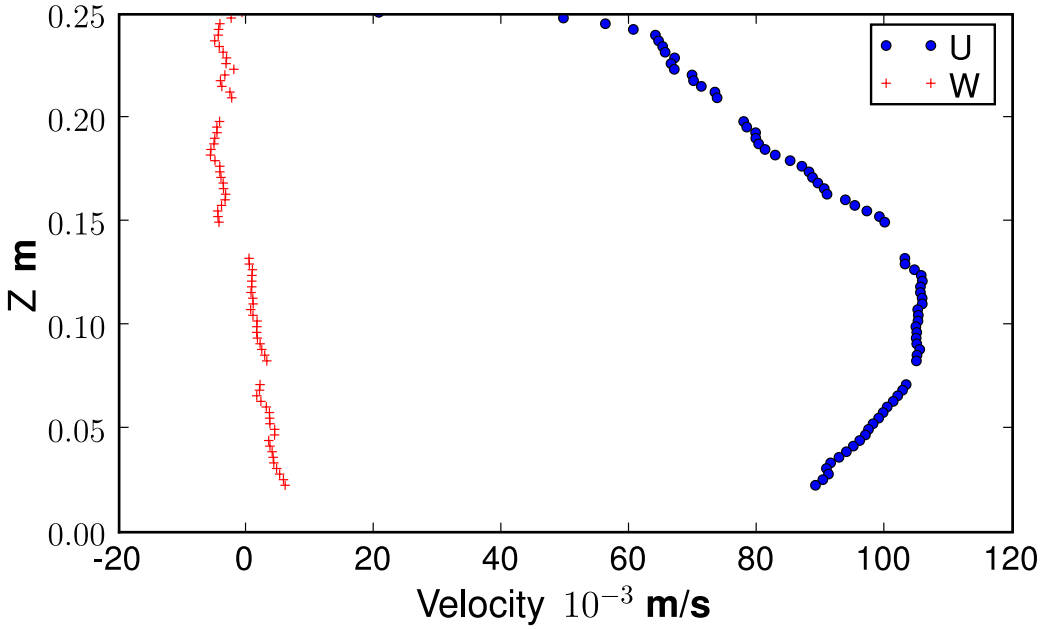

(a) Mean velocity

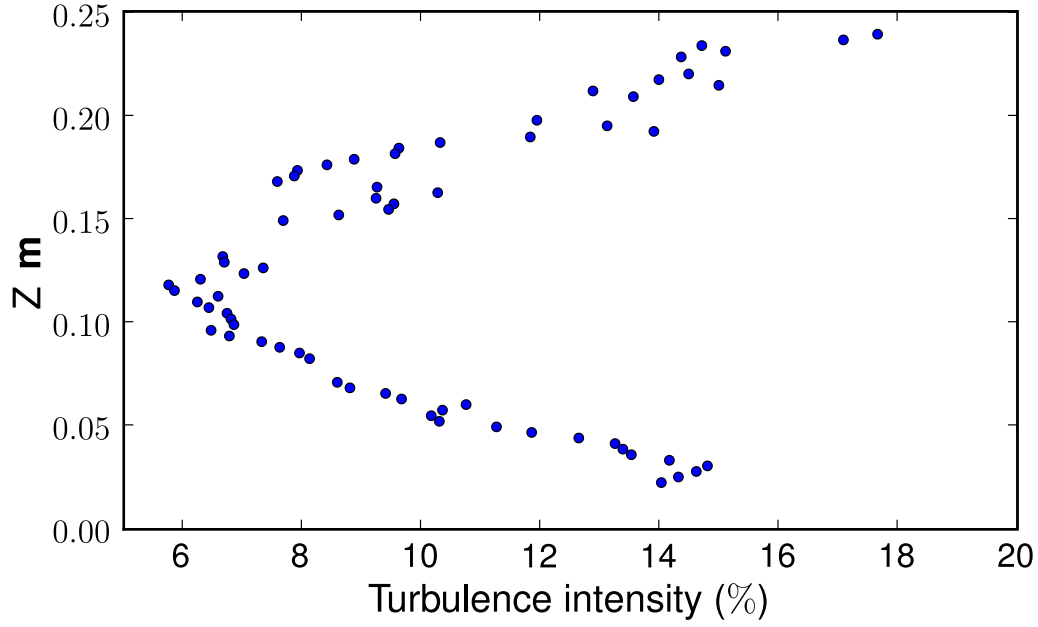

(b) Turbulence intensity

Figure 3.1: Inlet flow profiles: plan view

Variable	Units	Value (measured)
h	m	0,03
b	m	0,25
Q	l/s	0,59
U_{bulk}	m/s	0,079
$\langle\Delta\rho\rangle_o$	kg/ m^3	2,0
$U_{o\,max}$	m/s	0,106
Re_o	-	2300
R_λ	-	98
$\langle u'u'\rangle_o$	m^2/ s^2	69×10^{-6}
$\langle w'w'\rangle_o$	m^2/ s^2	34×10^{-6}
$\langle v'v'\rangle_o$	m^2/ s^2	24×10^{-6}
$\langle u'w'\rangle_o$	m^2/ s^2	-7×10^{-6}
$\langle u'v'\rangle_o$	m^2/ s^2	-1×10^{-6}
I_o	-	0,078
τ_k	s	0,37
η	m	$0{,}6 \times 10^{-3}$
λ_g	m	$11{,}9 \times 10^{-3}$
k_o	m^2/ s^2	64×10^{-6}
ϵ_o	m^2/ s^3	8×10^{-6}
ν_t/ν	-	46
Ri_o	-	0,09
$\langle\Delta\rho\rangle_o h U_{bulk}$	kg/m,s	0,004 74

Table 3.1: Inlet flow conditions

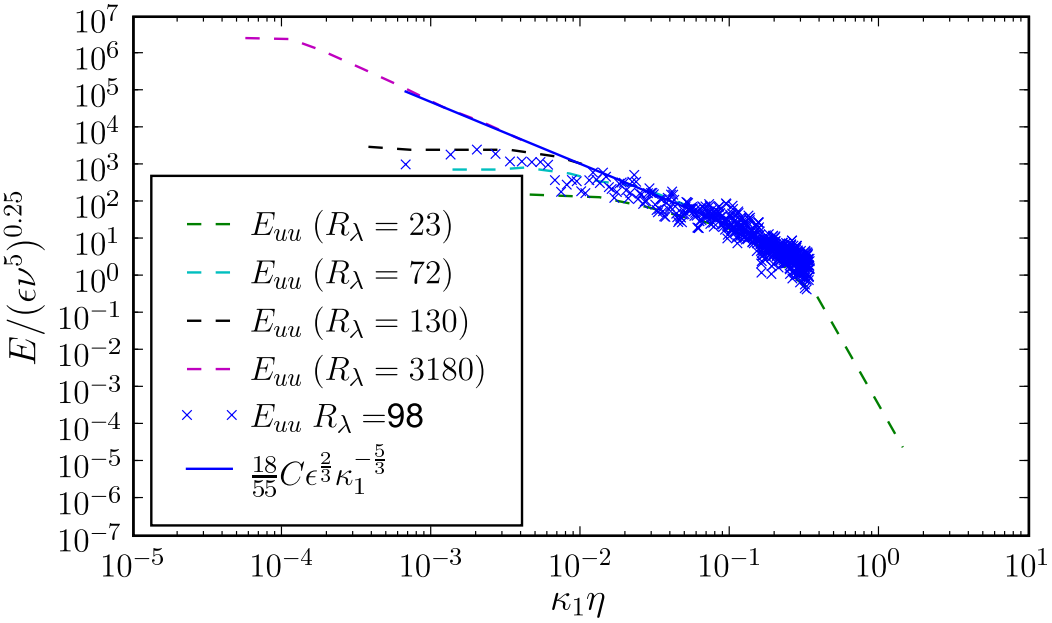

Figure 3.2: One dimensional, wavenumber-based, energy spectrum at centre of inlet: present research and Pope (2001, pg. 235)

3.2 Gravity current profiles: 0,9 m from the inlet

This section presents in detail the mean velocity, density and turbulence profiles for a gravity current 0,9 m from the inlet (the inlet conditions are given by table 3.1). In order to aid comparison with other gravity current and wall jet research (Buckee *et al.* (2001), Eriksson *et al.* (1998) and Ahlman (2006)) the outer, inner and depth-averaged scales of the current had to be measured. The definitions of these scales are presented in the following section.

3.2.1 Outer, inner and depth-averaged scales

A turbulent plane wall jet, which is related to a gravity current, can be divided into an inner region adjacent to the bed and an outer region further away from the bed. The outer and inner regions overlap, with the inner region located below $y/y_{0.5} < 0{,}1$ and the outer region located above $y^+ > 30$ (George *et al.*, 2000).

The characteristic velocity and lengthscales of the outer region of a wall jet are U_{max} and $y_{0.5}$. Figure 3.3 presents a definition sketch of U_{max} and $y_{0.5}$. The outer lengthscale $y_{0.5}$ is defined as the height at which the downstream velocity is equal to half the maximum downtream velocity. These outer scales are commonly used in the wall jet literature, but Buckee *et al.* (2001) also found them useful to collapse gravity current profiles.

The reason why $y_{0.5}$ is chosen as an outer scale is that its height can be measured more accurately than the height of the velocity maximum, or even the depth averaged height (which is an integrated value). The velocity maximum occurs within a region where dU/dy changes slowly, hence it is difficult to determine its precise height from low resolution velocity measurements. On the other hand, $y_{0.5}$ occurs in a region where dU/dy changes rapidly and hence its precise height can be determined more easily. This strong relationship between $y_{0.5}$ and the downstream velocity gradient also suggests $y_{0.5}$ to be a good indicator of the spreading rate of the current.

The characteristic velocity and lengthscales of the inner region of a wall jet are U^* and ν/U^*. The friction velocity U^* is defined as

$$U^* \equiv \sqrt{\frac{\tau_w}{\rho}} \tag{3.2.1}$$

where τ_w is the wall shear stress and ρ is the density of the fluid. From the inner velocity and lengthscales the dimensionless streamwise velocity U^+ and dimensionless cross-stream coordinate y^+ are defined as

$$U^+ = \frac{U}{U^*} \tag{3.2.2}$$

$$y^+ = \frac{yU^*}{\nu} \tag{3.2.3}$$

where y is the cross-stream coordinate (distance from the wall).

Historical gravity current research has also used depth-averaged scales to quantify the bulk properties of gravity currents (Parker *et al.*, 1987), (Garcia, 1993). These scales are obtained from the following moments:

$$U_d H_d = \int_0^\infty U \, dy \tag{3.2.4}$$

$$U_d^2 H_d = \int_0^\infty U^2 \, dy \tag{3.2.5}$$

$$U_d \langle \Delta\rho \rangle_d H_d = \int_0^\infty U \langle \Delta\rho \rangle \, dy \tag{3.2.6}$$

where U_d is the depth-averaged current velocity, H_d is the depth-averaged current thickness, $\langle \Delta\rho \rangle_d$ is the depth-averaged current excess density, $y = \infty$ refers to the height above the bed where the excess density profile becomes zero. Previous experimental studies integrated flow profiles from the bed to the free surface. The present research measured profiles only from the bed to approximately 75% of the flow depth. The upper 25% of the flow depth did not contain the gravity current body, but only a weak clear water return flow. The return flow near the free surface was caused by the entrainment flux of ambient water into the gravity current.

In order to compute depth-averaged variables representative of the gravity current body it was decided to integrate only up to the discernible edge of the gravity current. The clearest indication of the gravity current edge was the height where the excess density became zero. Integration from the bed to the height where the excess density profile became zero, avoided the necessity for integration over regions of negative streamwise velocity caused by the return flow.

Table 3.2 summarizes the gravity current flow conditions 0,9 m from the inlet, using the outer, inner and depth-averaged scales. Table 3.2 shows that the depth-averaged current velocity U_d has decreased from the inlet velocity of 0,079 m/s to 0,052 m/s. The depth-averaged current height H_d has increased from the inlet height of 0,03 m to 0,07 m. The depth-averaged excess density $\langle \Delta\rho \rangle_d$ has decreased

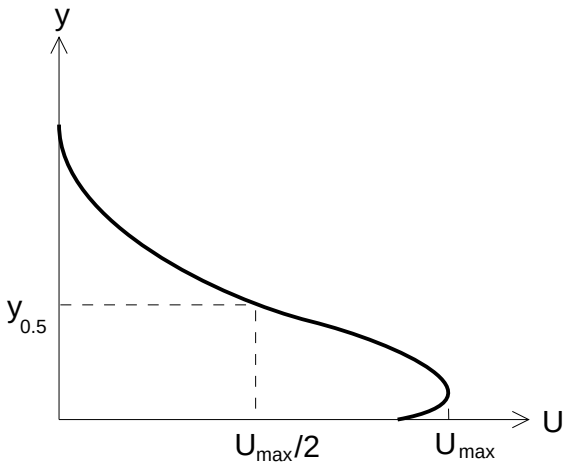

Figure 3.3: Outer length and velocity scales for a gravity current

from the inlet value of 2,0 kg/m^3 to 1,33 kg/m^3, indicating the dilution of the gravity current due to the entrainment of the overlying ambient water.

The bulk Richardson number Ri appearing in table 3.2 is given by

$$Ri = \frac{g\left(\langle\rho\rangle_d - \rho_w\right) H_d}{\rho_w U_d^2} \tag{3.2.7}$$

The bulk Richardson number Ri represents the ratio of buoyancy forces to inertia forces. Low bulk Richardson numbers $Ri < 1$ indicate that inertia forces dominate and hence the interface between the current and overlying fluid is unstable (Alavian *et al.*, 1992). Currents of low bulk Richardson number are known as supercritical currents. High bulk Richardson numbers $Ri > 1$ indicate that buoyancy forces stabilises the interface between the current and overlying fluid. Currents of high bulk Richardson number are known as subcritical currents. Table 3.2 indicates that the current was supercritical.

3.2.2 Mean velocities

Figures 3.4a, 3.4b and 3.5 present the mean U- and V-velocity profiles along the channel centreline. The velocity profiles of figures 3.4a and 3.5 are concatenations of three separately measured profiles. Each of the three profiles was obtained by photographing the flow at three different heights. The field of view at each height was limited, because of the short photographic object distance used. This allowed only a part of the velocity profile to be measured in a single experimental run.

Variable	Units	Value (measured)
U_{max}	m/s	0,062
$\langle\rho\rangle_{max}$	kg/ m^3	1,73
$y_{0.5}$	m	0,073
Re_{outer}	-	4500
U^*	m/s	0,0037
ν/U^*	m	0,000 27
U_d	m/s	0,052
H_d	m	0,070
$\langle\rho\rangle_d$	kg/ m^3	1,33
$\langle\Delta\rho\rangle_d H_d U_d$	kg/m,s	0,004 82
Ri	-	0,34

Table 3.2: Gravity current flow conditions near the inlet

The advantage of the short object distance was that the velocity profile could be measured to a high resolution. It can be seen that the profiles from the three independent experimental runs fit very well.

Figure 3.4a shows that the velocity maximum is located at a normalized height of $y/y_{0.5} = 0{,}37$. This height is greater than those mentioned by Buckee *et al.* (2001) for gravity currents and Eriksson *et al.* (1998) for wall-jets $0{,}1 < y/y_{0.5} < 0{,}17$. The difference in velocity maximum height is due to the shallower flume depth of 0,3 m used in this study, compared to the $\pm$1,5 m flume depths used in the other studies. A greater flume depth results in a smaller return flow velocity of the overlying ambient water. Ahlman (2006) also observed that the return flow velocity of the overlying ambient fluid increased the height of the velocity maximum for his compressible wall jet simulations.

The edge of the gravity current interface can be discerned by the decrease in slope of the streamwise velocity at $y/y_{0.5} = 1{,}5$. The edge of the return flow starts at $y/y_{0.5} = 2.0$ where the slope of the streamwise velocity increases again. Hence, below $y/y_{0.5} < 1.5$ the gravity current moves downstream and above $y/y_{0.5} > 2.0$ the ambient water moves upstream as a return flow. Furthermore, the supercritical bulk Richardson number indicates that the inertial forces dominate over the buoyancy forces. Hence, the U-profile is not driven purely by density differences, but rather a combination of density differences and inlet jet momentum.

Figure 3.4b shows the near-wall streamwise velocity profile in inner scaling. The measured streamwise velocity follows the law-of-the-wall between $30 < y^+ < 100$.

The law-of-the-wall is given by

$$U^+ = \frac{1}{\kappa} ln\left(Ey^+\right) \tag{3.2.8}$$

where $\kappa \approx 0{,}41$ is the von Karman constant and $E \approx 9{,}8$ is an empirical constant. Numerical models often assume that the near-wall streamwise velocity distribution follows equation 3.2.8. Figure 3.4b shows that this is a reasonable assumption.

Figure 3.5 shows that an upward velocity peak of 0,022 is located at $y/y_{0.5} = 0{,}5$, while the greatest downward velocity (due to the entrainment of the overlying ambient water into the current) is located at the edge of the gravity current interface $1{,}5 < y/y_{0.5} < 2$.

3.2.3 Mean excess density

Figure 3.6 presents the mean excess density profiles of the PIV-S measurements, as well as those of the siphon samples. Saline gravity currents are conservative flows, which means that their depth-averaged excess density flux is independent of downstream location x. The PIV-S profile had to be adjusted slightly so that the measured depth-averaged excess density flux $\langle \Delta\rho \rangle_d H_d U_d$ was within 2% of the inlet excess density flux. Figure 3.6 shows that the difference between the adjusted PIV-S profile and the siphon profile was small.

The supercritical bulk Richardson number in table 3.2 indicates that the interface between the gravity current and clear water is not very stable, allowing mixing to occur with the ambient water at the interface. This is also indicated in table 3.2 by the decrease in maximum excess density from $2\,\mathrm{kg/m^3}$ at the inlet to $1{,}73\,\mathrm{kg/m^3}$.

3.2.4 Mean velocity gradients

Boundary-layer type flows are characterised by dominant cross-stream gradients. Figure 3.7 shows that the cross-stream gradient dU/dy dominates the other gradients. Hence the assumption that gravity currents can be approximated as boundary layer type flows is reasonable. Figure 3.7 shows that dU/dy becomes zero at the velocity maximum, as well as at the interface. No turbulent kinetic energy is produced through shearing at these locations, since shear production $\mathcal{P}$ is defined as

$$\mathcal{P} = -\langle \bar{u}'\bar{u}' \rangle : \bar{\bar{S}} \tag{3.2.9}$$

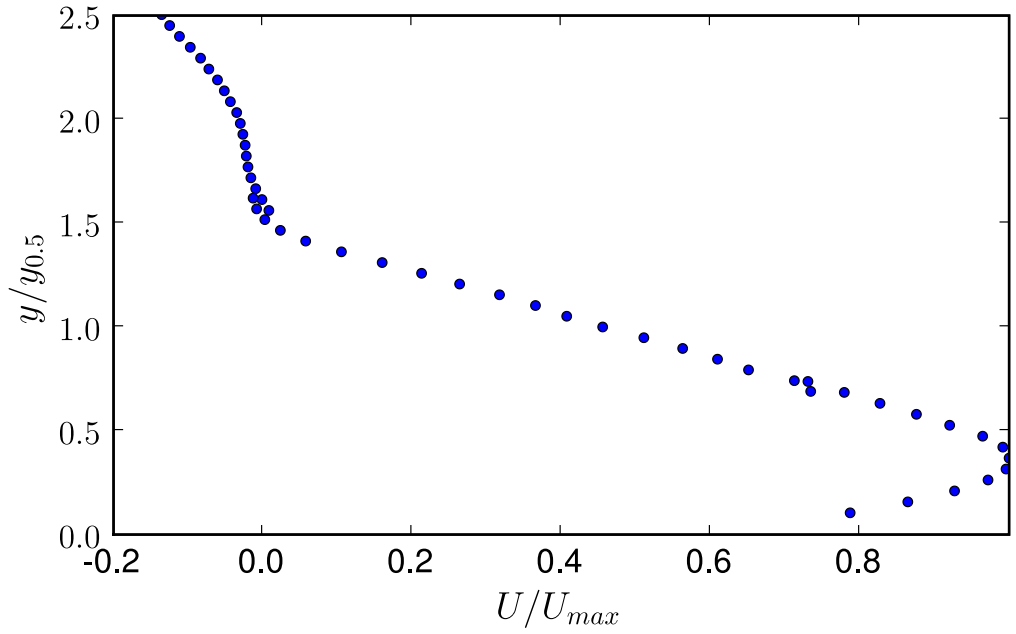

(a) outer scaling

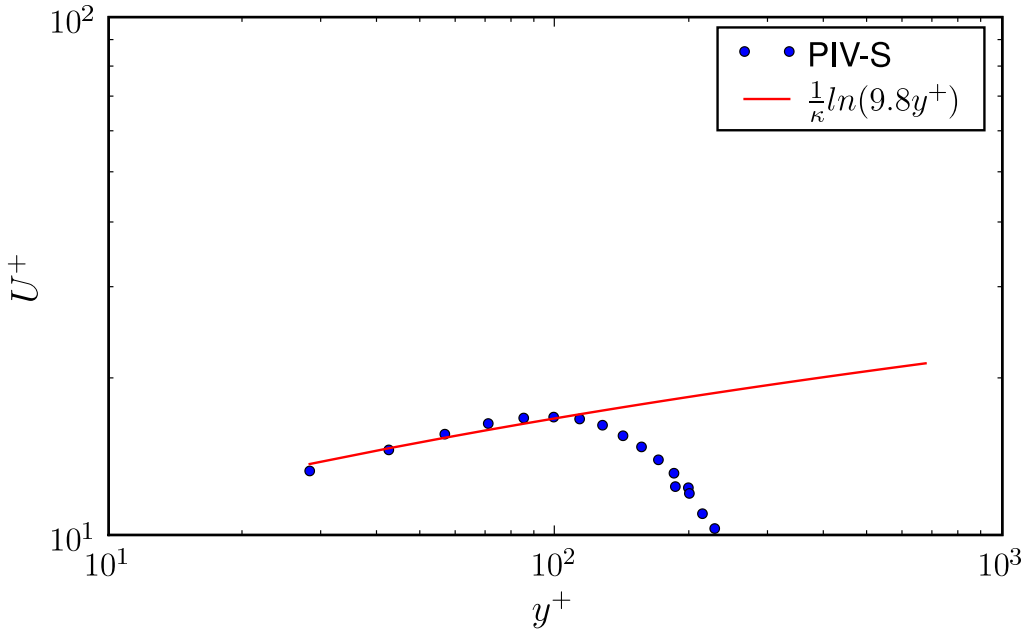

(b) inner scaling

Figure 3.4: Mean streamwise velocity: present research

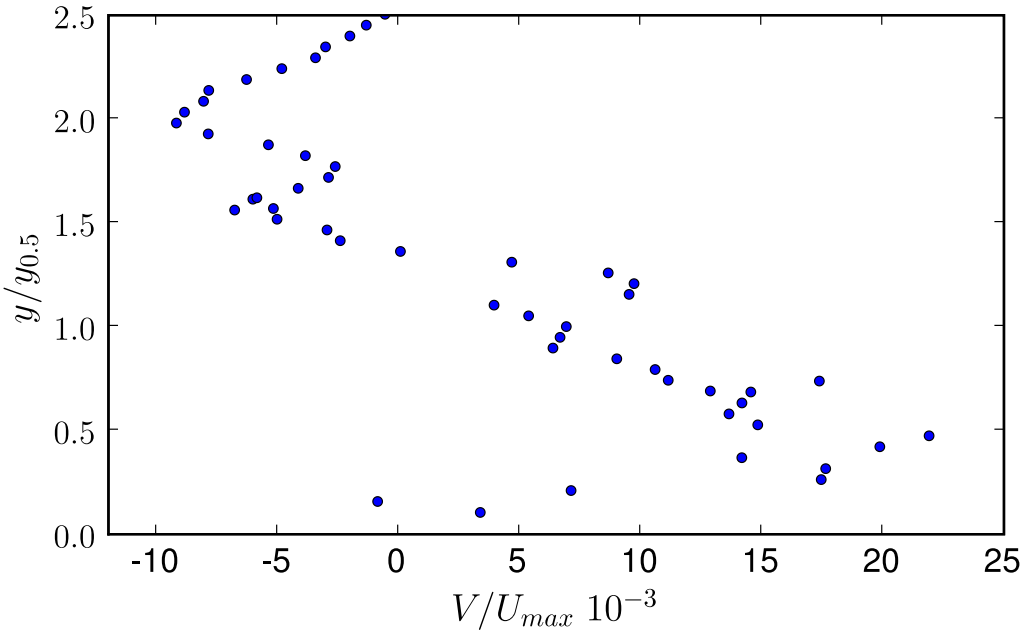

Figure 3.5: Mean cross-stream velocity: present research

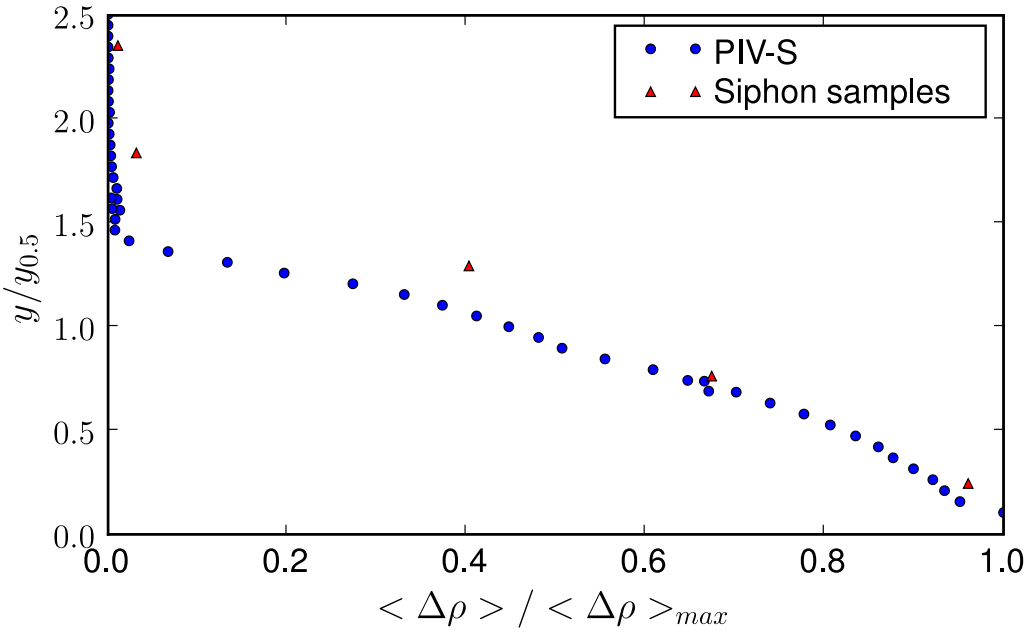

Figure 3.6: Mean excess density: present research

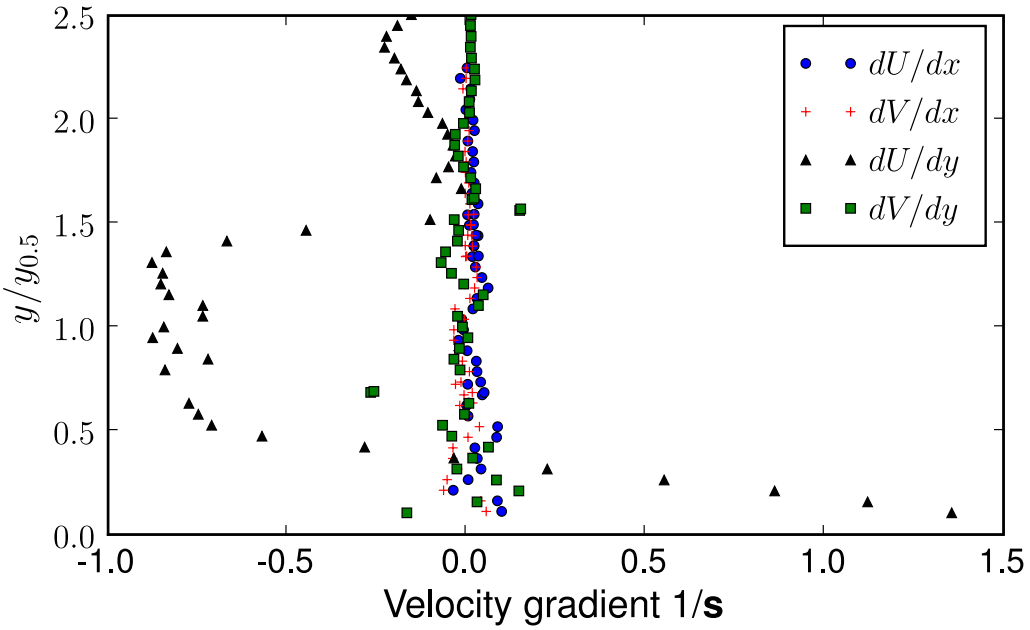

Figure 3.7: Mean velocity gradients: present research

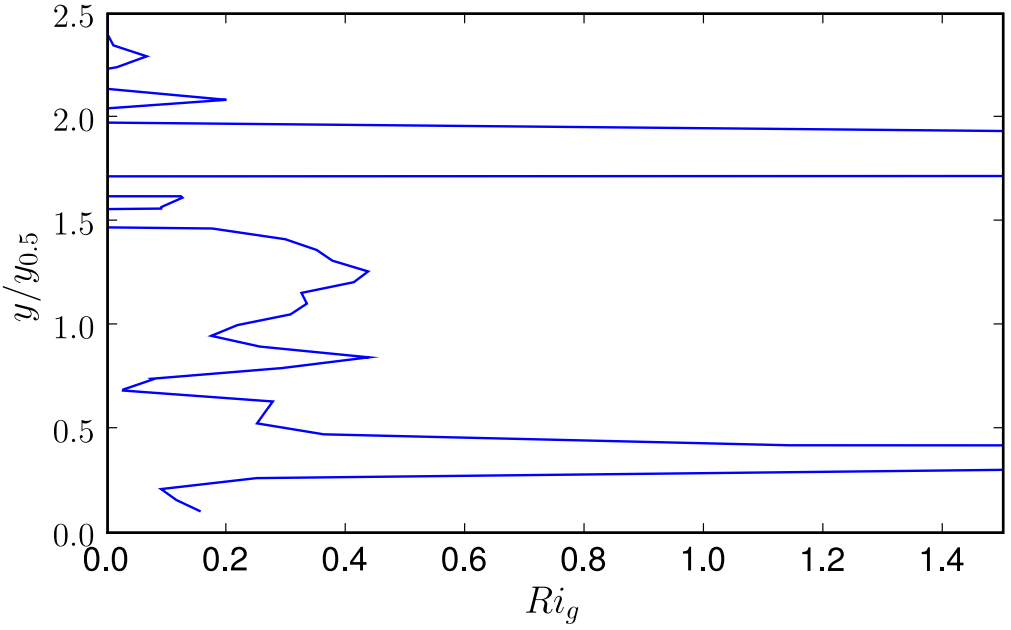

Figure 3.8: Gradient Richardson number: present research

where $\langle \bar{u}'\bar{u}' \rangle$ is the Reynolds stress tensor and $\bar{\bar{S}}$ is the mean rate-of-strain (velocity gradient) tensor.

3.2.5 Gradient Richardson number

Figure 3.8 presents the gradient Richardson number profile, which is defined as

$$Ri_g \equiv -\frac{g}{\rho} \frac{\frac{\partial \langle \rho \rangle}{\partial y}}{\left(\frac{\partial U}{\partial y}\right)^2} \tag{3.2.10}$$

Unlike the bulk Richardson number, which is a depth-averaged quantity, the gradient Richardson number indicates whether a point within the flow is stably stratified or not. According to Turner (1973), when $Ri_g > 0{,}25$ turbulence cannot be maintained, unless an external energy source exists. Turbulence collapses when negative buoyancy production becomes too large relative to the positive shear production of k. The collapse of turbulence results in no turbulent mixing.

Figure 3.8 shows that below the velocity maximum $y/y_{0.5} < 0{,}26$, as well as between $0{,}5 < y/y_{0.5} < 1{,}5$, the gradient Richardson number is below or near the critical value of 0,25. This indicates that shear production is still large enough in these regions to maintain turbulent mixing. Hence the current is able to entrain the overlying ambient water. Garcia (1993) and Buckee *et al.* (2001) also measured gradient Richardson numbers below 0,25 for supercritical currents.

3.2.6 Reynolds stresses

Figures 3.9a and 3.9b present the measured $\langle u'u' \rangle$, $\langle v'v' \rangle$ and $\langle u'v' \rangle$ Reynolds stress profiles in outer and inner scaling. It shows that the $\langle u'u' \rangle$ Reynolds stress profile has two positive peaks: an inner peak of 4,87 at $y^+ = 30$ and an outer peak of 0,0168 at $y/y_{0.5} = 1$. The local minimum $\langle u'u' \rangle$ Reynolds stress is located at $y^+ = 100$, which is at the velocity maximum. The $\langle v'v' \rangle$ Reynolds stress profile has only a positive outer peak of 0,0075 at $y/y_{0.5} = 0{,}8$. The absence of an inner peak can be attributed to the wall damping the near-wall v-velocity fluctuations. The $\langle u'v' \rangle$ Reynolds stress profile has an inner negative peak of $-0{,}77$ at $y^+ = 30$ and an outer positive peak of 0,0047 at $y/y_{0.5} = 0{,}75$. Furthermore, $\langle u'v' \rangle = 0$ below the velocity maximum at $y^+ = 85$.

It is possible that the inner $\langle u'u' \rangle$ and $\langle u'v' \rangle$ peaks might be located below $y^+ < 30$, since $y^+ = 30$ was the point of measurement nearest to the bed. For instance Ahlman (2006) found for the compressible wall jet that $\langle u'u' \rangle$ peaked at $y^+ = 13$, while $\langle u'v' \rangle$ peaked at $y^+ = 18$

Figure 3.9a also reveals the relationship between the shear Reynolds stress $\langle u'v' \rangle$ and the degree of anisotropy within the gravity current: At the inner peak of $\langle u'v' \rangle$ maximum anisotropy occurs, with $\langle u'u' \rangle$ eight times greater than $\langle v'v' \rangle$. Further from the bed the degree of anisotropy decreases as the magnitude of $\langle u'v' \rangle$ decreases. At $y^+ = 85$, $\langle u'v' \rangle$ becomes zero and the degree of anisotropy is near a minimum. Further away from the bed the degree of anisotropy again increases as $\langle u'v' \rangle$ increases and reaches another local maximum at $y/y_{0.5} = 0{,}75$. Above this height $\langle u'v' \rangle$ decreases, as does the degree of anisotropy.

The peak heights of the measured $\langle u'u' \rangle$, $\langle v'v' \rangle$ and $\langle u'v' \rangle$ Reynolds stress profiles correspond approximately to the peak heights of the wall jet profiles measured by Eriksson *et al.* (1998) (figures 3.10a, 3.10b and 3.10c). This resemblance points to the fact that near the inlet the gravity current is governed by processes similar to that of a non-buoyant wall jet. However, the measured peak values and those of Eriksson *et al.* (1998) are different. This shows that the *horizontal* gravity current does not have the self-similar properties of the non-buoyant wall jet. A self-similar wall jet spreads linearly, while its velocity maximum decreases as $x^{-1/2}$ (Eriksson *et al.*, 1998), (Ahlman, 2006). The lack of self-similarity in the gravity current is due to stable density gradient continuously reducing the turbulence intensities.

The $\langle u'u' \rangle$ Reynolds stress profile of Buckee *et al.* (2001) (figure 3.11) also shows two positive peaks: an inner peak at $y/y_{0.5} = 0{,}043$ and an outer peak at $y/y_{0.5} = 0{,}83$. This outer peak height is lower than the measured outer peak height of the present research, $y/y_{0.5} = 1$. The differences between the results obtained from the present research and those of Buckee *et al.* (2001) might be attributable to the following causes: (1) Buckee *et al.* (2001) measured gravity currents on an inclined bed slope of 2%. Measurements were taken 2,9 m from the inlet. Hence it is probable that these profiles were taken in the self-similar region, in contrast to the present research which measured profiles of a horizontal gravity current closer to the inlet at 0,9 m. (2) Buckee *et al.* (2001) investigated gravity currents with much greater density differences ($\Delta\rho/\rho \approx 2\%$). (3) Another reason might be that the variances/Reynolds stresses of Buckee *et al.* (2001) were not fully converged, due to the small number of independent samples collected (a point time series was 12 s long).

Buckee *et al.* (2001) concluded that for supercritical flow the maximum value of k occurs above the velocity maximum. The present research also suggests that

the peak value of k occurs at the outer peak heights of the Reynolds stresses $0{,}8 < y/y_{0.5} < 1$, which is above the velocity maximum $y/y_{0.5} = 0{,}37$.

Brørs and Eidsvik (1992) have argued, numerically, that the $k - \epsilon$ turbulence model incorrectly predicts negligible turbulent kinetic energy at the velocity maximum. This would lead to an underprediction of turbulent mass and momentum transport past the velocity maximum. Figure 3.9a shows that $\langle u'u' \rangle$ profile has a local minimum at the velocity maximum. However, the measured turbulence intensity I at the velocity maximum was moderately high ($I \approx 10\%$). A moderately high turbulence intensity indicated that the turbulent momentum transport was significant through the velocity maximum 0,9 m from the inlet.

3.2.7 Reynolds fluxes

Figures 3.12a and 3.12b present the $\langle \Delta\rho' u' \rangle$ and $\langle \Delta\rho' v' \rangle$ Reynolds flux profiles in outer and inner scaling. The most notable feature of this figure is the large anisotropy between the two Reynolds fluxes $\langle \Delta\rho' u' \rangle \approx 4.5 \langle \Delta\rho' v' \rangle$. It also shows that the $\langle \Delta\rho' u' \rangle$ Reynolds flux profile has a positive outer peak of 0,0117 at $1 < y/y_{0.5} < 1{,}2$ and a negative inner peak of $-0{,}0082$ at $y^+ = 70$. The height of the outer Reynolds flux peak corresponds to the height of the outer $\langle u'u' \rangle$ Reynolds stress peak ($y/y_{0.5} = 1$). The difference in magnitude between the outer and inner peaks is due to the larger lengthscales existing in the outer region of the flow. These large energy containing eddies are responsible for most of the turbulent mass transport.

The $\langle \Delta\rho' v' \rangle$ Reynolds flux profile has a single positive outer peak of 0,0027 at $0{,}7 < y/y_{0.5} < 0{,}9$. The height of this outer Reynolds flux peak corresponds to the height of the outer $\langle v'v' \rangle$ Reynolds stress peak ($y/y_{0.5} = 0{,}8$). The positive $\langle \Delta\rho' v' \rangle$ Reynolds flux peak indicates that positive velocity fluctuations $v - \langle v \rangle > 0$ are associated with positive density fluctuations $\Delta\rho - \langle \Delta\rho \rangle > 0$. That is, upward velocity fluctuations are associated with density fluctuations of denser fluid. A positive $\langle \Delta\rho' v' \rangle$ Reynolds flux also indicates that negative velocity fluctuations $v - \langle v \rangle < 0$ are associated with negative density fluctuations $\Delta\rho - \langle \Delta\rho \rangle < 0$. That is, downward velocity fluctuations are associated with density fluctuations of less dense fluid. This is in accordance with the stable stratification of the gravity current $d\langle \Delta\rho \rangle / dy < 0$, where denser fluid underlies less dense fluid. Hence, dense fluid packets are transported upwards and less dense fluid packets are transported downwards by turbulent mixing.

The positive $\langle \Delta\rho' u' \rangle$ Reynolds flux peak at $1 < y/y_{0.5} < 1{,}2$ indicates that

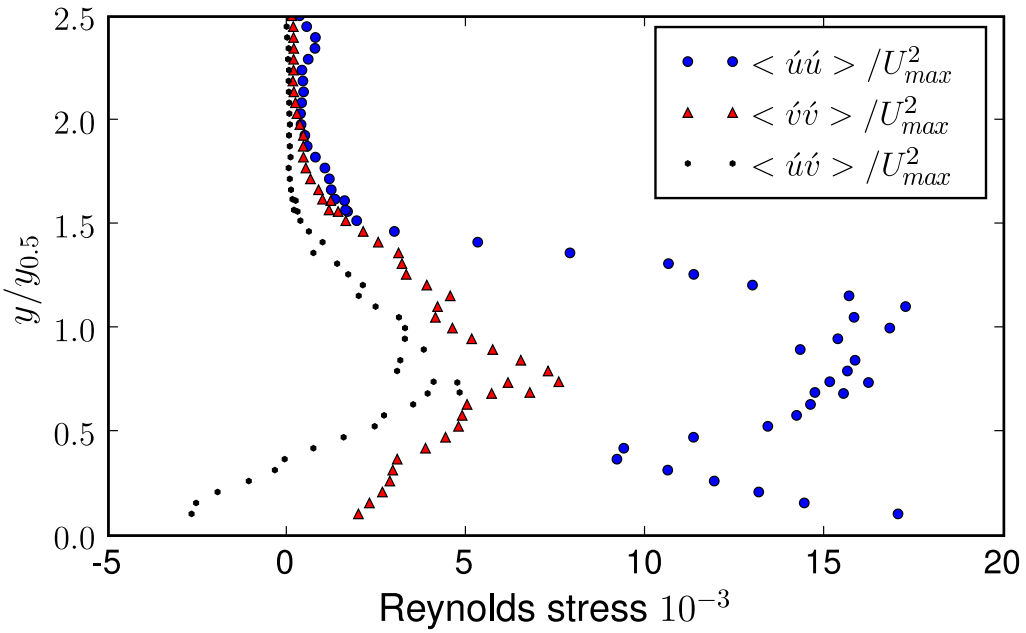

(a) outer scaling

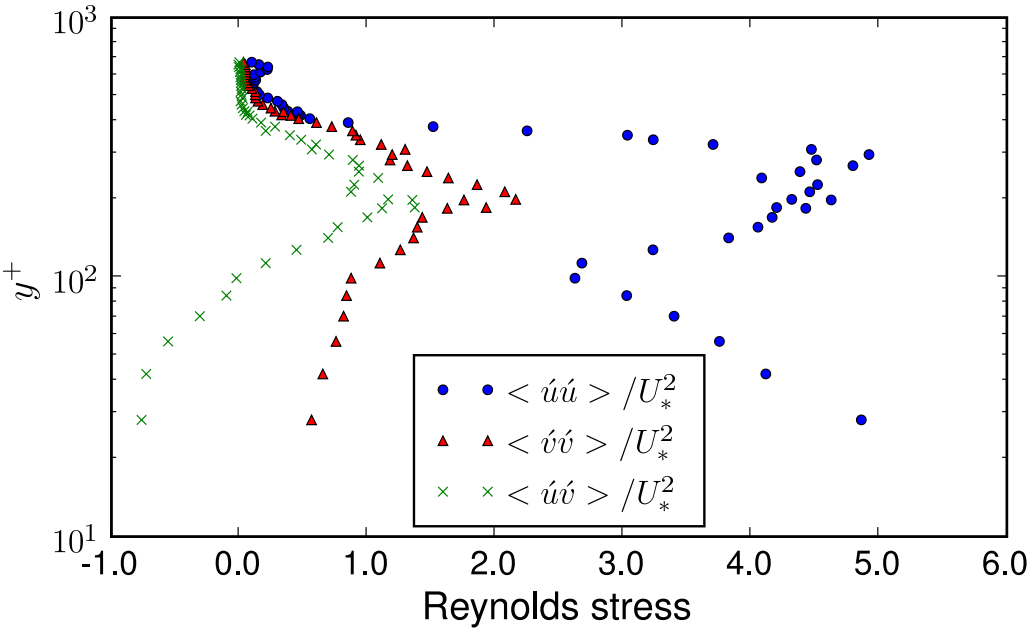

(b) inner scaling

Figure 3.9: Gravity current Reynolds stress profiles: present research

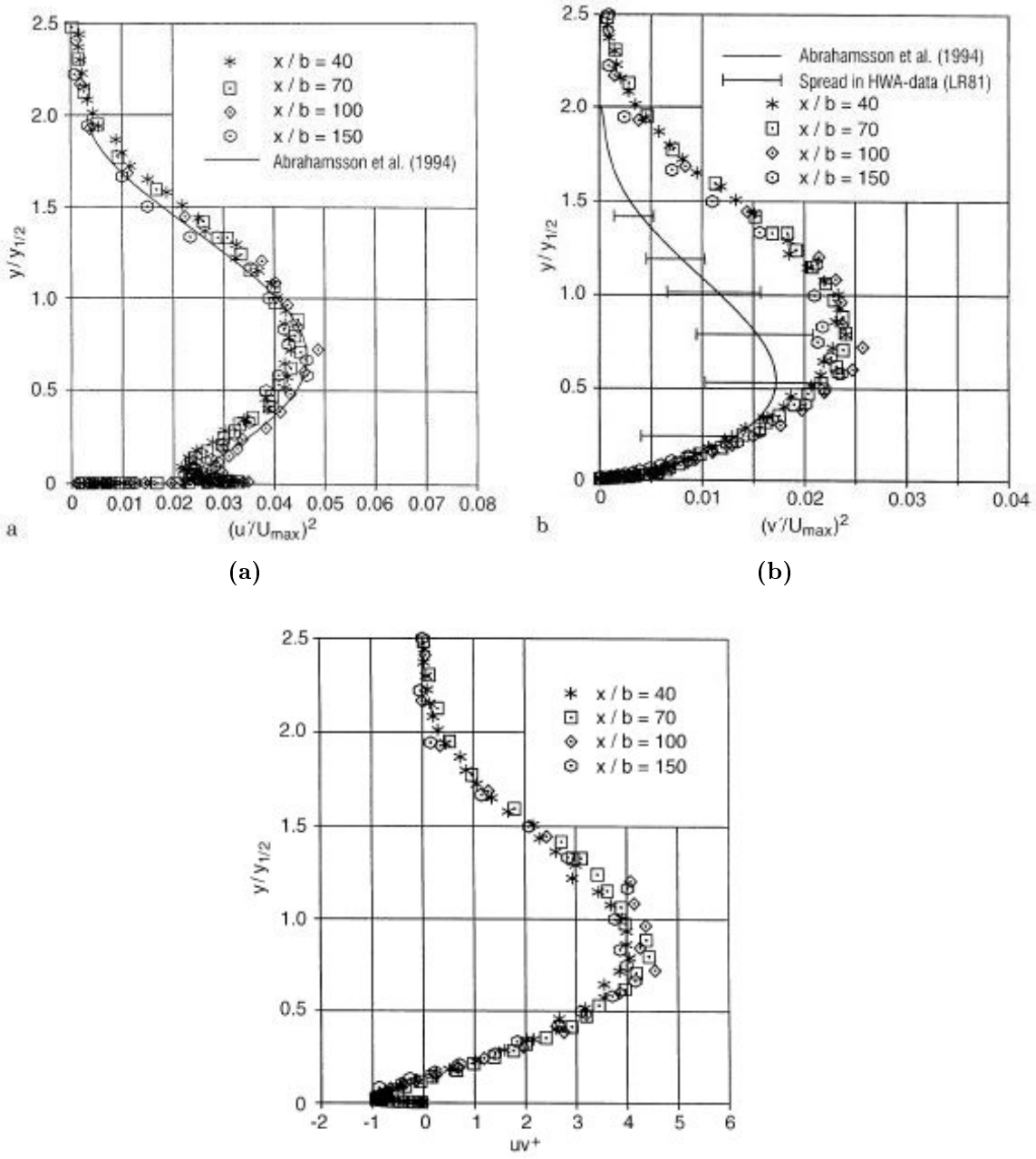

(a) (b)

(c)

Figure 3.10: Wall-jet Reynolds stress profiles (outer scaling): Eriksson *et al.* (1998)

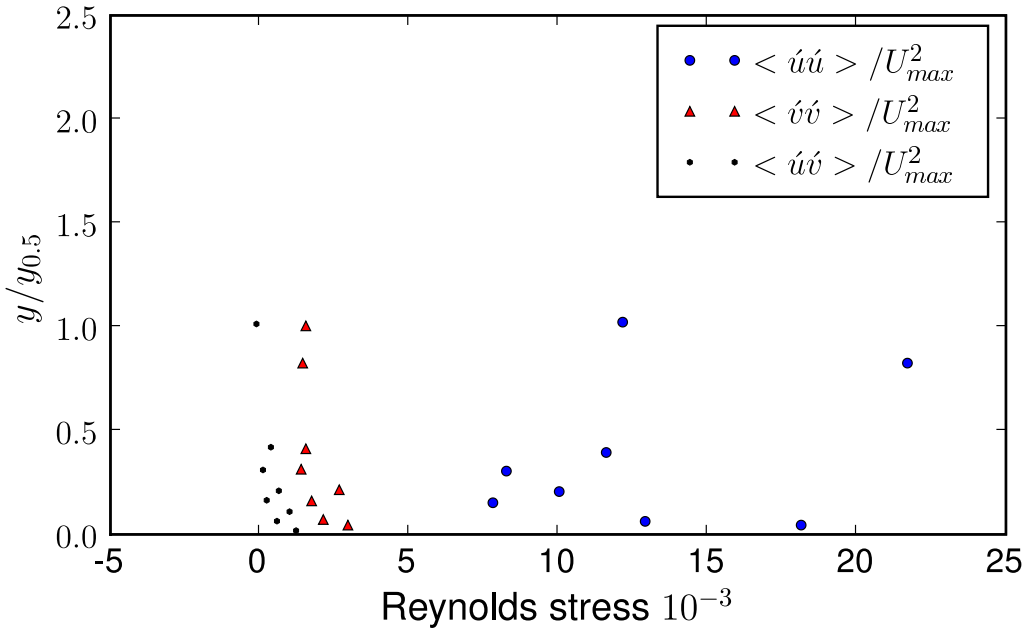

Figure 3.11: Gravity current Reynolds stress profiles (outer scaling): Buckee *et al.* (2001)

denser fluid is transported downstream, while less dense fluid is transported upstream by turbulent mixing. The small negative inner peak of $\langle \Delta\rho' u' \rangle$ at $y^+ = 70$ indicates that less dense fluid is transported downstream and denser fluid is transported upstream by turbulent mixing.

Furthermore, figure 3.12a shows that the $\langle \Delta\rho' u' \rangle$ and $\langle \Delta\rho' v' \rangle$ Reynolds fluxes are very small in the region of the velocity maximum ($y/y_{0.5} = 0{,}37$). Hence very little mass is transported through the velocity maximum. Buckee *et al.* (2001) refered to this region as a slow diffusion zone (SDZ). However, it should be remembered that section 3.3.5 showed that momentum is transported through the velocity maximum.

Ahlman (2006) performed a direct numerical simulation (DNS) for a compressible neutrally-buoyant wall jet. Figures 3.13a and 3.13b show the streamwise and cross-stream Reynolds fluxes of the DNS simulation. The streamwise Reynolds flux has a small negative inner peak and large positive outer peak, while the cross-stream Reynolds flux has a single positive outer peak. These results are similar to the measurements resulting from the present research. The streamwise inner peak is located at $y^+ \approx 20$. The outer peaks of both the streamwise and cross-stream

fluxes are centered around $y/y^{\theta}_{0.5} \approx 1$, where $y^{\theta}_{0.5}$ is the scalar halfwidth. Ahlman (2006) found that the growth rate of the scalar halfwidth was approximately equal to the velocity halfwidth $y_{0.5}$, hence the simulated Reynolds flux profiles plotted in terms of the velocity halfwidth would look similar to figures 3.13a and 3.13b. Ahlman (2006) concluded from figures 3.13a and 3.13b that the streamwise and cross-stream Reynolds fluxes were approximately equal for the neutrally-buoyant wall jet. Comparison of these two figures with figure 3.12a shows that gravity significantly dampens the cross-stream Reynolds flux, and hence the vertical turbulent transport of mass, for negatively buoyant gravity currents.

3.2.8 Excess density variance

Figure 3.14a presents the excess density intensity $\sqrt{\langle \Delta\rho'\Delta\rho' \rangle / \langle \Delta\rho \rangle^2_{max}}$ profile in outer scaling. The profile has a positive outer peak and a positive inner peak. The outer peak of 0,181 is located at $y/y_{0.5} = 1$, which corresponds to the height of the outer $\langle u'u' \rangle$ Reynolds stress peak ($y/y_{0.5} = 1$). The inner peak is located at $y^+ = 30$, which corresponds to the height of the inner $\langle u'u' \rangle$ Reynolds stress peak ($y^+ = 30$). The close correspondence between the excess density intensity and the $\langle u'u' \rangle$ variance profile is supported by the large $\langle \Delta\rho'u' \rangle$ covariance, as presented in the previous section. Furthermore, the excess density intensity profile has a local minimum at $y^+ = 70$, which is below the velocity maximum.

The excess density intensity quantifies the variability of the fluid density at a point. It therefore indicates the degree of turbulent mixing at a point. Hence, the most mixing occurs in the outer region $y/y_{0.5} = 1$ above the velocity maximum, where the large energy containing eddies occur. The least mixing occurs just below the velocity maximum $y^+ = 70$.

Figure 3.14b presents the scalar intensity profile for the DNS simulation Ahlman (2006). The profile has a very wide single outer peak between $0.24 < y/y_{0.5} < 1.5$. The location of the outer peak of the present research also falls within this region ($y/y_{0.5} = 1$).

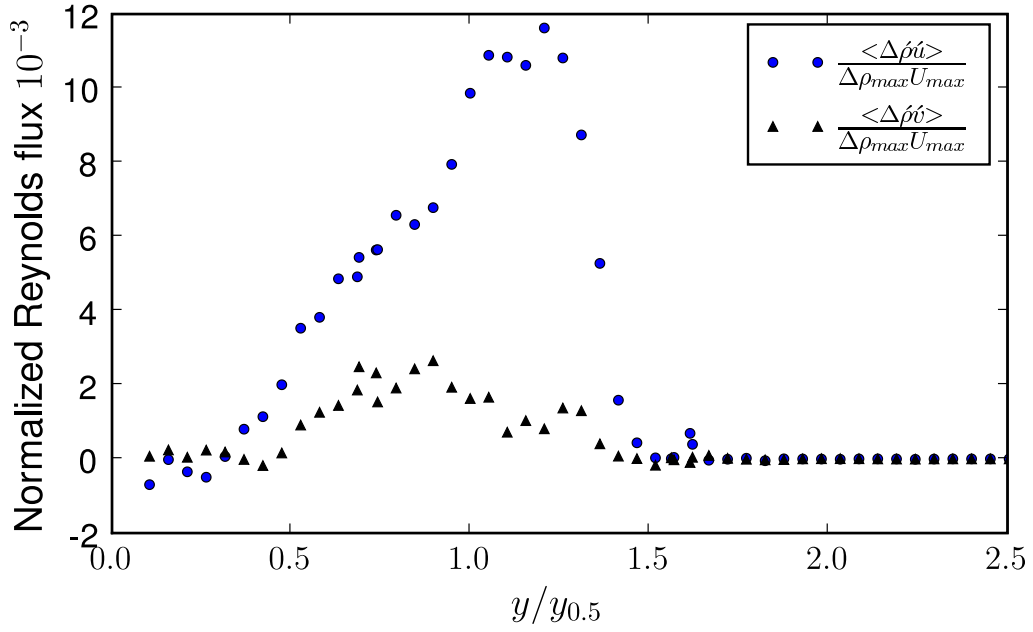

(a) outer scaling

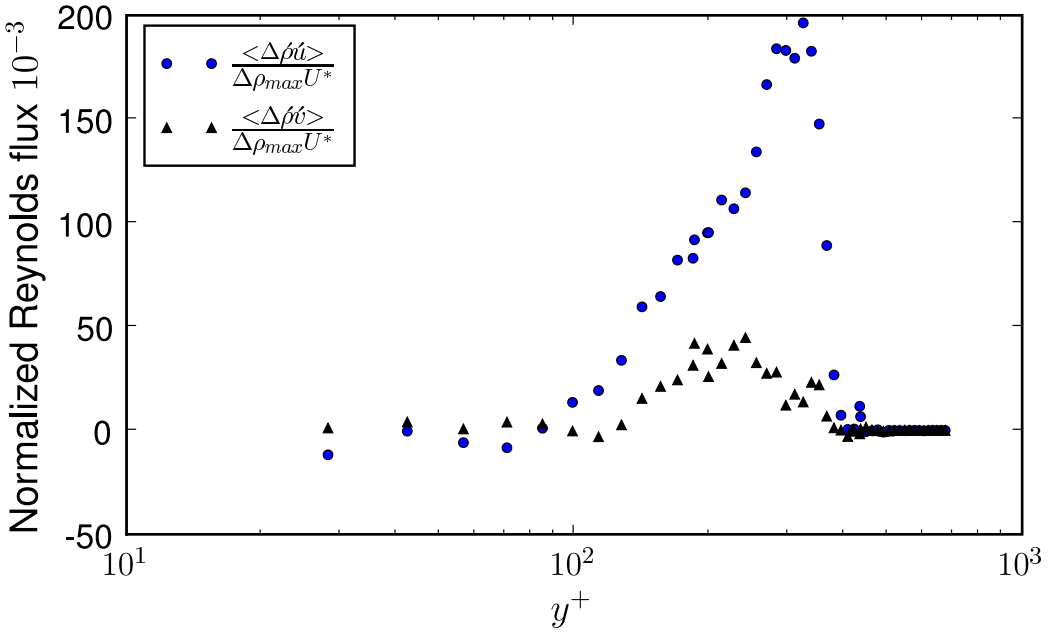

(b) inner scaling

Figure 3.12: Gravity current Reynolds flux profiles: present research

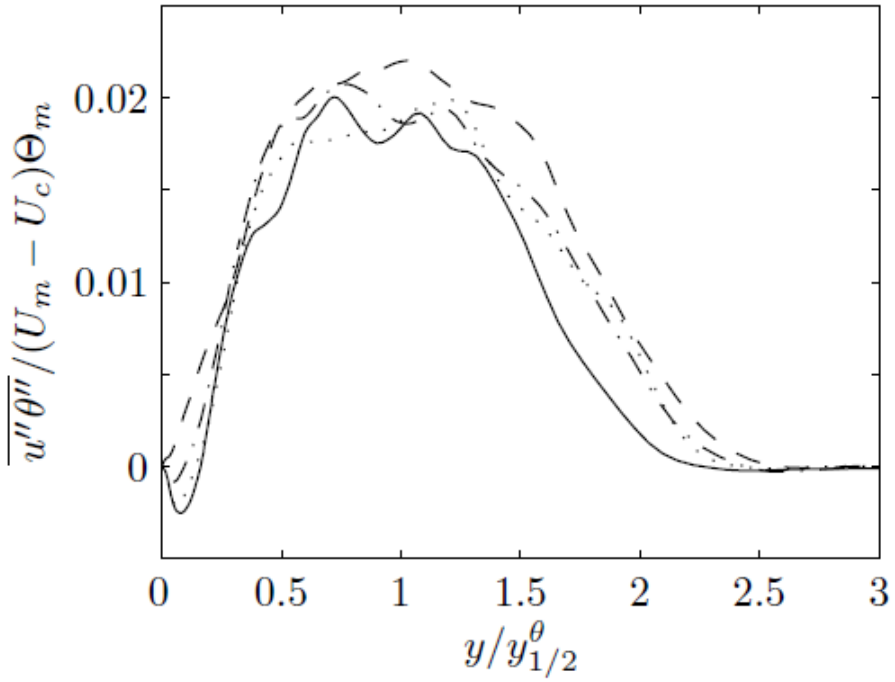

(a) Streamwise flux (u-component)

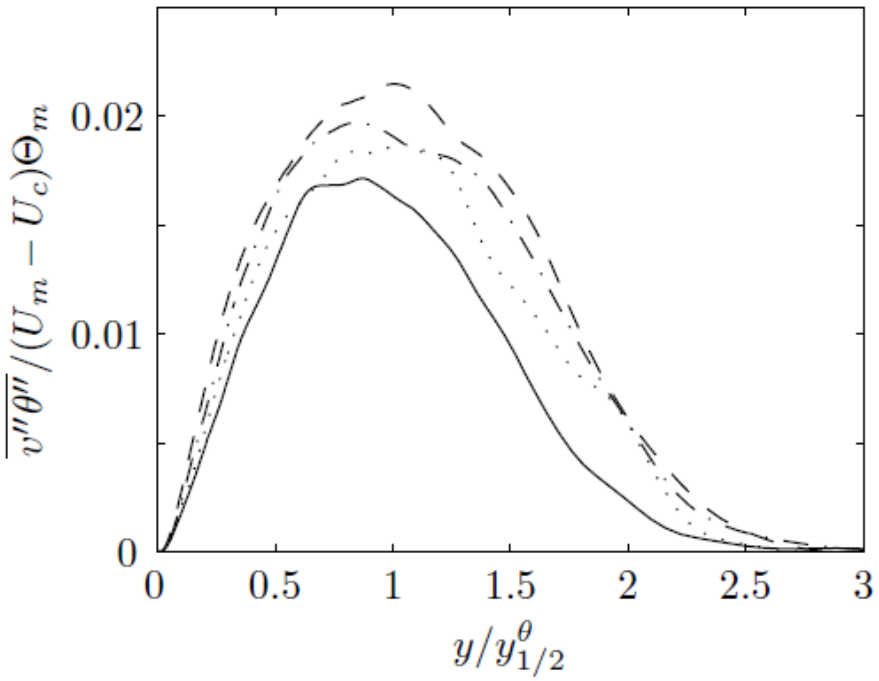

(b) Cross-stream flux (v-component)

Figure 3.13: Wall-jet Reynolds flux profiles (outer scaling):Ahlman (2006)

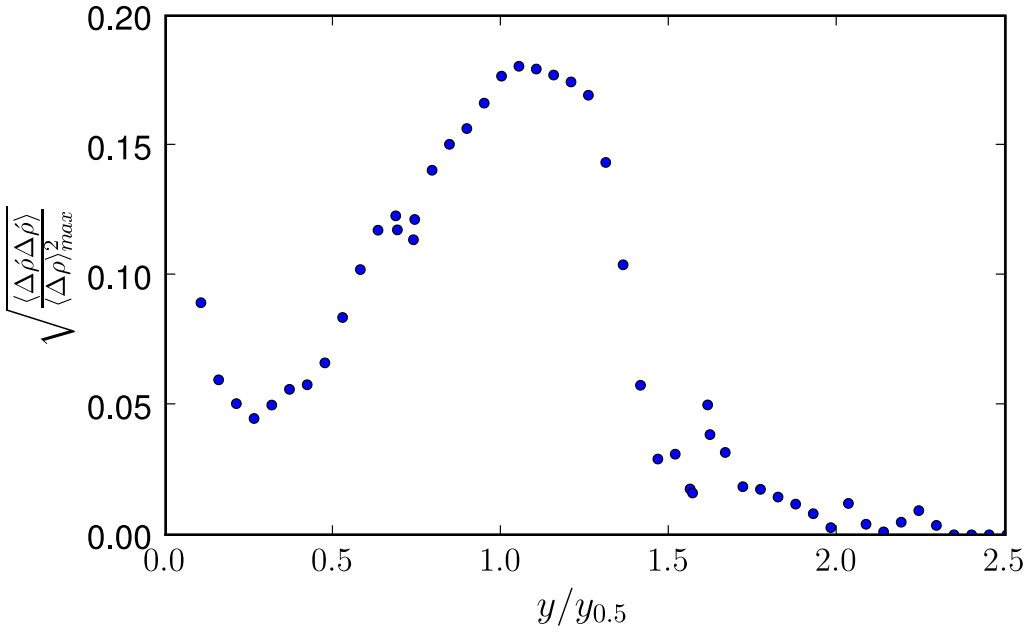

(a) Gravity current excess density intensity: present research

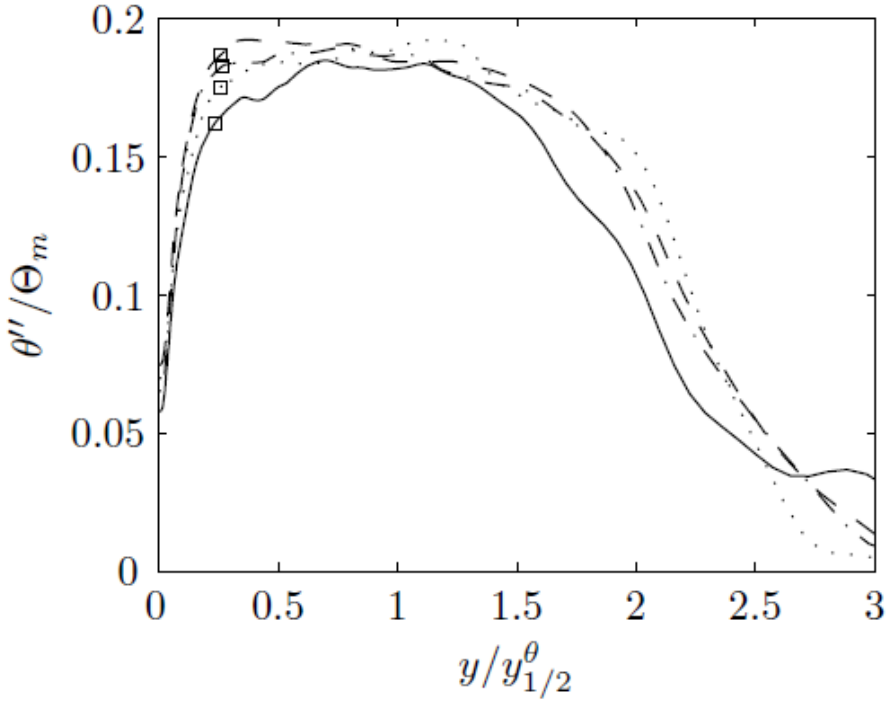

(b) Wall-jet scalar intensity: Ahlman (2006)

Figure 3.14: Profiles of gravity current excess density intensity and wall-jet scalar intensity (outer scaling)

3.2.9 Production of k

For a boundary layer-type flow the production of turbulent kinetic energy through shearing is given by

$$\mathcal{P} = -\langle u'v' \rangle \frac{dU}{dy} \tag{3.2.11}$$

while production of turbulent kinetic energy through buoyancy is given by

$$G_b = -\frac{g}{\rho_w} \langle \Delta\rho' v' \rangle \tag{3.2.12}$$

Figures 3.15a and 3.15b presents the partial budget of turbulent kinetic energy in outer and inner scaling. It shows that positive shear production $\mathcal{P}$ dominates over negative buoyancy production G_b. This is in accordance with the gradient Richardson number being near or below the critical value of 0,25 (figure 3.8), which implies that the shear production is able to offset the buoyancy production.

The $\mathcal{P}$ profile has two positive peaks: an outer peak of 0,0036 at $0{,}75 < y/y_{0.5} < 0{,}9$ and an inner peak of 0,077 at $y^+ = 30$. The outer $\mathcal{P}$ peak, corresponds to the height of the outer $\langle u'v' \rangle$ Reynolds stress peak $y/y_{0.5} = 0{,}75$, while the inner $\mathcal{P}$ peak, corresponds to the height of the inner $\langle u'v' \rangle$ Reynolds stress peak $y^+ = 30$.

The G_b profile has a single negative outer peak of $-0{,}000\,87$ between $0{,}7 < y/y_{0.5} < 0{,}9$, which corresponds to the height of the outer $\langle \Delta\rho' v' \rangle$ Reynolds flux peak. The negative peak implies that buoyancy acts as a sink and converts turbulent kinetic energy into potential energy.

Figure 3.15a shows that buoyancy production occurs primarily in the outer region and is negligible in the inner region. Numerical models often use semi-empirical wall functions as bed boundary conditions. These wall functions often assume that turbulence is in local equilibrium $\mathcal{P} \approx \epsilon$ near the bed. Local equilibrium occurs when the rate of change of k, the diffusive transport of k and buoyancy production of k is negligible. Figure 3.15b shows that $\mathcal{P} \approx \epsilon$ for a small region between $50 < y^+ < 70$. Hence the use of the local equilibrium assumption in wall functions is reasonable.

Buckee *et al.* (2001) found that for supercritical currents the greatest production of k occurred near the bed, due to shear. However, figure 3.15a shows that shear production occurs both at the bed and in the outer region of the gravity current. Buckee *et al.* (2001) also reported regions of negative shear production. The present research does not show such a region.

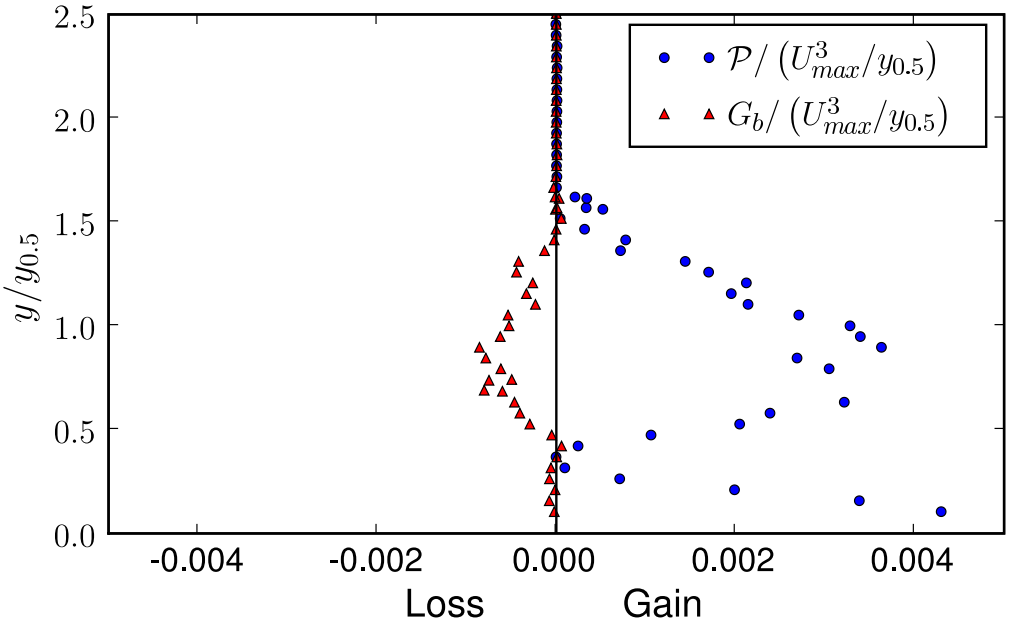

(a) outer scaling

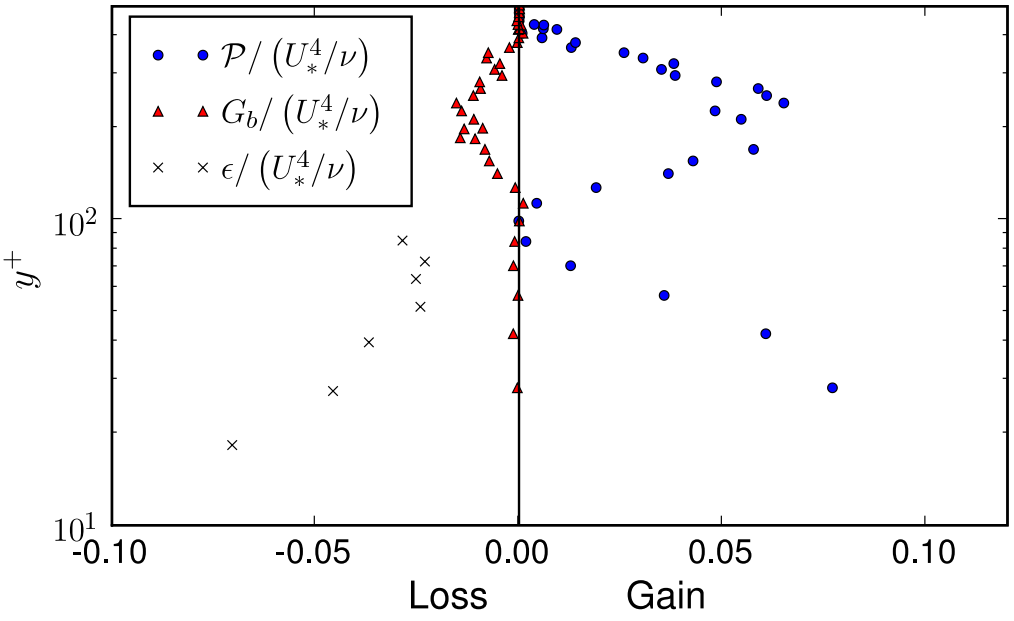

(b) inner scaling

Figure 3.15: Partial budget of turbulent kinetic energy: present research

3.2.10 Turbulent viscosity, diffusivity and Schmidt number

The Boussinesq hypothesis is analogous to Newton's law of viscosity. For boundary layer-type flows the Boussinesq hypothesis relates the $\langle u'v' \rangle$ Reynolds stress to the mean dU/dy velocity gradient as follows

$$\langle u'v' \rangle = \nu_t \frac{\partial U}{\partial y} \tag{3.2.13}$$

where ν_t is the turbulent viscosity. Equation 3.2.13 was used to compute the turbulent viscosity ratio ν_t/ν profile of the gravity current. Figure 3.16a presents the measured turbulent viscosity ratio ν_t/ν profile in outer scaling. It shows that ν_t/ν has a positive outer peak between $0{,}65 < y/y_{0.5} < 0{,}9$. This peak is less than half the inlet value ($\nu_t/\nu = 46$), which indicates that the level of turbulence has decreased significantly over the first 0,9 m of the flume.

The flux-gradient hypothesis is analogous to Fick's first law of molecular diffusion. For boundary layer-type flows the flux-gradient hypothesis relates the $\langle \Delta\rho' v' \rangle$ Reynolds flux to the mean $d\langle \Delta\rho \rangle/dy$ excess density gradient as follows

$$\langle \Delta\rho' v' \rangle = -\gamma_t \frac{d\langle \Delta\rho \rangle}{dy} \tag{3.2.14}$$

where γ_t is the turbulent diffusivity. Equation 3.2.14 was used to compute the turbulent diffusivity ratio γ_t/γ profile of the gravity current. Figure 3.16b presents the measured turbulent diffusivity ratio γ_t/γ profile in outer scaling. It shows that the turbulent diffusivity eclipses the molecular diffusivity by more than three orders of magnitude, with a large positive outer peak between $0{,}8 < y/y_{0.5} < 1$. Numerical models often quantify the turbulent diffusion by assuming that

$$\gamma_t = \frac{\nu_t}{\sigma_t} \tag{3.2.15}$$

where σ_t is the turbulent Schmidt number. Figure 3.17 presents the measured turbulent Schmidt number profile. There is considerable scatter in the data. The turbulent Schmidt number for the supercritical gravity current appears to be in the region of $1 < \sigma_t < 2$.

Rodi (1980, pg. 15,19) mentions that $\sigma_t \approx 0{,}9$ for near wall flows and increases with the degree of stratification and, hence, bulk Richardson number. Furthermore, Huang *et al.* (2005) found that their numerical gravity current model gave the best results for $\sigma_t = 1{,}3$. Figure 3.17 supports these observations.

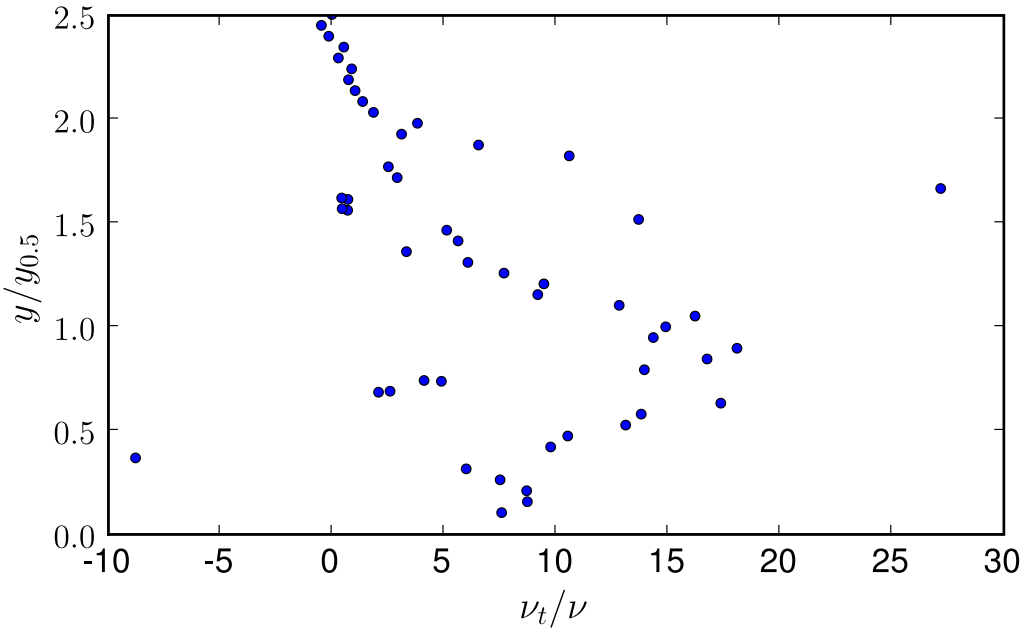

(a) Turbulent viscosity ratio

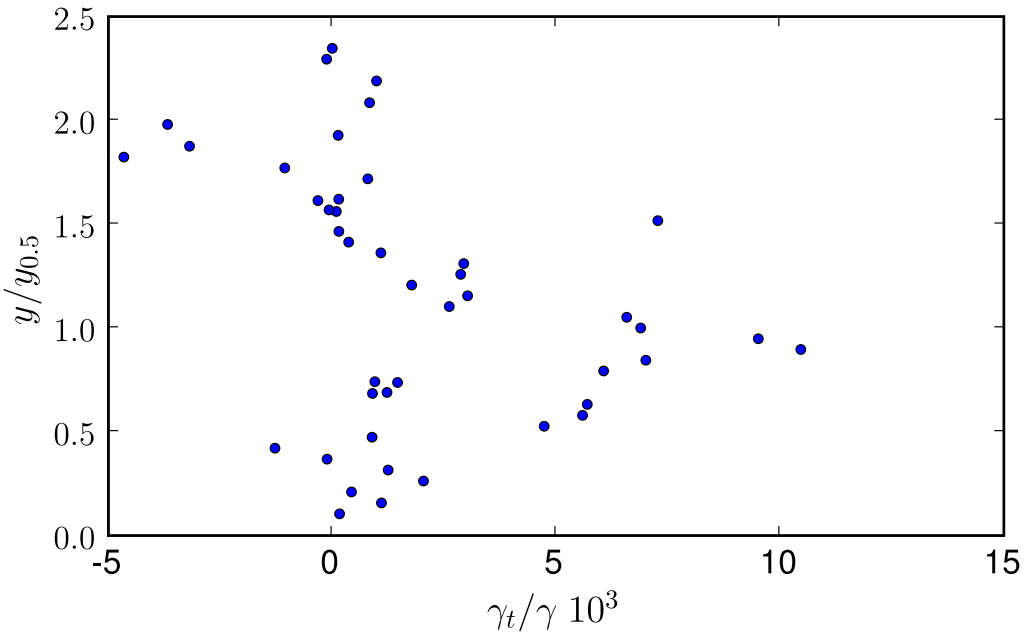

(b) Turbulent diffusivity ratio

Figure 3.16: Turbulent viscosity and diffusivity ratio profiles (outer scaling): present research

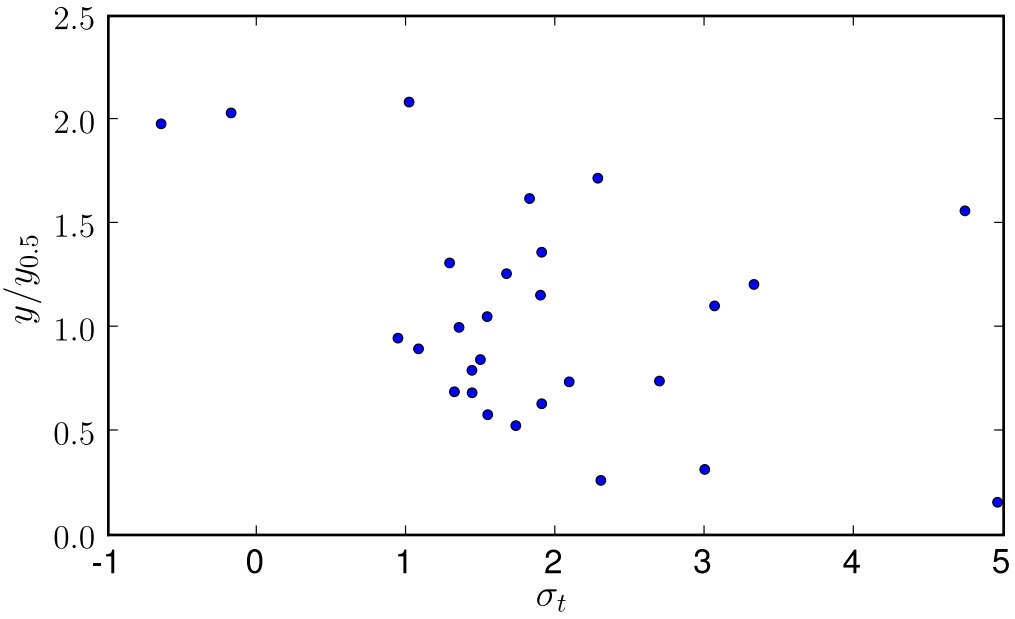

Figure 3.17: Turbulent Schmidt number: present research

3.2.11 Energy spectra

Figure 3.18 presents the measured one-dimensional frequency based energy spectra, as well as the computed three-dimensional inertial subrange at $y/y_{0.5} = 0.44$. At low frequencies $< 1{,}0\,\text{Hz}$, the measured $E_{uu}(f)$ spectrum dominates the measured $E_{vv}(f)$ spectrum, by a ratio of $7:1$. In the case of isotropic turbulence the ratio is $2:1$ (Pope, 2001, pg. 229). The large $7:1$ ratio indicates that the large, low frequency eddies are anisotropic. The anisotropy is due to stable stratification damping the low frequency, vertical velocity fluctuations. Kneller *et al.* (1999) also presented the u-velocity energy spectrum for a saline gravity current. They found that the greatest contribution to the turbulent kinetic energy came from the low frequencies ($< 10\,\text{Hz}$). Figure 3.18 supports their observation by showing that the production subrange $< 1{,}0\,\text{Hz}$ contains the frequencies with the largest amounts of energy. Figure 3.18 also shows the three-dimensional inertial subrange estimates $E(f, \epsilon_u)$ and $E(f, \epsilon_v)$, which are given by:

$$E(f, \epsilon_u) = C \left(\frac{U_{ref} \epsilon_u}{2\pi} \right)^{\frac{2}{3}} f^{-\frac{5}{3}} \tag{3.2.16}$$

$$E(f, \epsilon_v) = C \left(\frac{U_{ref} \epsilon_v}{2\pi} \right)^{\frac{2}{3}} f^{-\frac{5}{3}} \tag{3.2.17}$$

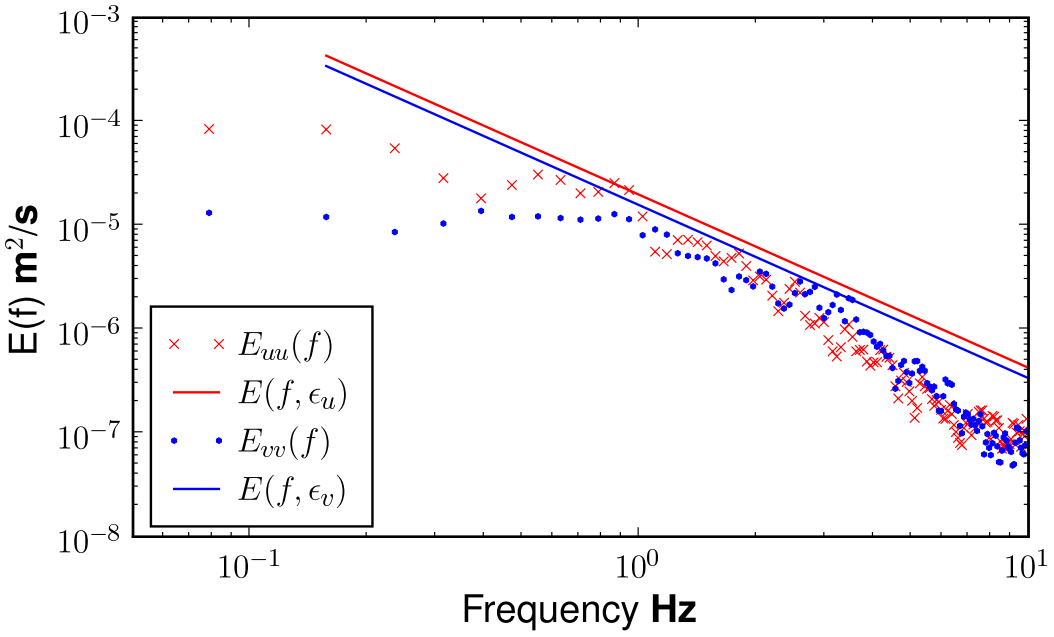

Figure 3.18: Energy spectra of u- and v-velocities at $y/y_{0.5} = 0.44$: present research

where ϵ_u and ϵ_v are the dissipation rate of turbulent kinetic energy estimates. The values of ϵ_u and ϵ_v were computed, as outlined in section 2.6.4, using the measured $E_{uu}(f)$ and $E_{vv}(f)$ spectra. $E(f, \epsilon_u)$ and $E(f, \epsilon_v)$ have a -5/3 slope, but do not collapse onto one another, which also suggests that the turbulence is anisotropic. Furthermore, the measured $E_{uu}(f)$ spectrum only has a -5/3 slope for frequencies between 0,5 Hz $< f <$ 3,0 Hz. This is a fairly narrow inertial subrange, which indicates that the Reynolds number, and hence turbulence, was quite low.

3.3 Gravity current profiles: 2,4 m from the inlet

This section presents in detail the mean velocity, density and turbulence profiles for a gravity current 2,4 m from the inlet (the inlet conditions are given in table 3.1). Table 3.3 summarizes the gravity current flow conditions 2,4 m from the inlet, using outer, inner and depth-averaged scales. It shows that the depth-averaged current velocity U_d has decreased, from 0,052 m/s at 0,9 m from the inlet, to 0,038 m/s. The depth-averaged current height H_d has increased from 0,07 m to 0,124 m. The depth-averaged excess density has decreased from 1,33 kg/m^3 to 1,03 kg/m^3. All these changes in the depth-averaged scales indicate the entrainment of low momentum ambient water into the gravity current.

The bulk Richardson number Ri indicates that the current is near to the point of becoming subcritical $Ri = 0{,}88$. This indicates that the buoyancy and inertial forces are nearly in balance. Hence the interface between the current and the overlying ambient water has increased in stability. The amount of entrainment is therefore much less than it was at 0,9 m from the inlet. This is shown by the small decrease in depth-averaged excess density $\langle \Delta\rho \rangle_d$ from 1,33 kg/m^3 to 1,03 kg/m^3 over a distance of 1,5 m. The bulk Richardson number also indicates that the current is driven mainly by density differences and not by inlet jet momentum.

3.3.1 Mean velocities

Figure 3.19a presents the mean U-velocity profiles on the flume centreline, 2,4 m and 0,9 m from the inlet. The two profiles collapse well between $0.0 < y/y_{0.5} < 1.5$. However, it seems that at 2,4 m the U-profile of the return flow has merged with that of the gravity current. This was not the case with the U-profile at 0,9 m, where the current was below $y/y_{0.5} < 1.5$ and the return flow above $y/y_{0.5} > 2$. The U-profile at 2,4 m has a velocity maximum at $y/y_{0.5} = 0{,}4$, which is comparable to the height of $y/y_{0.5} = 0{,}37$ for the velocity maximum at 0,9 m.

Figure 3.19b shows the near-wall streamwise velocity profile in inner scaling. The measured streamwise velocity follows the law-of-the-wall (equation 4.4.7) between $45 < y^+ < 130$. Hence the use of the law-of-the-wall as a bed boundary condition is reasonable. Furthermore, figure 3.20 shows an upward velocity peak of 0,012 at $y/y_{0.5} = 0{,}67$. The V-velocity profile does not show downward flow above the velocity maximum, indicating that there is very little entrainment of ambient water into the current at 2,4 m.

Variable	Units	Value (measured)
U_{max}	m/s	0,0487
$\langle\rho\rangle_{max}$	kg/ m^3	1,67
$y_{0.5}$	m	0,109
Re_{outer}	-	5300
U^*	m/s	0,0027
$\frac{\nu}{U^*}$	m	0,000 37
U_d	m/s	0,038
H_d	m	0,124
$\langle\rho\rangle_d$	kg/ m^3	1,03
$\langle\rho\rangle_d H_d U_d$	kg/m,s^3	0,0049
Ri	-	0,88

Table 3.3: Gravity current flow conditions far from inlet

3.3.2 Mean excess density

Figure 3.21 presents the mean excess density profiles of the PIV-S measurements at 0,9 m and 2,4 m, as well as the siphon measurements at 2,4 m. The siphon profile at 2,4 m and the PIV-S profile at 0,9 m appear to collapse well. However, the PIV-S profile at 2,4 m was adjusted so that the measured depth-averaged excess density flux $\langle\Delta\rho\rangle_d H_d U_d$ was within 3% of the inlet excess density flux. With this adjustment the two PIV-S profiles do not collapse and hence do not show self-similarity.

3.3.3 Mean velocity gradients

Figure 3.22 presents the mean velocity gradient profiles. Although the dU/dy velocity gradient has decreased in magnitude from 0,9 Hz (figure 3.7) to 0,5 Hz, it still remains the dominant velocity gradient. Hence the gravity current still shows the characteristics of a boundary layer-type flow. The velocity gradient dU/dy becomes zero at the velocity maximum $y/y_{0.5} = 0{,}4$, where no turbulent kinetic energy is produced through shear.

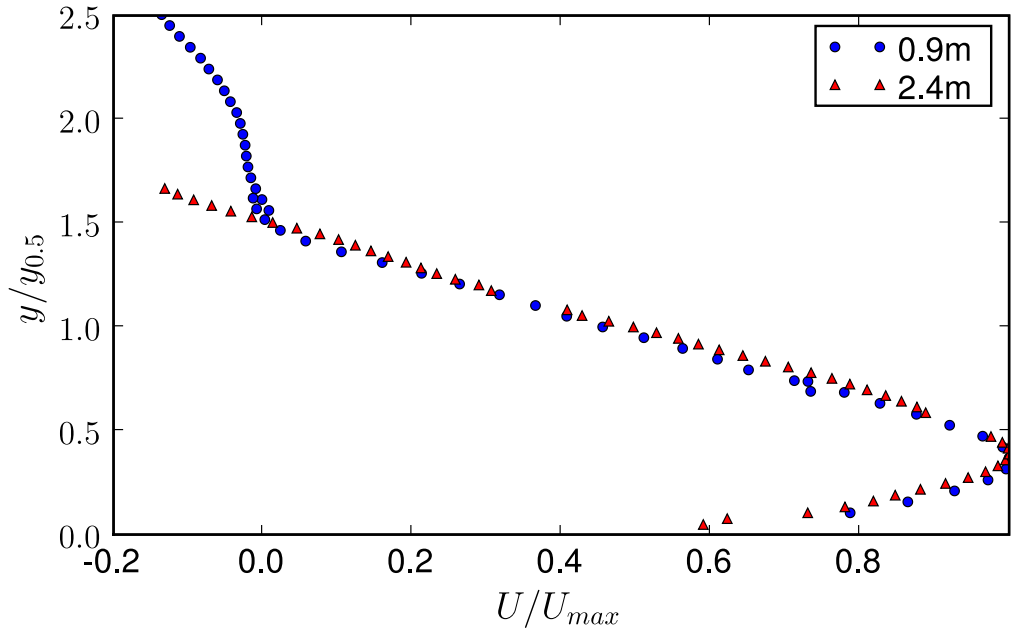

(a) outer scaling

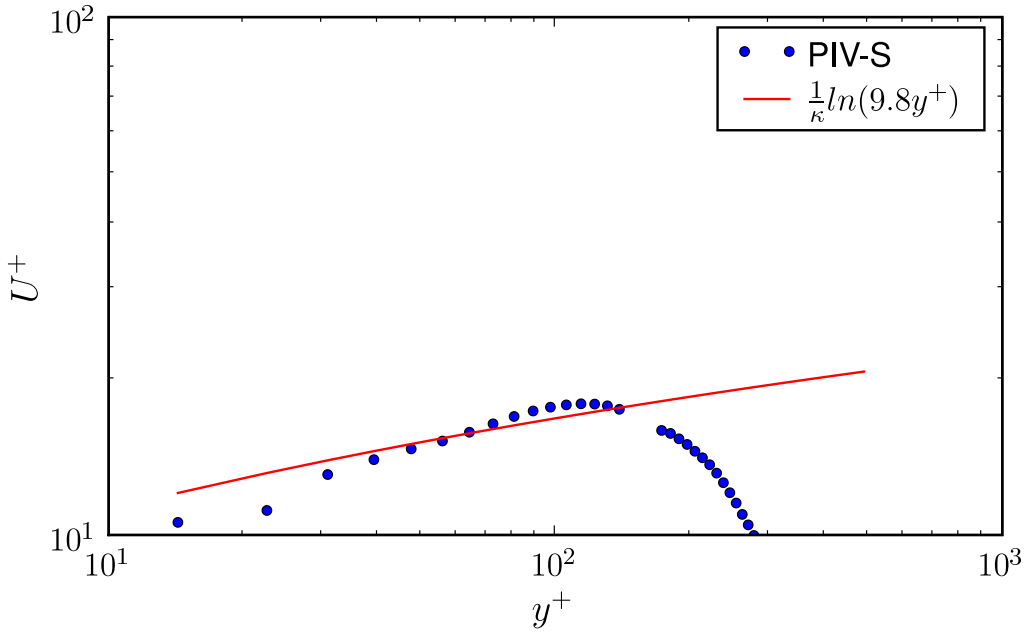

(b) inner scaling

Figure 3.19: Mean streamwise velocity: present research

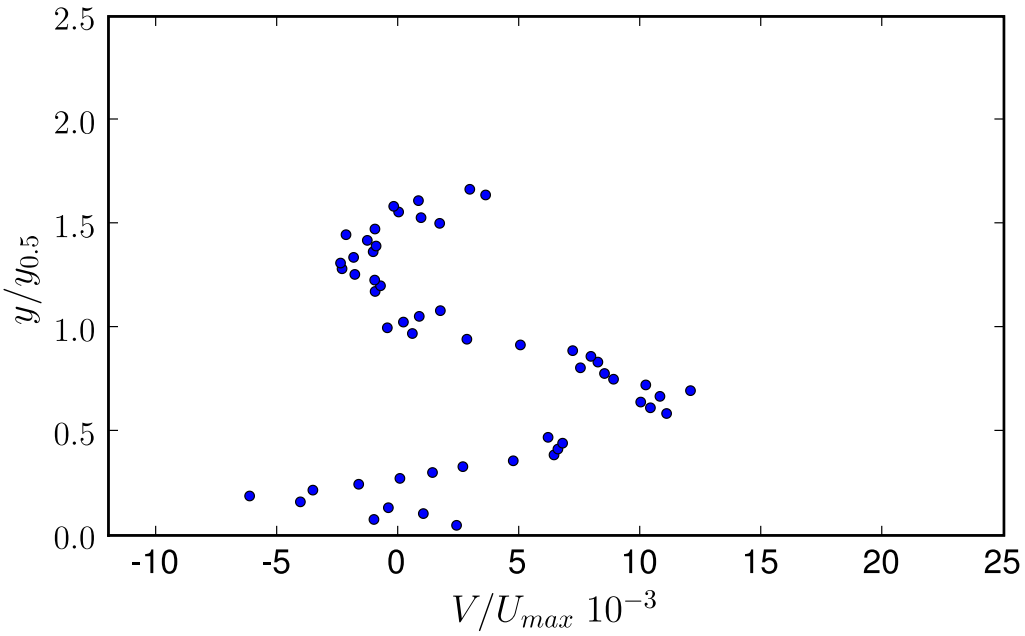

Figure 3.20: Mean cross-stream velocity: present research

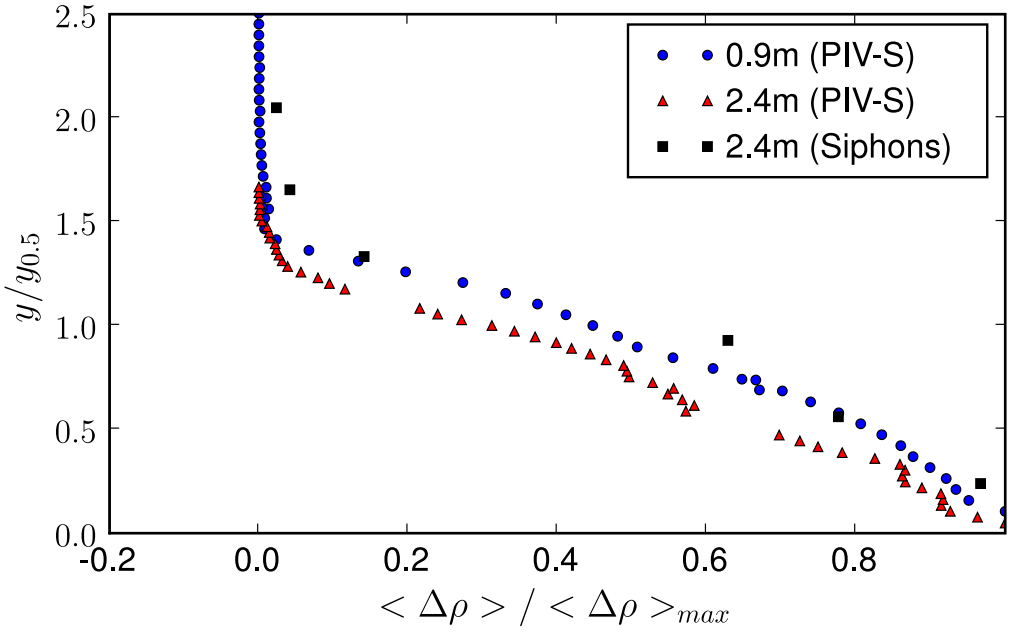

Figure 3.21: Mean excess density: present research

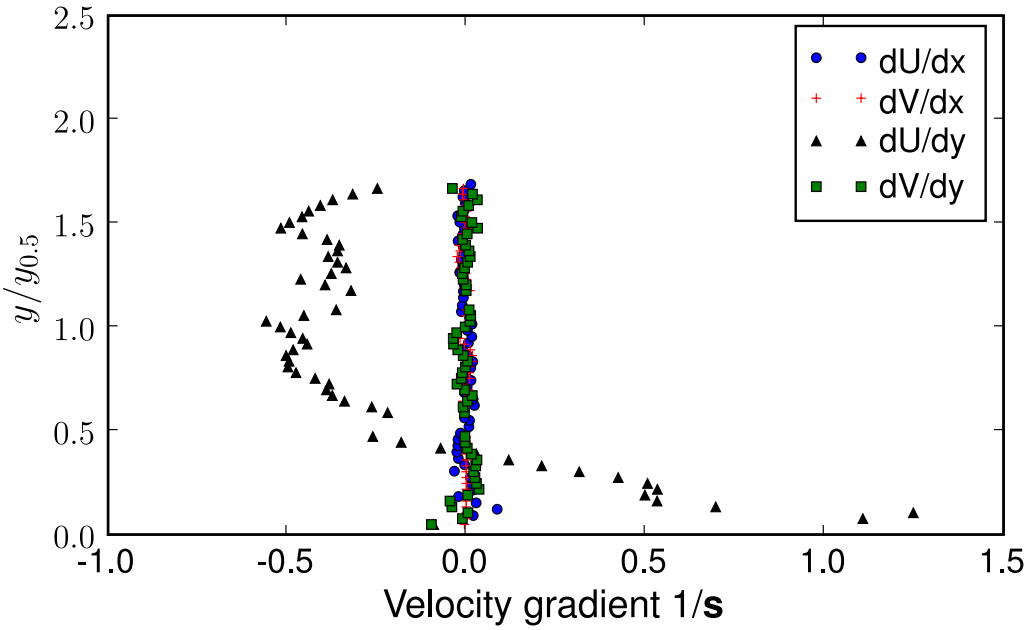

Figure 3.22: Mean velocity gradients: present research

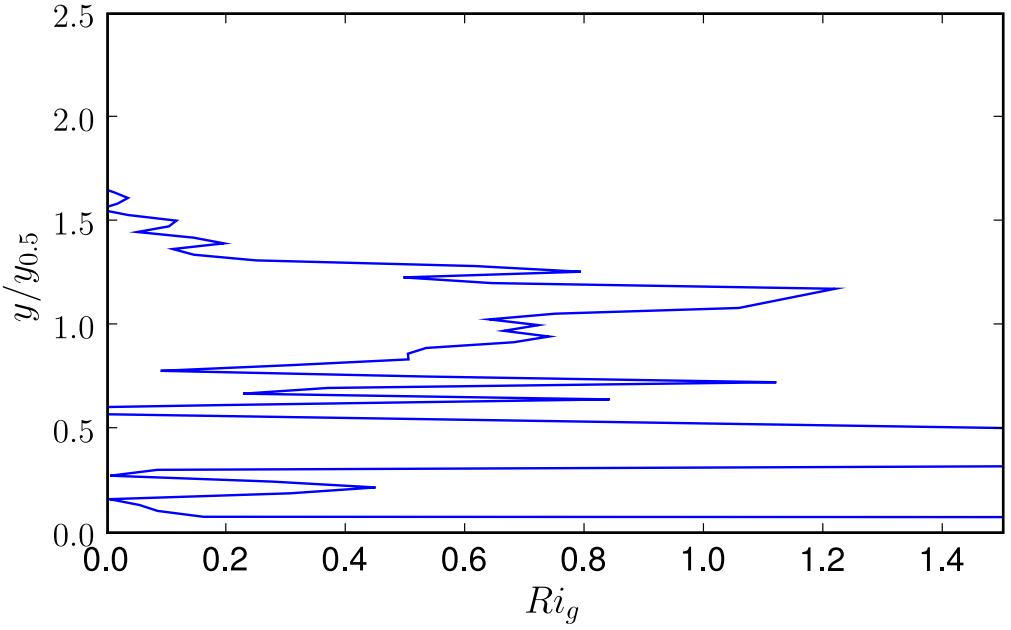

Figure 3.23: Gradient Richardson number: present research

3.3.4 Gradient Richardson number

Figure 3.23 presents the gradient Richardson number profile. It shows that Ri_g is above the critical value of 0,25 for most of the flow depth. Hence the positive shear production of k is unable to offset the negative buoyancy production and hence turbulence cannot be maintained. However, some turbulent kinetic energy is produced through shear near the bed. This turbulent kinetic energy can be transported upwards, increasing the low turbulence levels in the outer region of the gravity current. Nevertheless, figure 3.23 suggests that turbulent mixing is very limited throughout most of the current depth.

3.3.5 Reynolds stresses

Figures 3.24a and 3.24b present the measured $\langle u'u' \rangle$, $\langle v'v' \rangle$ and $\langle u'v' \rangle$ Reynolds stress profiles in outer and inner scaling at 2,4 m from the inlet. The most noticable feature of the Reynolds stress profiles is the disappearance of the outer stress peaks. Figures 3.25a, 3.25b and 3.26a compares each Reynolds stress profile at 2,4 m with its corresponding profile at 0,9 m. None of the profiles collapse, indicating that the turbulent stress structure of the gravity current is not self-similar between $0{,}9\,\text{m} < x < 2{,}4\,\text{m}$.

Figures 3.24a and 3.24b show that at 2,4 m the $\langle u'u' \rangle$ Reynolds stress profile has two positive peaks: an inner peak of 5,88 at $y^+ = 22$ and a reduced outer peak of 0,0044 at $y/y_{0.5} = 0{,}75$. A local minimum of 0,766, between the two peaks, is located at $0{,}33 < y/y_{0.5} < 0{,}48$. The $\langle v'v' \rangle$ Reynolds stress profile shows a new positive inner peak of 0,517 at $y^+ = 50$. Furthermore, the $\langle u'v' \rangle$ Reynolds stress profile shows a negative inner peak of $-0{,}633$ at $y^+ = 40$ and becomes zero at $y^+ = 100$.

The disappearance of the outer Reynolds stress peaks is due to the strong stratification in the outer region, indicated by the large gradient Richardson number. The gradient Richardson number ($Ri_g > 0{,}25$) shows that positive shear production is unable to offset the negative buoyancy production and hence turbulence collapses in the outer region. Near the bed the shear production is still able to offset the buoyancy production, which explains the existence of the inner Reynolds stress peaks.

The relationship between the Reynolds shear stress $\langle u'v' \rangle$ and the degree of anisotropy can again be noted: Maximum anisotropy in the inner region occurs

near the inner peak of $\langle u'v' \rangle$. Further away from the bed the degree of anisotropy decreases as the magnitude of $\langle u'v' \rangle$ decreases. At $y^+ = 100$ $\langle u'v' \rangle$ becomes zero and the degree of anisotropy is at a minimum. Further away from the bed the degree of anisotropy remains more or less the same, since $\langle u'v' \rangle$ remains uniform and small. Furthermore, the turbulence intensity at the velocity maximum (based on the $\langle u'u' \rangle$ Reynolds stress) has decreased from 10% to 7%, which is still moderate. This indicates that turbulent momentum transport remains significant at the velocity maximum. This is due to the upward transport of turbulent kinetic energy produced by shear near the bed.

Figure 3.26b presents the Reynolds stress profiles for a subcritical gravity current (Buckee *et al.*, 2001). Similar to figure 3.24a, the $\langle u'u' \rangle$ Reynolds stress profile also shows a reduced outer peak at $y/y_{0.5} = 0{,}9$ and an inner peak at $y/y_{0.5} = 0{,}09$. Furthermore, the $\langle v'v' \rangle$ Reynolds stress profile also shows an inner peak at $y/y_{0.5} = 0{,}1$. Buckee *et al.* (2001) concluded that for subcritical flow the maximum value of k occurs near the bed. The $\langle u'u' \rangle$ and $\langle v'v' \rangle$ profiles of the present study also suggest a maximum k value near the bed, due to the inner Reynolds stress peaks being unaffected by the stable stratification.

3.3.6 Reynolds fluxes and excess density variance

Figures 3.27a and 3.27b present the $\langle \Delta\rho' u' \rangle$ and $\langle \Delta\rho' v' \rangle$ Reynolds flux profiles in outer and inner scaling. Similar to figure 3.24a, the most notable feature is the disappearance of the outer Reynolds flux peaks. Figures 3.28a and 3.28b compare each Reynolds flux profile at 2,4 m with its corresponding profile at 0,9 m. None of the profiles collapse, indicating that the turbulent flux structure of the gravity current is also not self-similar between $0{,}9\,\text{m} < x < 2{,}4\,\text{m}$.

Figures 3.27a and 3.27b show that the $\langle \Delta\rho' u' \rangle$ Reynolds flux profile has a very weak positive outer peak of 0,001 87 at $y/y_{0.5} = 0{,}72$, which corresponds to the height of the weak outer $\langle u'u' \rangle$ Reynolds stress peak ($y/y_{0.5} = 0{,}75$). The positive $\langle \Delta\rho' u' \rangle$ peak indicates that denser fluid is transported downstream and less dense fluid upstream. Furthermore, the $\langle \Delta\rho' u' \rangle$ Reynolds flux profile has a negative inner peak of $-0{,}0279$ at $y^+ = 15$, which corresponds to the height of the inner $\langle u'u' \rangle$ Reynolds stress peak ($y^+ = 22$).

The $\langle \Delta\rho' v' \rangle$ Reynolds flux profile shows a single positive inner peak of 0,0173 at $y^+ = 50$, which corresponds to the height of the inner $\langle v'v' \rangle$ Reynolds stress peak ($y^+ = 50$). The positive $\langle \Delta\rho' v' \rangle$ peak indicates that dense fluid is transported upwards and less dense fluid downwards. This is in accordance with stable density

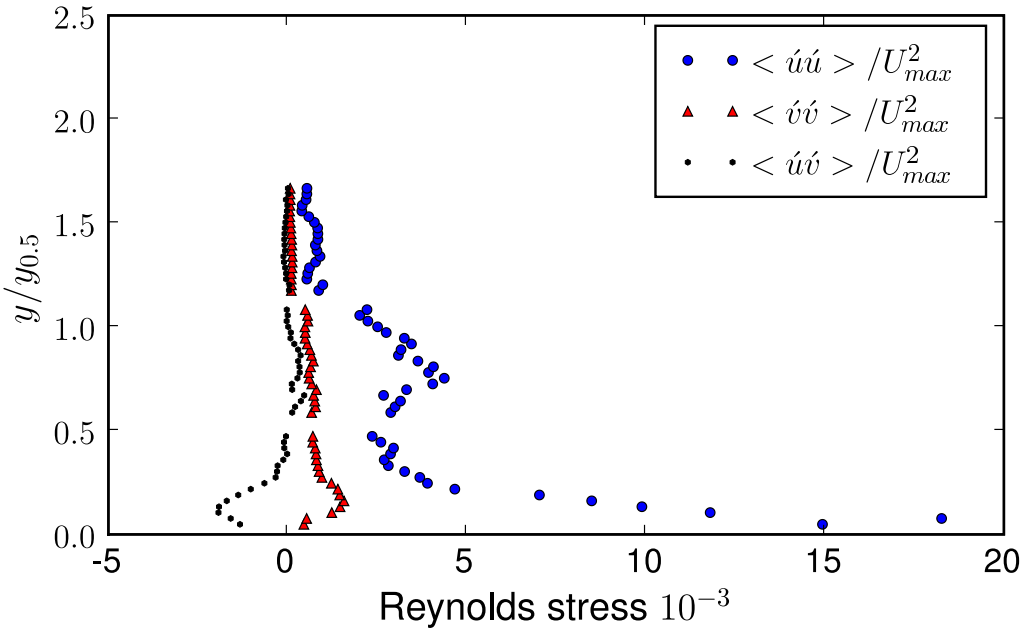

(a) outer scaling

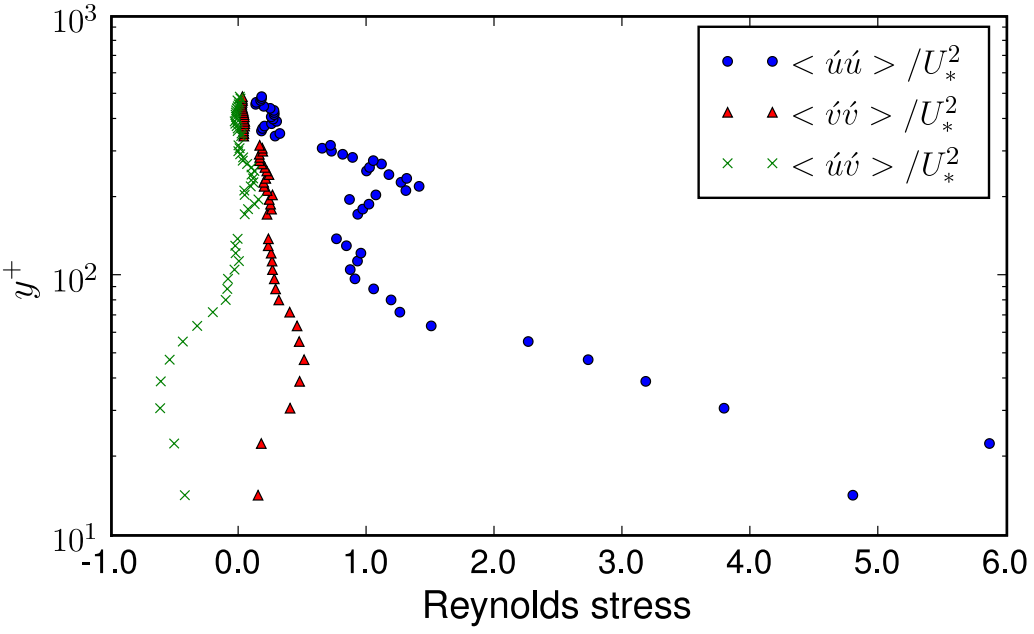

(b) inner scaling

Figure 3.24: Gravity current Reynolds stress profiles at 2,4 m: present research

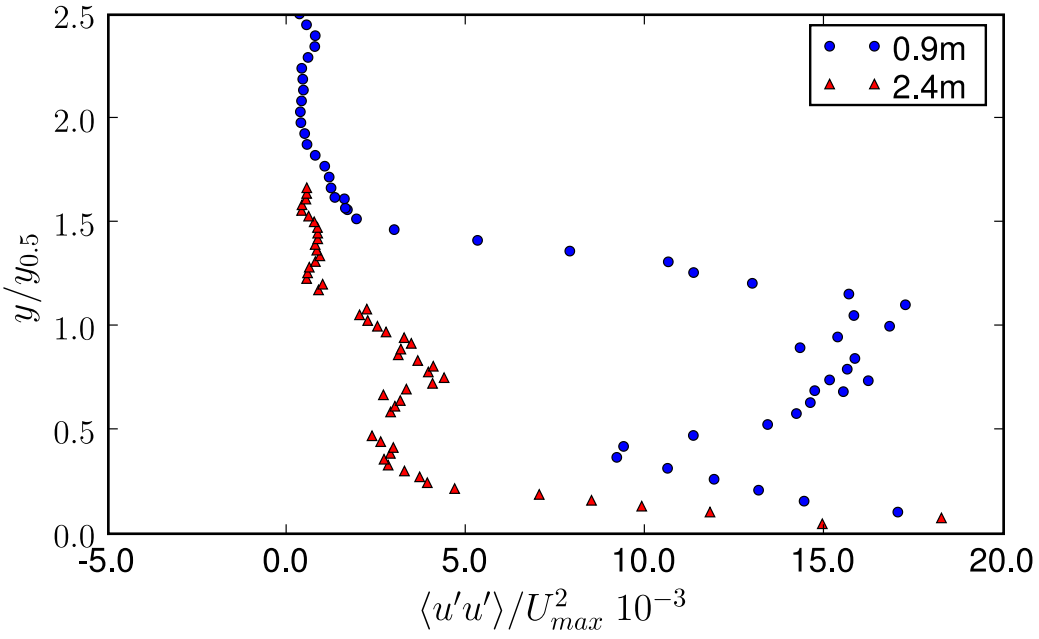

(a) $\langle u'u' \rangle$

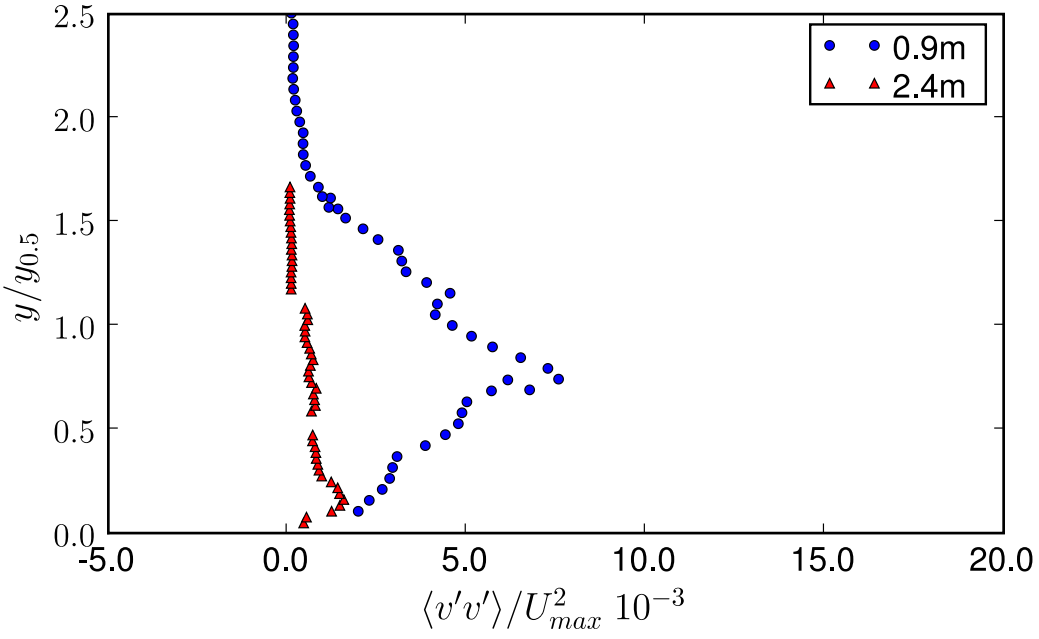

(b) $\langle v'v' \rangle$

Figure 3.25: Reynolds stress profiles at $0{,}9\,\mathrm{m}$ **and** $2{,}4\,\mathrm{m}$**: present research**

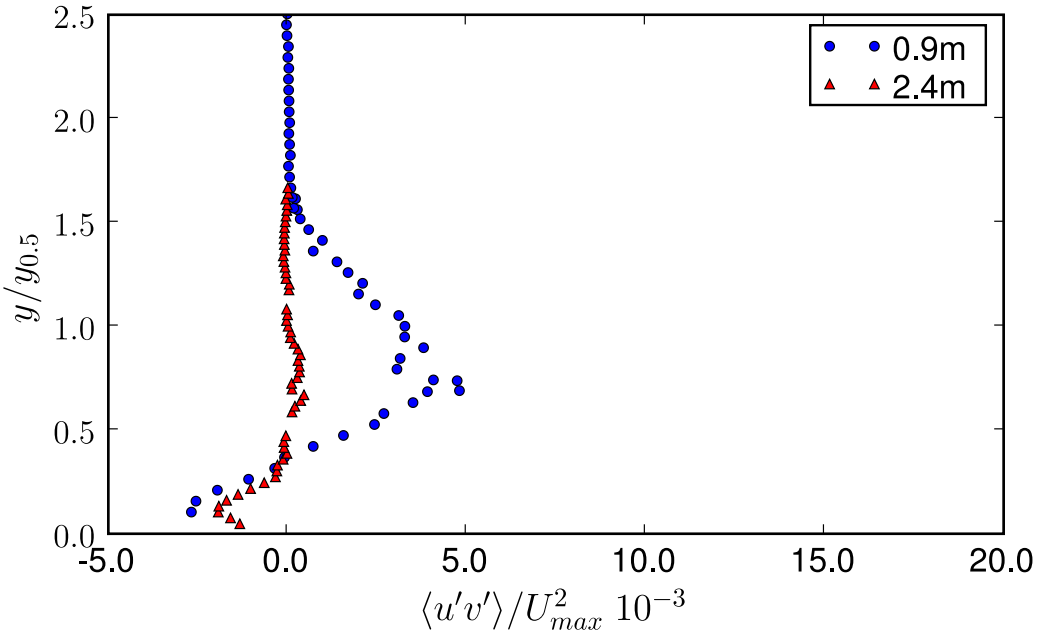

(a) $\langle u'v' \rangle$ **Reynolds stress profiles at** $0{,}9\,\mathrm{m}$ **and** $2{,}4\,\mathrm{m}$**: present research**

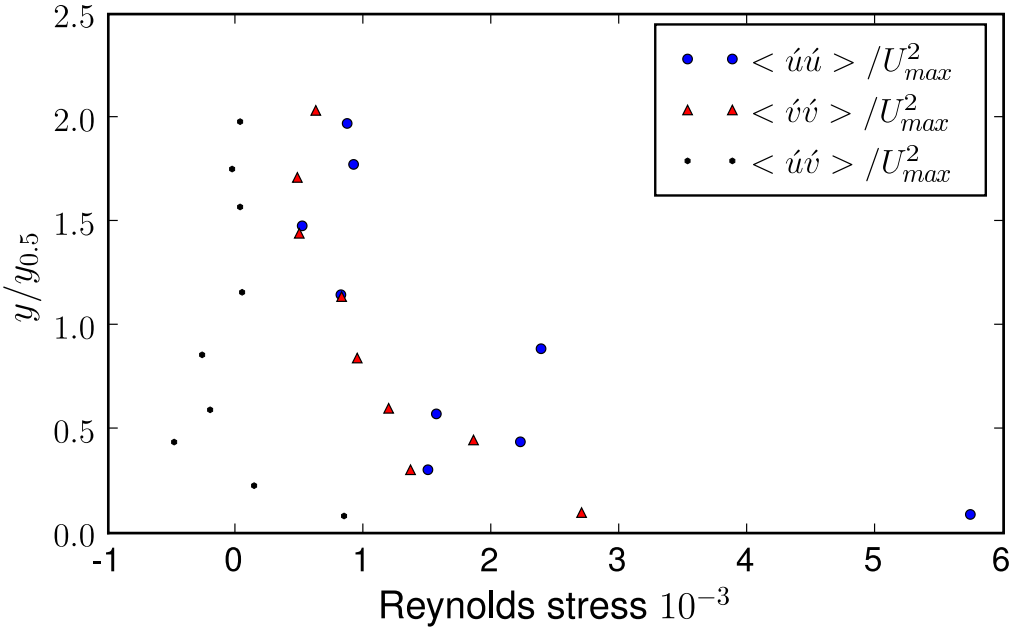

(b) Gravity current Reynolds stresses (outer scaling): Buckee *et al.* (2001)

Figure 3.26

gradient $d\langle\Delta\rho\rangle/dy < 0$ of figure 3.21. Both Reynolds flux profiles have decreased by approximately a factor of five in comparison with the profiles in figure 3.12a. This indicates how the stable stratification has dampened the turbulent mass transport within the gravity current.

Figure 3.29a presents the excess density intensity $\sqrt{\langle\Delta\rho'\Delta\rho'\rangle/\Delta\rho^2_{max}}$ profiles at 0,9 m and 2,4 m in outer scaling. Instead of a positive outer peak, the 2,4 m profile shows a plateau between $0{,}3 < y/y_{0.5} < 1$, with maximum value of 0,107. The strong reduction of the outer Reynolds stress and flux peaks, due to stable stratification, has removed the outer peak, which appears in the 0,9 m profile. This indicates that the outer region is no longer the primary region of turbulent mixing.

Figure 3.29b presents the excess density variance profile of a subcritical current (Buckee *et al.*, 2001). Unfortunately the profile could not be normalized, since the maximum excess density scale $\langle\Delta\rho\rangle_{max}$ was not mentioned. However, figure 3.29b also suggests that for gravity currents having high bulk Richardson numbers the outer region does not dominate the turbulent mixing.

3.3.7 Production of k

Figures 3.30a and 3.30b present the shear and buoyancy production profiles in outer scaling and inner scaling. Due to the reduction of the outer Reynolds stress and flux peaks, the outer shear and buoyancy production peaks have also been reduced. It can be seen that buoyancy and shear production occurs primarily in the inner region.

The $\mathcal{P}$ profile has a positive inner peak of 0,105 at $y^+ = 30$, which corresponds to the height of the negative inner $\langle u'v'\rangle$ Reynolds stress peak $y^+ = 40$. The G_b profile has a small negative inner peak of $-0{,}014$ at $y^+ = 52$, which indicates that buoyancy acts as a sink and converts turbulent kinetic energy into potential energy. The height of the inner G_b peak corresponds to the height of the positive inner $\langle\Delta\rho'v'\rangle$ Reynolds flux peak.

Figure 3.30b suggests that local equilibrium of turbulent kinetic energy $\mathcal{P} \approx \epsilon$ does not hold in the inner region of a gravity current having a critical or subcritical bulk Richardson number. This is probably due to the presence of the inner G_b peak. The consequence is that numerical models of subcritical gravity currents may need to model the bed boundary condition using 'non-equilibrium' wall functions. These are wall functions that relax the assumption that $\mathcal{P} \approx \epsilon$

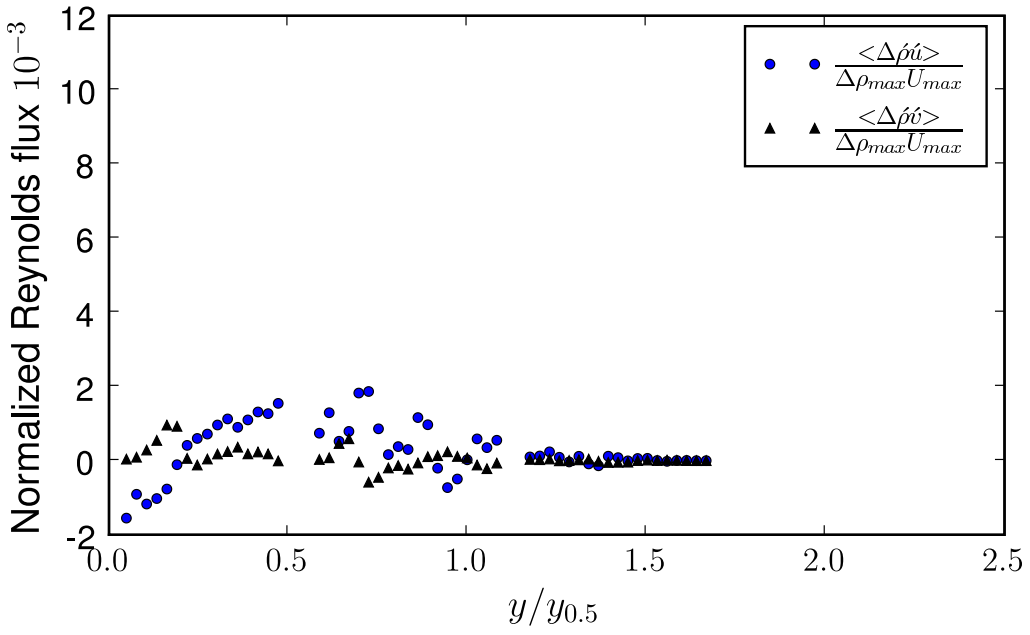

(a) outer scaling

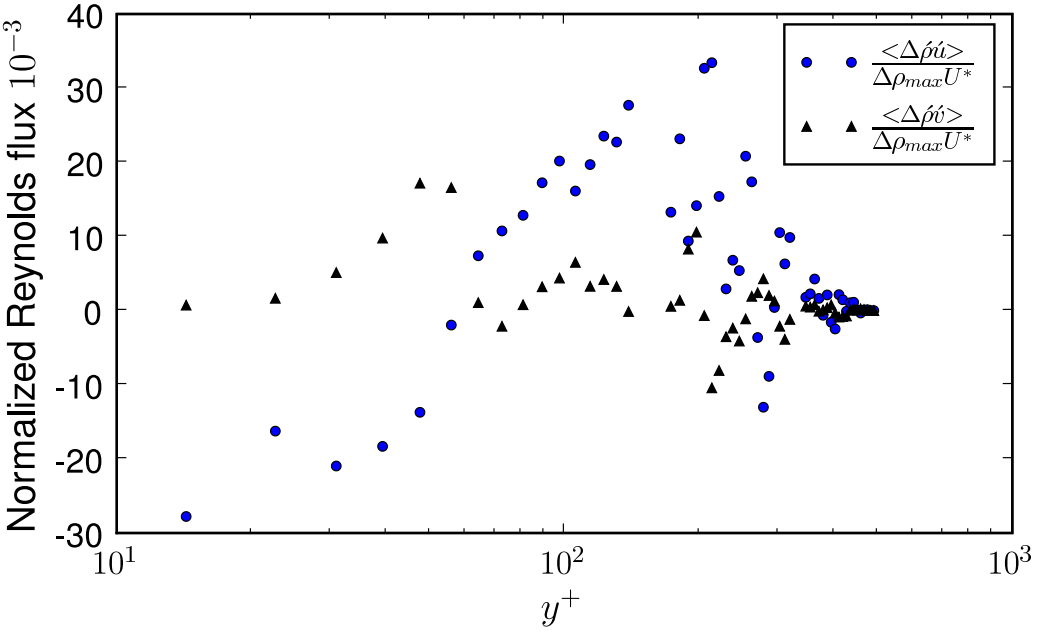

(b) inner scaling

Figure 3.27: Gravity current Reynolds flux profiles at 2,4 m: present research

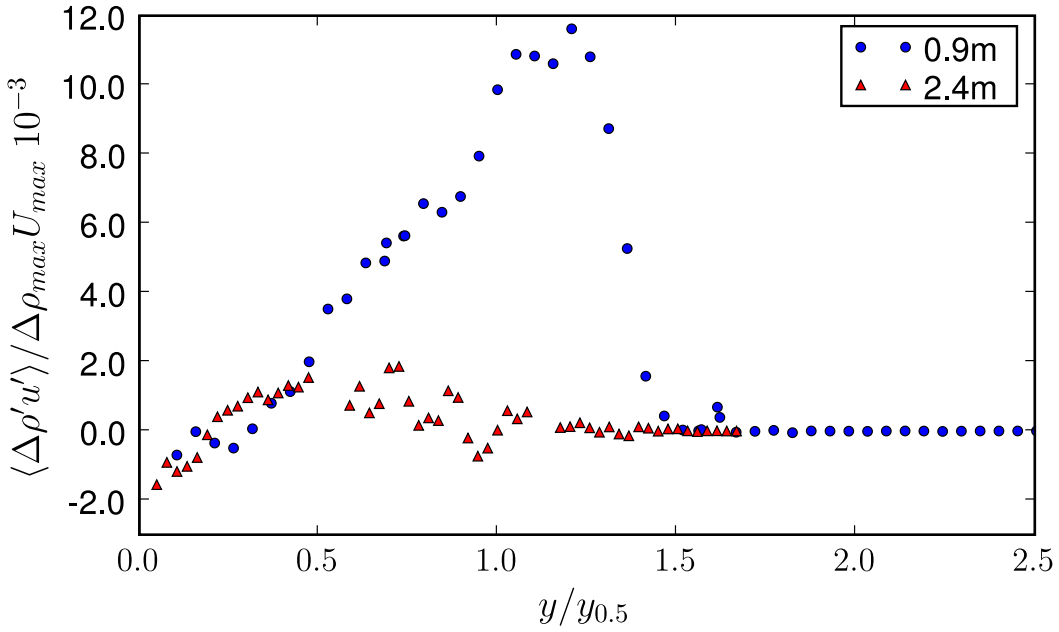

(a) Streamwise Reynolds flux

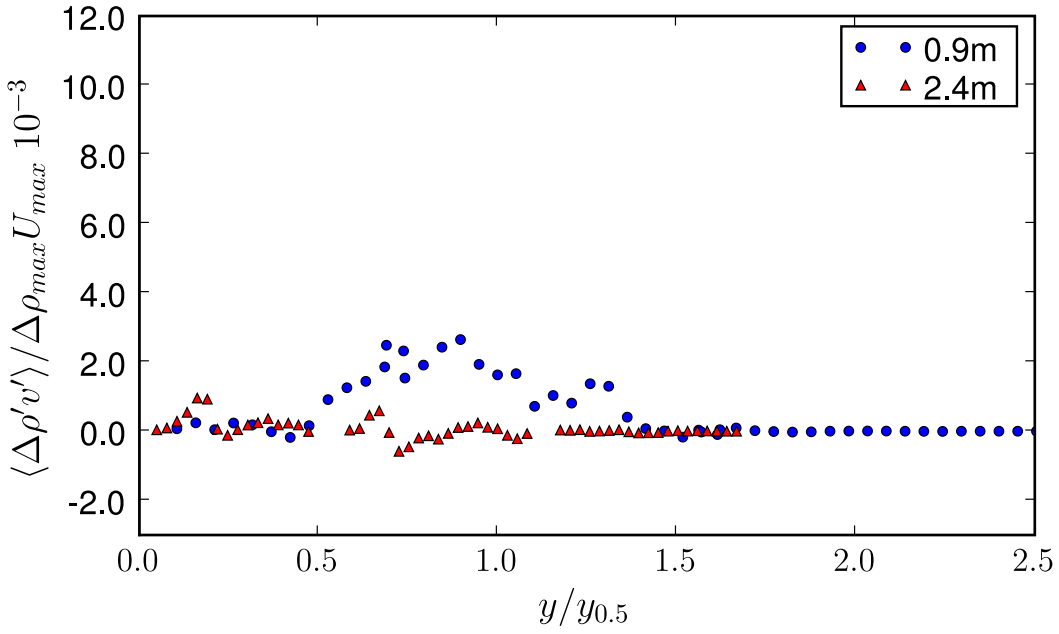

(b) Cross-stream Reynolds flux

Figure 3.28: Gravity current Reynolds flux profiles at 0,9 m **and** 2,4 m **(outer scaling): present research**

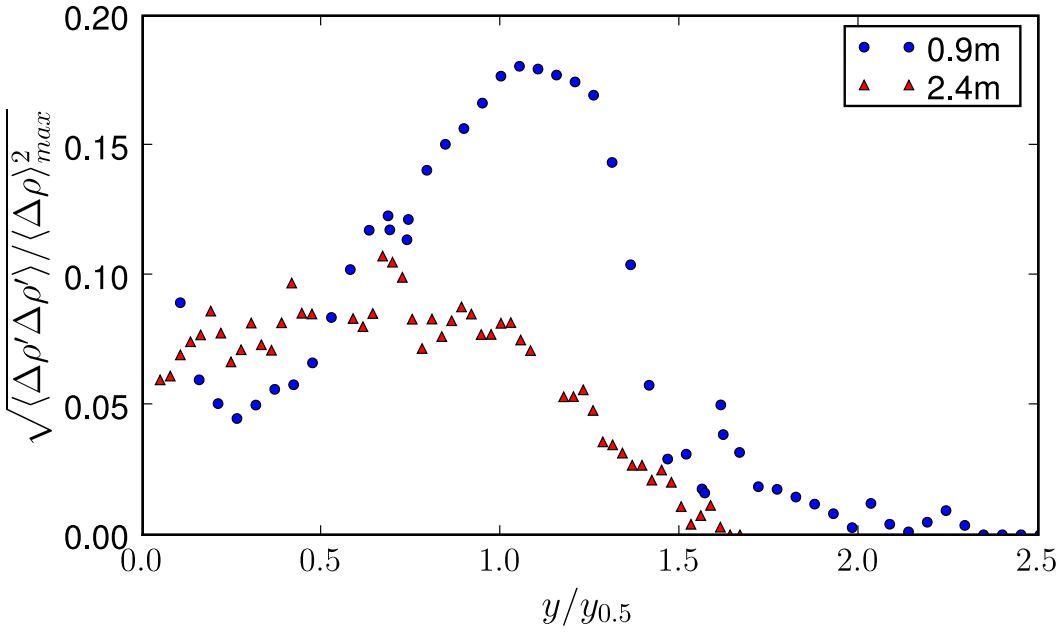

(a) Gravity current excess density intensity at 0,9 m and 2,4 m: present research

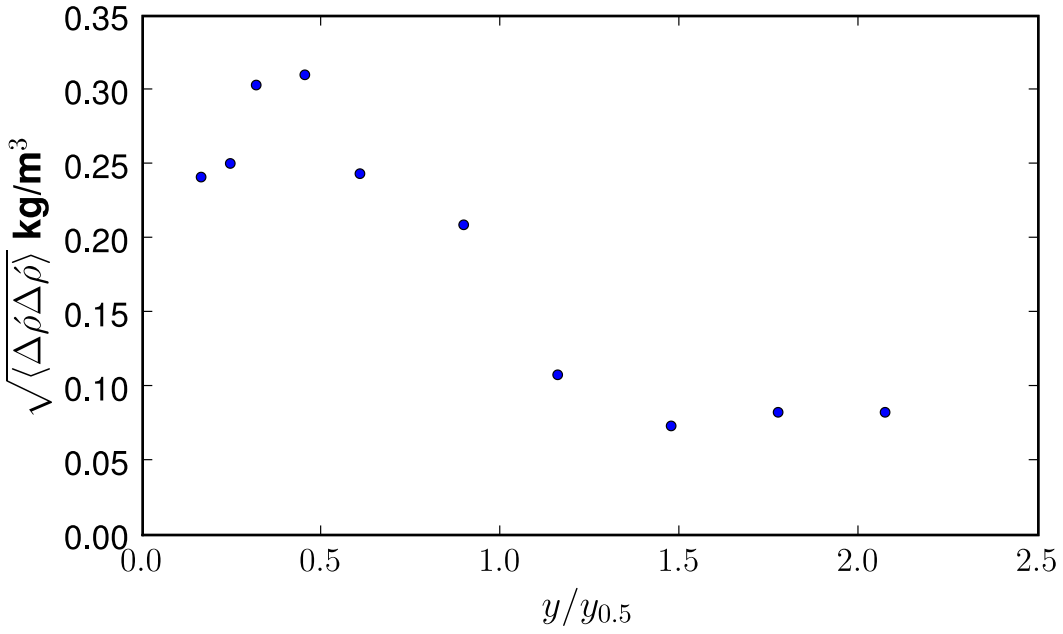

(b) Gravity current excess density standard deviation: Buckee *et al.* (2001)

Figure 3.29: Profiles of gravity current excess density intensity and standard deviation (outer scaling)

Buckee *et al.* (2001) found that for subcritical currents the greatest production of k occurred near the bed and above the velocity maximum due to shear. Figure 3.30b shows that shear production occurs primarily in the inner region. Furthermore, Buckee *et al.* (2001) reported regions of negative shear production. The present study does not reveal such a region.

3.3.8 Turbulent viscosity, diffusivity and Schmidt number

Figure 3.31a presents the measured turbulent viscosity ratio ν_t/ν profiles at 0,9 m and 2,4 m in outer scaling. The ν_t/ν profile at 2,4 m shows a greatly reduced outer peak and an inner peak. Figure 3.31b shows the inner peak at $y^+ = 50$. The maximum value of ν_t/ν, at the inner peak, is less than 20% of the inlet value. The profile shows that tubulence has collapsed. The laminar viscosity is of the same magnitude as the turbulent viscosity.

Figure 3.32a shows the turbulent diffusivity ratio γ_t/γ profiles at 0,9 m and 2,4 m in outer scaling. The scatter of the 2,4 m profile around a value of zero suggests that the turbulent diffusion of mass has become negligible within the gravity current. Furthermore, the turbulent Schmidt number profile in figure 3.32b also shows scatter between $-1 < \sigma_t < 2$. The scatter in the turbulent Schmidt number suggests that the flux-gradient hypothesis is no longer valid, due to the collapse of turbulence.

3.3.9 Energy spectra

Figure 3.33 presents the measured one-dimensional frequency based energy spectra, as well as the computed three-dimensional inertial subrange at $y/y_{0.5} = 0.47$. At low frequencies $< 0{,}5$ Hz, the measured $E_{uu}(f)$ spectrum dominates the measured $E_{vv}(f)$ spectrum, by a ratio of approximately 14 : 1. This large ratio indicates the anisotropy between the large, low frequency eddies. Figure 3.33 also shows the three-dimensional inertial subrange estimates $E(f, \epsilon_u)$ and $E(f, \epsilon_v)$, which were computed from equations 3.2.16 and 3.2.17. The two estimates, having a -5/3 slope, do not collapse, also indicating that the turbulence is anisotropic. Furthermore, the measured $E_{uu}(f)$ spectrum has a -5/3 slope only for frequencies between 0,2 Hz<f<1,0 Hz. This is a very narrow inertial subrange, which indicates that the Reynolds number, and hence turbulence, was very low.

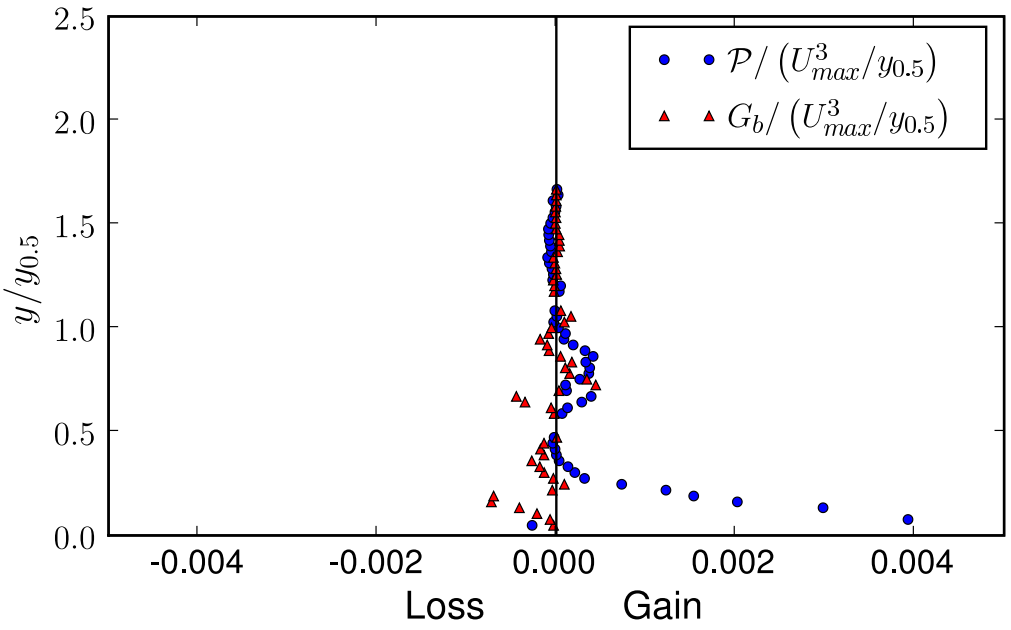

(a) outer scaling

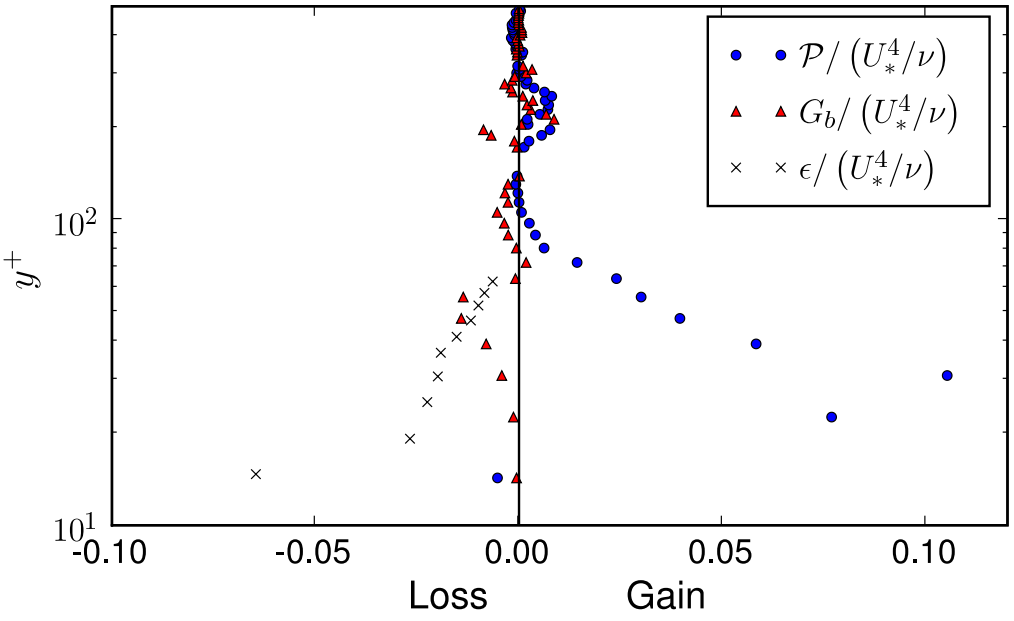

(b) inner scaling

Figure 3.30: Partial budget of turbulent kinetic energy: present research

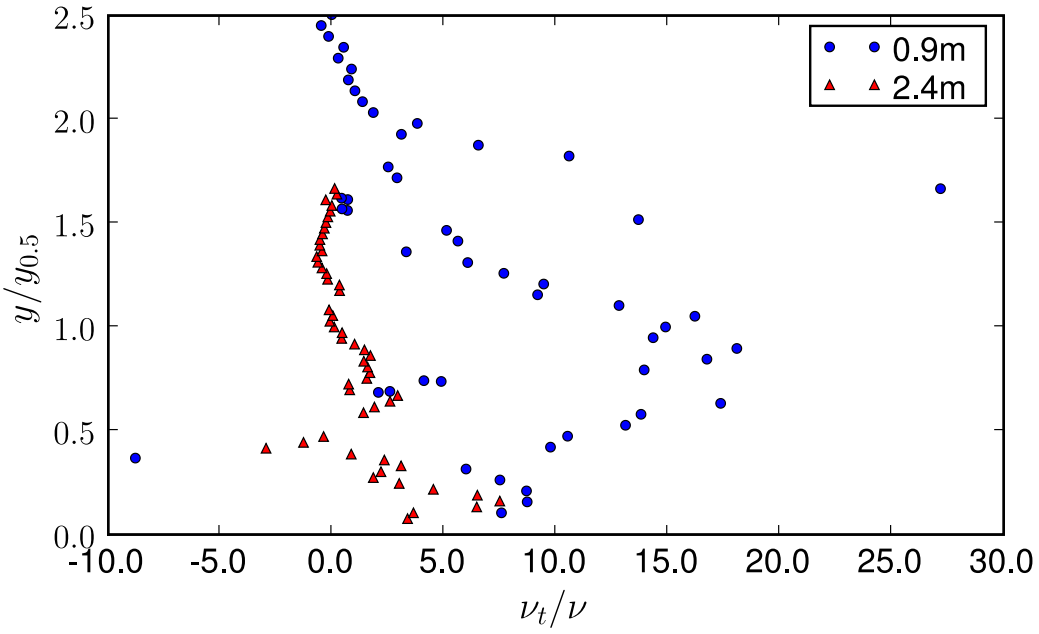

(a) outer scaling (at 0,9 m and 2,4 m)

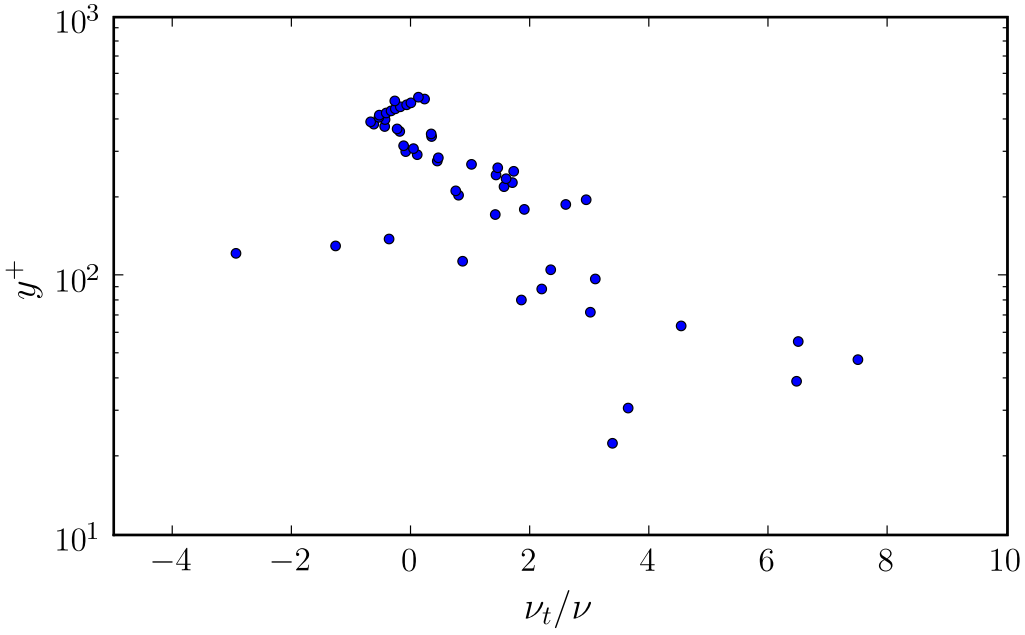

(b) inner scaling (at 2,4 m)

Figure 3.31: Turbulent viscosity ratio profiles: present research

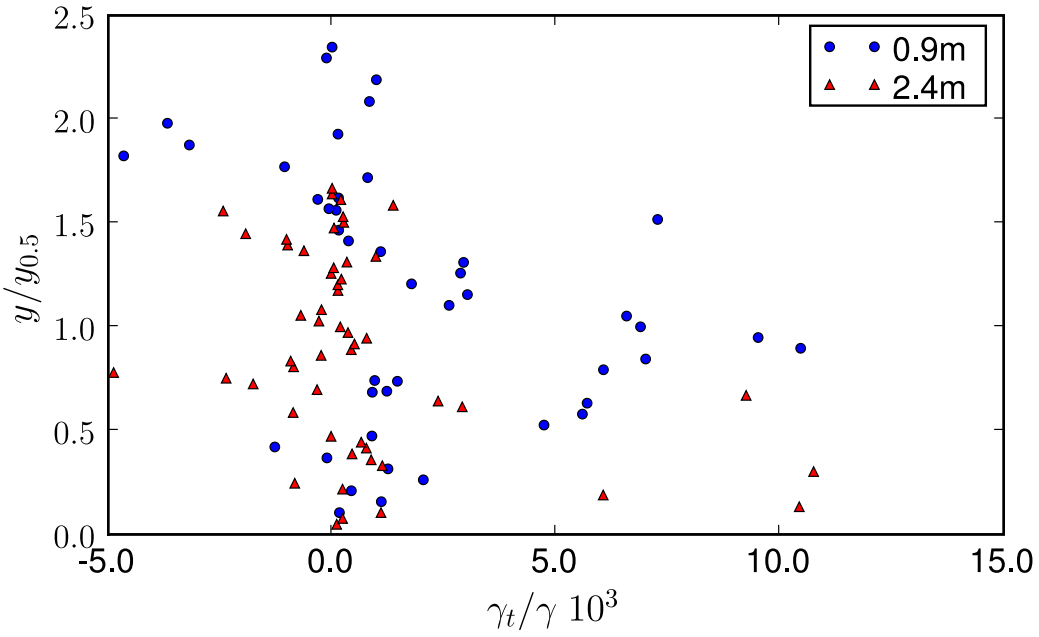

(a) Turbulent diffusivity (at 0,9 m and 2,4 m)

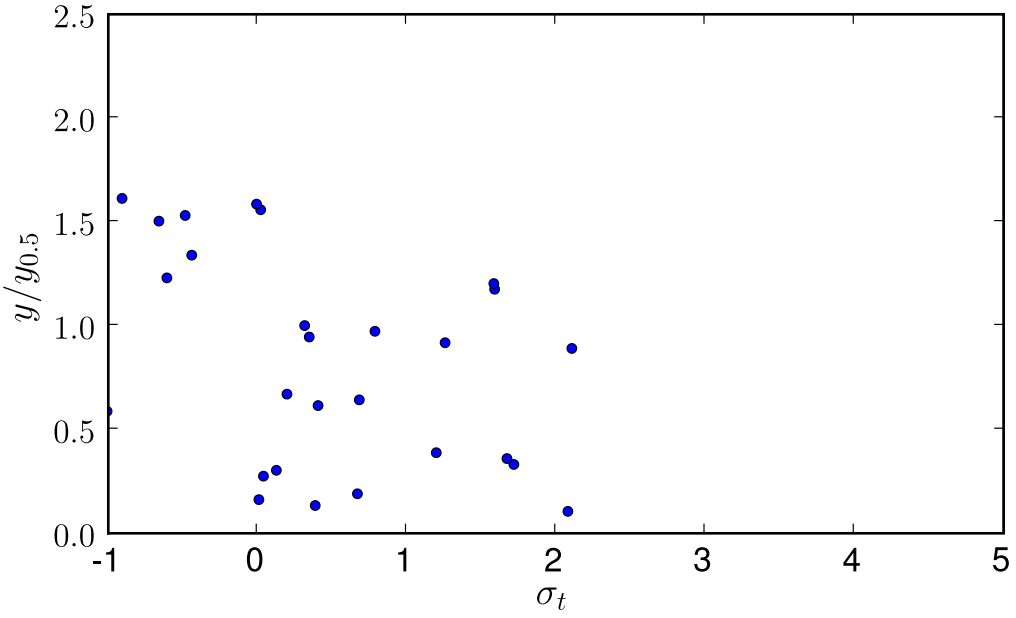

(b) Turbulent Schmidt number (at 2,4 m)

Figure 3.32: Turbulent diffusivity and Schmidt number profiles (outer scaling): present research

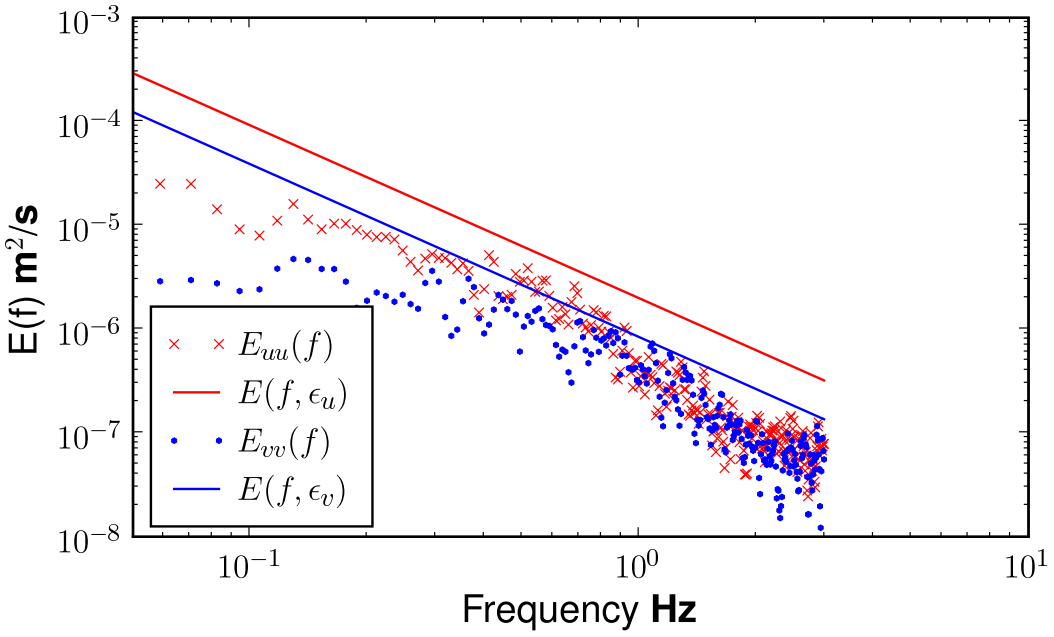

Figure 3.33: Energy spectra of u- and v-velocities at $y/y_{0.5} = 0.47$: present research

3.4 Summary

This chapter has presented the measurements of a horizontal, dilute saline gravity current. The inlet excess density difference was 2 kg/m^3. The saline gravity current was conservative in the sense that the depth-averaged excess density remained constant with downstream distance. Measurements were taken at the inlet and at 0,9 m and 2,4 m downstream from the inlet. The profiles, in particular the turbulence profiles, did not exhibit self-similarity at these locations, due to the continuous reduction of turbulence intensities by the stable density gradient. The gravity current dynamics were therefore comparable to the heated free surface jet studied by Hossain and Rodi (1977). The continuous reduction of turbulence intensities resulted in a reduction in turbulent mixing at the interface. Hence the stability of the interface increased, which was indicated by a bulk Richardson number which varied with downstream distance. At the inlet and 0,9 m downstream the bulk Richardson number was respectively 0,09 and 0,34, indicating that the current was supercritical. At a position 2,4 m from the inlet the bulk Richardson number was near critical, with a value of 0,88.

Profiles of mean velocity, mean excess density, Reynolds stresses, Reynolds

fluxes, excess density variance, shear production of turbulent kinetic energy, buoyancy production of turbulent kinetic energy, turbulent viscosity ratio, turbulent diffusivity ratio and turbulent Schmidt number were measured at downstream positions 0,9 m and 2,4 m from the inlet. Point measurements of energy spectra, near the top of the velocity maximum, were also taken at these downstream positions. Mean streamwise velocity measurements near the bed showed a log-law velocity distribution near the bed.

The spatial distribution of Reynolds stresses and fluxes were determined by measuring their profiles. Strong Reynolds stress anisotropy was measured at 0,9 m and 2,4 m. The heights of the gravity current Reynolds stress peaks at 0,9 m were similar to those of a neutrally-buoyant wall-jet (Eriksson *et al.*, 1998). The peak values differed from those of a wall-jet, due to the lack of self-similarity. The $\langle u'u' \rangle$ Reynolds stress profile showed a positive inner and outer peak. The $\langle v'v' \rangle$ Reynolds stress profile showed a single positive outer peak, while the $\langle u'v' \rangle$ Reynolds stress profile showed a positive outer peak and a negative inner peak. The outer peaks almost disappeared at a downstream position of 2,4 m, due to the collapse of turbulence in the outer region. The $\langle u'u' \rangle$ Reynolds stress profile showed a weak positive outer peak and a strong positive inner peak. The $\langle v'v' \rangle$ Reynolds stress profile showed a single positive inner peak, while the $\langle u'v' \rangle$ Reynolds stress profile showed a single negative inner peak. The shearing near the bed allowed the inner peaks to be sustained within the stable stratification. The Reynolds stress profiles suggest that k attains a local minimum at the velocity maximum; however, k does not become negligible there. For example, turbulence intensities at the velocity maximum at 0,9 m and 2,4 m were moderately high, ranging between 10% and 7%.

Energy spectra point measurements at 0,9 m and 2,4 m which were slightly above the velocity maximum also revealed the anisotropic turbulent momentum transport within the gravity current. Kneller *et al.* (1999) noted that the large scale, low frequency < 10 Hz eddies transported most of the turbulent kinetic energy within the gravity current. The energy spectra of the present research support this observation. The measured energy spectra also showed that the inertial subrange was fairly narrow at 0,9 m and 2,4 m, due to the low turbulence levels of the gravity current.

The heights of the gravity current Reynolds flux peaks at 0,9 m were similar to the those of a neutrally buoyant wall-jet (Ahlman, 2006). However, where the $\langle \theta'u' \rangle$ and $\langle \theta'v' \rangle$ peak values were more or less the same for the neutrally buoyant wall-jet, the $\langle \Delta\rho'u' \rangle$ and $\langle \Delta\rho'v' \rangle$ peak values differed significantly for the gravity current. Due to gravity, the $\langle \Delta\rho'v' \rangle$ Reynolds flux was significantly reduced. Hence the gravity current exhibited strong Reynolds flux anisotropy at 0,9 m. The $\langle \Delta\rho'u' \rangle$ Reynolds flux showed a small negative inner peak and a large positive outer peak.

The $\langle \Delta\rho' v' \rangle$ Reynolds flux showed a reduced positive outer peak. The Reynolds flux peaks were also strongly reduced at a position of 2,4 m, similar to the corresponding Reynolds stress peaks. The $\langle \Delta\rho' u' \rangle$ Reynolds flux profile shows a weak positive outer peak and negative inner peak. The $\langle \Delta\rho' v' \rangle$ shows a very small positive inner peak. The main original contribution of the present chapter is the quantification of the turbulent mass transport. To the author's knowledge no Reynolds flux profiles have been published for a gravity current. These profiles required the simultaneous measurement of density and velocity.

The influence of the stable stratification on the gravity current turbulence was determined by measuring profiles of gradient Richardson number, shear production of turbulent kinetic energy, buoyancy production of turbulent kinetic energy, turbulent viscosity ratio and turbulent diffusivity ratio.

According to Turner (1973) turbulence cannot be maintained when $Ri_g > 0.25$. The gradient Richardson number profile at 0,9 m showed values less than this critical value, except at the velocity maximum. This indicates that, except at the velocity maximum, shear production of turbulent kinetic energy was able to offset the negative buoyancy production and turbulence was maintained. The gradient Richardson number at 2,4 m showed values far exceeding the critical value, indicating that shear production was unable to offset buoyancy production, leading to a collapse of turbulence.

The turbulent viscosity ratio profile at 0,9 m showed a single outer peak, with a value less than half the inlet value. This indicated that turbulence had already been significantly reduced, due to stable stratification. At 2,4 m the outer peak has disappeared, but an inner peak remains with a magnitude less than 20% the inlet value. At this location the turbulent viscosity and kinematic viscosities were approximately equal, indicating very low levels of turbulence within the current. The turbulent diffusivity ratio at 0,9 m showed a single positive outer peak. At this location turbulent diffusivity overwhelmed molecular diffusivity by three to four orders of magnitude. At 2,4 m the turbulent diffusivity ratio profile is scattered around a value of zero, indicating that the turbulence is probably too low for the flux-gradient hypothesis to be used.

The shear and buoyancy production profiles at 0,9 m showed that shear production dominated over buoyancy production. The shear production profile had a positive outer and inner peak, while the buoyancy production profile had a single outer peak. For a small region near the bed local equilibrium of turbulent kinetic energy existed with $\mathcal{P} \approx \epsilon$. Furthermore, the shear and buoyancy production profiles at 2,4 m showed that the outer peaks had disappeared, due to the conditions indicated by the large gradient Richardson number. The shear production profile

still had a positive inner peak near the bed. The appearance of a small inner peak in buoyancy production prevented local equilibrium of turbulent kinetic energy in the near bed region. The shear production profiles did not reveal regions of negative production, in contrast to the findings of Buckee *et al.* (2001).

Excess density intensity profiles indicate the degree of turbulent mixing within the current. The profile at 0,9 m revealed a positive inner and outer peak. The large positive outer peak indicated that turbulent mixing was significant in the outer region of the current. At 2,4 m the outer peak had disappeared due to the collapse of turbulence. Hence the outer region was no longer the primary region of turbulent mixing.

Finally, although the present experimental configuration revealed how stable stratification influenced the gravity current turbulence it is probably not enough to draw definitive conclusions. It is therefore recommended that additional experimental studies be carried out with different inlet conditions and more measurement locations downstream of the inlet.

Chapter 4

Numerical model and results

Numerical models are important tools by means of which the evolution and impact of gravity currents may be studied. They are not limited to the scale restrictions of experimental studies. They are, however, limited by the underlying assumptions of the governing equations and the computational effort required to obtain the solution.

Gravity current models have to be derived from different mixture theories, depending on whether the density differences are caused by mixture inhomogeneities of different phases or of different species. Furthermore, different adaptations are required to theories in order to properly model the physical, chemical and biological behaviour of the mixture constituents. Saline gravity current models can be based on multispecies mixture theory, the mixture being composed of two unreactive species, namely H_2O and $NaCl$. Multispecies models usually consist of a continuity and momentum differential equation for the mixture and a mass fraction transport differential equation for each species.

Gravity current models also need to account for the transportive behaviour of turbulence under anisotropic, stratified conditions. Direct simulation of all the length and timescales occurring in a turbulent flow is far beyond the computational abilities of present day computers. Reynolds-averaging removes the small scale, high frequency turbulent fluctuations in the governing equations from the mean values. These Reynolds-averaged Navier-Stokes (RANS) models solve the Reynolds-averaged continuity, Navier-Stokes and scalar transport equations. They do not simulate the full spectrum of turbulence length and timescales, nor do they assume that the gravity current flow is self-similar. They are, therefore, more general than depth-averaged models, which assume self-similarity (Parker *et al.*,

1986).

Reynolds-averaging of the governing equations introduces second order moments, which accounts for the correlation between different fluctuating quantities. Closure is required for these second order moments in order to solve the Reynolds-averaged equations. Introduction of the Boussinesq and flux-gradient hypotheses, as well as a turbulence model, provides closure for these moments. The computational effort required by RANS models makes them practical for industrial use.

Historical numerical studies have focused on applying multispecies and multiphase RANS models on gravity current flows which are approximately self-similar. However, these models are able to model situations where the flow is not self-similar. For example, where an underflow separates from the bed and becomes an interflow or where the underflow accelerates/decelerates due to a change in bed slope. Few experimental data exist for evaluating the accuracy of this feature in RANS models. The previous chapter provides experimental data by which to evaluate the accuracy of the model under conditions where the turbulence structure of the gravity current was not self-similar.

This chapter presents a multispecies RANS gravity current model, the results of which are compared with the measurements of chapter 3. The first part of the chapter presents the governing equations, as well as the software used to solve these equations. This is followed by presentation of the turbulence models and boundary conditions used by the numerical model. The solution technique is then presented. It is shown that the solution is grid independent and properly converged. Furthermore, sensitivity analyses are performed on the turbulence models and various inlet conditions. Finally, the accuracy of the numerical model is evaluated against the experimental data of chapter 3.

4.1 Computational Fluid Dynamics software

The present research used the computational fluid dynamics (CFD) software package 'FLUENT' to compare the results of a numerical gravity current model with the measurements of chapter 3. The primary reason for using FLUENT was to avoid the time consuming necessity of developing a custom software code.

FLUENT is a computer program which can model fluid flow and heat transfer in complex geometries using the finite volume method. The FLUENT package contains: FLUENT the computer program, Gambit a preprocessor for geometry

modelling and mesh generation, as well as TGrid an additional preprocessor, which generates volume meshes from boundary meshes. The first version of FLUENT was launched in 1983 and the present version is FLUENT 6.3 (2007). It is developed under a quality management system which is ISO 9001:2000 and TickIT registered. The software package comes with extensive technical support, primarily through an online User Services Centre. The User Services Centre provides product documentation (Getting started guide, User guide, Tutorial guide and User-defined function manual), online forums, online searches of previous solutions and online request forms.

The features of FLUENT the program include:

- Modelling of steady and unsteady flows in two-dimensional and three-dimensional geometries.
- Modelling of incompressible and compressible flow.
- Modelling of inviscid flow, laminar flow and turbulent flow (turbulence models include: $k - \epsilon$ models, Reynolds Stress Models (RSM), Detached Eddy Simulation (DES) and Large Eddy Simulation (LES)).
- Modelling of near-wall regions with wall-functions or a two-layer approach.
- Modelling of species transport and chemical reactions.
- Modelling of multiphase flows (multiphase models include: Eulerian model, mixture model and discrete phase model).
- Unstructured grid technology for meshes which contain elements of various shapes.
- Dynamic meshing for modelling domains with deforming and sliding meshes.
- Extensive postprocessing capabilities (text output, line plots, contour plots, vector plots and animations).
- User-defined functions can be programmed in C by the user to customize FLUENT (for example, material properties and boundary conditions).

The steps involved in creating and solving the gravity current model with the FLUENT package are:

1. Start the preprocessor, Gambit

2. Define the flow domain and create the mesh
3. Exit Gambit and start the program FLUENT
4. Load the mesh and user-defined functions into FLUENT
5. Set up the solver (2D, unsteady, time-discretization scheme)
6. Set up the operating conditions (specify the gravity vector, reference pressure and reference density)
7. Set up the multispecies model (specify the materials and their properties, such as density and viscosity)
8. Set up the turbulence model (specify the model and empirical coefficients, specify the near-wall treatment)
9. Set up the boundary conditions (specify the conditions at the inlet, outlet and walls)
10. Set up the residuals (residual type and minimum acceptable value for convergence)
11. Set up the pressure-velocity coupling algorithm and spatial discretization schemes for the solution variables
12. Initialize the solution (specify initial values for the solution variables)
13. Specify the time-step size, number of time-steps and maximum number of iterations per time-step
14. Solve the governing equations for each time-step
15. Plot and save the results

4.2 Governing equations for a multispecies mixture

Gravity currents are driven primarily by gravity acting on a density difference between the current itself and its surroundings. The density difference can be caused by either thermal inhomogeneities or mixture composition inhomogeneities. The density difference of the gravity current measured in chapter 3 was due to composition inhomogeneities of different chemical species ($NaCl$ and H_2O).

Table 4.1 presents the definitions used by a general multispecies mixture model. The model comprises a mixture continuity equation, a mixture momentum equation and $N-1$ mass fraction ω_α transport equations for the N species occurring in the mixture. The last mass fraction N is calculated from the mass fraction constraint given in table 4.1. In addition to these governing equations, two constitutive equations relate mixture density and mixture viscosity to species mass fraction. Finally, a turbulence model is linked to the mixture model to provide closure for the Reynolds stresses and Reynolds fluxes occurring in the mixture momentum and species mass fraction transport equations.

The saline gravity current measured in chapter 3 was a two species mixture, without any chemical reactions. The species were H_2O and $NaCl$. The composition of this mixture can be expressed simply in terms of $NaCl$ mass fraction ω (the mass fraction of the only other species H_2O is $1-\omega$).

$\alpha = 1...N$	Species index
ω_α	Mass fraction of species α (mass of α per unit mass of mixture)
$\sum_1^N \omega_\alpha = 1$	Mixture mass fractions constraint
$\rho_\alpha = \rho\omega_\alpha$	Mass density of species α (mass of α, per unit volume of mixture)
$\rho = \sum_{\alpha=1}^N \rho_\alpha$	Mass density of mixture (mass of mixture, per unit volume of mixture)
$\bar{u}_\alpha$	Velocity of species α (with respect to fixed coordinates)
$\bar{u} = \sum_{\alpha=1}^N \omega_\alpha \bar{u}_\alpha$	Velocity of mixture (with respect to fixed coordinates)
$\bar{j}_\alpha = \rho_\alpha (\bar{u}_\alpha - \bar{u})$	Diffusive flux of species α

Table 4.1: Definitions of multispecies mixture variables (Bird *et al.*, 2002)

4.2.1 Continuity equation for species α

Consider a material volume, which may be considered to be a deformable volume, moving with the flow always containing the same fluid particles. From this Lagrangean viewpoint the mass within the material volume cannot change with time

$$\frac{d}{dt}\int_{V(t)} \rho_\alpha dV = 0 \tag{4.2.1}$$

where t is time, V is the volume of the material volume at time t, ρ_α is the instantaneous density of species α. Substituting the Leibniz theorem (equation C.3.3) gives

$$\int_{V(t)} \frac{\partial \rho_\alpha}{\partial t} dV + \int_{A(t)} \rho_\alpha \bar{n} \cdot \bar{u}_\alpha dA = 0 \tag{4.2.2}$$

where $\bar{n}$ is the normal vector of the surface of the material volume, A is the surface of the material volume at time t and $\bar{u}_\alpha$ is the velocity of species α. Substituting the Gauss divergence theorem (equation C.1.1) gives

$$\int_{V(t)} \left[\frac{\partial \rho_\alpha}{\partial t} + \bar{\nabla} \cdot (\rho_\alpha \bar{u}_\alpha) \right] dV = 0 \tag{4.2.3}$$

For an arbitrary control volume the integral value can only be zero if the integrand is zero and hence

$$\frac{\partial \rho_\alpha}{\partial t} + \bar{\nabla} \cdot (\rho_\alpha \bar{u}_\alpha) = 0 \tag{4.2.4}$$

Equation 4.2.4 is the general continuity equation of species α. A more practical form can be derived as follows: Substituting the definition of $\bar{j}_\alpha$ (table 4.1) into equation 4.2.4 gives

$$\frac{\partial \rho_\alpha}{\partial t} + \bar{\nabla} \cdot (\rho_\alpha \bar{u}) + \bar{\nabla} \cdot \bar{j}_\alpha = 0 \tag{4.2.5}$$

Substituting the definition of ρ_α (table 4.1) into equation 4.2.5 gives

$$\frac{\partial \rho \omega_\alpha}{\partial t} + \bar{\nabla} \cdot (\rho \omega_\alpha \bar{u}) + \bar{\nabla} \cdot \bar{j}_\alpha = 0 \tag{4.2.6}$$

Substituting Fick's first law of molecular diffusion

$$\bar{j}_\alpha = -\rho \gamma \bar{\nabla} \omega_\alpha \tag{4.2.7}$$

into equation 4.2.6 gives

$$\frac{\partial \rho \omega_\alpha}{\partial t} + \bar{\nabla} \cdot (\rho \omega_\alpha \bar{u}) = \bar{\nabla} \cdot \left(\rho \gamma \bar{\nabla} \omega_\alpha \right) \tag{4.2.8}$$

where γ is the molecular diffusion coefficient of species α in water. In the case of $NaCl$ in water $\gamma = 1{,}61 \times 10^{-9}$. Equation 4.2.8 is the continuity equation for species α, assuming Fickian diffusion (FLUENT 6.3, pg. 14-3).

4.2.1.1 Dilute approximation

The gravity current measured in chapter 3 is a dilute mixture $\Delta\rho/\rho_w \ll 1$, since the maximum excess density difference ($\Delta\rho = 2\,\mathrm{kg/m^3}$) is very small compared to the

density of the ambient water ($\rho_w = 998{,}2364\,\mathrm{kg/m^3}$). This allows equation 4.2.8 to be simplified as follows: Substituting the first two terms with the total derivative gives

$$\rho \frac{D\omega_\alpha}{D\,t} = \bar{\nabla} \cdot \left(\rho\gamma\bar{\nabla}\omega_\alpha\right) \tag{4.2.9}$$

Decomposing the mixture density into a constant reference density ρ_w and an excess density $\Delta\rho$

$$\rho = \rho_w + \Delta\rho \tag{4.2.10}$$

and substituting the decomposition into equation 4.2.9 gives

$$\left(\rho_w + \Delta\rho\right) \frac{D\omega_\alpha}{D\,t} = \bar{\nabla} \cdot \left[\left(\rho_w + \Delta\rho\right)\gamma\bar{\nabla}\omega_\alpha\right] \tag{4.2.11}$$

Dividing by the reference density ρ_w gives

$$\left(1 + \frac{\Delta\rho}{\rho_w}\right) \frac{D\omega_\alpha}{D\,t} = \bar{\nabla} \cdot \left[\left(1 + \frac{\Delta\rho}{\rho_w}\right)\gamma\bar{\nabla}\omega_\alpha\right] \tag{4.2.12}$$

Equation 4.2.12 shows for dilute mixtures $\Delta\rho/\rho_w \ll 1$, density variations are negligible. Hence the density of the mixture ρ in equation 4.2.8 may be replaced with the reference density ρ_w giving

$$\frac{\partial\rho_w\omega_\alpha}{\partial t} + \bar{\nabla} \cdot \left(\rho_w\omega_\alpha\bar{u}\right) = \bar{\nabla} \cdot \left(\rho_w\gamma\bar{\nabla}\omega_\alpha\right) \tag{4.2.13}$$

But since ρ_w is constant, equation 4.2.13 reduces to

$$\frac{\partial\omega_\alpha}{\partial t} + \bar{\nabla} \cdot \left(\omega_\alpha\bar{u}\right) = \bar{\nabla} \cdot \left(\gamma\bar{\nabla}\omega_\alpha\right) \tag{4.2.14}$$

Equation 4.2.14 is the continuity equation for species α, assuming Fickian diffusion and dilute mixtures (Rodi, 1980, pg. 5).

4.2.2 Continuity equation of the mixture

Summation of all N species continuity equations (equation 4.2.4) gives the continuity equation for the mixture

$$\sum_{\alpha=1}^{N} \frac{\partial\rho_\alpha}{\partial t} + \sum_{\alpha=1}^{N} \bar{\nabla} \cdot \left(\rho_\alpha\bar{u}_\alpha\right) = 0 \tag{4.2.15}$$

$$\frac{\partial}{\partial t}\sum_{\alpha=1}^{N} \rho_\alpha + \bar{\nabla} \cdot \sum_{\alpha=1}^{N} \left(\rho_\alpha\bar{u}_\alpha\right) = 0 \tag{4.2.16}$$

Substitution of the definitions of the mixture density and mixture velocity (table 4.1) gives

$$\frac{\partial \rho}{\partial t} + \bar{\nabla} \cdot (\rho \bar{u}) = 0 \tag{4.2.17}$$

Equation 4.2.17 is the general continuity equation for compressible and incompressible flows (FLUENT 6.3, pg. 9-3), (Bird *et al.*, 2002).

4.2.2.1 Incompressible approximation

The gravity current measured in chapter 3 occurred at a very low Mach number, $u/a \ll 0{,}1$, since the maximum velocity ($u \approx 0{,}05\,\mathrm{m/s}$) is very small compared to the speed of sound in water ($a \approx 1500\,\mathrm{m/s}$). Hence the flow can be treated as being incompressible. This allows equation 4.2.17 to be simplified as follows: Expanding the divergence term and substituting the total derivative gives

$$\frac{\partial \rho}{\partial t} + \bar{u} \cdot \bar{\nabla} \rho + \rho \bar{\nabla} \cdot \bar{u} = 0 \tag{4.2.18}$$

$$\frac{D\,\rho}{D\,t} + \rho \bar{\nabla} \cdot \bar{u} = 0 \tag{4.2.19}$$

where $\frac{D\rho}{Dt}$ is the rate of change of density for a fluid particle that moves with the flow. Since the flow is incompressible $\frac{D\rho}{Dt} = 0$ and the continuity equation of the mixture simplifies to the kinematic condition

$$\bar{\nabla} \cdot \bar{u} = 0 \tag{4.2.20}$$

Equation 4.2.20 is the general continuity equation for incompressible flows (Rodi, 1980, pg. 5).

4.2.3 Momentum equation of the mixture

Consider a material volume, which may be considered to be a deformable volume moving with the flow always containing the same fluid particles. From this Lagrangean viewpoint the rate of change of momentum of the material volume is equal to the net surface and body forces acting on it

$$\frac{d}{dt} \int_{V(t)} \rho \bar{u} dV = \int_{A(t)} \bar{n} \cdot \left(-p^* \bar{\bar{I}} + \bar{\bar{\tau}} \right) dA + \int_{V(t)} \rho \bar{g} dV \tag{4.2.21}$$

where t is time, V is the volume of the material volume at time t, ρ is the instantaneous density of the mixture, $\bar{u}$ is the instantaneous mass-averaged velocity vector

of the mixture, A is the surface of the material volume, $\bar{n}$ is the normal vector of the material volume surface, p^* is the absolute instantaneous pressure, $\bar{\bar{I}}$ is the identity tensor, $\bar{\bar{\tau}}$ is the instantaneous viscous stress tensor and $\bar{g}$ is the gravity acceleration vector.

The viscous stress tensor $\bar{\bar{\tau}}$ is proportional to the sum of the instantaneous rate-of-strain tensor $\bar{\bar{s}}$ and the volumetric deformation rate $\bar{\nabla} \cdot \bar{u}$.

$$\bar{\bar{\tau}} = \mu \left[2\bar{\bar{s}} - \frac{2}{3} \left(\bar{\nabla} \cdot \bar{u} \right) \bar{\bar{I}} \right] \tag{4.2.22}$$

with

$$\bar{\bar{s}} = \frac{1}{2} \left[\bar{\nabla}\bar{u} + \left(\bar{\nabla}\bar{u} \right)^T \right] \tag{4.2.23}$$

where μ is the dynamic viscosity of the mixture and T is the transpose of a tensor.

Substituting the Leibniz theorem (equation C.3.3) into equation 4.2.21 gives

$$\int_{V(t)} \frac{\partial \rho \bar{u}}{\partial t} dV + \int_{A(t)} \bar{n} \cdot \rho \bar{u} \bar{u} dA = \int_{A(t)} \bar{n} \cdot \left(-p^* \bar{\bar{I}} + \bar{\bar{\tau}} \right) dA + \int_{V(t)} \rho \bar{g} dV \tag{4.2.24}$$

Substituting the Gauss divergence theorem (equation C.1.1) gives

$$\int_{V(t)} \left[\frac{\partial \rho \bar{u}}{\partial t} + \bar{\nabla} \cdot \rho \bar{u} \bar{u} + \bar{\nabla} \cdot \left(p^* \bar{\bar{I}} - \bar{\bar{\tau}} \right) - \rho \bar{g} \right] dV = \bar{0} \tag{4.2.25}$$

Finally, for an arbitrary control volume the integral value can only be zero if the integrand is zero and hence

$$\frac{\partial \rho \bar{u}}{\partial t} + \bar{\nabla} \cdot \rho \bar{u} \bar{u} = \bar{\nabla} \cdot \left(-p^* \bar{\bar{I}} + \bar{\bar{\tau}} \right) + \rho \bar{g} \tag{4.2.26}$$

Equation 4.2.26 is the general momentum equation for compressible and incompressible flows (FLUENT 6.3, pg. 9-4).

4.2.3.1 The Boussinesq approximation

The gravity current measured in chapter 3 is a dilute mixture $\Delta\rho/\rho_w \ll 1$. This allows equation 4.2.26 to be simplified as follows: Expansion of the left-hand side gives

$$\bar{u} \left[\frac{\partial \rho}{\partial t} + \bar{\nabla} \cdot (\rho \bar{u}) \right] + \rho \left[\frac{\partial \bar{u}}{\partial t} + \bar{u} \cdot \bar{\nabla} \bar{u} \right] = -\bar{\nabla} p^* + \bar{\nabla} \cdot \bar{\bar{\tau}} + \rho \bar{g} \tag{4.2.27}$$

Which simplifies, when substituting the general continuity equation (equation 4.2.17) into the first term on the left-hand side and taking the total derivative of the second term

$$\rho \frac{D\,\bar{u}}{D\,t} = -\bar{\nabla} p^* + \bar{\nabla} \cdot \bar{\bar{\tau}} + \rho \bar{g} \tag{4.2.28}$$

By defining hydrostatic equilibrium as a reference state ($\bar{u} = \bar{0}$), equation 4.2.28 becomes

$$\bar{0} = -\bar{\nabla} p_r + \rho_w \bar{g} \tag{4.2.29}$$

Decomposing the mixture density into a constant reference density ρ_w and an excess density $\Delta\rho$

$$\rho = \rho_w + \Delta\rho \tag{4.2.30}$$

and similarly for pressure

$$p^* = p_r + p \tag{4.2.31}$$

followed by substitution into eq. 4.2.28 gives

$$(\rho_w + \Delta\rho) \frac{D\bar{u}}{D\,t} = -\bar{\nabla} (p_r + p) + \bar{\nabla} \cdot \bar{\bar{\tau}} + (\rho_w + \Delta\rho)\, \bar{g} \tag{4.2.32}$$

Substitution of equation 4.2.29 gives

$$(\rho_w + \Delta\rho) \frac{D\bar{u}}{D\,t} = -\bar{\nabla} p + \bar{\nabla} \cdot \bar{\bar{\tau}} + \Delta\rho \bar{g} \tag{4.2.33}$$

Dividing by the reference density ρ_w gives

$$\left(1 + \frac{\Delta\rho}{\rho_w}\right) \frac{D\bar{u}}{D\,t} = \frac{1}{\rho_w} \bar{\nabla} \cdot \left(-p\bar{\bar{I}} + \bar{\bar{\tau}}\right) + \frac{\Delta\rho}{\rho_w} \bar{g} \tag{4.2.34}$$

Equation 4.2.34 shows that for dilute mixtures $\Delta\rho/\rho_w \ll 1$, the inertial force term is relatively unaffected by density variations, contrary to the last term (the body force term) (Turner, 1973, pg. 9). The Boussinesq approximation is used when the density variations in the inertial force term are neglected, but not those in the body force term:

$$\frac{D\bar{u}}{D\,t} = \frac{1}{\rho_w} \bar{\nabla} \cdot \left(-p\bar{\bar{I}} + \bar{\bar{\tau}}\right) + \frac{\Delta\rho}{\rho_w} \bar{g} \tag{4.2.35}$$

Equation 4.2.35 is the momentum equation for dilute mixtures, based on the Boussinesq approximation (Rodi, 1980, pg. 5).

4.2.4 Reynolds-averaging of the governing equations

The solution of equations 4.2.8, 4.2.17 and 4.2.26 on a computational grid fine enough to resolve the smallest turbulent length and timescales is far beyond the

memory and processing capabilities of present day computers. Instead, the mean is taken from these equations, which removes the small scale, high frequency fluctuations. This results in a modified set of equations which are computationally less expensive to solve. Reynolds (1894) proposed to decompose instantaneous quantities into mean values and fluctuating values as follows (Pope, 2001, pg. 83):

$$\bar{u} = \bar{U} + \bar{u}' \tag{4.2.36}$$
$$p = P + p' \tag{4.2.37}$$
$$\omega_\alpha = \langle \omega_\alpha \rangle + \omega'_\alpha \tag{4.2.38}$$
$$\Delta\rho = \langle \Delta\rho \rangle + \Delta\rho' \tag{4.2.39}$$

where the instantaneous values are given by the left-hand side of equations 4.2.36 to 4.2.39, the mean values by the first term on the right hand-side and the fluctuating values by the second term on the right-hand side. Furthermore, the mean of the fluctuating values is equal to zero (Pope, 2001, pg. 42)

$$\langle \bar{u}' \rangle = \bar{0} \tag{4.2.40}$$
$$\langle p' \rangle = 0 \tag{4.2.41}$$
$$\langle \omega'_\alpha \rangle = 0 \tag{4.2.42}$$
$$\langle \Delta\rho' \rangle = 0 \tag{4.2.43}$$

In statistically stationary flows the mean can be estimated from the time average, for example

$$\bar{U} = \lim_{T\to\infty} \frac{1}{T} \int_{t_0}^{t_0+T} \bar{u}\, dt \tag{4.2.44}$$

where T is the integration time, which is large with respect to the timescale of the turbulent fluctuations. In statistically non-stationary flows the mean can be estimated from the ensemble average, for example

$$\bar{U} = \frac{1}{N} \sum_{i=1}^{N} \bar{u} \tag{4.2.45}$$

where N is the number of independent, identically distributed realizations. In the present research Reynolds averaging is applied to the simplified governing equations 4.2.14, 4.2.20 and 4.2.35. These equations assume that the mixture is dilute. Their non-linear terms contain only constant reference densities, which avoids the derivation of density correlations when applying Reynolds averaging. Taking the mean of equations 4.2.14, 4.2.20 and 4.2.35, followed by substitution of equations 4.2.36, 4.2.37, 4.2.38 and 4.2.39 into terms representing means of products of $\bar{u}$, p, ω_α and $\Delta\rho$ gives the following Reynolds-averaged equations

4.2.5 Continuity equation for species α: Reynolds-averaged

Taking the mean of equation 4.2.14 gives

$$\frac{\partial\langle\omega_\alpha\rangle}{\partial t} + \bar{\nabla}\cdot(\langle\omega_\alpha\bar{u}\rangle) = \bar{\nabla}\cdot\left(\gamma\bar{\nabla}\langle\omega_\alpha\rangle\right) \tag{4.2.46}$$

Substituting equation 4.2.36 and 4.2.38 into the second term on the left-hand side gives

$$\frac{\partial\langle\omega_\alpha\rangle}{\partial t} + \bar{\nabla}\cdot\left(\langle\omega_\alpha\rangle\bar{U}\right) = \bar{\nabla}\cdot\left[\gamma\bar{\nabla}\langle\omega_\alpha\rangle - \langle\omega'_\alpha\bar{u}'\rangle\right] \tag{4.2.47}$$

where $\langle\omega'_\alpha\bar{u}'\rangle$ is the Reynold flux. Equation 4.2.47 is the Reynolds-averaged continuity equation of species α, assuming Fickian diffusion and dilute mixtures (Rodi, 1980, pg. 6).

The relationship between the Reynolds fluxes $\langle\omega'\bar{u}'\rangle$ (used in this chapter) and $\langle\Delta\rho'\bar{u}'\rangle$ (used in chapter 3) is obtained as follows: Noting that the density equation 2.4.1 is linear

$$\rho = 711{,}8182\omega + \rho_w \tag{4.2.48}$$

and rewriting equation 4.2.48 in terms of excess density

$$\Delta\rho = \rho - \rho_w = 711{,}8182\omega \tag{4.2.49}$$

Furthermore, decomposing the instantaneous excess density $\Delta\rho$ into mean $\langle\Delta\rho\rangle$ and fluctuation $\Delta\rho'$ values

$$\Delta\rho' = \Delta\rho - \langle\Delta\rho\rangle \tag{4.2.50}$$

followed by dividing by a constant gives

$$\frac{\Delta\rho'}{711{,}8182} = \frac{\Delta\rho}{711{,}8182} - \langle\frac{\Delta\rho}{711{,}8182}\rangle \tag{4.2.51}$$

Substitution of equation 4.2.49 gives

$$\frac{\Delta\rho'}{711{,}8182} = \omega - \langle\omega\rangle = \omega' \tag{4.2.52}$$

Hence the relationship between the Reynolds fluxes $\langle\omega'\bar{u}'\rangle$ and $\langle\Delta\rho'\bar{u}'\rangle$ is simply

$$\langle\omega'\bar{u}'\rangle = \langle\left(\frac{\Delta\rho}{711{,}8182}\right)'\bar{u}'\rangle = \frac{\langle\Delta\rho'\bar{u}'\rangle}{711{,}8182} \tag{4.2.53}$$

Similarly, the relationship between $\langle\omega'\omega'\rangle$ and $\langle\Delta\rho'\Delta\rho'\rangle$ is given by

$$\langle\omega'\omega'\rangle = \frac{\langle\Delta\rho'\Delta\rho'\rangle}{711{,}8182^2} \tag{4.2.54}$$

4.2.6 Continuity equation of the mixture: Reynolds-averaged

Taking the mean of equation 4.2.20, followed by substitution of equation 4.2.40 gives

$$\bar{\nabla} \cdot \bar{U} = 0 \tag{4.2.55}$$

$$\bar{\nabla} \cdot \bar{u}' = 0 \tag{4.2.56}$$

Equation 4.2.55 is the Reynolds-averaged continuity equation for incompressible flows (Rodi, 1980, pg. 6).

4.2.7 Momentum equation of the mixture: Reynolds-averaged

Expanding the total derivative of equation 4.2.35, followed by substituting equation 4.2.20, gives

$$\frac{\partial \bar{u}}{\partial t} + \bar{\nabla} \cdot (\bar{u}\bar{u}) = \frac{1}{\rho_w} \bar{\nabla} \cdot \left(-p\bar{\bar{I}} + \bar{\bar{\tau}} \right) + \frac{\Delta\rho}{\rho_w} \bar{g} \tag{4.2.57}$$

Taking the mean gives

$$\frac{\partial \bar{U}}{\partial t} + \bar{\nabla} \cdot \langle \bar{u}\bar{u} \rangle = \frac{1}{\rho_w} \bar{\nabla} \cdot \left(-P\bar{\bar{I}} + \langle \bar{\bar{\tau}} \rangle \right) + \frac{\langle \Delta\rho \rangle}{\rho_w} \bar{g} \tag{4.2.58}$$

with the mean viscous stress tensor and mean linear deformation rate tensor defined as

$$\langle \bar{\bar{\tau}} \rangle = 2\mu \bar{\bar{S}} \qquad \bar{\bar{S}} = \frac{1}{2} \left[\bar{\nabla}\bar{U} + \left(\bar{\nabla}\bar{U} \right)^T \right] \tag{4.2.59}$$

Substitution of equation 4.2.36 into the second term on the left-hand side of equation 4.2.58 gives

$$\frac{\partial \bar{U}}{\partial t} + \bar{\nabla} \cdot \left(\bar{U}\bar{U} \right) + \bar{\nabla} \cdot \langle \bar{u}'\bar{u}' \rangle = \frac{1}{\rho_w} \bar{\nabla} \cdot \left(-P\bar{\bar{I}} + \langle \bar{\bar{\tau}} \rangle \right) + \frac{\langle \Delta\rho \rangle}{\rho_w} \bar{g} \tag{4.2.60}$$

Using equation 4.2.55 to obtain the total derivative from the first two terms on the left-hand side gives

$$\frac{D\,\bar{U}}{D\,t} = \frac{1}{\rho_w} \bar{\nabla} \cdot \left(-P\bar{\bar{I}} + \langle \bar{\bar{\tau}} \rangle - \rho_w \langle \bar{u}'\bar{u}' \rangle \right) + \frac{\langle \Delta\rho \rangle}{\rho_w} \bar{g} \tag{4.2.61}$$

where $-\rho_w \langle \bar{u}'\bar{u}' \rangle$ is the Reynolds stress tensor. Equation 4.2.61 is the Reynolds-averaged momentum equation for dilute mixtures, based on the Boussinesq approximation (Rodi, 1980, pg. 6).

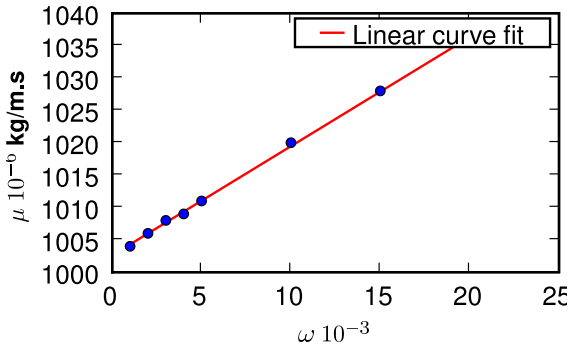

Figure 4.1: Dynamic viscosity dependence on $NaCl$ mass fraction (CRC handbook of chemistry and physics, pg. 8-73)

4.2.8 Density and viscosity equations

In addition to the three governing equations (equations 4.2.47, 4.2.55 and 4.2.61), two equations relating density and viscosity to $NaCl$ mass fraction ω are also required. Figure 2.11a presented experimental data on the relationship between mixture density and $NaCl$ mass fraction (CRC handbook of chemistry and physics, pg. 8-73), from which the following least-squares line fit was derived

$$\rho = 711.8182\omega + 998.2364 \tag{4.2.62}$$

where ω is the instantaneous $NaCl$ mass fraction. Appendix B.1 presents the FLUENT source code for equation 2.4.1

Figure 4.1 presents experimental data on the relationship between mixture dynamic viscosity and $NaCl$ mass fraction (CRC handbook of chemistry and physics, pg. 8-73). A least-squares line fit to this data gives

$$\mu = 0.001685\omega + 0.001003 \tag{4.2.63}$$

Appendix B.2 presents the FLUENT source code for equation 4.2.63.

4.3 Turbulence Model

The previous section presented the governing equations for a general multispecies mixture model. Chapter 3 showed the measured gravity current to be a negatively buoyant, stably stratified, horizontal 2D boundary-layer type flow. The boundary-layer form of equations 4.2.47, 4.2.55 and 4.2.61 can be derived by neglecting the

insignificant terms through an order-of-magnitude analysis. The reader is refered to Parker *et al.* (1986), Hossain and Rodi (1977), Pope (2001, pg. 111) and (Tennekes and Lumley, 1973, pg. 136) for the derivation of these equations.

The boundary layer equations for gravity current flow contain only the $\langle u'v' \rangle$ shear Reynolds stress and the $\langle \Delta\rho' v' \rangle$ Reynolds flux. This indicates that the significant turbulence fluxes are the vertical flux of mass and u-momentum. In order to obtain closure for $\langle u'v' \rangle$ and $\langle \Delta\rho' v' \rangle$ a turbulence model needs to be linked to the governing equations. There is a wide range of turbulence models, varying in sophistication, which can provide such a link.

The present research used two different turbulence models, namely the standard $k-\epsilon$ turbulence model and the RNG $k-\epsilon$ turbulence model. Both can be classified as eddy viscosity models. These turbulence models compute Reynolds stresses and Reynolds fluxes through the Boussinesq and flux-gradient hypothesis using k and ϵ transport equations. These hypotheses and the turbulence model equations are presented below.

4.3.1 Boussinesq hypothesis

The Boussinesq hypothesis is analogous to Newton's law of viscosity. It relates the Reynolds stresses to the mean velocity gradients (Rodi, 1980, pg. 10), (FLUENT 6.3, pg. 12-5), (Pope, 2001, pg. 92)

$$-\langle \bar{u}'\bar{u}' \rangle = \nu_t \left[\bar{\nabla}\bar{U} + \bar{\nabla}\bar{U}^T \right] - \frac{2}{3} \left(k + \nu_t \bar{\nabla} \cdot \bar{U} \right) \bar{\bar{I}} \tag{4.3.1}$$

where ν_t is the turbulent viscosity, which is a property of the flow and not of the fluid. The 2/3 term on the right-hand side of equation 4.3.1 ensures that the sum of the normal Reynolds stresses is equal to $2k$. However, this term implies isotropy between the three normal Reynolds stresses, since two-thirds of k is allocated to each normal Reynolds stress. This assumption is not realistic for gravity current flow, since figures 3.9a and 3.24a showed the normal Reynolds stresses to be anisotropic. The consequence of this incorrect assumption is, however, negligible, since equation 4.3.1 gives a reasonable estimate of the shear Reynolds stress $\langle u'v' \rangle$, which is the only significant Reynolds stress in the boundary-layer equations. Gravity current modellers such as Bournet *et al.* (1999), Choi and Garcia (2002) and Huang *et al.* (2005) have used the Boussinesq hypothesis with reasonable success.

4.3.2 Flux-gradient hypothesis

The flux-gradient hypothesis is analogous to Fick's first law for molecular diffusion. It relates the Reynolds fluxes to the mean mass fraction gradients (Rodi, 1980, pg. 12), (FLUENT 6.3, pg. 14-3), (Pope, 2001, pg. 93, 94)

$$\langle \omega' \bar{u}' \rangle = -\gamma_t \bar{\nabla} \langle \omega \rangle = -\frac{\nu_t}{\sigma_t} \bar{\nabla} \langle \omega \rangle \tag{4.3.2}$$

or in terms of excess density

$$\langle \Delta\rho' \bar{u}' \rangle = -\frac{\nu_t}{\sigma_t} \bar{\nabla} \langle \Delta\rho \rangle \tag{4.3.3}$$

where γ_t is the turbulent diffusion coefficient and σ_t is the turbulent Schmidt number. The flux-gradient hypothesis performs poorly in estimating *simultaneously* the streamwise and cross-stream Reynolds fluxes for a horizontal gravity current. This is shown through examination of equation 4.3.2: The right-hand side of equation 4.3.2 results in an approximately vertical vector, since cross-stream gradients of boundary-layer type flows are much greater than the streamwise gradients. However, figures 3.12a and 3.27a show that the streamwise Reynolds flux is greater than the cross-stream Reynolds flux. Hence, the left-hand side of equation should be an approximately horizontal vector. Although the flux-gradient hypothesis incorrectly predicts the orientation of the Reynolds flux vector, it does give a reasonable estimate of the cross-stream Reynolds flux, which is the only significant Reynolds flux in the boundary-layer equations. Appendix B.3 presents the FLUENT source code to compute the effective diffusivity of $NaCl$ species for a constant turbulent Schmidt number. The effective diffusivity γ_{eff} is given by:

$$\gamma_{eff} = \gamma + \frac{\nu_t}{\sigma_t} \tag{4.3.4}$$

4.3.3 Conservation of k

Subtracting the momentum equation 4.2.35 from the Reynolds-averaged momentum equation 4.2.61, followed by substitution of equations 4.2.36, 4.2.37 and 4.2.38 gives

$$\frac{\partial \bar{u}'}{\partial t} + \bar{\nabla} \cdot \left(\bar{u}\bar{u} - \bar{U}\bar{U} \right) = -\frac{1}{\rho_w} \bar{\nabla} p' + \nu \bar{\nabla} \cdot \bar{\nabla} \bar{u}' + \bar{\nabla} \cdot \langle \bar{u}' \bar{u}' \rangle + \frac{\Delta\rho'}{\rho_w} \bar{g} \tag{4.3.5}$$

substitution of

$$\langle \bar{u}\bar{u} \rangle = \bar{U}\bar{U} + \langle \bar{u}' \bar{u}' \rangle \tag{4.3.6}$$

gives the conservation equation for fluctuating velocity

$$\frac{\partial \bar{u}'}{\partial t} + \bar{\nabla} \cdot (\bar{u}\bar{u} - \langle \bar{u}\bar{u} \rangle) = -\frac{1}{\rho_w} \bar{\nabla} p' + \nu \bar{\nabla} \cdot \bar{\nabla} \bar{u}' + \frac{\Delta \rho'}{\rho_w} \bar{g} \tag{4.3.7}$$

The conservation of turbulent kinetic energy is derived by postmultiplying equation 4.3.7 by $\bar{u}'$, followed by taking the mean:

$$\langle \frac{\partial \bar{u}'}{\partial t} \cdot \bar{u}' \rangle + \langle \bar{\nabla} \cdot (\bar{u}\bar{u} - \langle \bar{u}\bar{u} \rangle) \cdot \bar{u}' \rangle = \langle -\frac{1}{\rho_w} \bar{\nabla} p' \cdot \bar{u}' \rangle + \langle \nu \bar{\nabla} \cdot \bar{\nabla} \bar{u}' \cdot \bar{u}' \rangle + \langle \frac{\Delta \rho'}{\rho_w} \bar{g} \cdot \bar{u}' \rangle \tag{4.3.8}$$

However, equation 4.3.8 is not the final form of the conservation of k. The derivation of the final form is presented term by term below in 5 steps:

1. Post-multiplying the first term on the left-hand side of equation 4.3.7 by $\bar{u}'$ and noting that
$$\frac{\partial}{\partial t} (\bar{u}' \cdot \bar{u}') = 2 \frac{\partial \bar{u}'}{\partial t} \cdot \bar{u}' \tag{4.3.9}$$
followed by taking the mean gives the **rate of change of** k
$$\langle \frac{\partial \bar{u}'}{\partial t} \cdot \bar{u}' \rangle = \frac{\partial \langle \bar{u}' \cdot \bar{u}' \rangle}{\partial t} = \frac{\partial k}{\partial t} \tag{4.3.10}$$

2. Post-multiplying the first term on the right-hand side of equation 4.3.7 by $\bar{u}'$ and noting that
$$\bar{\nabla} \cdot p' \bar{u}' = \bar{\nabla} p' \cdot \bar{u}' + p' \bar{\nabla} \cdot \bar{u}' \tag{4.3.11}$$
followed by taking the mean gives **the transport of** k **by pressure**
$$\langle -\frac{1}{\rho_w} \bar{\nabla} p' \cdot \bar{u}' \rangle = -\frac{1}{\rho_w} \bar{\nabla} \cdot \langle p' \bar{u}' \rangle \tag{4.3.12}$$

3. Post-multiplying the third term on the right-hand side of equation 4.3.7 by $\bar{u}'$ and taking the mean gives the **production of** k **by buoyancy**
$$\langle \frac{\Delta \rho'}{\rho_w} \bar{g} \cdot \bar{u}' \rangle = \frac{1}{\rho_w} \bar{g} \cdot \langle \Delta \rho' \bar{u}' \rangle \tag{4.3.13}$$

4. Post-multiplying the second term on the right-hand side of equation 4.3.7 by $\bar{u}'$ and noting the following:

$$\nu\bar{\nabla}\cdot\left[\bar{\nabla}\bar{u}'\cdot\bar{u}'\right]=\nu\bar{\nabla}\cdot\left(\bar{\nabla}\bar{u}'\right)\cdot\bar{u}'+\nu\bar{\nabla}\bar{u}':\left(\bar{\nabla}\bar{u}'\right)^T \tag{4.3.14}$$

Substituting

$$\bar{\nabla}\bar{u}'=2\bar{\bar{s}}'-\left(\bar{\nabla}\bar{u}'\right)^T \tag{4.3.15}$$

into equation 4.3.14 gives

$$2\nu\bar{\nabla}\cdot[\bar{\bar{s}}'\cdot\bar{u}']-\nu\bar{\nabla}\cdot\left[\left(\bar{\nabla}\bar{u}'\right)^T\cdot\bar{u}'\right]=\nu\bar{\nabla}\cdot\left(\bar{\nabla}\bar{u}'\right)\cdot\bar{u}'+\nu\bar{\nabla}\bar{u}':\left(\bar{\nabla}\bar{u}'\right)^T \tag{4.3.16}$$

Substituting

$$\nu\bar{\nabla}\cdot\left[\left(\bar{\nabla}\bar{u}'\right)^T\cdot\bar{u}'\right]=\nu\bar{\nabla}\bar{u}':\bar{\nabla}\bar{u}' \tag{4.3.17}$$

into equation 4.3.16 gives

$$2\nu\bar{\nabla}\cdot[\bar{\bar{s}}'\cdot\bar{u}']-\nu\bar{\nabla}\bar{u}':\bar{\nabla}\bar{u}'=\nu\bar{\nabla}\cdot\left(\bar{\nabla}\bar{u}'\right)\cdot\bar{u}'+\nu\bar{\nabla}\bar{u}':\left(\bar{\nabla}\bar{u}'\right)^T \tag{4.3.18}$$

$$\nu\bar{\nabla}\cdot\left(\bar{\nabla}\bar{u}'\right)\cdot\bar{u}'=2\nu\bar{\nabla}\cdot[\bar{\bar{s}}'\cdot\bar{u}']-\nu\left[\bar{\nabla}\bar{u}':\bar{\nabla}\bar{u}'+\bar{\nabla}\bar{u}':\left(\bar{\nabla}\bar{u}'\right)^T\right] \tag{4.3.19}$$

Noting further that

$$\bar{\bar{s}}' = \left(\bar{\bar{s}}'\right)^T \tag{4.3.20}$$

$$2\bar{\bar{s}}':\left(\bar{\bar{s}}'\right)^T = \bar{\nabla}\bar{u}':\bar{\nabla}\bar{u}'+\bar{\nabla}\bar{u}':\left(\bar{\nabla}\bar{u}'\right)^T \tag{4.3.21}$$

Substituting equation 4.3.19 into equation 4.3.21 gives

$$\nu\bar{\nabla}\cdot\left(\bar{\nabla}\bar{u}'\right)\cdot\bar{u}'=2\nu\bar{\nabla}\cdot[\bar{\bar{s}}'\cdot\bar{u}']-2\nu\bar{\bar{s}}':\left(\bar{\bar{s}}'\right)^T \tag{4.3.22}$$

Taking the mean gives **the transport of k by viscous stresses, as well as the rate of dissipation of k**

$$\langle\nu\bar{\nabla}\cdot\left(\bar{\nabla}\bar{u}'\right)\cdot\bar{u}'\rangle=2\nu\bar{\nabla}\cdot\langle\bar{\bar{s}}'\cdot\bar{u}'\rangle-2\nu\langle\bar{\bar{s}}':\left(\bar{\bar{s}}'\right)^T\rangle \tag{4.3.23}$$

5. Substituting

$$\bar{u}=\bar{U}+\bar{u}' \tag{4.3.24}$$

and

$$\langle\bar{u}\bar{u}\rangle=\bar{U}\bar{U}+\langle\bar{u}'\bar{u}'\rangle \tag{4.3.25}$$

into the second term on the left-hand side of equation 4.3.7 gives

$$\bar{\nabla}\cdot(\bar{u}\bar{u}-\langle\bar{u}\bar{u}\rangle)= \bar{\nabla}\cdot\left[\bar{U}\bar{U}+\bar{u}'\bar{U}+\bar{U}\bar{u}'+\bar{u}'\bar{u}'\right]-\bar{\nabla}\cdot\left[\bar{U}\bar{U}+\langle\bar{u}'\bar{u}'\rangle\right] \tag{4.3.26}$$

Substituting equations 4.2.55 and 4.2.56 gives

$$\bar{\nabla}\cdot(\bar{u}\bar{u}-\langle\bar{u}\bar{u}\rangle)=\bar{u}'\cdot\bar{\nabla}\bar{U}+\bar{U}\cdot\bar{\nabla}\bar{u}'+\bar{u}'\cdot\bar{\nabla}\bar{u}'-\bar{\nabla}\cdot\langle\bar{u}'\bar{u}'\rangle \tag{4.3.27}$$

Post-multiplying equation 4.3.27 by $\bar{u}'$ gives

$$\bar{\nabla}\cdot(\bar{u}\bar{u}-\langle\bar{u}\bar{u}\rangle)\cdot\bar{u}'=\bar{u}'\cdot\bar{\nabla}\bar{U}\cdot\bar{u}'+\bar{U}\cdot\bar{\nabla}\bar{u}'\cdot\bar{u}'+\bar{u}'\cdot\bar{\nabla}\bar{u}'\cdot\bar{u}'-\bar{\nabla}\cdot\langle\bar{u}'\bar{u}'\rangle\cdot\bar{u}' \tag{4.3.28}$$

Substituting

$$\bar{U}\cdot\bar{\nabla}\bar{u}'\cdot\bar{u}' = \bar{U}\cdot\bar{\nabla}\left(\frac{\bar{u}'\cdot\bar{u}'}{2}\right) \tag{4.3.29}$$

$$\bar{u}'\cdot\bar{\nabla}\bar{u}'\cdot\bar{u}' = \frac{1}{2}\bar{\nabla}\cdot[\bar{u}'\bar{u}'\cdot\bar{u}'] \tag{4.3.30}$$

$$\bar{u}'\cdot\bar{\nabla}\bar{U}\cdot\bar{u}' = \bar{u}'\bar{u}':\left(\bar{\nabla}\bar{U}\right)^T \tag{4.3.31}$$

gives

$$\bar{\nabla}\cdot(\bar{u}\bar{u}-\langle\bar{u}\bar{u}\rangle)\cdot\bar{u}' =$$
$$\bar{u}'\bar{u}':\left(\bar{\nabla}\bar{U}\right)^T+\langle\bar{u}\rangle\cdot\bar{\nabla}\left(\frac{\bar{u}'\cdot\bar{u}'}{2}\right)+\frac{1}{2}\bar{\nabla}\cdot[\bar{u}'\bar{u}'\cdot\bar{u}']-\bar{\nabla}\cdot\langle\bar{u}'\bar{u}'\rangle\cdot\bar{u}' \tag{4.3.32}$$

Taking the mean gives **the production of k by shear, the transport of k by convection and the transport of k by Reynolds stresses**

$$\langle\bar{\nabla}\cdot(\bar{u}\bar{u}-\langle\bar{u}\bar{u}\rangle)\cdot\bar{u}'\rangle=\langle\bar{u}'\bar{u}'\rangle:\left(\bar{\nabla}\bar{U}\right)^T+\bar{U}\cdot\bar{\nabla}k+\bar{\nabla}\cdot\frac{1}{2}\langle\bar{u}'\bar{u}'\cdot\bar{u}'\rangle \tag{4.3.33}$$

Substituting equations 4.3.10, 4.3.12, 4.3.13, 4.3.23, 4.3.33 into equation 4.3.8 gives the final form of the conservation equation of k (Rodi, 1980, pg. 21)

$$\frac{\partial k}{\partial t}+\bar{U}\cdot\bar{\nabla}k+\bar{\nabla}\cdot\left[\frac{1}{2}\langle\bar{u}'\bar{u}'\cdot\bar{u}'\rangle+\frac{\langle p'\bar{u}'\rangle}{\rho_w}-2\nu\langle\bar{\bar{s}}'\cdot\bar{u}'\rangle\right]=$$
$$-\langle\bar{u}'\bar{u}'\rangle:\left(\bar{\nabla}\bar{U}\right)^T-2\nu\langle\bar{\bar{s}}':(\bar{\bar{s}}')^T\rangle+\frac{1}{\rho_w}\bar{g}\cdot\langle\Delta\rho'\bar{u}'\rangle \tag{4.3.34}$$

where the terms on the left-hand side are respectively: the rate of change of k, the transport of k by convection, the transport of k by Reynolds stress, the transport of k by pressure and the transport of k by viscous stresses. The terms on the right-hand side are respectively: the production of k by shear, the rate of dissipation of k and the production of k by buoyancy. Defining

$$\bar{T} = \frac{1}{2}\langle\bar{u}'\bar{u}'\cdot\bar{u}'\rangle+\frac{\langle p'\bar{u}'\rangle}{\rho_w}-2\nu\langle\bar{\bar{s}}'\cdot\bar{u}'\rangle \tag{4.3.35}$$

$$\mathcal{P} = -\langle\bar{u}'\bar{u}'\rangle:\left(\bar{\nabla}\bar{U}\right)^T \tag{4.3.36}$$

$$\epsilon = 2\nu\langle\bar{\bar{s}}':(\bar{\bar{s}}')^T\rangle \tag{4.3.37}$$

$$G_b = \frac{1}{\rho_w}\bar{g}\cdot\langle\Delta\rho'\bar{u}'\rangle \tag{4.3.38}$$

gives the summarised form of equation 4.3.34 as (Pope, 2001, pg. 126)

$$\frac{\partial k}{\partial t} + \bar{U} \cdot \bar{\nabla} k + \bar{\nabla} \cdot \bar{T} = \mathcal{P} - \epsilon + G_b \tag{4.3.39}$$

4.3.4 Standard $k - \epsilon$ model

The standard $k - \epsilon$ turbulence model was introduced by Launder and Spalding (1974). It has been widely used in industry, due to its simplicity and ability to model a wide variety of flows. The equations for the standard $k - \epsilon$ model can be derived as follows:

Applying the Boussinesq hypothesis (equation 4.3.1) to the shear production term $\mathcal{P}$ in equation 4.3.36 gives

$$\mathcal{P} = \left[\nu_t \left[\bar{\nabla}\bar{U} + \left(\bar{\nabla}\bar{U}\right)^T\right] - \frac{2}{3}\left(k + \nu_t \bar{\nabla} \cdot \bar{U}\right)\bar{\bar{I}}\right] : \left(\bar{\nabla}\bar{U}\right)^T \tag{4.3.40}$$

which simplifies due to the continuity equation 4.2.55 to

$$\mathcal{P} = \nu_t \left[\bar{\nabla}\bar{U} + \left(\bar{\nabla}\bar{U}\right)^T\right] : \left(\bar{\nabla}\bar{U}\right)^T \tag{4.3.41}$$

$$= 2\nu_t \bar{\bar{S}} : \bar{\bar{S}}^T \tag{4.3.42}$$

Although not part of the standard $k - \epsilon$ model, the shear production term may be simplified even further for the gravity current measured in chapter 3, by noting from figures 3.7 and 3.22 that

$$\frac{\partial U}{\partial x} \approx 0 \tag{4.3.43}$$

$$\frac{\partial V}{\partial y} \approx 0 \tag{4.3.44}$$

$$\frac{\partial V}{\partial x} \approx 0 \tag{4.3.45}$$

Substitution of equations 4.3.43, 4.3.44 and 4.3.45 into equation 4.3.41 gives a simplified equation for $\mathcal{P}$:

$$\mathcal{P} = \nu_t \left(\frac{\partial U}{\partial y}\right)^2 \tag{4.3.46}$$

Applying the flux-gradient hypothesis (equation 4.3.2) to the turbulent kinetic energy transport term $\bar{T}$ in equation 4.3.35 gives

$$\bar{T} = \left(-\frac{\nu_t}{\sigma_k}\bar{\nabla} k\right) \tag{4.3.47}$$

where $\sigma_k = 1$.

Applying the flux-gradient hypothesis also to the buoyancy production term G_b in equation 4.3.38 gives

$$G_b = \frac{1}{\rho_w}\bar{g} \cdot \langle \Delta\rho' \bar{u}' \rangle \tag{4.3.48}$$

$$= -\frac{1}{\rho_w}\bar{g} \cdot \frac{\nu_t}{\sigma_t}\bar{\nabla}\langle \Delta\rho \rangle \tag{4.3.49}$$

where σ_t is the turbulent Schmidt number.

Substituting equations 4.3.42, 4.3.47 and 4.3.49 in equation 4.3.39 gives the model equation for k (FLUENT 6.3, pg. 12-13)

$$\frac{\partial k}{\partial t} + \langle \bar{u} \rangle \cdot \bar{\nabla} k = \bar{\nabla} \cdot \left(\frac{\nu_t}{\sigma_k} \bar{\nabla} k \right) + 2\nu_t \bar{\bar{S}} : \bar{\bar{S}}^T - \epsilon - \frac{1}{\rho_w}\bar{g} \cdot \frac{\nu_t}{\sigma_t}\bar{\nabla}\langle \Delta\rho \rangle \tag{4.3.50}$$

It is possible to derive an exact transport equation for the dissipation rate of turbulent kinetic energy ϵ. However, such an equation contains many complex and unmeasurable correlations (Rodi, 1980, pg. 27), (Versteeg and Malalasekera, 1995, pg. 70). The standard $k-\epsilon$ model uses a transport equation for ϵ, which assumes ϵ source and sink terms that are proportional to the source and sink terms of k (equation 4.3.50) (FLUENT 6.3, pg. 12-13, 12-24).

$$\frac{\partial \epsilon}{\partial t} + \langle \bar{u} \rangle \cdot \bar{\nabla} \epsilon = \bar{\nabla} \cdot \left(\frac{\nu_t}{\sigma_\epsilon} \bar{\nabla} \epsilon \right) + C_{1\epsilon} \frac{\epsilon}{k} \left(2\nu_t \bar{\bar{S}} : \bar{\bar{S}}^T \right) - C_{2\epsilon} \frac{\epsilon}{k} (\epsilon) - C_{1\epsilon} C_{3\epsilon} \frac{\epsilon}{k} \left(\frac{1}{\rho_w}\bar{g} \cdot \frac{\nu_t}{\sigma_t}\bar{\nabla}\langle \Delta\rho \rangle \right) \tag{4.3.51}$$

where $\sigma_\epsilon = 1{,}3$, $C_{1\epsilon} = 1{,}44$, $C_{2\epsilon} = 1{,}92$, $C_{3\epsilon} = \tanh \left| \frac{V}{U} \right|$. The ϵ/k factor in equation 4.3.51 ensures that the source and sink terms are dimensionally correct. The turbulent viscosity ν_t is computed from k and ϵ by (FLUENT 6.3, pg. 12-13)

$$\nu_t = C_\mu \frac{k^2}{\epsilon} \tag{4.3.52}$$

where $C_\mu = 0{,}09$.

The standard $k-\epsilon$ model assumes that the flow is fully turbulent and hence it cannot be used in the viscosity affected near-wall region. Wall-functions or a two-layer approach are required to bridge the viscous sublayer at the wall.

The model is known to perform poorly for rotating flows, swirling flows, secondary flows in long non-circular ducts, axisymmetric jets in stagnant surroundings, far wakes, mixing layers and flows with large velocity gradients (Versteeg and Malalasekera, 1995, pg. 74). The gravity current measured in chapter 3 did not show any of these characteristics.

4.3.5 Renormalization Group $k-\epsilon$ model

The Renormalization Group (RNG) $k-\epsilon$ turbulence model is derived from instantaneous Navier-Stokes equations using the 'Renormalization Group' method (Yakhot *et al.*, 1992). The model equation for k is given by (FLUENT 6.3, pg. 12-15)

$$\frac{\partial k}{\partial t} + \langle \bar{u} \rangle \cdot \bar{\nabla} k = \bar{\nabla} \cdot \left(\frac{\nu_{eff}}{\sigma_k} \bar{\nabla} k \right) + 2\nu_t \bar{\bar{S}} : \bar{\bar{S}}^T - \epsilon - \frac{1}{\rho_w} \bar{g} \cdot \frac{\nu_t}{\sigma_t} \bar{\nabla} \langle \Delta\rho \rangle \tag{4.3.53}$$

The model equation for ϵ is given by (FLUENT 6.3, pg. 12-15).

$$\begin{aligned} &\frac{\partial \epsilon}{\partial t} + \langle \bar{u} \rangle \cdot \bar{\nabla} \epsilon = \\ &\bar{\nabla} \cdot \left(\frac{\nu_{eff}}{\sigma_\epsilon} \bar{\nabla} \epsilon \right) + C_{1\epsilon} \frac{\epsilon}{k} \left(2\nu_t \bar{\bar{S}} : \bar{\bar{S}}^T \right) - C^*_{2\epsilon} \frac{\epsilon}{k} (\epsilon) - C_{1\epsilon} C_{3\epsilon} \frac{\epsilon}{k} \left(\frac{1}{\rho_w} \bar{g} \cdot \frac{\nu_t}{\sigma_t} \bar{\nabla} \langle \Delta\rho \rangle \right) \end{aligned} \tag{4.3.54}$$

The constant $C^*_{2\epsilon}$ is given by (FLUENT 6.3, pg. 12-17)

$$C^*_{2\epsilon} \equiv C_{2\epsilon} + \frac{C_\mu \eta^3 \left(1 - \frac{\eta}{\eta_0} \right)}{1 + \beta \eta^3} \tag{4.3.55}$$

with

$$\eta \equiv \sqrt{2\bar{\bar{S}} : \bar{\bar{S}}^T} \frac{k}{\epsilon} \tag{4.3.56}$$

where $\eta_0 = 4{,}38$, $\beta = 0{,}012$, $C_\mu = 0.0845$, $C_{1\epsilon} = 1.42$, $C_{2\epsilon} = 1{,}68$ and $C_{3\epsilon} = \tanh \left| \frac{V}{U} \right|$. Equation 4.3.55 contains a strain-rate correction term, which improves the accuracy of the RNG model for large strain-rate flows.

The analytically derived turbulent Prandtl number σ_x is given by (FLUENT 6.3, pg. 12-16)

$$\left| \frac{\frac{1}{\sigma_x} - 1.3929}{\frac{1}{\sigma_0} - 1.3929} \right|^{0.6321} \left| \frac{\frac{1}{\sigma_x} + 2.3929}{\frac{1}{\sigma_0} + 2.3929} \right|^{0.3679} = \frac{\nu}{\nu_{eff}} \tag{4.3.57}$$

where σ_x represents σ_k, σ_ϵ or σ_t. When σ_k or σ_ϵ are computed $\sigma_0 = 1$. When σ_t is computed $\sigma_0 = \sigma$, where σ is the molecular Schmidt number.

The analytically derived differential equation for the turbulent viscosity is given by (FLUENT 6.3, pg. 12-15)

$$d\left(\frac{\rho^2 k}{\sqrt{\epsilon\mu}}\right) = 1.72\frac{\hat{\nu}}{\sqrt{\hat{\nu}^3 - 1 + C_\nu}}d\hat{\nu} \tag{4.3.58}$$

with

$$\hat{\nu} = \frac{\nu_{eff}}{\nu} \tag{4.3.59}$$

where $C_\nu \approx 100$. The RNG $k-\epsilon$ model has a number of advantages over the standard $k-\epsilon$ model. The RNG model does not assume high Reynolds number flows and can therefore be applied in the viscous affected near-wall region. The RNG also has a better performance for swirling and large strain-rate flows. Rodi (1980, pg. 15) mentions that σ_t varies with the degree of stable stratification. Equation 4.3.57 allows σ_t to vary with the level of turbulence, which is dependent on the degree of stable stratification.

4.4 Grid, boundary conditions and initial conditions

A continuous gravity current can be divided into two parts: a head and a body. The head is the foremost part of the gravity current, which sheds eddies behind it as it moves downstream. The motion of the head is inherently unsteady, non-uniform and the most complex part of the current to model. The body is the uniform, steady region behind the head. Chapter 3 presented measurements of the gravity current body. The main focus of the simulations is therefore also the body.

In order to obtain a stable, grid independent and computationally inexpensive solution a number of aspects have to be considered. These include the overall grid layout, boundary conditions and the near-wall grid. For instance, defining a vertical wall at the downstream end of the domain would result in an internal hydraulic bore moving upstream, after the head had reached that wall. As the bore moves upstream it changes the flow profile of the body. Hence, an unsteady simulation which is run for an indefinite length of time with a wall at the downstream end, would produce profiles different from those measured in chapter 3.

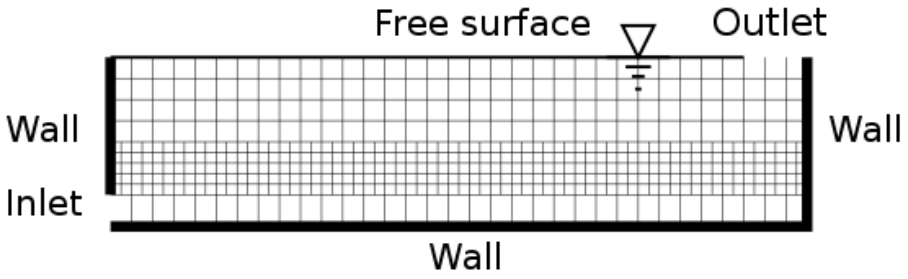

(a) Computational grid and boundary conditions

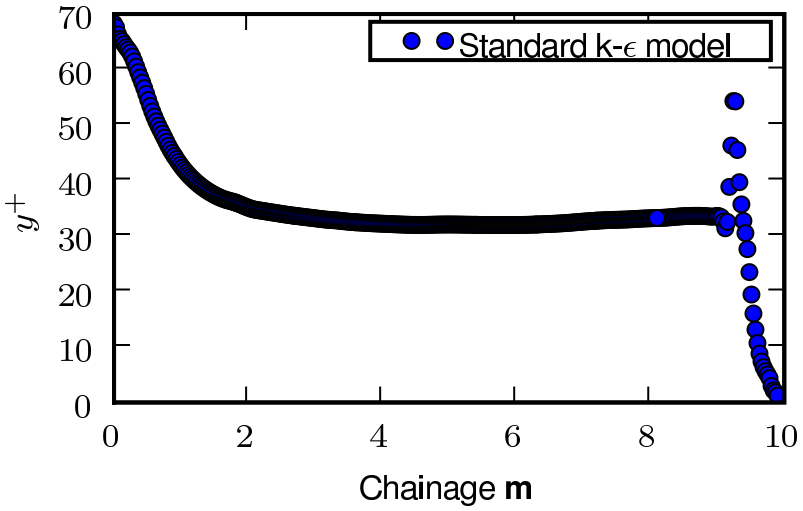

(b) Cell centroid profile for bed adjacent cells ($k-\epsilon$ model)

Figure 4.2: Overall grid and near-wall grid quality

Similarly, defining a uniform flow boundary condition at the downstream end of the domain would also poorly model the gravity current of chapter 3. The reason being that the uniform boundary condition would be violated when the gravity current head reached the end of the domain, since it is non-uniform. If such a situation did occur the solution would become unstable, due to reverse flow at this boundary. The best approach to model the above gravity current is by treating it as an unsteady flow with a wall at the downstream end. The simulation is terminated before the head reaches the downstream wall. This wall should be sufficiently far from the measuring locations (0,9 m and 2,4 m), so that when the simulation is terminated, the influence of the head has become negligible at that point.

4.4.1 Grid topology

For the overall grid layout it was decided to use square cells instead of rectangular cells with large aspect ratios. Large aspect ratio rectangles allowed the number of cells along the streamwise direction to be reduced, without reducing the number of cells in the cross-stream direction. Hence a high cross-stream resolution could be maintained with fewer cells. This seemed useful, since figures 3.7 and 3.22 showed that the velocity gradients are much greater in the cross-stream direction than the streamwise direction. However, large aspect ratios could impede the convergence and accuracy of the solution (FLUENT 6.3, pg. 6-23). It was therefore decided to use only square cells, to avoid compromising the accuracy of the solution.

Figure 4.2a shows a schematic layout of the modeled flume and its computational grid. The modeled flume was 0,3 m high and 9,9 m long. The 0,3 m height was similar to the flow depth used for the gravity current measurements of chapter 3. The 9,9 m length allowed 300 s of flow to be simulated before the gravity current head reached the downstream wall. Furthermore, the vertical inlet was 0,03 m high and the horizontal outlet was 0,3 m long.

The program FLUENT uses an unstructured grid technology, which does not require i,j,k-indexing to locate neighboring cells. This technology removes constraints that a structured solver might have imposed on the overall structure and topology of a grid. This feature was used to combine a low resolution grid in the top part of the modeled flume with a higher resolution grid in the bottom part of the modeled flume. The low resolution grid reduced the computational effort, but did not compromise the solution since the gradients of the solution variables were small near the free surface. Figure 4.2a shows, schematically, the two grid resolutions used for the modelled flume.

4.4.2 Boundary conditions

Figure 4.2a shows that the computational domain is surrounded by an inlet, an outlet, free surface and walls. Section 3.1 presented the measured flow conditions at the inlet of the flume. These conditions were used as the inlet boundary conditions for the gravity current model. The inlet was modelled in FLUENT by using a 'velocity inlet' (FLUENT 6.3, pg. 7-29). The mixture density ρ at the inlet face was computed from equation 2.4.1 by using the measured mass fraction value ω. The convective fluxes of mass, momentum, species and turbulence through the inlet

faces were computed from

$$\int \rho\phi\bar{U} \cdot d\bar{A} = \sum_{i=1}^{N} \rho_i \phi_i \bar{U}_i \cdot d\bar{A}_i \tag{4.4.1}$$

where ϕ is a scalar quantity (which can be U, V, $\langle\omega\rangle$, k or ϵ), ρ is the density of the mixture at the inlet, $\bar{U}$ is the mean velocity vector at the inlet, $\bar{A}$ is the surface vector at the inlet, i is the inlet face index, N is the number of faces at the inlet, ϕ_i is the scalar value at face i, ρ_i is the mixture density at face i, $\bar{U}_i$ is the velocity vector at face i and $\bar{A}_i$ is the surface vector at inlet face i. The pressure was allowed to float between $1\,\text{Pa} < P < 5 \times 10^{10}\,\text{Pa}$ to provide the prescribed inlet velocity. Table 4.2 presents the values specified at the inlet.

The free surface was modeled in FLUENT by using a 'symmetry boundary condition' (FLUENT 6.3, pg. 7-95). A symmetry boundary condition assumes that the velocity component normal to the symmetry axis is zero, as well as the gradients of all the other flow variables normal to the symmetry axis. Furthermore, the absolute pressure at the free surface is known to be equal to atmospheric pressure (101 320 Pa). In FLUENT the absolute pressure is computed as the sum of a reference pressure and a gauge pressure. Since the gauge pressure at the free surface is zero, the reference pressure for the computational domain could be set equal to 101 320 Pa at the midpoint of the free surface. Choi and Garcia (2002), Bournet *et al.* (1999) and Huang *et al.* (2005) also approximated the free surface with a symmetry boundary condition.

The flow of the gravity current exited the damping tank by way of a weir. This weir was modeled in FLUENT by using a horizontal 'pressure outlet' (FLUENT 6.3, pg. 7-52). The pressure outlet requires specifying a gauge pressure. By specifying the gauge pressure as 0 Pa, the absolute pressure at the outlet was equal to the atmospheric pressure (the absolute pressure is equal to the sum of a reference pressure and the gauge pressure). The pressure at the outlet face was computed as the average between the interior pressure and the specified gauge pressure. The face values of all the other flow variables (U, V, $\langle\omega\rangle$, k and ϵ) are extrapolated from the interior of the solution domain, by assuming that the gradient normal to the outlet boundary is zero. The velocity component normal to the outlet face V is allowed to float to whatever value is necessary to provide the prescribed gauge pressure, provided that the continuity equation is satisfied. In the case of reverse flow other scalar values ($\langle\omega\rangle$, k and ϵ) also need to be specified, during the solution process. For such a situation the $NaCl$ mass fraction was set to zero, while k and ϵ were set equal to their corresponding values at the inlet.

Variable	Units	Value (measured)
U	m/s	0,079
V	m/s	0,0
$\langle\omega\rangle$	-	0,002 81
k	$\mathrm{m}^2/\mathrm{s}^2$	$6{,}875 \times 10^{-5}$
ϵ	$\mathrm{m}^2/\mathrm{s}^3$	$1{,}38 \times 10^{-5}$

Table 4.2: Inlet boundary conditions

4.4.3 Wall functions

The no-slip condition is the appropriate boundary condition for the velocity components at the bed:

$$U = 0 \tag{4.4.2}$$
$$V = 0 \tag{4.4.3}$$

Equations 4.4.2 and 4.4.3 appear simple to implement, but the multilayer structure of the gravity current near the wall is a significant obstacle for the standard $k-\epsilon$ and RNG $k-\epsilon$ turbulence models. George *et al.* (2000) have shown that a turbulent plane wall jet, which is related to a gravity current, can be divided into an inner region next to the bed and an outer region further away from the bed. The characteristic velocity and lengthscales of the inner region are U^* and ν/U^*, with the friction velocity U^* defined as

$$U^* \equiv \sqrt{\frac{\tau_w}{\rho}} \tag{4.4.4}$$

where τ_w is the wall shear stress and ρ is the density of the fluid. From these scales the dimensionless streamwise velocity U^+ and dimensionless cross-stream coordinate y^+ are defined as

$$U^+ = \frac{U}{U^*} \tag{4.4.5}$$
$$y^+ = \frac{yU^*}{\nu} \tag{4.4.6}$$

where y is the cross-stream coordinate (distance from the wall).

The inner region can be further subdivided into a viscous sublayer, a buffer layer and a log-law layer. The viscous sublayer is located immediately next to the wall $y^+ < 5$ and is dominated by viscous stresses. The buffer layer is located further

out from the wall $5 < y^+ < 30$ and in this region viscous and turbulent stresses dominate. The log-law layer is located in the region approximately $30 < y^+ < 500$ and turbulent stresses dominate in this region (Versteeg and Malalasekera, 1995, pg. 59).

The standard $k - \epsilon$ turbulence model is only valid in regions where turbulent stresses dominate. Hence this model cannot be applied in the viscous sublayer and buffer layer. Wall functions can, however, be used to bridge the viscosity affected region, by 'linking' the turbulence dominated regions of the flow with the walls of the domain. Wall functions are non-dimensional, semi-empirical profiles. By scaling these universal profiles by estimates of the inner scales, the absolute flow profiles can be obtained.

4.4.3.1 Law-of-the-wall and roughness effects

The velocity wall function, or 'law-of-the-wall' is given by

$$U^+ = \frac{1}{\kappa} ln\left(Ey^+\right) - \Delta B \tag{4.4.7}$$

where U^+ is the dimensionless streamwise velocity, $\kappa \approx 0{,}41$ is the von Karman constant, $E \approx 9{,}8$ is an empirical constant and ΔB is a constant accounting for bed roughness. Figures 3.4b and 3.19b showed that the inner region of the measured gravity current had a velocity profile similar to equation 4.4.7.

In addition to the viscous lengthscale ν/U^*, roughness elements can introduce a second lengthscale k_s to the inner region. The roughness height k_s refers to the equivalent sand roughness height of the roughness elements. In order to differentiate which lengthscale is dominant the dimensionless roughness height k_s^+ is defined as (Nezu and Nakagawa, pg. 25), (FLUENT 6.3, pg. 7-86)

$$k_s^+ \equiv \frac{k_s U^*}{\nu} \tag{4.4.8}$$

The dimensionless roughness height can be used to classify the bed as: hydraulically smooth ($k_s^+ \leq 2{,}25$), incompletely rough ($2{,}25 < k_s^+ \leq 90$) or completely rough ($k_s^+ > 90$). This classification is used to calculate ΔB from the following empirical functions (FLUENT 6.3, pg. 7-88)

$$\Delta B = \begin{cases} 0 & k_s^+ \leq 2.25 \\ \frac{1}{\kappa} ln\left(\frac{k_s^+ - 2.25}{87.75} + C_s k_s^+\right) sin\left[0.4258\left(ln\, k_s^+ - 0.811\right)\right] & 2.25 < k_s^+ \leq 90 \\ \frac{1}{\kappa} ln\left(1 + C_s k_s^+\right) & k_s^+ > 90 \end{cases} \tag{4.4.9}$$

where C_s is the roughness constant, which is determined by the roughness type. The gravity current experiments of chapter 3 were conducted in a perspex flume, having a roughness height of $k_s \approx 0$. Hence the bed was hydraulically smooth and $\Delta B = 0$.

4.4.3.2 Standard wall functions

The wall shear stress τ_w is required to determine the dimensionless velocity U^+ and cross-stream coordinate y^+. An expression for τ_w can be derived as follows: The Kolmogorov-Prandtl expression for turbulent viscosity is given by (Rodi, 1980, pg. 21)

$$\nu_t = C_\mu \frac{k^2}{\epsilon} \tag{4.4.10}$$

where $C_\mu = 0{,}09$. Assuming that turbulence is in local equilibrium $\mathcal{P} \approx \epsilon$ (which occurs when the rate of change of k, the diffusive transport of k and buoyancy production of k is negligible) gives

$$\sqrt{\frac{\tau}{\rho}} = C_\mu \sqrt{k} \tag{4.4.11}$$

where τ is the total shear stress. Assuming further that $\tau = \tau_w$ across the wall adjacent cell gives the local equilibrium condition

$$U^* = C_\mu^{\frac{1}{4}} \sqrt{k} \tag{4.4.12}$$

Substitution into the law-of-the-wall (equation 4.4.7) gives an expression of the wall shear stress (Craft *et al.*, 2004)

$$\tau_w = \frac{\rho C_\mu^{\frac{1}{4}} \sqrt{k} \kappa U}{ln\left(\frac{Ey}{\nu} C_\mu^{\frac{1}{4}} \sqrt{k}\right)} \tag{4.4.13}$$

Rodi (1980, pg. 45) suggested that equations 4.4.3 and 4.4.7, in conjunction with the following wall functions, be used as wall boundary conditions

$$k_p = \frac{U^{*2}}{\sqrt{C_\mu}} \tag{4.4.14}$$

$$\epsilon_p = \frac{U^{*3}}{\kappa y} \tag{4.4.15}$$

$$\frac{\partial \langle \omega \rangle}{\partial y} = 0 \tag{4.4.16}$$

where k_p is the turbulent kinetic energy at the wall adjacent node and ϵ_p is the dissipation rate of turbulent kinetic energy at the wall adjacent node. Equation 4.4.16 imposes a zero diffusive flux for $\langle\omega\rangle$ at the wall (the convective flux for $\langle\omega\rangle$ is already specified as zero by equation 4.4.3). The gravity current models of Bournet *et al.* (1999) and Choi and Garcia (2002) used equations 4.4.3, 4.4.7, 4.4.14, 4.4.15 and 4.4.16.

Figures 3.15b and 3.30b showed that $\mathcal{P} \approx \epsilon$ for a small region above the bed. Hence the local equilibrium condition (equation 4.4.12) can be used for a small region above the bed. Craft *et al.* (2004) mentions that local equilibrium often does not hold throughout the wall adjacent cell. Instead, they suggest that as a boundary condition for k, the cell-averaged shear production $\mathcal{P}_{cell}$ and dissipation rate ϵ_{cell} be used in equation 4.3.50 or 4.3.53 and that the diffusion of turbulent kinetic energy at the wall face be neglected. This suggestion relaxes the assumption that $\mathcal{P} \approx \epsilon$. This approach is more appropriate for gravity current models, since buoyancy production is inherently part of the flow and may become significant in the wall-adjacent cell if the cell is large. The present research used the non-equilibrium approach of (Craft *et al.*, 2004), which is presented in the next section.

4.4.3.3 Non-equilibrium wall functions

In the non-equilibrium approach the wall adjacent cell is divided into two layers (Kim and Choudhury, 1995), (Craft *et al.*, 2004), a fully turbulent layer and the viscous layer next to the wall. The thickness of the viscous layer y_v is computed from

$$y_v \equiv \frac{11.225\mu}{\rho C_\mu^{\frac{1}{4}} \sqrt{k_p}} \tag{4.4.17}$$

In the viscous layer the following profiles are used for k, ϵ and the turbulent stress τ_t (FLUENT 6.3, pg. 12-66)

$$k = \left(\frac{y}{y_v}\right)^2 k_p \tag{4.4.18}$$

$$\epsilon = \frac{2\nu k}{y^2} \tag{4.4.19}$$

$$\tau_t = 0 \tag{4.4.20}$$

In the fully turbulent layer the following profiles are used for k, ϵ and τ_t (FLUENT 6.3, pg. 12-66)

$$k = k_p \tag{4.4.21}$$

$$\epsilon = \frac{k^{\frac{3}{2}}}{\kappa C_\mu^{-\frac{3}{4}} y} \tag{4.4.22}$$

$$\tau_t = \tau_w \tag{4.4.23}$$

Note that substitution of the local equilibrium condition (equation 4.4.12) into the law-of-the-wall (equation 4.4.7) and differentiation gives

$$\frac{\partial U}{\partial y} = \frac{\tau_w}{\rho C_\mu^{\frac{1}{4}} \sqrt{k} \kappa y} \tag{4.4.24}$$

which can be used to estimate $\mathcal{P}$ by

$$\mathcal{P} = \tau_w \frac{\partial U}{\partial y} = \frac{\tau_w^2}{\rho C_\mu^{\frac{1}{4}} \sqrt{k} \kappa y} \tag{4.4.25}$$

The cell-averaged production $\mathcal{P}_{cell}$ and dissipation rate ϵ_{cell} can then be computed by (FLUENT 6.3, pg. 12-66)

$$\mathcal{P}_{cell} \equiv \frac{1}{y_n} \int_0^{y_n} \tau_t \frac{\partial U}{\partial y} dy = \frac{1}{\kappa y_n} \frac{\tau_w^2}{\rho C_\mu^{\frac{1}{4}} \sqrt{k_p}} \ln\left(\frac{y_n}{y_v}\right) \tag{4.4.26}$$

$$\epsilon_{cell} \equiv \frac{1}{y_n} \int_0^{y_n} \epsilon dy = \frac{1}{y_n} \left[\frac{2\nu}{y_v} + \frac{\sqrt{k_p}}{\kappa C_\mu^{-\frac{3}{4}}} \ln\left(\frac{y_n}{y_v}\right) \right] k_p \tag{4.4.27}$$

where $y_n = 2y_p$ is the height of the wall adjacent cell. This allows the budget of turbulent kinetic energy to be responsive to the proportion of viscous sublayer and fully turbulent layer of the wall adjacent cell. The model equation for k (equation 4.3.50 or 4.3.53) at the wall adjacent cell is modified by substitution of equations 4.4.26 and 4.4.27, together with zero diffusion of k at the wall face. This modified equation acts as a boundary condition for k_p.

The present research used equations 4.4.15 and 4.4.16 as boundary conditions for ϵ and $\langle\omega\rangle$. Application of the above non-equilibrium wall-functions requires that the wall adjacent cell centres be placed within the log-law layer $30 < y^+ < 300$ (FLUENT 6.3, pg. 12-75). Figure 4.2b shows that for the first 9,5 m of the flume the cell centres are further than 30 wall units ($y^+ > 30$). Hence, figure 4.2b indicates that the grid resolution near the bed is adequate for the non-equilibrium wall-functions to be used.

4.4.4 Initial conditions

The unsteady gravity current model can only be solved once initial conditions are specified. Section 2.1 showed that the flume contained quiescent water prior to the introduction of the saline inflow. This implies that the mean velocity and $NaCl$ mass fraction was initially zero throughout the flume. Due to the absence of fluid motion, no turbulence was present and the vertical pressure distribution throughout the flume was hydrostatic.

Turbulence can, initially, be removed from the gravity current model by specifying that $k = 0$ and $\epsilon \neq 0$ throughout the computational domain. This results in $\nu_t = 0$ and $\gamma_t = 0$ and hence the Boussinesq and flux-gradient hypothesis produces no turbulent mass and momentum fluxes. The initial value of ϵ throughout the flume was set equal to its inlet value. Table 4.3 presents the initial conditions for the interior of the solution domain.

Figures 4.3 and 4.4 show qualitively that the initial value of ϵ does not influence the downstream development of the gravity current. In order to compare profiles of different scenarios quantitatively, the depth-averaged difference δ_d is introduced (present research):

$$\delta_d \left[\phi, \text{reference}, \text{alternative}\right] = \frac{1}{L}\int_0^L \frac{\left|\phi\left(y, \text{ alternative}\right) - \phi\left(y, \text{ reference}\right)\right|}{max\left[\phi\left(y, \text{ reference}\right)\right]} dy \tag{4.4.28}$$

where y is the height above the bed, $\phi\left(y, \text{reference}\right)$ is the reference profile of scalar quantity ϕ, $\phi\left(y, \text{alternative}\right)$ is the alternative profile of scalar quantity ϕ, L is the height of the shortest profile and max is the profile maximum. For example, $\delta_d\left[U, \epsilon = 1{,}38 \times 10^{-5}, \epsilon = 1{,}38 \times 10^{-3}\right]$ is the depth-averaged difference between the U-profile for the reference initial condition $\epsilon = 1{,}38 \times 10^{-5}$ and the U-profile for the alternative initial condition $\epsilon = 1{,}38 \times 10^{-3}$.

Tables A.1 and A.2 present the depth-averaged differences for alternative initial conditions of ϵ. They show that there is less than 1% difference between the reference U-profile of $\epsilon = 1{,}38 \times 10^{-5}$ and the alternative U-profiles of $\epsilon = 1{,}38 \times 10^{-4}$ or $\epsilon = 1{,}38 \times 10^{-3}$. The depth-averaged differences for the $\langle\Delta\rho\rangle$-profiles are less than 1,5%. These small depth-averaged differences indicate that initial values of ϵ do not influence the downstream development of the gravity current. Hossain and Rodi (1977) also noted that, for their stably stratified surface jet model, the initial conditions did not influence the downstream development of the flow.

Variable	Units	Value
Gauge pressure	pa	0,0
U	m/s	0,0
V	m/s	0,0
k	$\mathrm{m}^2/\mathrm{s}^2$	0,0
ϵ	$\mathrm{m}^2/\mathrm{s}^3$	$1{,}38 \times 10^{-5}$
$\langle\omega\rangle$	-	0,0

Table 4.3: Initial conditions

4.5 Solution technique

The program FLUENT uses the finite volume method to discretize the governing differential equations into algebraic equations. The program provides two numerical methods (solvers) to solve these algebraic equations. The density-based solver was developed for high-speed compressible flows, while the pressure-based solver was developed for low-speed incompressible flows. Section 4.2.2.1 showed that the gravity current of the present research was incompressible and hence the pressure-based solver was used.

4.5.1 Scalar transport equations: discretization

The pressure-based solver uses the following discretized form of the general scalar transport equation

$$\frac{\partial \rho\phi}{\partial t}V + \sum_{f}^{N} \rho_f \bar{U}_f \phi_f \cdot \bar{A}_f = \sum_{f}^{N} \rho_f \gamma_\phi \bar{\nabla}\phi_f \cdot \bar{A}_f + S_\phi V \tag{4.5.1}$$

where ϕ is a scalar quantity (which can be $\langle\omega\rangle$, k or ϵ), ρ is the mixture density, V is the volume of the cell, f is the face index of the cell, N is the total number of faces of the cell, ρ_f is the mixture density at the cell face, $\bar{U}_f$ is the velocity at the cell face, ϕ_f is the scalar value at the cell face, $\bar{A}_f$ is the surface vector of the cell face, γ_ϕ is the diffusion coefficient of the scalar ϕ and S_ϕ is the source of ϕ. Discrete scalar values of ϕ are stored at the cell centres. However equation 4.5.1 contains ϕ_f face values. Hence interpolation schemes are required to compute face values from the cell centre values.

Face values of ϕ for the diffusion term (first term on the right-hand side of equation 4.5.1) were interpolated from a second order accurate central difference

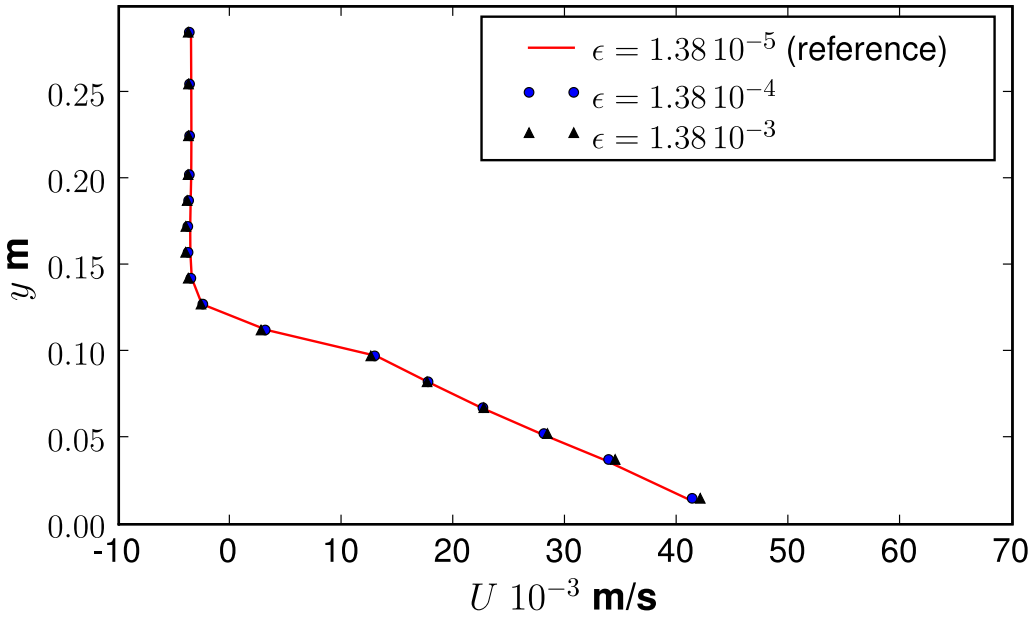

(a) 0,9 m **from the inlet**

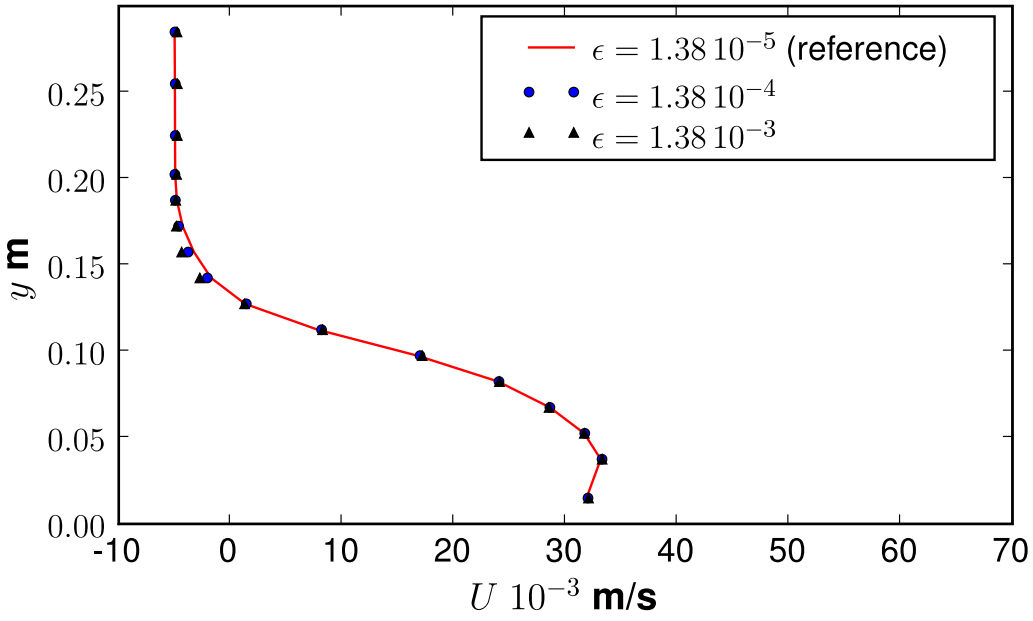

(b) 2,4 m **from the inlet**

Figure 4.3: Simulated U-profiles for different initial values of ϵ, based on standard $k-\epsilon$ model: present research

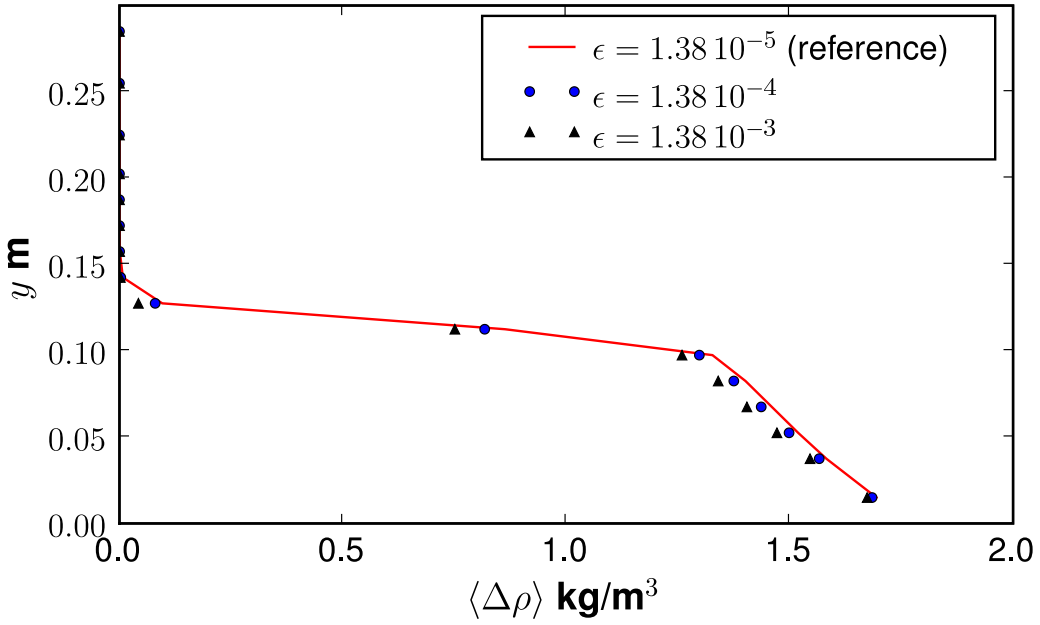

(a) 0,9 m **from the inlet**

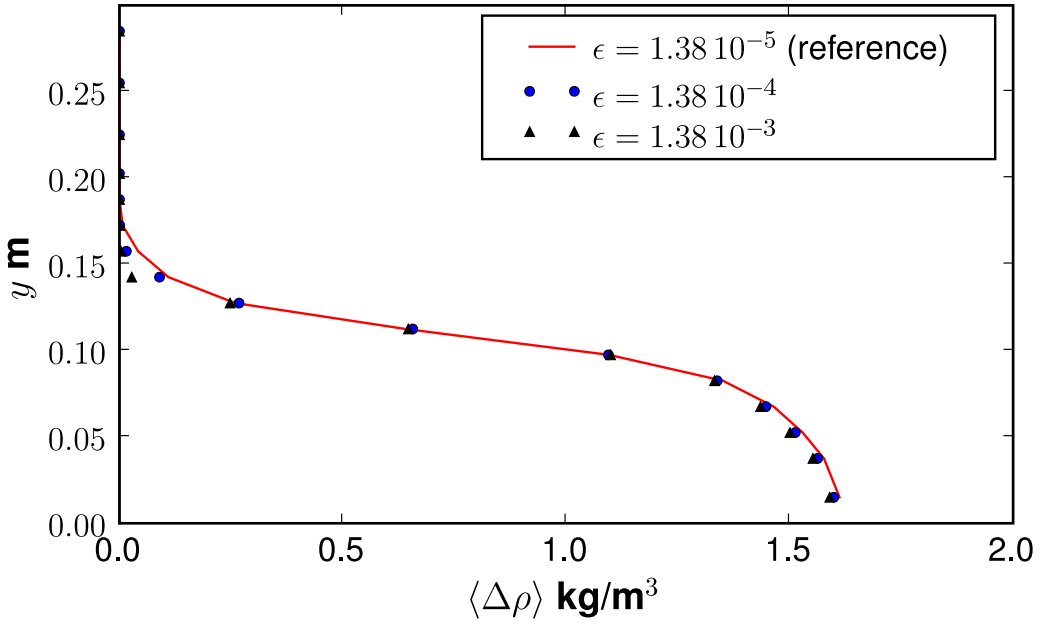

(b) 2,4 m **from the inlet**

Figure 4.4: Simulated $\langle \Delta\rho \rangle$-profiles for different initial values of ϵ, based on standard $k - \epsilon$ model: present research

scheme (FLUENT 6.3, pg. 25-10). Face values of ϕ for the convection term (second term on the left-hand side of equation 4.5.1) were interpolated from a second order upwind scheme as follows (FLUENT 6.3, pg. 25-12)

$$\phi_f = \phi + \bar{\nabla}\phi \cdot \bar{r} \tag{4.5.2}$$

where ϕ is the cell centre value, $\bar{\nabla}\phi$ is the gradient of ϕ in the upstream cell and $\bar{r}$ is the displacement vector from the upstream cell centre to the face centre. It was found that the second order upwind schemes allowed reasonably quick convergence while keeping false diffusion levels negligible. Huang *et al.* (2005) discretized the convective terms of their turbidity current model by blending a first order accurate upwind scheme with a second order accurate central difference scheme. Bournet *et al.* (1999) used the first order accurate hybrid scheme to discretize the convective terms of their temperature induced gravity current. First order upwind schemes should be avoided when the flow is not aligned with the grid, because they are prone to false diffusion (Versteeg and Malalasekera, 1995, pg. 119).

The transient term (first term on the left-hand side of equation 4.5.1) was discretised using a second-order backward difference scheme (FLUENT 6.3, pg. 25-17)

$$\frac{\partial \phi}{\partial t} = \frac{3\phi^{n+1} - 4\phi^n + \phi^{n-1}}{2\Delta t} \tag{4.5.3}$$

where ϕ^{n+1} is the value of ϕ at the next time level $t + \Delta t$, ϕ^n is the value of ϕ at the present time level t and ϕ^{n-1} is the value of ϕ at the previous time level $t - \Delta t$. The face values of ϕ for the convection and diffusion terms referred to next time level, making the time integration fully implicit (FLUENT 6.3, pg. 25-18). Implicit schemes were also used by Huang *et al.* (2005) (second-order accurate) and Bournet *et al.* (1999) (first-order accurate).

4.5.2 Mixture momentum and continuity equations: discretization

The pressure-based solver also uses equation 4.5.1 as the discretized form of the mixture momentum and continuity equations. For example, by setting $\phi = U$ the discretized U-momentum equation is obtained. Similarly, the discretized continuity equation can be obtained by setting $\phi = 1$. These discretized equations contain face values of velocity and pressure.

The required face pressure values are interpolated from cell center values using the body-force weighted scheme(FLUENT 6.3, pg. 25-24). This scheme computes

the face pressure by assuming that the normal gradient of the difference between pressure and body forces is constant. The face velocity values are interpolated from cell centre values using a procedure similar to Rhie and Chow (1983). This procedure prevents the unrealistic checker-boarding of the pressure field.

Table 4.4 summarizes the interpolation schemes used for all the flow variables. In addition to selecting accurate interpolation schemes, under-relaxation factors also need to be specified for the equations being solved. Under-relaxation factors play an important role in the stability and convergence rate of the numerical solver (FLUENT 6.3, pg. 25-75). It was found that the rate of convergence was most sensitive to the momentum and pressure under-relaxation factors. Table 4.5 presents the under-relaxation factors used for all the flow variables.

4.5.3 Pressure-velocity coupling

For the pressure-velocity coupling, the Pressure-Implicit with Splitting of Operators (PISO) scheme was selected, due to its ability to rapidly converge in unsteady problems (FLUENT 6.3, 25-29, 25-72), (Versteeg and Malalasekera, 1995, pg. 150). Huang *et al.* (2005) also used this scheme for their turbidity current model. Under the PISO scheme the greatest convergence rate was achieved when only one skewness correction iteration was used and no neighbour correction iterations. Bournet *et al.* (1999) used the SIMPLEST scheme for their temperature induced gravity currents. For problems in which the momentum equations are not strongly coupled to the scalar variable (for example temperature or species), the PISO scheme has been shown to require less computational effort than SIMPLE (Semi-Implicit Method for Pressure-Linked Equations) variants. However, for strongly coupled problems the computational effort for the PISO scheme is the same as SIMPLE variants.

Round-off errors can be significant for flows driven by buoyant forces having small density differences, as well as for scalar diffusion calculations with low concentrations of one species (MARNET-CFD, 2003, pg. 25). Therefore a 64-bit (double-precision) representation of real numbers was used (FLUENT 6.3, pg. 1-1).

Variable	Scheme
Pressure	Body force weighted
Density	Second order upwind
Momentum	Second order upwind
k	Second order upwind
ϵ	Second order upwind
$\langle\omega\rangle$	Second order upwind

Table 4.4: Interpolation schemes for solution variables

Variable	under-relaxation factor
Pressure	0,6
Density	1,0
Body forces	1,0
Momentum	0,35
k	0,8
ϵ	0,8
ν_t	1,0
$\langle\omega\rangle$	1,0

Table 4.5: Under-relaxation factors for solution variables

4.5.4 Grid independence

In order to capture all the features of the gravity current flow, a fine enough grid has to be used. If the grid is too coarse, the solution will be sensitive to the grid resolution. As the grid is refined, computational cost increases but the solution becomes insensitive to the grid resolution. The aim is, therefore to find the coarsest possible grid, requiring the lowest computational effort, while remaining insensitive to the grid resolution.

A grid independent solution was found by simulating the same gravity current on successively refined grids. The grid resolutions used were 5x330 (5 cell rows by 330 cell columns), 10x330, 16x660 and 25x1320. It should be noted that all the grids were locally refined in the region of the gravity current body (figure 4.2a). Furthermore, the number of cell columns refers to the region of local grid refinement. For example, there are 660 cell columns in the locally refined region for the 16x660 grid, but the region above the gravity current body has a coarser resolution with fewer cell columns.

Figures 4.5a and 4.6a show that, at 0,9 m, grid independent profiles are obtained for grids 16x660 and finer. Figures 4.5b and 4.6b show that at 2,4 m grid independent profiles are obtained for grids 10x330 and finer. Tables A.3 and A.4 also show that the depth-averaged differences for the U and $\langle\Delta\rho\rangle$-profiles are less than 1% for grids finer than 16x660. A 16x660 grid was therefore used as the default grid, since it yielded grid independent profiles at 0,9 m *and* 2,4 m for the lowest computational effort.

4.5.5 Residual independence

The level of convergence of the solution is generally assessed on the size of the residuals of the discretized equations. Large residuals indicate an unconverged solution. Different residual criteria exist by which to assess solution convergence. The present research used the scaled residual as convergence criterion. It is defined as (FLUENT 6.3, 25-123):

$$R^{\phi} = \frac{\sum_{cells} |\sum_{nb} a_{nb}\phi_{nb} + b - a_p\phi_p|}{\sum_{cells} |a_p\phi_p|} \tag{4.5.4}$$

where R^{ϕ} is the scaled residual of scalar quantity ϕ at cell p, ϕ_p is the discrete value of the scalar quantity at the centre of cell p, a_p is the centre coefficient of the discretised equation, ϕ_{nb} is the discrete value of the scalar quantity at the centre of the neighbour cell, a_{nb} is the influence coefficient of the neighbour cell and b is the constant part of the source term in the discretised equation.

Solution convergence was declared after each time-step when all the scaled residuals of the governing equations (continuity, U-momentum, V-momentum, $\langle\omega\rangle$, k and ϵ) were less than a maximum allowable value. By decreasing the maximum allowable value, the convergence criterion became more restrictive which in turn required a higher computational effort. Figures 4.7 and 4.8 presents the mean velocity and excess density profiles at 0,9 m and 2,4 m from the inlet, for scaled residual sizes of 10^{-2}, 10^{-3}, 10^{-4} and 10^{-5}. They show that there is very little difference between scaled residual sizes of 10^{-4} and 10^{-5}. Tables A.5 and A.6 also show that the depth-averaged differences for the U and $\langle\Delta\rho\rangle$-profiles are negligible for scaled residuals smaller than 10^{-4}. The default scaled residual was therefore chosen to be 10^{-4}, which gave a converged solution for the lowest computational effort.

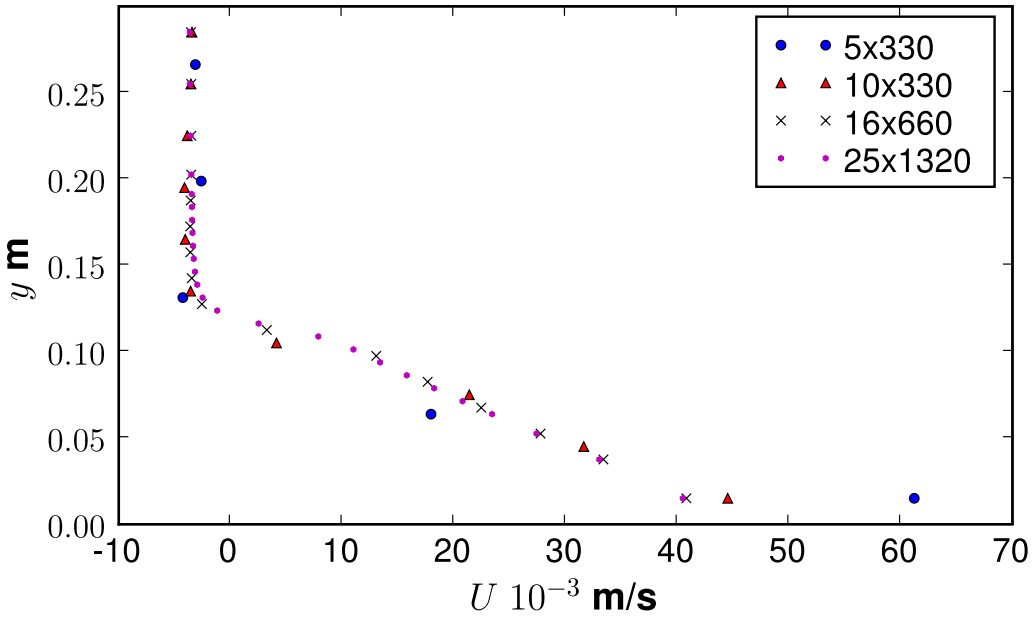

(a) 0,9 m **from the inlet**

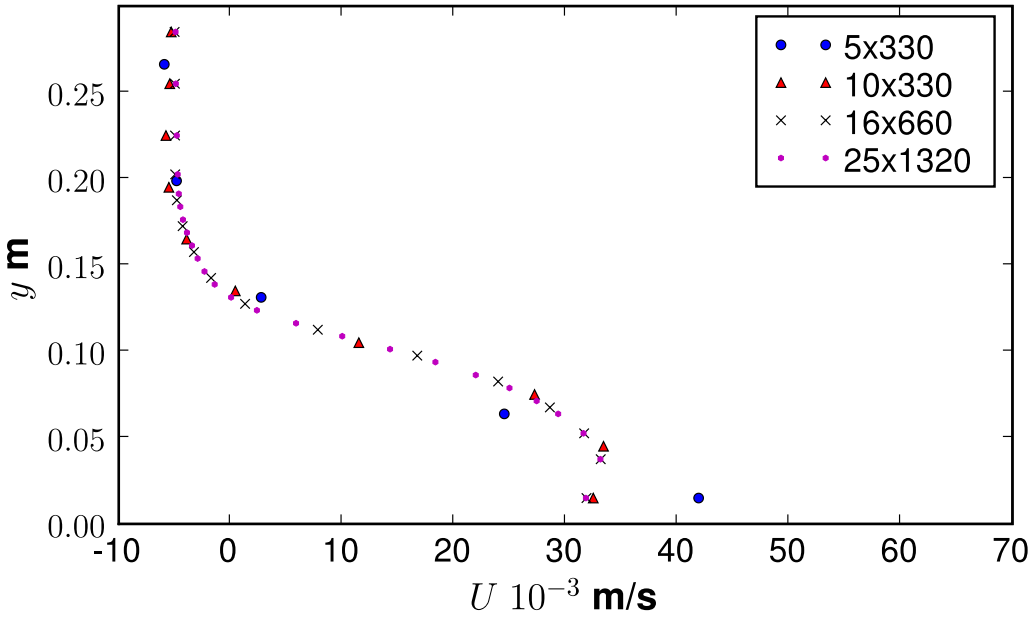

(b) 2,4 m **from the inlet**

Figure 4.5: Simulated U-profiles for different grid resolutions with standard $k-\epsilon$ model: present research

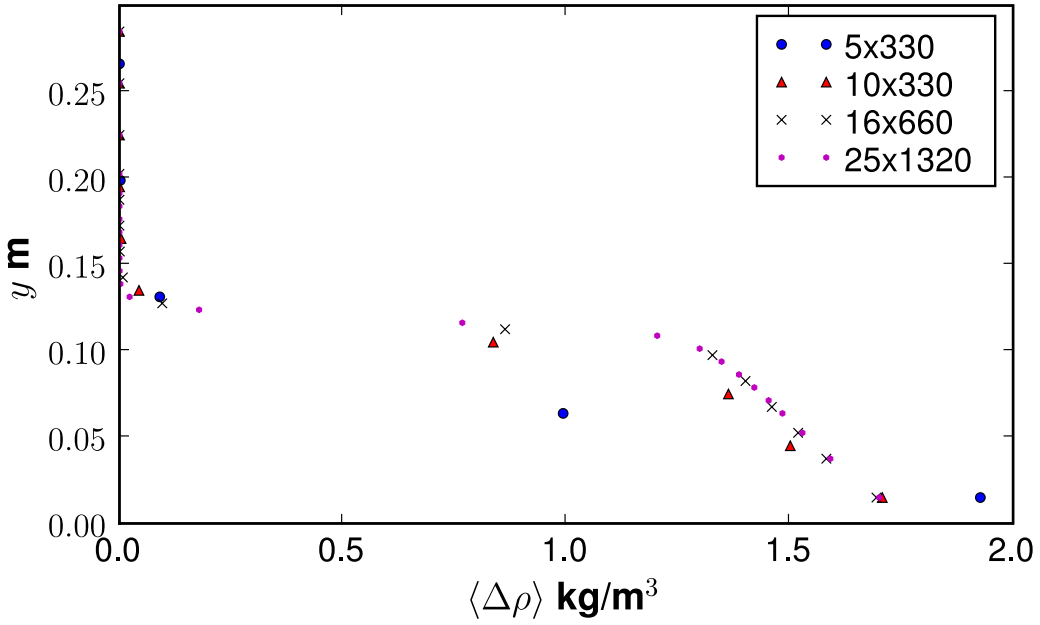

(a) 0,9 m **from the inlet**

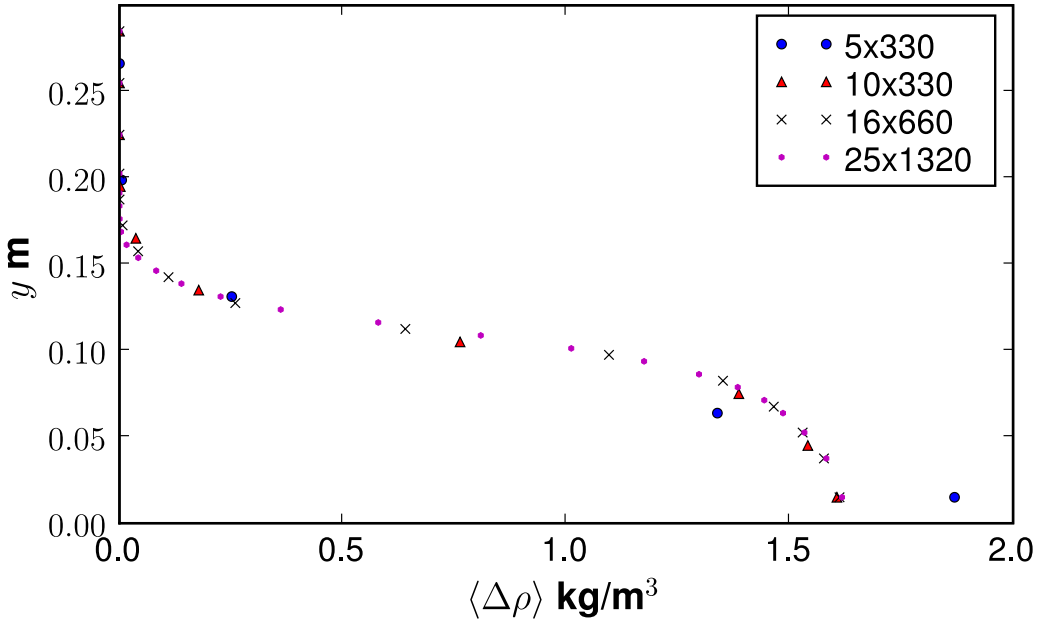

(b) 2,4 m **from the inlet**

Figure 4.6: Simulated $\langle\Delta\rho\rangle$-profiles for different grid resolutions with standard $k-\epsilon$ model: present research

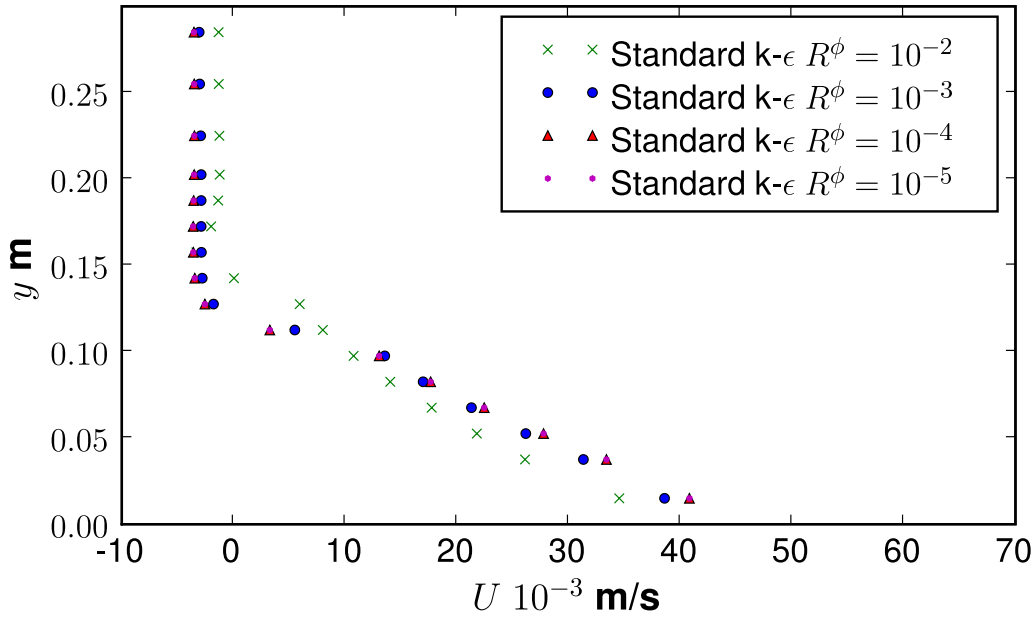

(a) 0,9 m **from the inlet**

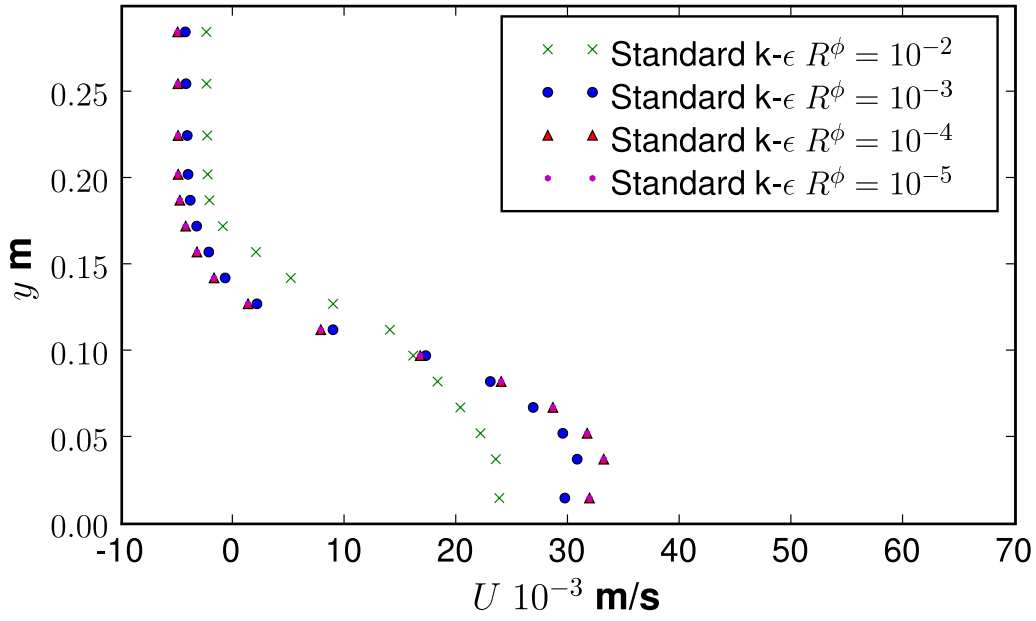

(b) 2,4 m **from the inlet**

Figure 4.7: Simulated U-profiles for different scaled residuals R^ϕ with standard $k-\epsilon$ model: present research

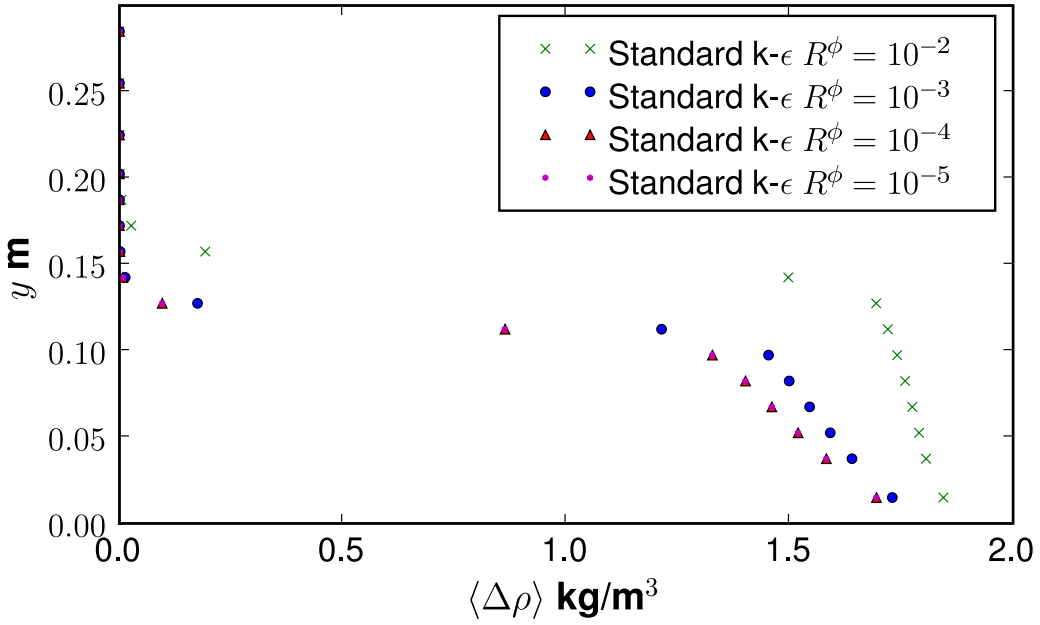

(a) 0,9 m **from the inlet**

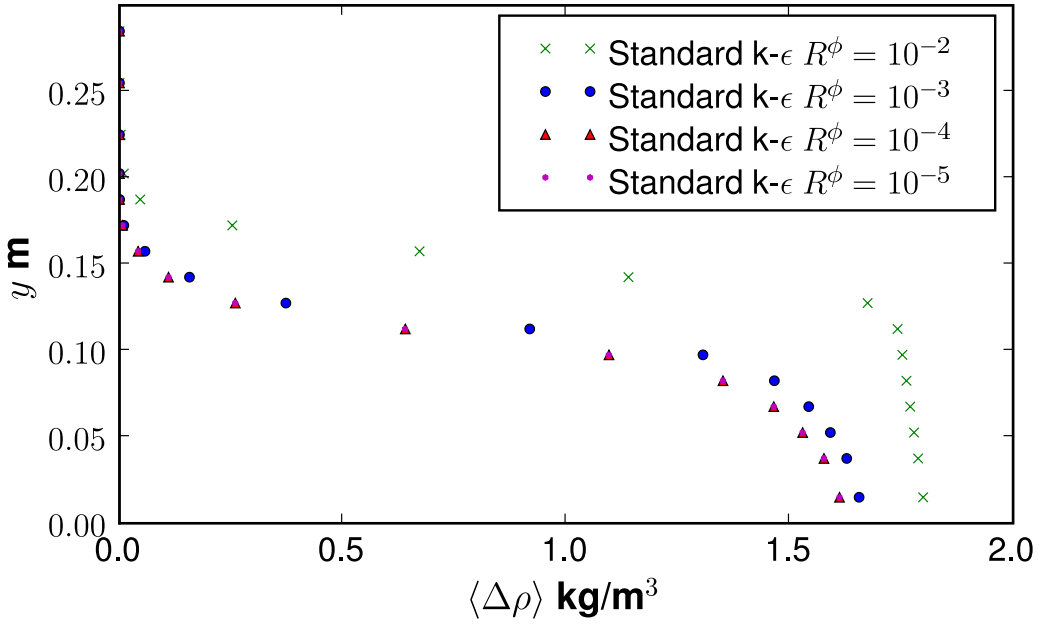

(b) 2,4 m **from the inlet**

Figure 4.8: Simulated $\langle\Delta\rho\rangle$-profiles for different scaled residuals R^ϕ with standard $k-\epsilon$ model: present research

4.5.6 Flume depth dependence

Historical experimental research has measured gravity currents in flumes of various depths. For example, Buckee *et al.* (2001) measured a gravity current in a flume with a depth of 1,5 m, while the measurements of chapter 3 were made in a flume with a depth of 0,3 m. It is important to know how deep a flume should be in order to produce velocity and excess density profiles which will be independent of the flume depth. Figure 4.9 presents the simulated U-profiles for different flume depths at 0,9 m and 2,4 m. The U-profiles show a dependence on the flume depth if the flume depth is shallow, $< 0{,}3$ m, in the return flow region $y > 0{,}15$ m. However, the U-profiles are relatively independent of flume depth in the region of the gravity current. Figure 4.10 shows that the simulated $\langle \Delta\rho \rangle$ profiles are dependent on the flume depth for depths $< 0{,}3$ m. Figures 4.9 and 4.10 therefore suggest that the measured PIV-S profiles of chapter 3 were independent of the flume depth.

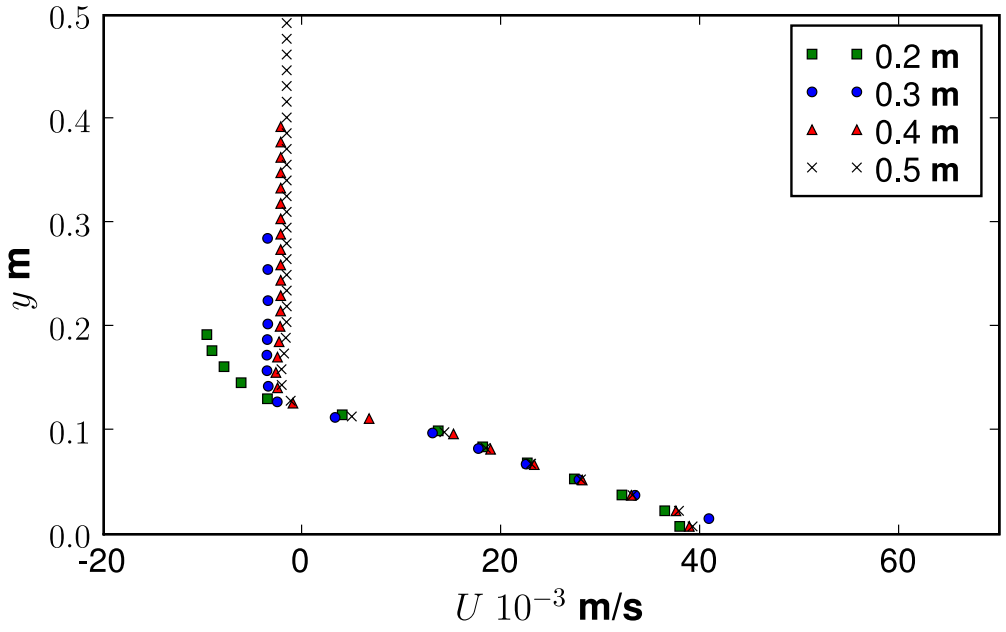

(a) 0,9 m **from the inlet**

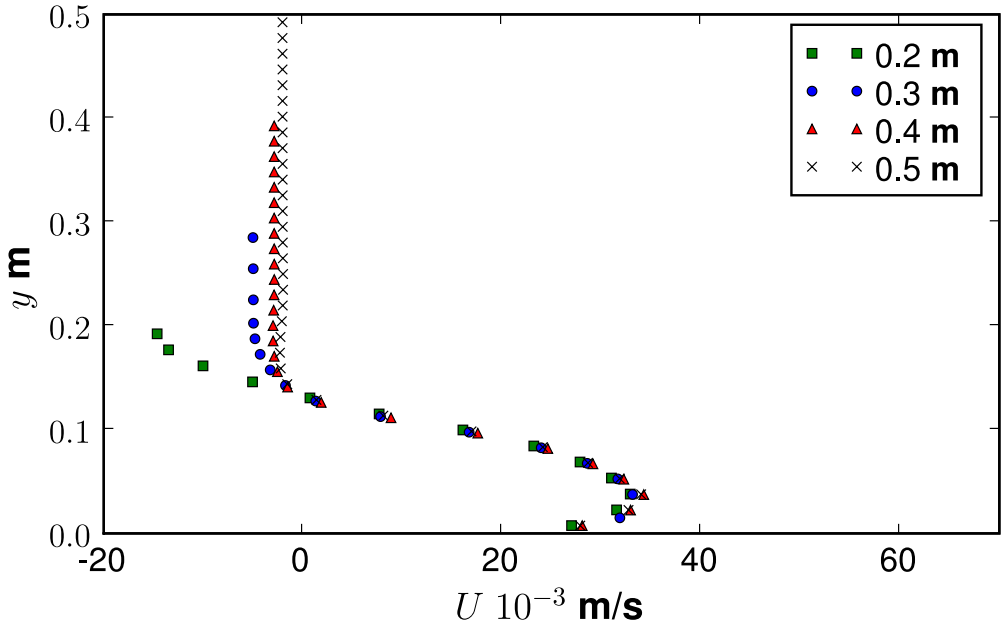

(b) 2,4 m **from the inlet**

Figure 4.9: Simulated U-profiles for different flume depths with standard $k-\epsilon$ model: present research

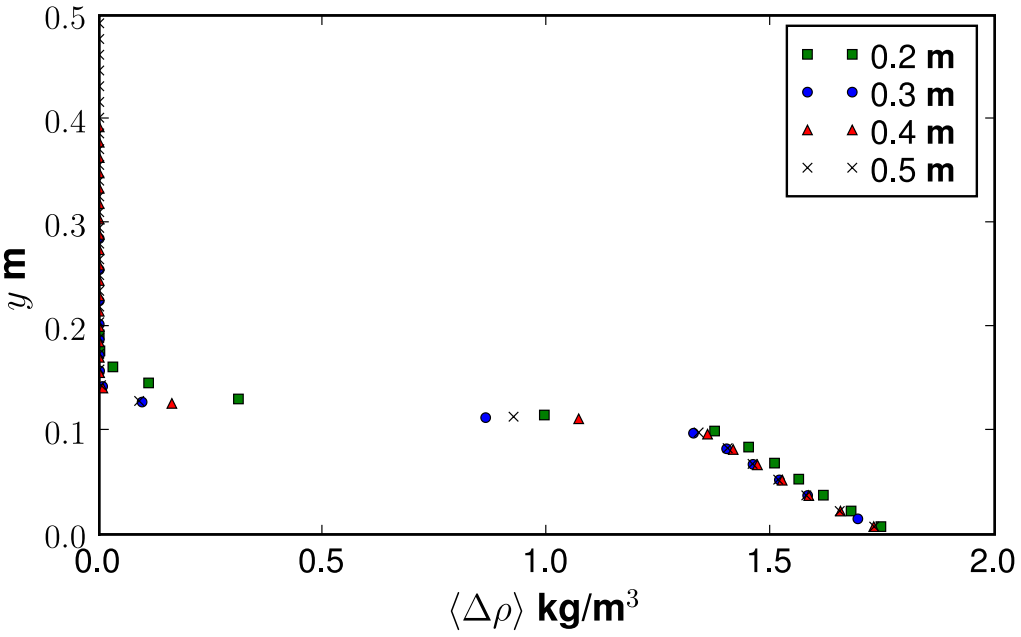

(a) 0,9 m **from the inlet**

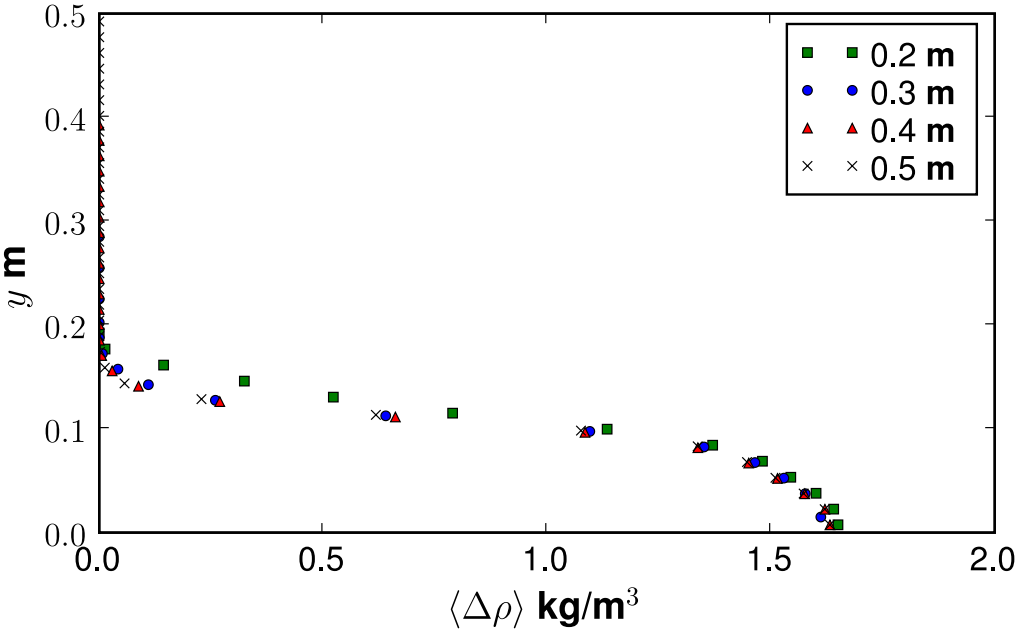

(b) 2,4 m **from the inlet**

Figure 4.10: Simulated $\langle\Delta\rho\rangle$-profiles for different flume depths with standard $k-\epsilon$ model: present research

4.6 Sensitivity analysis of turbulence models

Section 4.3 showed that the Reynolds-averaged equations do not form a closed system, due to the presence of second order moments. The system can only be closed when it is linked to a turbulence model. The accuracy of the solution is therefore dependent on the accuracy of the turbulence model used. The present research considered five computationally inexpensive turbulence models. Two were standard $k-\epsilon$ models with constant turbulent Schmidt numbers ($\sigma_t = 0{,}7$ and $\sigma_t = 1{,}3$) and the other three were Renormalization-group (RNG) $k-\epsilon$ models. Two RNG models used constant turbulent Schmidt numbers ($\sigma_t = 0{,}7$ and $\sigma_t = 1{,}3$), while the third RNG model used a variable turbulent Schmidt number (equation 4.3.57).

A major difference between the standard $k-\epsilon$ and RNG $k-\epsilon$ turbulence models were that the RNG models had time dependent profiles, whereas the standard $k-\epsilon$ models did not. At a position of 0,9 m the profiles of the RNG models had a period of approximately 7,7 s. The periodicity of the RNG models was due to equation 4.3.58 being used to compute the turbulent viscosity. All the profiles of the RNG models were time averaged to eliminate periodicity.

Another factor which contributed to the difference between the profiles of the five models was the turbulent Schmidt number. The turbulent Schmidt number gives the ratio between turbulent momentum diffusivity and turbulent mass diffusivity. The standard $k-\epsilon$ models show the influence of the turbulent Schmidt number most clearly in figure 4.11a. The lower Schmidt number $\sigma_t = 0{,}7$ resulted in a larger turbulent diffusion coefficient and hence a larger Reynolds flux (equation 4.3.2). Therefore a large upward diffusive flux of dense fluid occurred, resulting in the step-like $\langle\Delta\rho\rangle$ profile. In contrast, the higher Schmidt number $\sigma_t = 1{,}3$ resulted in a smaller turbulent diffusion coefficient and hence a smaller Reynolds flux. The upward diffusive flux was smaller, resulting in a smoother $\langle\Delta\rho\rangle$ profile. The smaller diffusive flux resulted in a reduction of the turbulent mixing and dilution of the current. Hence the near bed $\langle\Delta\rho\rangle$ value was greater for the $\sigma_t = 1.3$ models than the $\sigma_t = 0.7$ models. Both the standard $k-\epsilon$ and RNG $k-\epsilon$ models showed this effect in figures 4.11a and 4.11b. Figure 4.11a also shows that the standard $k-\epsilon$ model is more sensitive to the turbulent Schmidt number at 0,9 m (supercritical region) than the RNG models. In contrast, figure 4.11b shows that the RNG model is more sensitive to the turbulent Schmidt number at 2,4 m (near critical region) than the standard $k-\epsilon$ models.

Figures 4.12a and 4.12b show less pronounced differences between the U profiles for the five turbulence models. High turbulent Schmidt numbers $\sigma_t = 1.3$ produced

marginally greater maximum velocities compared to low turbulent Schmidt numbers $\sigma_t = 0.7$. The reduction in maximum velocity by the low turbulent Schmidt numbers was due to the decrease in the density difference, which was the driving force of the gravity current.

Figure 4.13 presents the $\langle \Delta\rho \rangle$ contour time series for the standard $k - \epsilon$ turbulence model ($\sigma_t = 1{,}3$), while figure 4.14 presents the $\langle \Delta\rho \rangle$ contour time series for the RNG model with variable turbulent Schmidt number. The most notable difference between the two turbulence models is that the RNG model correctly predicts the occurrence of transverse vortices, due to the Kelvin-Helmholtz instability, while the $k-\epsilon$ model does not. The occurrence of the transverse vortices is limited to the supercritical region, near the inlet, as well as the rear of the gravity current head. Figures 4.13e and 4.14e show that the RNG model has a lower spreading rate than the standard $k-\epsilon$ model. The permanent transverse vortices near the inlet resulted in periodic flow profiles. Finally, it can be seen that both the standard $k - \epsilon$ and RNG $k - \epsilon$ turbulence models predict approximately the same propagation speed for the gravity current front.

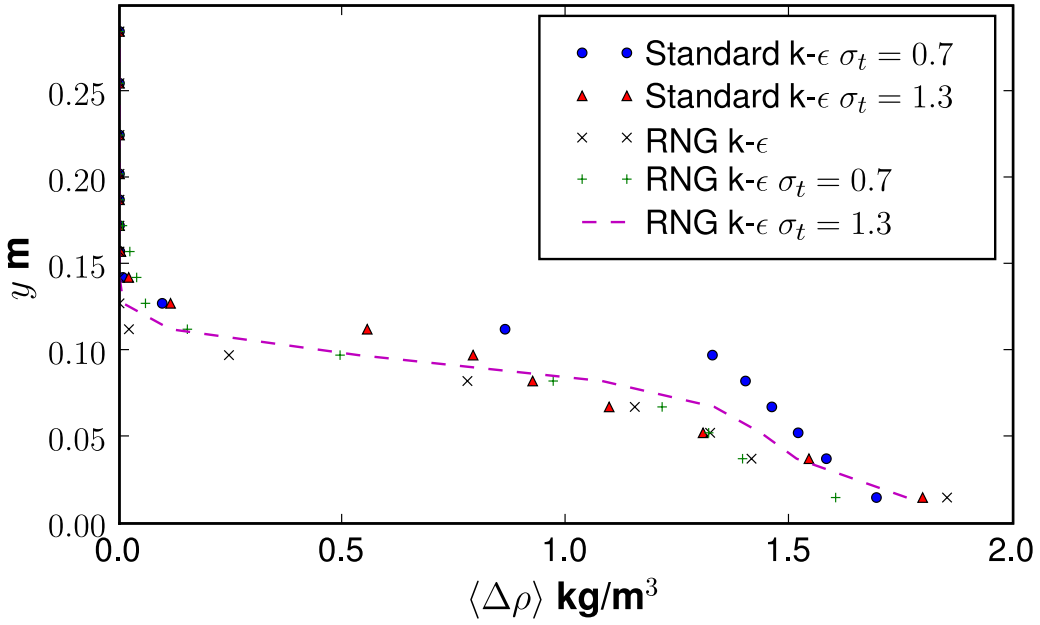

(a) 0,9 m **from the inlet**

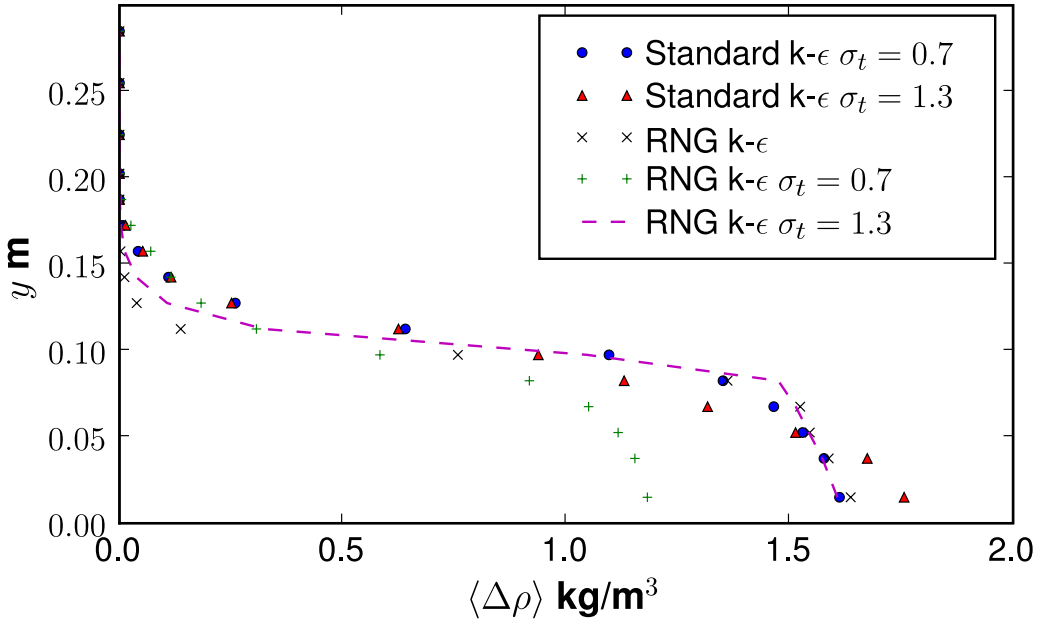

(b) 2,4 m **from the inlet**

Figure 4.11: Simulated $\langle \Delta\rho \rangle$-profiles for different turbulence models and turbulent Schmidt numbers σ_t: present research

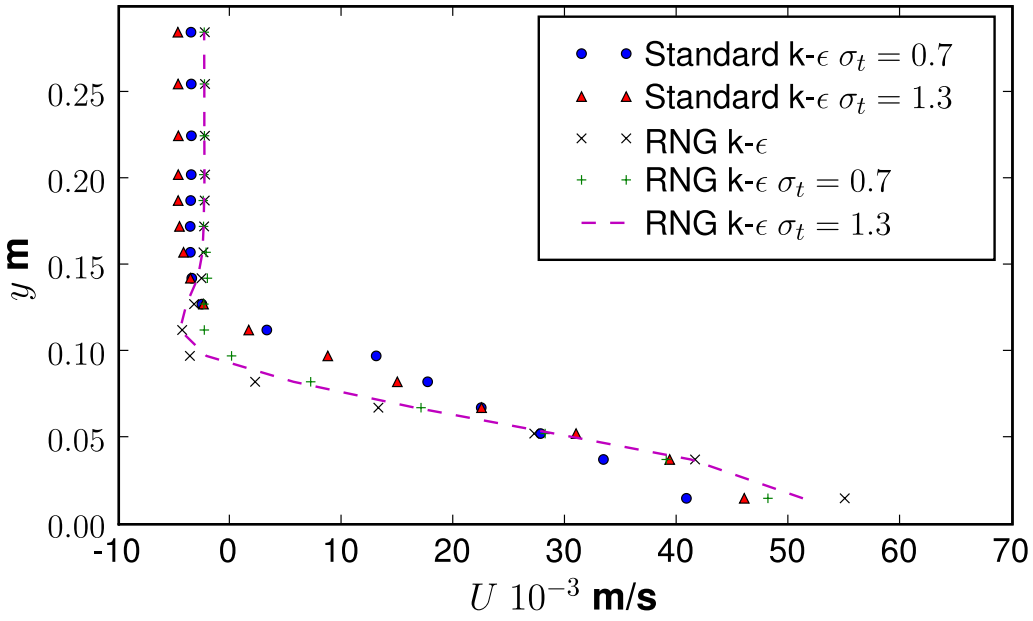

(a) 0,9 m **from the inlet**

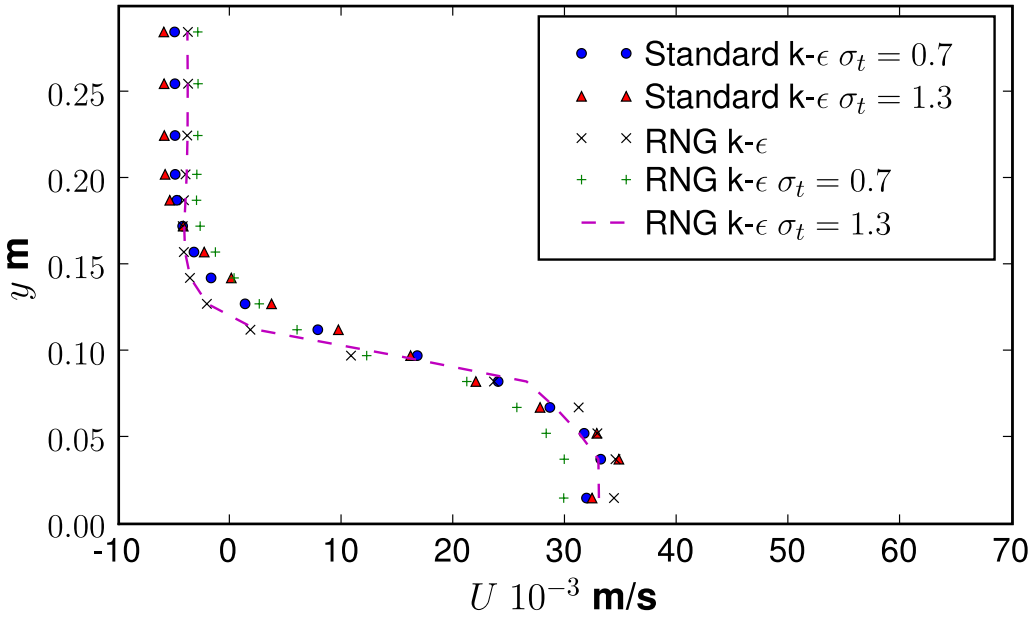

(b) 2,4 m **from the inlet**

Figure 4.12: Simulated U-profiles for different turbulence models and turbulent Schmidt numbers σ_t: present research

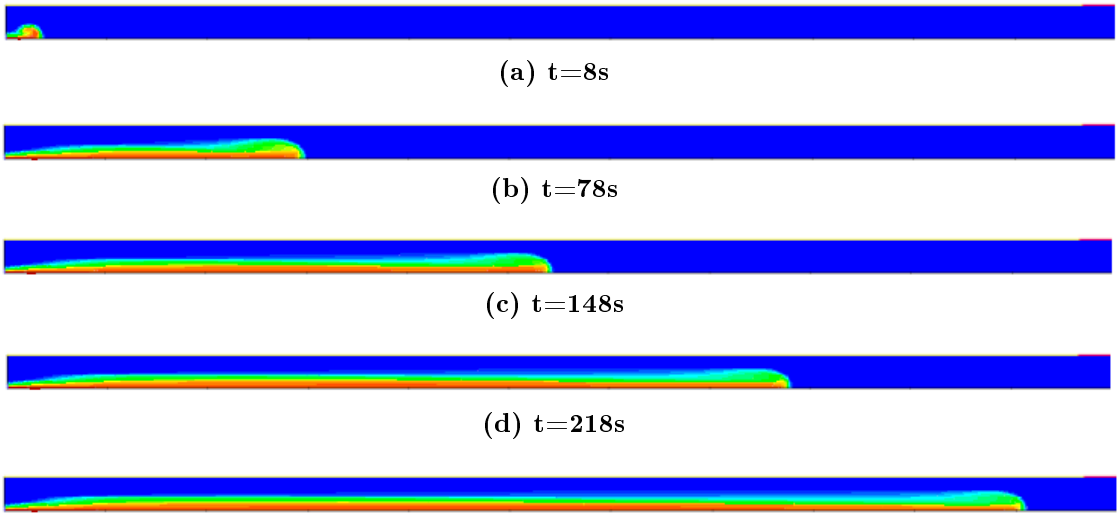

(a) t=8s

(b) t=78s

(c) t=148s

(d) t=218s

(e) t=288s

Figure 4.13: Simulated $\langle \Delta\rho \rangle$ contour time series: standard $k-\epsilon$ model with $\sigma_t = 1{,}3$: present research

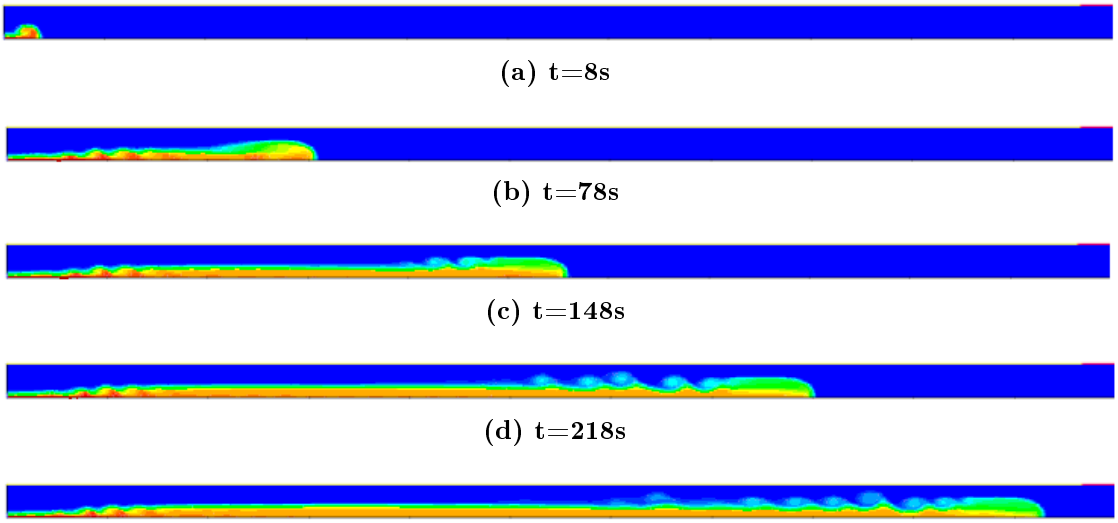

(a) t=8s

(b) t=78s

(c) t=148s

(d) t=218s

(e) t=288s

Figure 4.14: Simulated $\langle \Delta\rho \rangle$ contour time series: RNG $k-\epsilon$ model: present research

4.7 Sensitivity analysis of inlet conditions

Sections 4.5.4 and 4.5.5 showed that a 16x660 grid and a scaled residual of 10^{-4} were required to properly solve the governing equations using a standard $k-\epsilon$ turbulence model with $\sigma_t = 0{,}7$. This section investigates the change in downstream profiles due to different inlet conditions using this model.

Figures 4.15 and 4.16 present the U and $\langle\Delta\rho\rangle$ profiles at 0,9 m and 2,4 m from the inlet for different inlet velocities. Figures 4.15a and 4.15b show that an increase in inlet velocity results in an increase in the velocity maximums. Figures 4.16a and 4.16b show that this increase in inlet velocity results in greater mixing at the interface, leading to a broader, more dilute current. Furthermore, the return flow also increases with increased inlet velocity. Tables A.7 and A.8 present the depth-averaged differences for the U and $\langle\Delta\rho\rangle$-profiles. They show that a 20% increase in inlet velocity results in a $8\% - 12\%$ difference in the U-profile and a $7\% - 9\%$ difference in the $\langle\Delta\rho\rangle$-profile.

Figures 4.15a and 4.15b also shows that a decrease in inlet velocity results in reduced velocity maximums. Figures 4.16a and 4.16b show that this decrease in inlet velocity results in a narrower, less dilute current. Tables A.7 and A.8 show that a 20% decrease in inlet velocity results in a $5\% - 9\%$ difference in the U-profile and a 6% difference in the $\langle\Delta\rho\rangle$-profile. These moderate depth-averaged differences indicate that the gravity current model is sensitive to the value of the inlet velocity.

Figures 4.17 and 4.18 presents the U and $\langle\Delta\rho\rangle$ profiles at 0,9 m and 2,4 m from the inlet for different inlet $NaCl$ mass fractions. Figures 4.17a and 4.17b show that an increase in inlet $NaCl$ mass fraction increases the velocity maximums only slightly. Figures 4.18a and 4.18b show that the amount of mixing is also reduced only slightly due to the increased stable stratification. Tables A.9 and A.10 present the depth-averaged differences for the U and $\langle\Delta\rho\rangle$-profiles. They show that a 20% increase in mass fraction results in only a $2\% - 4\%$ difference in the U-profile, but a $6\% - 8\%$ difference in the $\langle\Delta\rho\rangle$-profile. A 80% increase in inlet mass fraction results in a $6\% - 10\%$ difference in the velocity profile and a $18\% - 23\%$ difference in the $\langle\Delta\rho\rangle$-profile. These depth-averaged differences indicate that the U-profile is only slightly altered by increased inlet mass fraction values, but that the $\langle\Delta\rho\rangle$-profile is significantly altered. By setting the inlet $NaCl$ mass fraction value equal to zero a wall-jet U-profile is obtained at 0,9 m (figure 4.17a). Similarly, an open-channel U-profile is obtained at 2,4 m.

Figures 4.19 and 4.20 presents the U and $\langle\Delta\rho\rangle$ profiles at 0,9 m and 2,4 m from the inlet for different inlet k values. Tables A.11 and A.12 present the depth-

averaged differences for these profiles. A 20% increase or decrease in the inlet k value results in depth-averaged difference of less than 0,1% for the U and $\langle\Delta\rho\rangle$ profiles. These very low depth-averaged differences indicate that the inlet k value does not significantly influence the downstream evolution of the gravity current.

Figures 4.21 and 4.22 presents the U and $\langle\Delta\rho\rangle$ profiles at 0,9 m and 2,4 m from the inlet for different inlet ϵ values. Tables A.13 and A.14 present the depth-averaged differences for these profiles. A 20% increase or decrease in the inlet ϵ value results in depth-averaged difference of less than 0,2% for the U and $\langle\Delta\rho\rangle$ profiles. These very low depth-averaged differences indicate that the inlet ϵ value does not significantly influence the downstream evolution of the gravity current. In conclusion, the downstream evolution of the gravity current is influenced primarily by the inlet velocity and $NaCl$ mass fraction and not the inlet turbulence conditions k and ϵ.

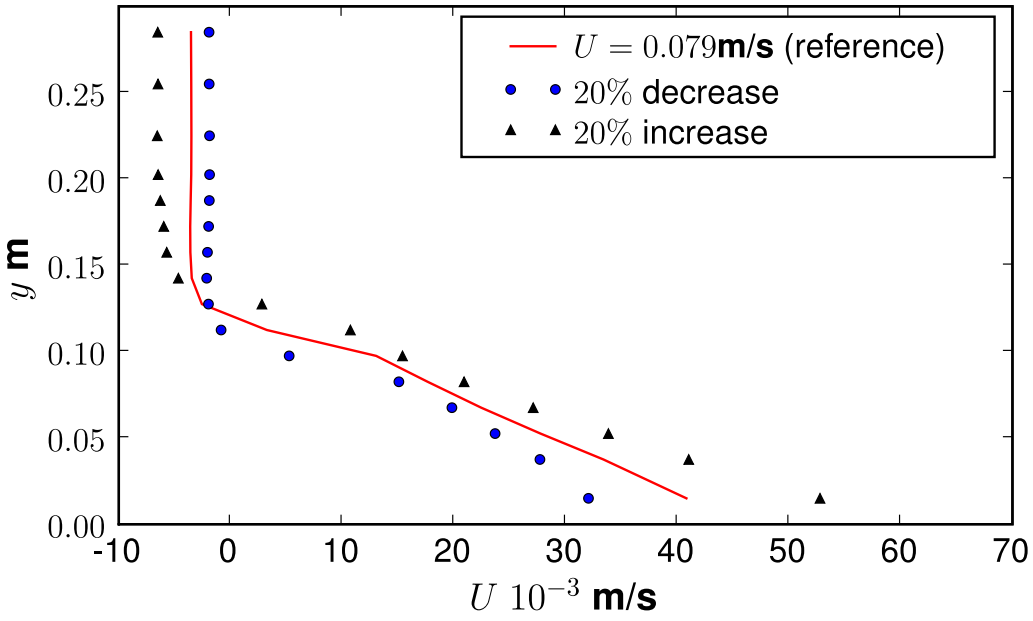

(a) 0,9 m **from the inlet**

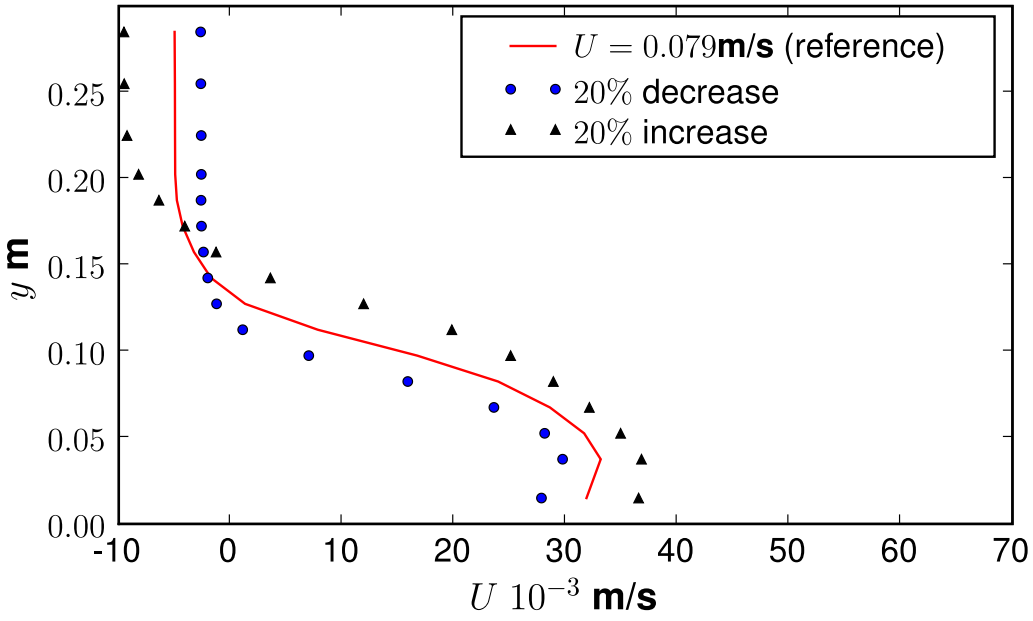

(b) 2,4 m **from the inlet**

Figure 4.15: Simulated U-profiles for different inlet velocities with standard $k-\epsilon$ model: present research

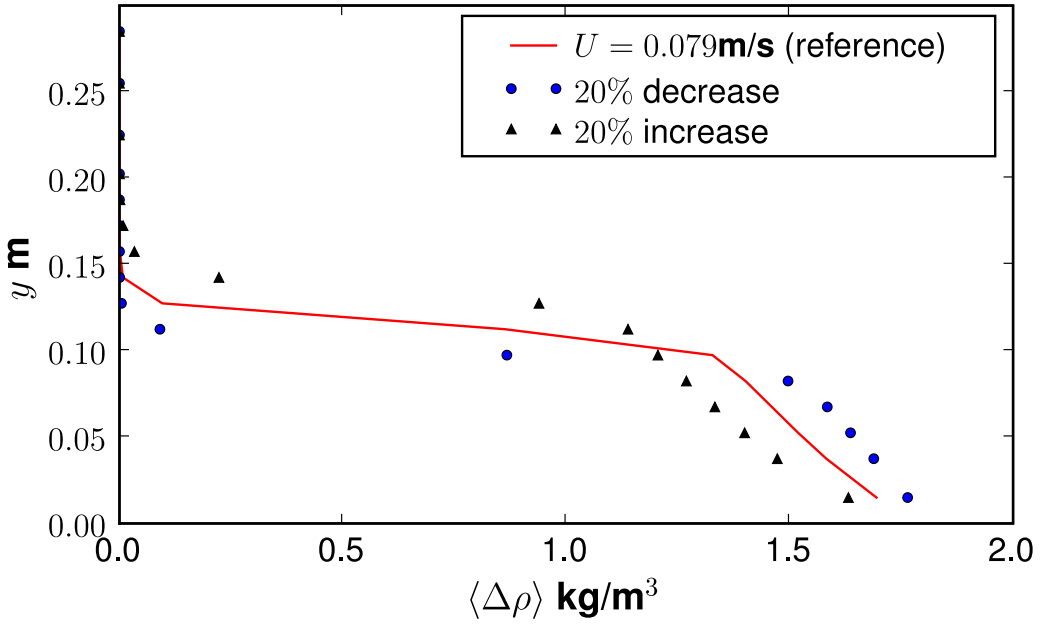

(a) 0,9 m **from the inlet**

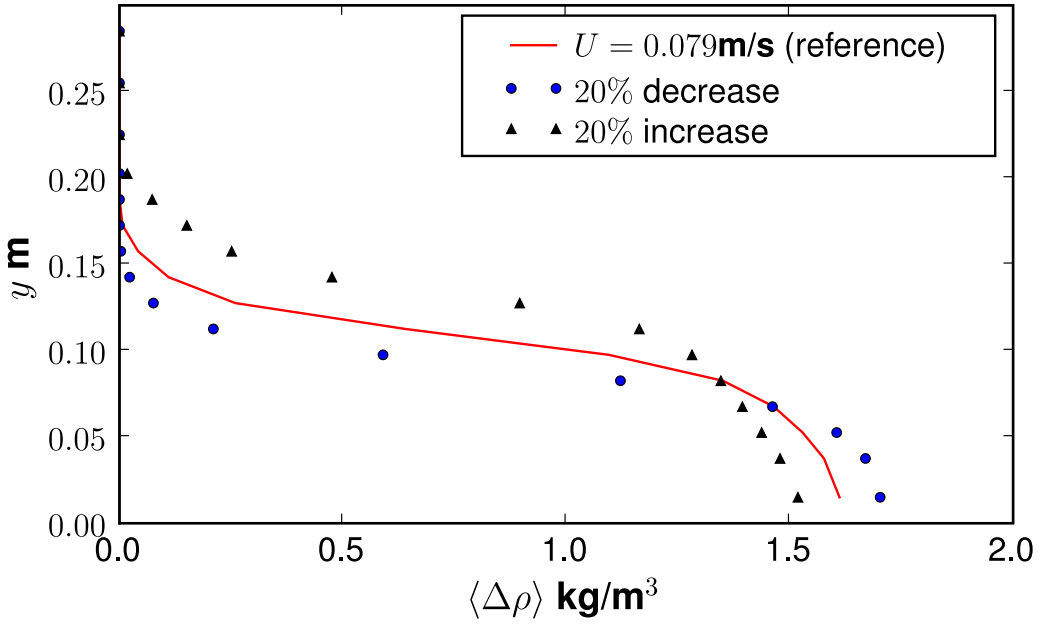

(b) 2,4 m **from the inlet**

Figure 4.16: Simulated $\langle \Delta\rho \rangle$-profiles for different inlet velocities with standard $k - \epsilon$ model: present research

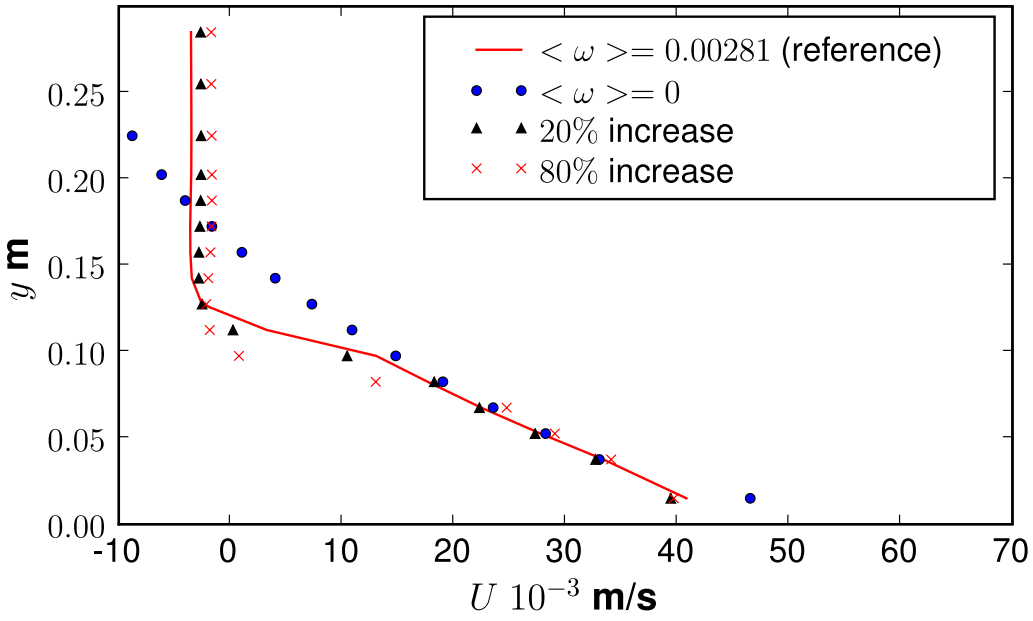

(a) 0,9 m **from the inlet**

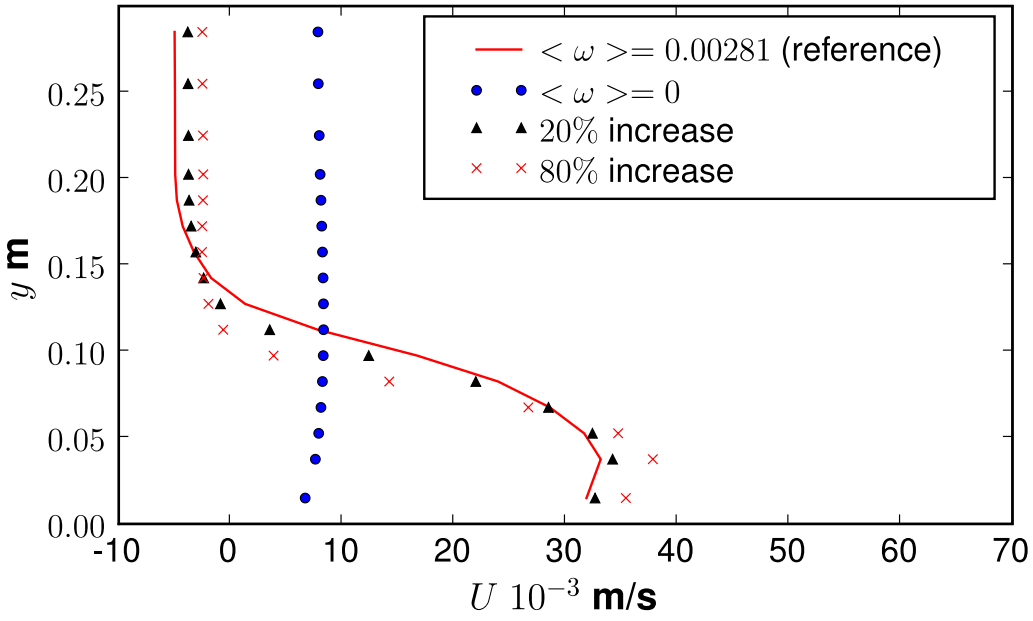

(b) 2,4 m **from the inlet**

Figure 4.17: Simulated U-profiles for different inlet $NaCl$ mass fractions with standard $k-\epsilon$ model: present research

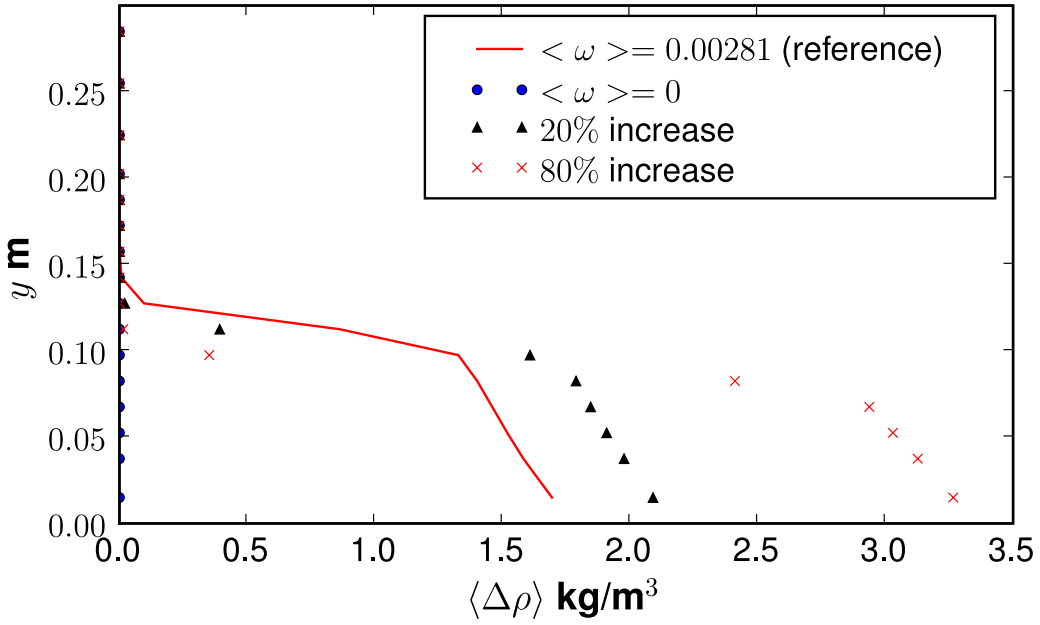

(a) 0,9 m **from the inlet**

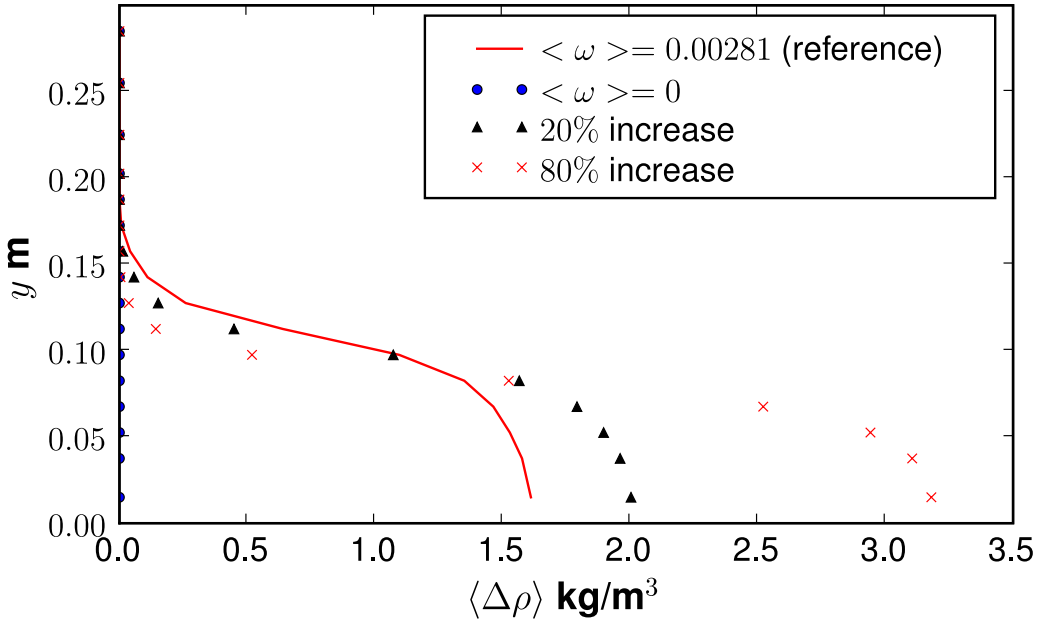

(b) 2,4 m **from the inlet**

Figure 4.18: Simulated $\langle \Delta\rho \rangle$-profiles for different inlet $NaCl$ mass fractions with standard $k - \epsilon$ model: present research

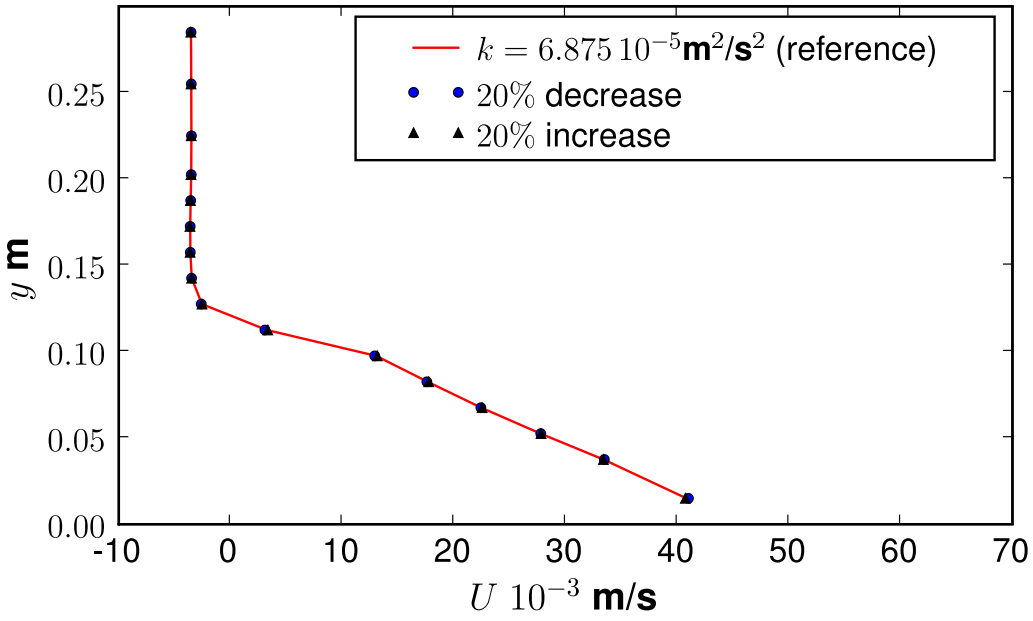

(a) 0,9 m **from the inlet**

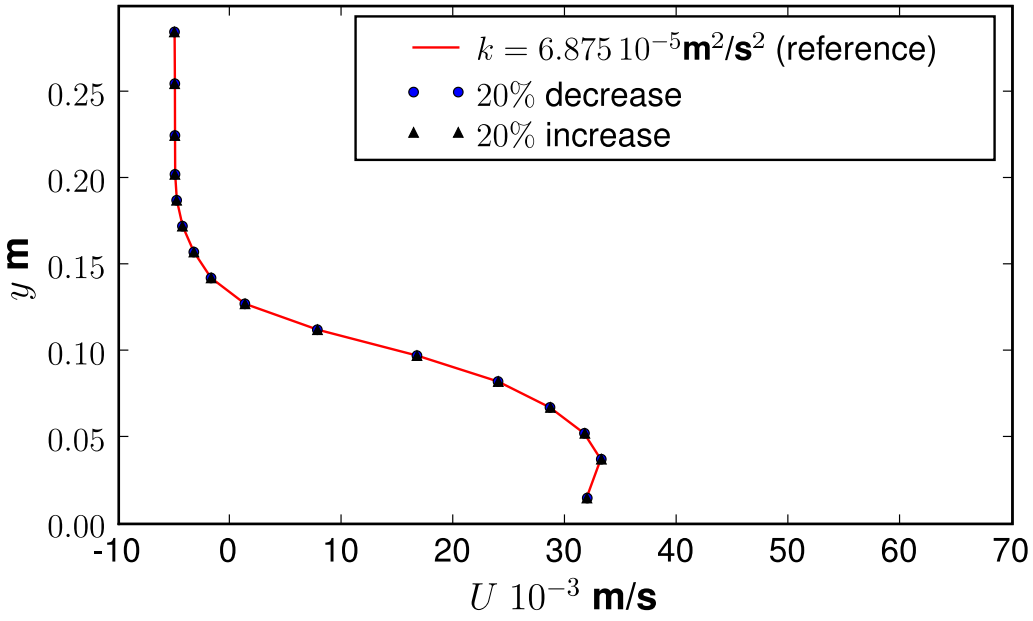

(b) 2,4 m **from the inlet**

Figure 4.19: Simulated U-profiles for different inlet k values with standard $k-\epsilon$ model: present research

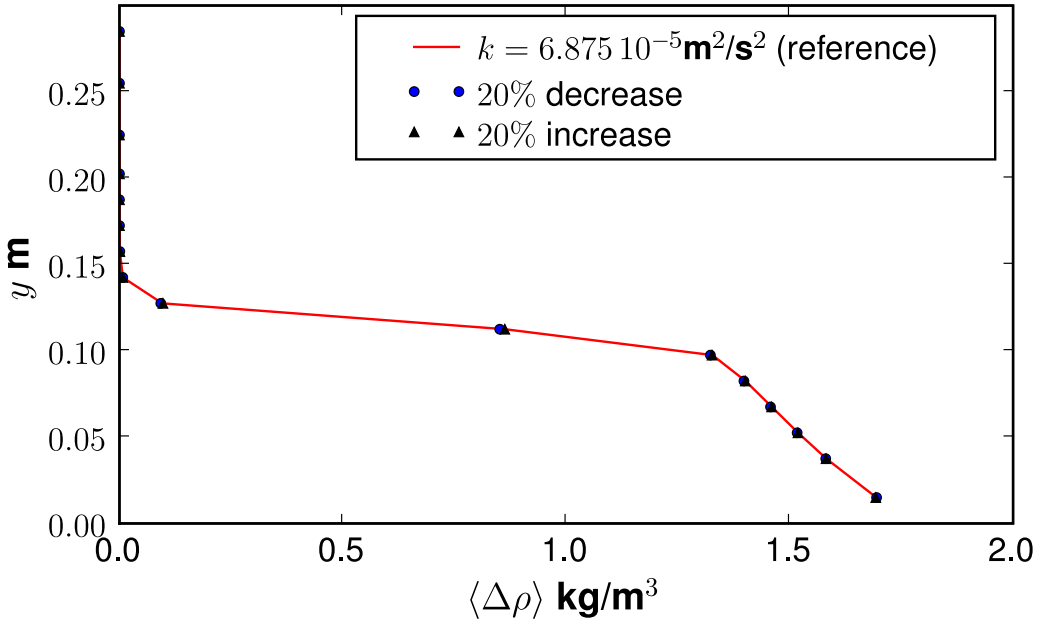

(a) 0,9 m **from the inlet**

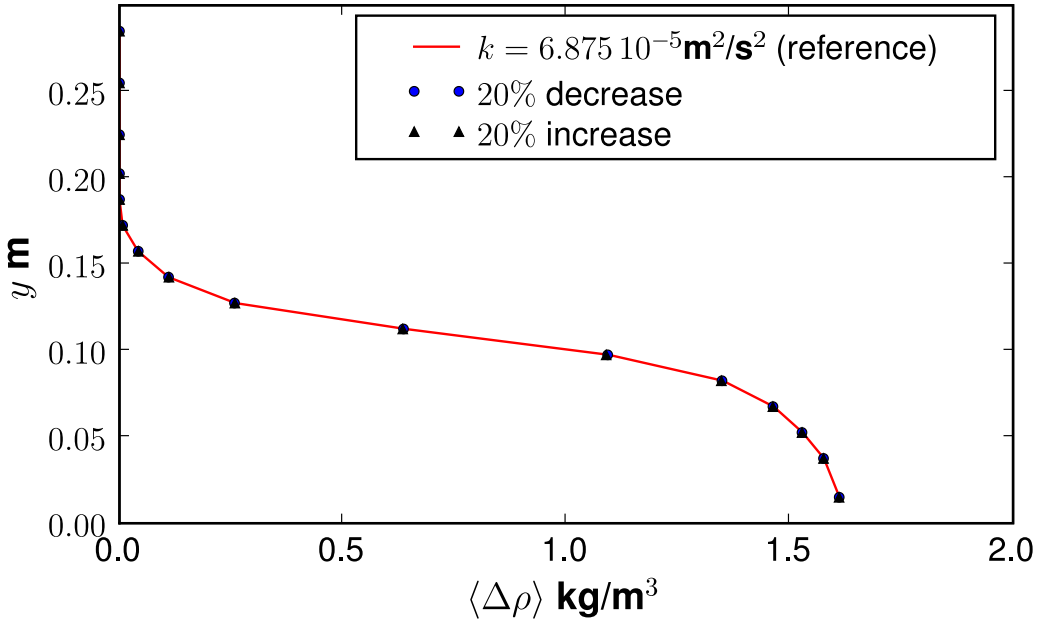

(b) 2,4 m **from the inlet**

Figure 4.20: Simulated $\langle \Delta\rho \rangle$-profiles for different inlet k values with standard $k - \epsilon$ model: present research

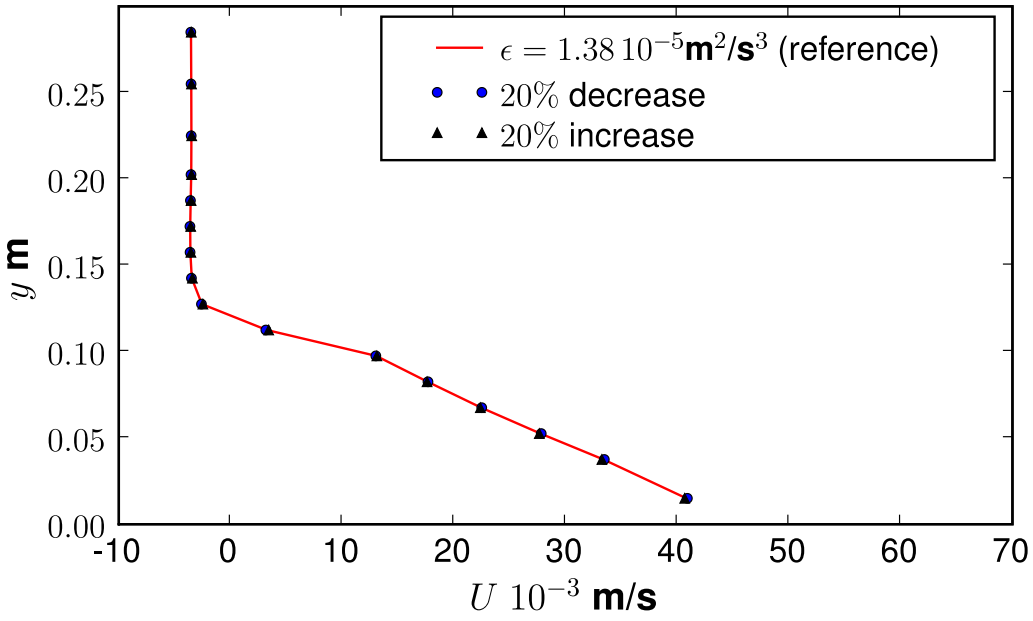

(a) 0,9 m **from the inlet**

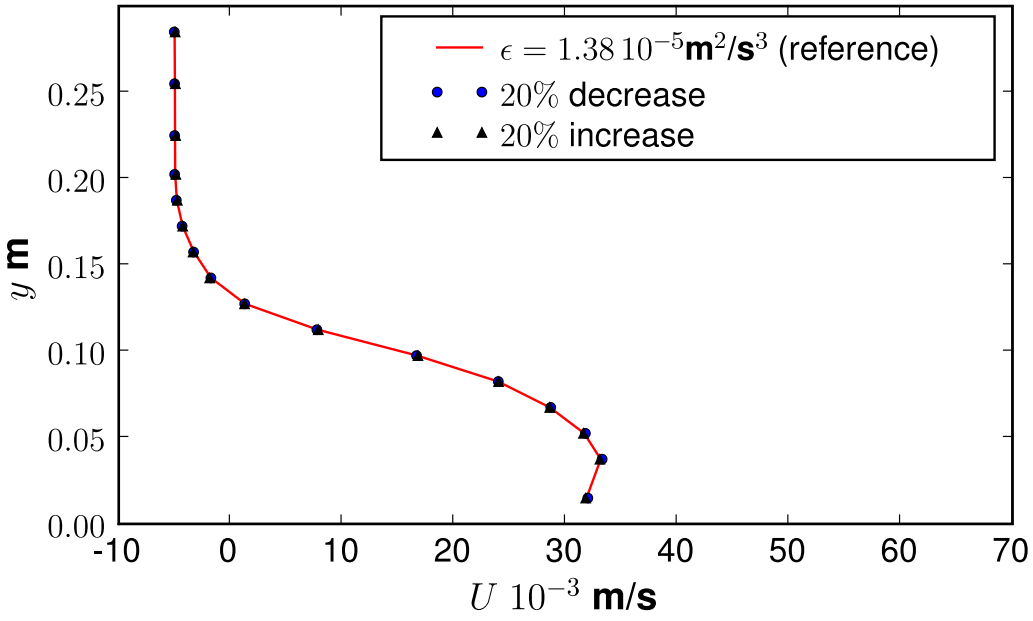

(b) 2,4 m **from the inlet**

Figure 4.21: Simulated U-profiles for different inlet ϵ values with standard $k-\epsilon$ model: present research

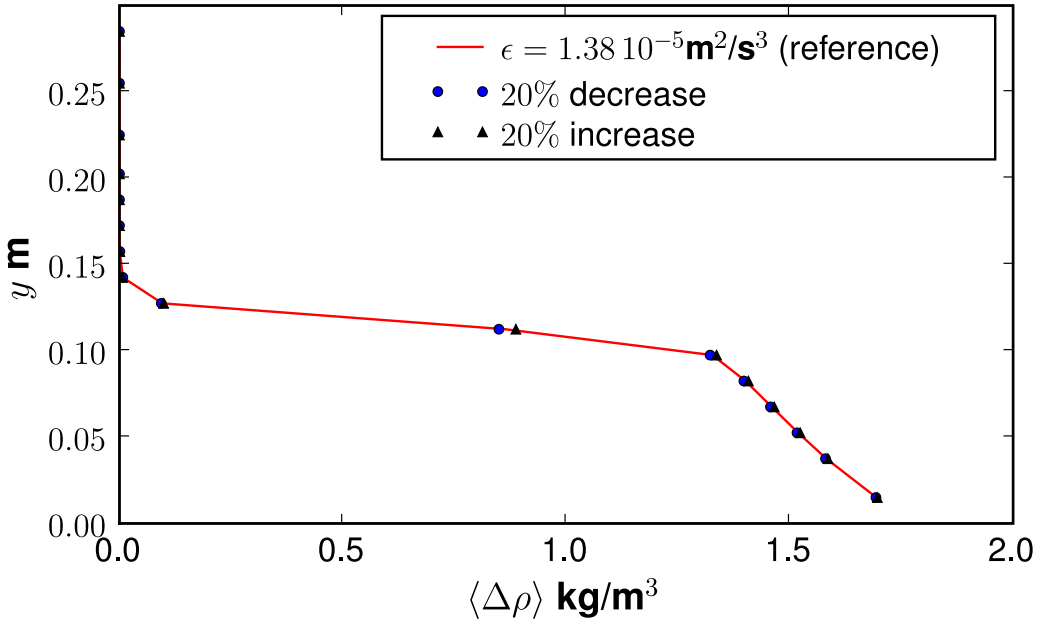

(a) 0,9 m **from the inlet**

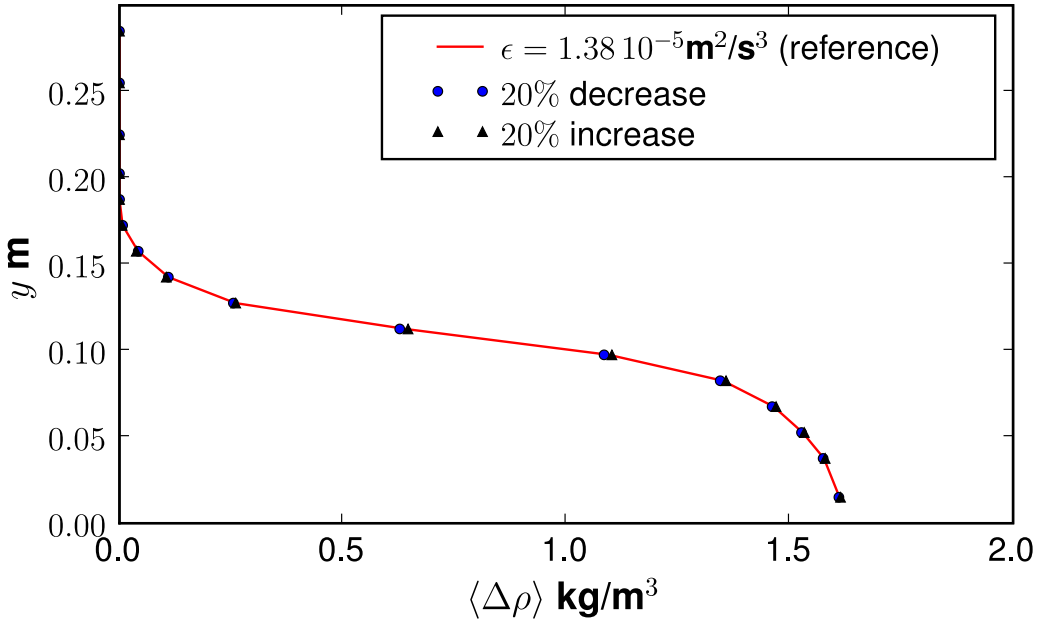

(b) 2,4 m **from the inlet**

Figure 4.22: Simulated $\langle \Delta\rho \rangle$-profiles for different inlet ϵ values with standard $k - \epsilon$ model: present research

4.8 Evaluation of model accuracy

Much historical and numerical research has focused on gravity currents moving along an inclined bed. These currents quickly reach an approximately self-similar state where only one lengthscale, velocity scale and excess density scale is required to describe all mean quantities in terms of a single geometrical variable. The profile shapes of mean quantities therefore remain similar with increasing downstream distance. In this state the current height increases linearly with increasing distance, while the current velocity remains constant. One of the aims of the present research was to evaluate the accuracy of a gravity current model in a region where self-similarity did not exist. The previous sections have investigated the sensitivity of the numerical model to grid resolution, convergence criterion, turbulence models and inlet conditions. This section evaluates the accuracy of the numerical model with the PIV-S measurements of chapter 3 for a region where self-similarity does not hold. This was done by comparing simulated and measured profiles, as well as comparing the downstream development of the flow scales.

4.8.1 Evaluation of simulated profiles

In order to compare PIV-S measured profiles with simulated profiles quantively the depth-averaged error ε_d is introduced (present research):

$$\varepsilon_d\left[\phi, \text{PIV-S,model}\right] = \frac{1}{L}\int_0^L \frac{\left|\phi\left(y,\text{ model}\right) - \phi\left(y,\text{ PIV-S}\right)\right|}{max\left[\phi\left(y,\text{ PIV-S}\right)\right]}dy \tag{4.8.1}$$

where y is the height above the bed, $\phi\left(y,\text{ PIV-S}\right)$ is the measured profile of scalar quantity ϕ, $\phi\left(y,\text{ model}\right)$ is the simulated profile of scalar quantity ϕ for a model scenario, L is the height of the shortest profile and max is the profile maximum.

The simulated and measured U profiles at 0,9 m and 2,4 m are presented in figures 4.23a and 4.23b. They show that all three numerical models underpredict the U-velocity for the gravity current. Furthermore, none of the models predict the negative velocity gradient, due to the return flow, at a depth of 0,15 m. At a position of 0,9 m the RNG model has the most accurate velocity gradient, while at 2,4 m the standard $k-\epsilon$ models have the most accurate velocity gradient. Table A.15 presents the depth-averaged error for the U profiles. It shows that the standard $k-\epsilon$ model with a turbulent Schmidt number of $\sigma_t = 1.3$ is within 10% of the PIV-S measurements at 0,9 m and within 20% at 2,4 m. The depth-averaged error of the other two models compares only slightly more poorly to the PIV-S measurements.

Figures 4.24a and 4.24b present the simulated and measured $\langle \Delta\rho \rangle$ profiles at 0,9 m and 2,4 m. They show that, in general, the numerical models overpredict $\langle \Delta\rho \rangle$, which follows from the conservation of depth-averaged excess density and the underprediction of the U velocity. Furthermore, at 2,4 m both the RNG and standard $k - \epsilon$ ($\sigma_t = 0.7$) models predict a stepped $\langle \Delta\rho \rangle$ profile, contrary to the smooth PIV-S profile. Table A.16 presents the depth-averaged error for the $\langle \Delta\rho \rangle$ profiles. It shows that the standard $k - \epsilon$ ($\sigma_t = 1.3$) and RNG models have the lowest error of approximately 10% at 0,9 m and 2,4 m. At 0,9 m the error of the standard $k - \epsilon$ ($\sigma_t = 0.7$) model is almost double that of the other two models.

The simulated and measured ν_t/ν profiles are presented in figures 4.25a and 4.25b. At 0,9 m the $\sigma_t = 0.7$ model correctly predicts the depth of the outer ν_t/ν peak, but overestimates its value by a factor of two. The $\sigma_t = 1.3$ model correctly predicts the value of the outer peak, but incorrectly suggests that it is located near the bed. At a position of 2,4 m both models correctly predict the inner ν_t/ν peak. Table A.17 presents the depth-averaged error for these profiles. It shows that the $\sigma_t = 1.3$ model has the lowest depth-averaged error of $16\% - 22\%$ at 0,9 m and 2,4 m.

Figures 4.26a and 4.26b present the simulated and measured $\langle \Delta\rho' v' \rangle$ profiles. Section 4.3.2 showed that the flux-gradient hypothesis incorrectly predicts the orientation of the Reynolds flux vector. However, figures 4.26a and 4.26b show that the flux-gradient hypothesis gives a reasonable estimate of the important cross-stream flux $\langle \Delta\rho' v' \rangle$. The $\sigma_t = 0.7$ model incorrectly predicts two peaks, while the $\sigma_t = 1.3$ model predicts, correctly, a single outer peak. Table A.18 presents the depth-averaged error for these profiles. It shows that the $\sigma_t = 1.3$ model has the lowest depth-averaged error of 15% at 0,9 m and 2,4 m. The $\sigma_t = 0.7$ model has an error of approximately 25%.

The simulated and measured $\mathcal{P}$ and G_b profiles at 0,9 m and 2,4 m are presented in figures 4.27a and 4.27b. At 0,9 m the $\sigma_t = 0.7$ model incorrectly predicts two buoyancy production peaks and two shear production peaks. The $\sigma_t = 1.3$ model correctly predicts single outer peaks for the buoyancy production and shear production. At 2,4 m both models correctly predict a weak outer shear production peak and an inner shear production peak. The $\sigma_t = 0.7$ model however, incorrectly, predicts an outer buoyancy production peak. Table A.19 presents the depth-averaged error for these profiles. The depth-averaged error for both models is less than 6% at 0,9 m and 2,4 m. The error of the $\sigma_t = 1.3$ model is slightly lower than that of the other model.

The evaluation of the gravity current model in terms of depth-averaged error suggests that the standard $k - \epsilon$ multispecies model with a turbulent Schmidt

number of $\sigma_t = 1.3$ produces the best results for a current which does not exhibit self-similarity. The depth-averaged errors are within $10\% - 20\%$ for the U-velocity and approximately 10% for $\langle \Delta\rho \rangle$.

4.8.2 Evaluation of flow scale development

Figure 4.28a presents the simulated and measured downstream development of the outer lenghtscale $y_{0.5}$. The downstream distance x and lengthscale $y_{0.5}$ has been normalized by the inlet height h. The simulated and measured lengthscales are in close agreement at $x/h = 30$. However, the model underpredicts the outer lengthscale at $x/h = 80$ by 0,38. The simulation shows that the current height increases linearly between $0 < x/h < 30$ and becomes constant for $x/h > 50$. This constancy occurs when no ambient water is entrained into the current and suggests that turbulence has collapsed for $x/h > 50$.

The simulated and measured downstream development of the excess density scale $\langle \omega \rangle_{max}$ is presented in figure 4.28b. The excess density scale has been normalized by the inlet excess density $\langle \omega \rangle_o$. The figure shows that the numerical model slightly underpredicts the excess density scale by 0,034 at $x/h = 30$ and 0,029 at $x/h = 80$. Similar to the outer lengthscale, $\langle \omega \rangle_{max}$ also approaches constancy for $x/h > 50$. This constancy also suggests that turbulence has collapsed, because turbulent mixing is the primary mechanism by which the current is diluted. Figure 4.29 presents the simulated and measured downstream development of the outer velocity scale U_{max}. The outer velocity scale has been normalized by the cross section-averaged inlet velocity U_{bulk}. It shows that the numerical model underpredicts the velocity scale by as much as 0,269 at $x/h = 30$ and 0,196 at $x/h = 80$. This underprediction was also shown in figures 4.23a and 4.23b.

In conclusion, the numerical model predicts reasonably well the downstream development of the outer length and excess density scales. In contrast, the difference between the measured and simulated downstream development of the outer velocity scale is quite large. Despite the low estimates of the outer velocity scale the model is able to simulate gravity current flow where self-similarity does not hold.

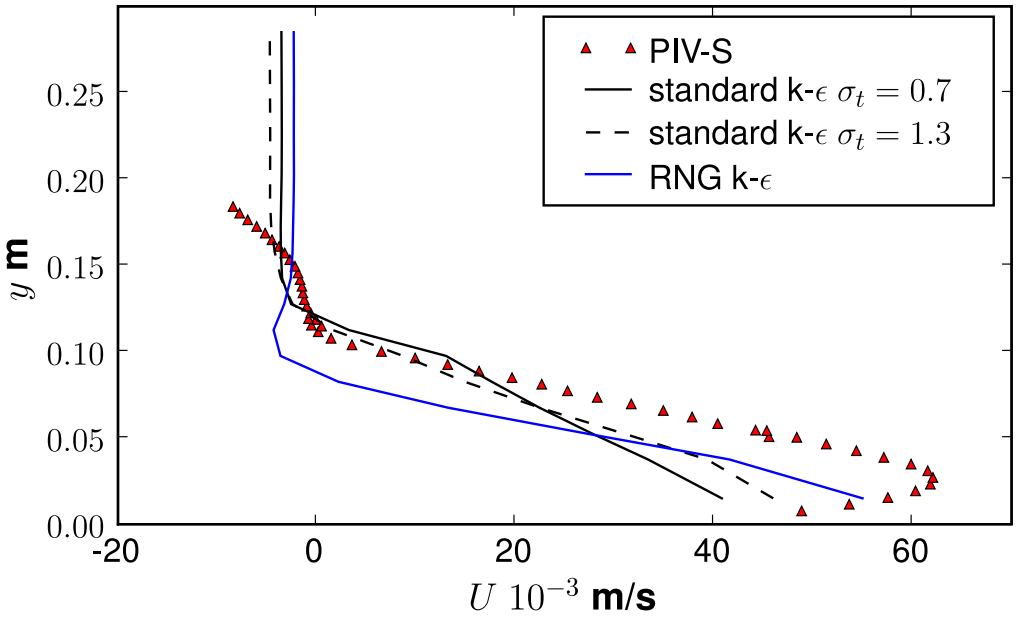

(a) 0,9 m **from the inlet**

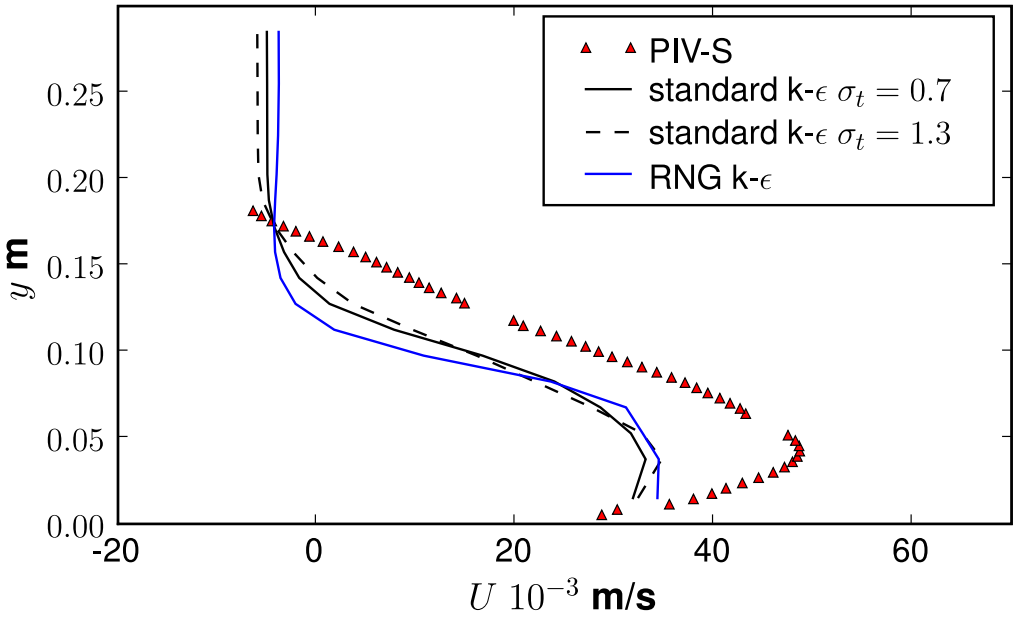

(b) 2,4 m **from the inlet**

Figure 4.23: Mean U-profiles: Simulated and PIV-S measurements: present research

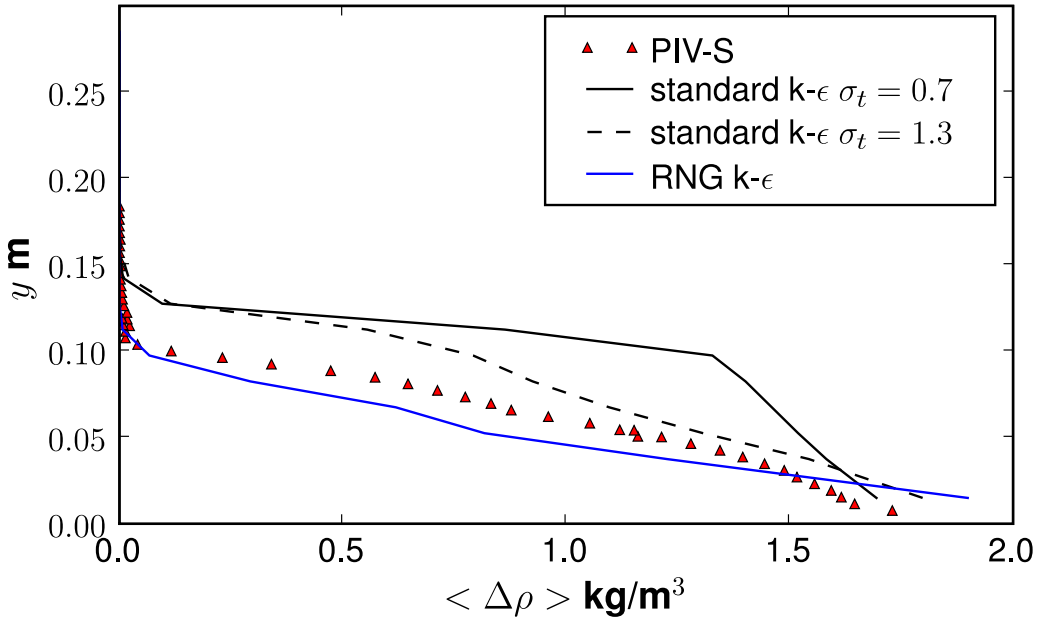

(a) 0,9 m **from the inlet**

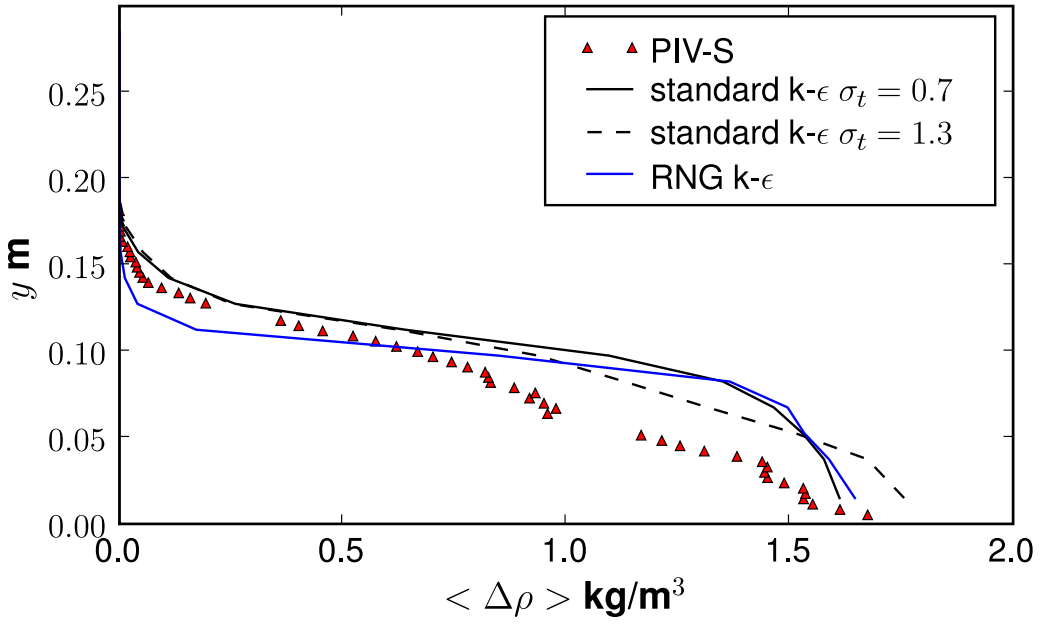

(b) 2,4 m **from the inlet**

Figure 4.24: Mean $\langle\Delta\rho\rangle$-profiles: Simulated and PIV-S measurements: present research

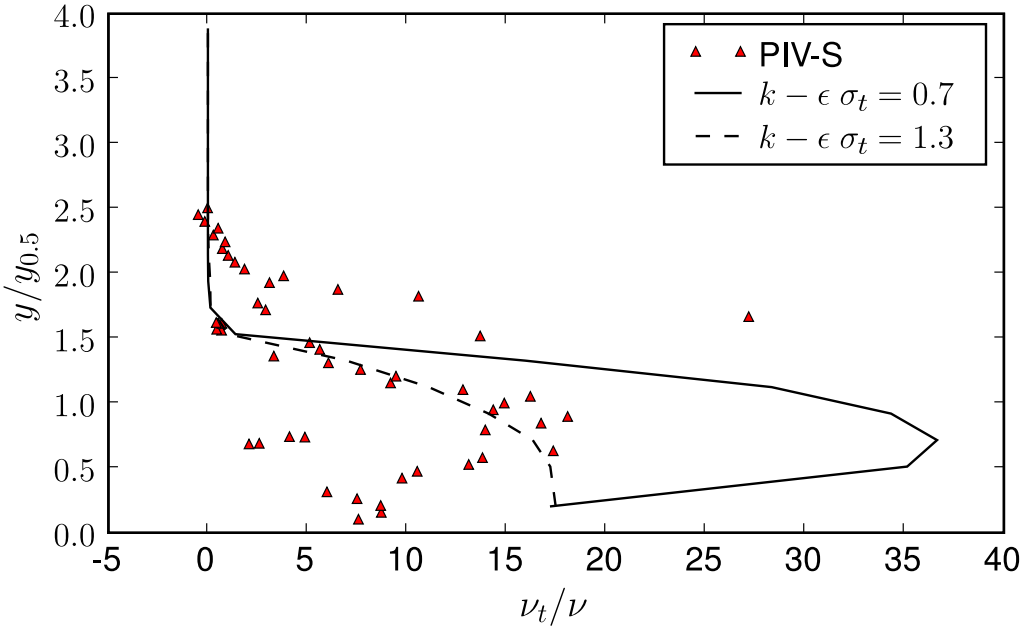

(a) 0,9 m **from the inlet**

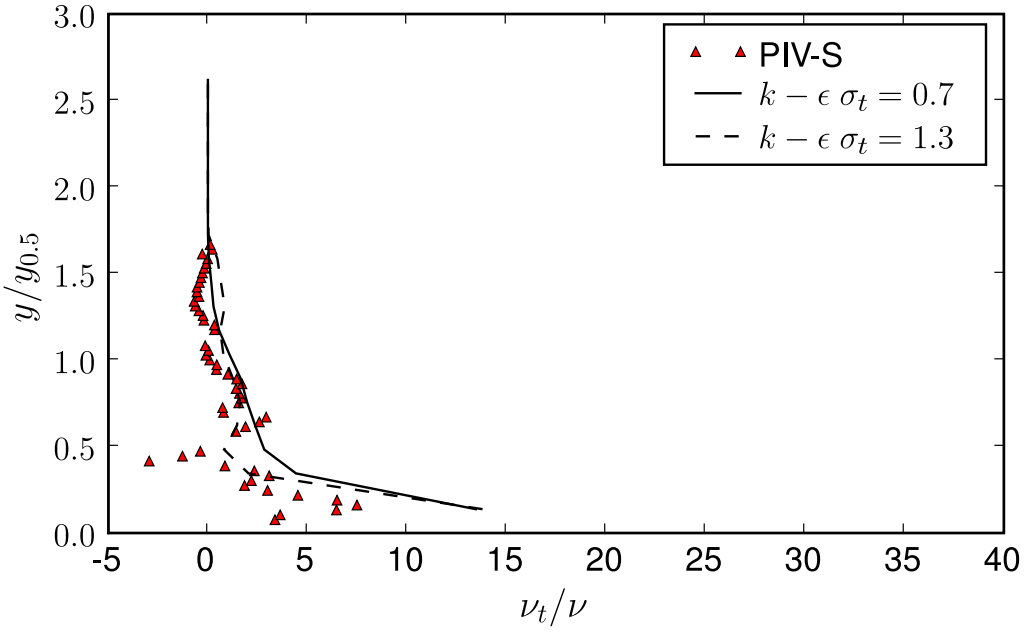

(b) 2,4 m **from the inlet**

Figure 4.25: ν_t/ν-profiles: Simulated and PIV-S measurements: present research

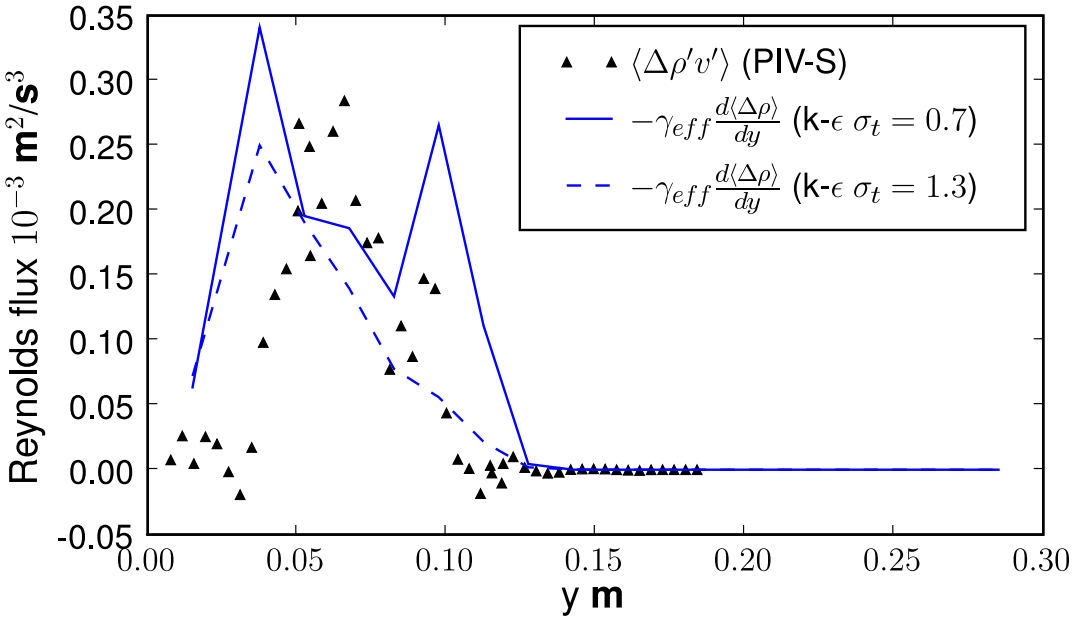

(a) 0,9 m **from the inlet**

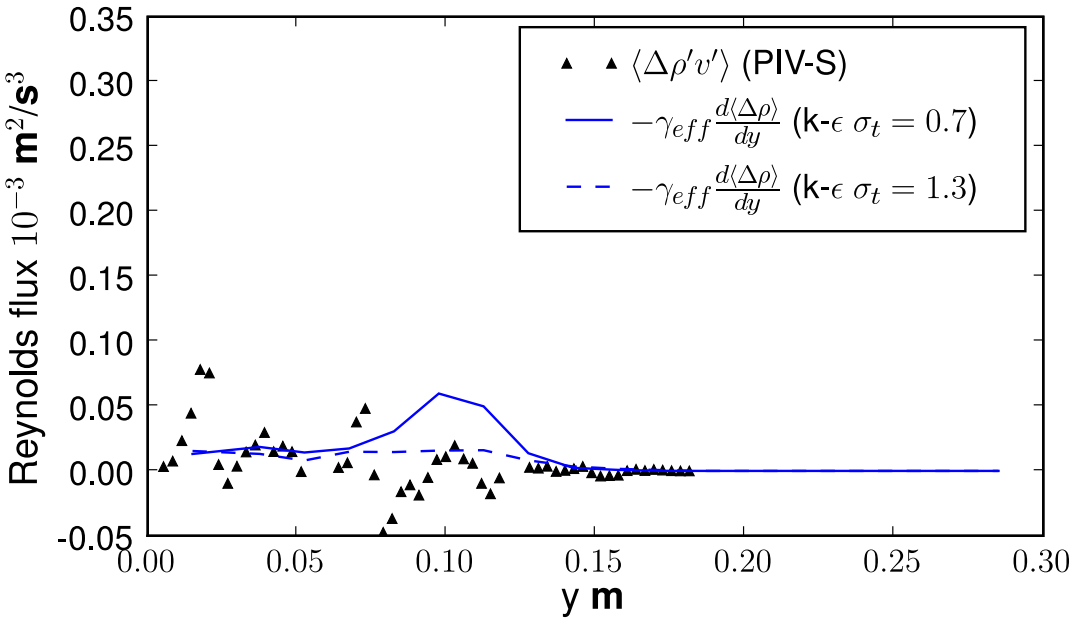

(b) 2,4 m **from the inlet**

Figure 4.26: $\langle \Delta\rho' v' \rangle$-profiles: Simulated and PIV-S measurements: present research

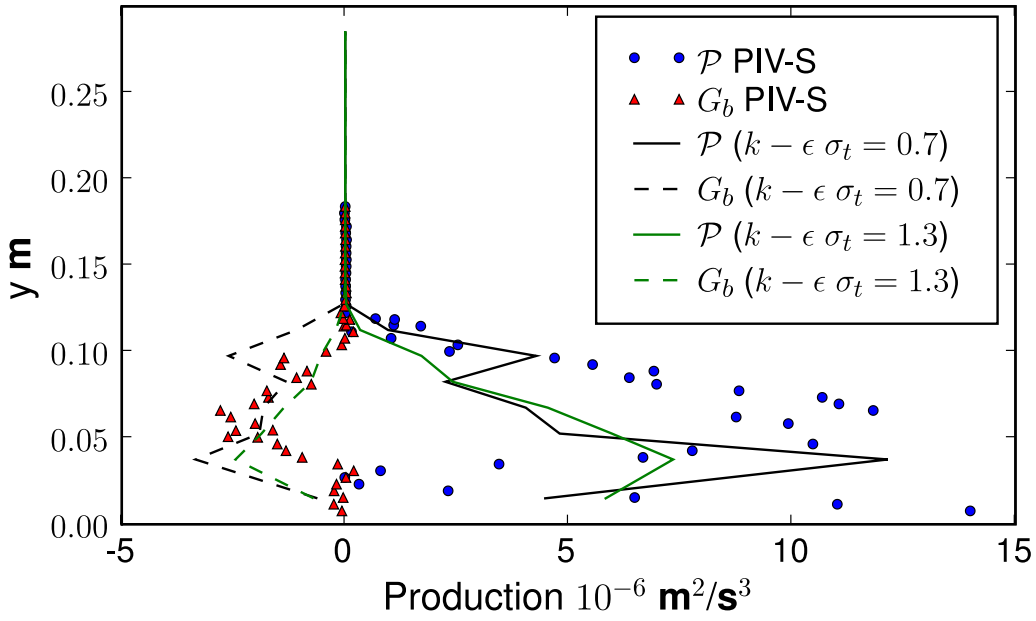

(a) 0,9 m **from the inlet**

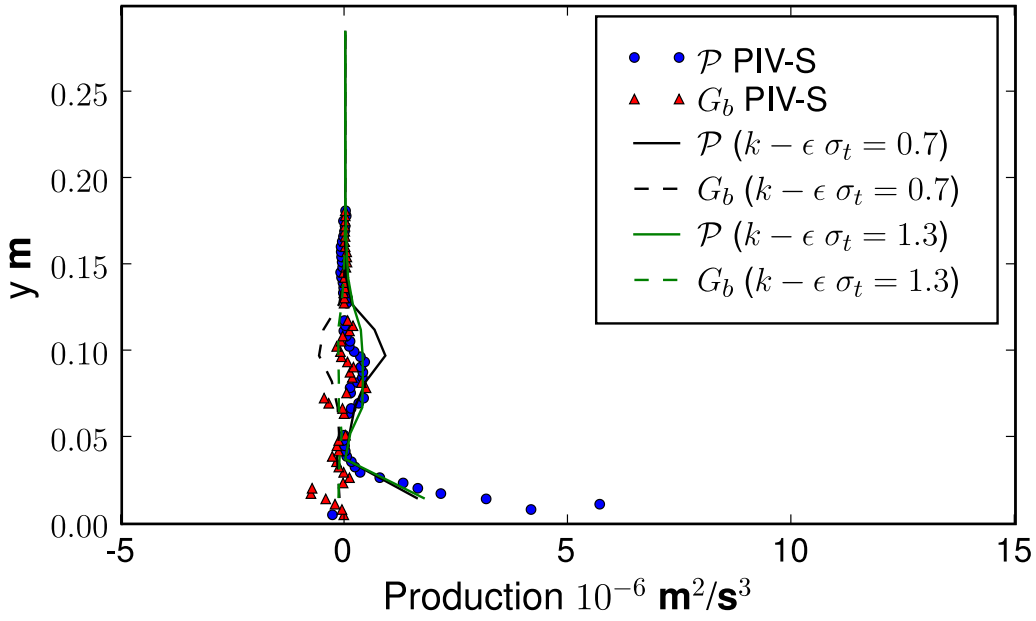

(b) 2,4 m **from the inlet**

Figure 4.27: $\mathcal{P}$- and G_b-profiles: Simulated and PIV-S measurements: present research

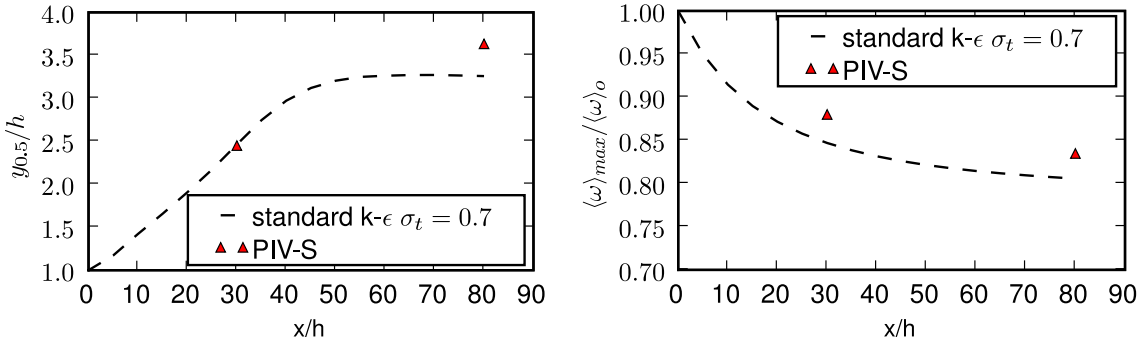

(a) Outer lengthscale $y_{0.5}$ **(b) Maximum $NaCl$ mass fraction $\langle\omega\rangle_{max}$**

Figure 4.28: Downstream development of gravity current: Simulated and PIV-S measurements: present research

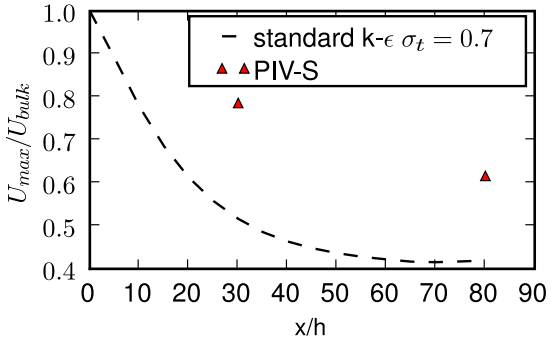

Figure 4.29: Downstream development of outer velocity scale U_{max}: Simulated and PIV-S measurements: present research

4.9 Summary

This chapter presented a 2D vertical, multispecies, Reynolds-averaged Navier-Stokes (RANS) gravity current model. The species simulated were $NaCl$ and H_2O, which did not react chemically. The program FLUENT was used to solve the governing equations. It was used to avoid the large amount of time which would have been required to develop a custom software code.

Multispecies mixture theory was used to derive the mixture continuity equation, mixture momentum equation and species transport equation. It was shown that for saline gravity currents these equations could be simplified by using the incompressible approximation, dilute approximation and Boussinesq approximation. Reynolds-averaging was applied to the simplified equations to remove the small scale, high frequency fluctuations from the mean values. The Reynolds-averaging introduced second-order moments describing the correlation between fluctuating quantities. In order to provide closure for the second-order moments, the Boussinesq and flux-gradient hypotheses were introduced. The turbulent viscosity, required by the Boussinesq and flux-gradient hypotheses, was computed from the standard $k-\epsilon$ model and the Renormalization Group theory (RNG) $k-\epsilon$ model.

It was shown that the flux-gradient hypothesis incorrectly predicted the orientation of the Reynolds flux vector. However, the gravity current had the characteristics of a boundary-layer type flow where the only significant Reynolds flux component is the cross-stream component $\langle \Delta\rho' v' \rangle$. Fortunately, the flux-gradient hypothesis provides a good estimate of the cross-stream component.

The modeled flume was similar to the flume used for the measurements of chapter 3. The inlet and outlet of the flume were modeled, respectively, by 'velocity inlet' and 'pressure outlet' boundary conditions. The free surface was modeled with a symmetry boundary condition and walls were modeled using non-equilibrium wall functions. The non-equilibrium wall functions relaxed the assumption that turbulence is in local equilibrium ($\mathcal{P} \approx \epsilon$) near the wall. The experimental results of chapter 3 showed that local equilibrium existed for a small region near the wall. However, if the wall adjacent cell is too large, buoyancy effects could compromise the local equilibrium assumption. Hence, although local equilibrium is a credible assumption, the non-equilibrium wall functions provide a more robust wall treatment.

An unstructured grid was applied to the modeled flume to minimize the number of cells required to obtain a numerical solution. The transient terms of the governing equations were discretized using a second-order implicit scheme. The diffusion

and convective terms were discretized using central difference and second-order upwind schemes respectively. Pressure gradients were discretized using a body force weighted scheme. The Pressure-Implicit with Splitting of Operators (PISO) scheme was used for the pressure-velocity coupling. This scheme provided the greatest convergence rate for the governing equations. Sensitivity analyses were performed for different grid resolutions in order to find the lowest resolution, which provided grid independent solutions. Sensitivity analyses were also performed for different magnitudes of scaled residuals, in order to find the largest scaled residual which provided a residual independent solution.

The unsteady governing equations also required the specification of initial conditions. The gauge pressure, mean velocity, $NaCl$ mass fraction and turbulent kinetic energy were set to zero to model a flume initially filled with quiescent water. The dissipation rate of turbulent kinetic energy ϵ was not set to zero, in order to avoid the turbulent viscosity becoming undefined. Sensitivity analyses were performed for different initial values of ϵ. It was found that the intial value of ϵ did not have a significant impact on the mean gravity current profiles. Sensitivity analyses were also performed for different flume depths. It was found that the lower section of the mean profiles, where gravity current flow occurs, was insensitive to the flume depth. The upper part of the mean profiles, where the return flow occurs, was sensitive to the flume depth, for flume depths $< 0{,}3\,\mathrm{m}$.

The performance of different turbulence models was also investigated. Sensitivity analyses were performed on five $k-\epsilon$ models. Two were standard $k-\epsilon$ models with constant turbulent Schmidt numbers ($\sigma_t = 0{,}7$ and $\sigma_t = 1{,}3$) and the other three were Renormalization-group (RNG) $k-\epsilon$ models. Two RNG models used constant turbulent Schmidt numbers ($\sigma_t = 0{,}7$ and $\sigma_t = 1{,}3$), while the third RNG model used a variable turbulent Schmidt number. The RNG models correctly predicted the occurrence of transverse vortices near the inlet and at the back of the gravity current head, while the standard $k-\epsilon$ models did not. The RNG models exhibited time-dependent profiles. Time-averaging was used to remove this periodicity when comparisons were made with the standard $k-\epsilon$ models. The sensitivity analysis showed that the turbulent Schmidt number has a significant impact on the mean gravity current profiles. Low turbulent Schmidt numbers produced slower currents with stepped excess density profiles, while high turbulent Schmidt numbers produced quicker currents with smooth profiles.

Sensitivity analyses were performed for different inlet conditions to investigate their impact on the downstream development of the gravity current. The analysis showed that the downstream development is sensitive to the inlet velocity and $NaCl$ mass fraction, but insensitive to inlet turbulence (k an ϵ). Increases in inlet velocities resulted in greater mixing and hence broader, more dilute currents.

Increases in inlet excess densities resulted in marginally quicker currents, with less turbulent mixing due to the increased stable stratification.

Finally, the accuracy of the multispecies RANS gravity current model was evaluated against the PIV-S measurements of chapter 3. Depth-averaged errors were computed from the simulated and measured profiles in regions where the turbulence structure was not self-similar. A comparison between the standard $k-\epsilon$ model with $\sigma_t = 0.7$ and the standard $k-\epsilon$ model with $\sigma_t = 1.3$ showed the latter model to produce smaller depth-averaged errors. Its depth-averaged errors for mean velocity, mean excess density, turbulent viscosity ratio, cross-stream Reynolds flux and shear production were respectively $10\% - 20\%$, 10%, $16\% - 22\%$, 15% and $4\% - 6\%$. The model generally underpredicted the mean streamwise velocity and overpredicted the excess density (because saline currents are conservative). Furthermore, the downstream development of the outer lenght scale $y_{0.5}$ and mass fraction scale $\langle\omega\rangle_{max}$ agreed well with the PIV-S measurements. The downstream development of these two scales showed that turbulence collapsed for $x/h > 50$, due to stable stratification. The model underpredicted the downstream development of the outer velocity scale U_{max}.

Chapter 5

Conclusions and Recommendations

5.1 Conclusions

This dissertation describes research in which a continuous, horizontal, dilute saline gravity current was measured. The gravity current had an inlet excess density difference of $2\,\mathrm{kg/m^3}$. The depth-averaged excess density did not vary with downstream distance, since the current was conservative. A time series of instantaneous velocity and excess density profiles were measured at the inlet, and at 0,9 m and 2,4 m downstream from the inlet. From this time series the mean velocity, mean excess density and turbulence profiles were computed. The measured profiles, in particular the turbulence profiles, were not self-similar at the measurement locations, because stable stratification continuously reduced the turbulence intensities. The dynamics were similar to the heated free surface jet studied by Hossain and Rodi (1977). At the inlet and 0,9 m downstream the bulk Richardson numbers were, respectively, 0,09 and 0,34, indicating that the current was supercritical. At a position 2,4 m from the inlet the bulk Richardson number was near critical with a value of 0,88.

The influence of the stable stratification on the gravity current turbulence was determined by measuring profiles of gradient Richardson number Ri_g, turbulent viscosity ratio ν_t/ν, turbulent diffusivity ratio γ_t/γ, as well as buoyancy and shear production of turbulent kinetic energy $G_b, \mathcal{P}$. The gradient Richardson number profile at 0,9 m showed that, except at the velocity maximum, shear production was able to offset buoyancy production and hence maintain turbulence. At 2,4 m the gradient Richardson number profile showed that shear production was unable

to offset buoyancy production anywhere in the flow. Hence turbulence could not be maintained at this location.

The turbulent viscosity ratio profile at 0,9 m had a single outer peak, whose value was half the inlet value. This indicated that interfacial shear contributed most to the positive production of turbulent kinetic energy and that negative buoyancy production attenuated turbulence significantly. At 2,4 m the outer peak disappeared, but an inner peak remained. The value of the inner peak was less than 20% of the inlet value. This indicated that turbulence had collapsed in the outer region and that the remaining turbulence of the inner region was due to the near-bed shear production. The turbulent diffusivity ratio profile at 0,9 m had a single outer peak, which indicated that turbulent mass transport occured primarily in the outer region. At 2,4 m the turbulent diffusivity ratio profile was scattered around zero, which indicated that the collapse of turbulence had resulted in negligible turbulent mass transport throughout the current.

The shear and buoyancy production profiles showed that shear production dominated buoyancy production at 0,9 m. The shear production profile had both an outer and an inner peak, while the buoyancy production had only a single outer peak. The outer peaks of shear and buoyancy production disappeared at 2,4 m, due to the stable stratification. No regions of negative shear production were found, as were measured by Buckee *et al.* (2001). The partial budget of turbulent kinetic energy at 0,9 m and 2,4 m showed that turbulence was in local equilibrium $\mathcal{P} \approx \epsilon$ for only a small region near the bed. Non-equilibrium wall functions, which relax the local equilibrium assumption, are therefore recommended for numerical gravity current models.

The spatial distribution of Reynolds stresses and Reynolds fluxes for a gravity current, whose turbulence structure was not self-similar, was determined by measuring the Reynolds flux $\langle \Delta\rho' \bar{u}' \rangle$ and Reynolds stress $\langle \bar{u}' \bar{u}' \rangle$ profiles. The Reynolds stress profiles at 0,9 m and 2,4 m showed that the turbulent momentum transport was anisotropic. At 0,9 m the outer and inner Reynolds stress peak heights were similar to the peak heights of a neutrally-buoyant wall-jet. The peak values did not correspond to those of a wall-jet, since the current was not self-similar. The outer Reynolds stress peaks disappeared at 2,4 m, due to the collapse of turbulence in the outer region. The inner peaks remained, due to the near-bed shear production. Even though the Reynolds stresses had local minima at the height of the velocity maximum, they were still large enough to give moderately high turbulence intensities ($7\% - 10\%$).

Energy spectra, taken at 0,9 m and 2,4 m, also showed that the Reynolds stresses were anisotropic. The spectra showed that the large scale, low frequency eddies

$< 10\,\text{Hz}$ transport most of the turbulent kinetic energy.

The Reynolds flux profiles at 0,9 m and 2,4 m showed that the turbulent mass transport was also anisotropic. At 0,9 m the outer peak heights were similar to the peak heights of a neutrally-buoyant wall-jet. In contrast to a neutrally-buoyant wall-jet, where the streamwise and cross-stream Reynolds flux components are similar in magnitude, the streamwise Reynolds flux $\langle \Delta\rho' u' \rangle$ of the gravity current dominated the cross-stream Reynolds flux $\langle \Delta\rho' v' \rangle$. This was due to gravity damping the vertical turbulent mass transport. The outer Reynolds flux peaks were attenuated at 2,4 m, similar to the outer Reynolds stress peaks. To the author's knowledge no Reynolds flux profiles have previously been published for a laboratory gravity current.

This dissertation also presented a 2D vertical, multispecies, Reynolds-averaged Navier-Stokes (RANS) gravity current model. The species simulated were $NaCl$ and H_2O, which did not react chemically. The model used the flux-gradient hypothesis to provide closure for the Reynolds fluxes appearing in the governing equations. The Reynolds flux measurements showed that the flux-gradient hypothesis incorrectly predicted the orientation of the Reynolds flux vector. However, the gravity current had the characteristics of a boundary-layer type flow, where the cross-stream Reynolds flux is the only important component. Despite the incorrect orientation estimate, the flux-gradient hypothesis gave a good estimate of the important cross-stream Reynolds flux component.

Various sensitivity analyses were performed on the RANS model: The mean velocity and mean excess density profiles proved to be insensitive to the initial conditions of ϵ. The lower part of the mean velocity and mean excess density profiles, where gravity current flow occurred, proved to be insensitive to differences in flume depth. The upper part of these profiles, where the return flow occurred, proved sensitive for flume depths $< 0{,}3\,\text{m}$. Furthermore, the mean velocity and excess density profiles proved sensitive to changes in inlet velocity and $NaCl$ mass fraction, but not inlet values of k and ϵ. Increases in inlet velocity resulted in greater velocity maximums, as well as increased mixing, which led to broader, more dilute currents. Increases in inlet $NaCl$ mass fraction resulted in marginally greater velocity maximums, with less turbulent mixing due to the increased stable density gradient.

The RNG $k - \epsilon$ model realistically predicted transverse vortices, due to the Kelvin-Helmholtz instability, near the inlet and at the back of the gravity current head. The standard $k - \epsilon$ model did not predict transverse vortices. A sensitivity analysis showed that low turbulent Schmidt numbers produced slower currents with thick, stepped excess density profiles, while high turbulent Schmidt numbers

produced faster currents with thin, smooth excess density profiles.

The standard $k-\epsilon$ model with a turbulent Schmidt number of $\sigma_t = 1.3$ gave depth-averaged errors of $10\% - 20\%$ for the mean velocity, 10% for the mean excess density, $16\% - 22\%$ for the turbulent viscosity ratio, 15% for the cross-stream Reynolds flux and $4\% - 6\%$ for the shear production.

Finally, this dissertation showed that particle image velocimetry scalar (PIV-S) technology was able to measure gravity current velocity and excess density profiles simultaneously and unintrusively. The technology requires a single camera and laser and no fluorescent dyes. The technology can work with a continuous laser, provided that the camera has a programmable electronic shutter. This dissertation has extended the application of the PIV-S technology to continuously stratified flows.

5.2 Recommendations

The experimental configuration used in this research revealed how turbulence interacted with the stable stratification of the gravity current. However, it is probably not enough to draw definitive conclusions. Additional experimental studies are therefore recommended with different inlet conditions and more measurement locations downstream of the inlet. Refractive index matching would probably be required for inlet excess density differences greater than $2\,\mathrm{kg/m^3}$.

The computed integral times of the present research showed that relatively long lag times were required to obtain uncorrelated and independent samples ($\approx 1\mathbf{s}$). The lag times used by Buckee *et al.* (2001) and Kneller *et al.* (1999) were significantly shorter and it may be that their computed averages were not fully converged due to the lack of independence between samples. It is therefore recommended that steady, continuous gravity current experimental runs should be longer than 300 s to ensure enough independent samples to compute stable averages.

Improvements to the PIV-S technology can be made in the following areas:

- Only half of the total number of images were used to compute the spatially averaged intensity profiles. Figure 2.7 showed that only the first image of an image pair was used. The signal to noise ratio of the computed spatially-averaged intensity could be improved by combining the two images of an image pair. This could be done by using the PIV displacement estimates to

properly align the two images of an image pair, followed by blending the two images into a single image. The resulting image will leave the particle pixel intensities relatively unaffected, while the non-particle pixel intensities will be decreased, resulting in a greater contrast between the particles and the background. This will result in an increase in the signal to noise ratio of the computed spatially-averaged image intensities.

- No validation and replacement algorithm for computed spatially-averaged intensities exists. A scheme similar to that of Westerweel and Scarano (2005), proposed for displacement estimates, might be used.

- The influence of light-sheet intensity attenuation on the computed spatially-averaged intensities could probably be eliminated as follows: For each profile (field of view) a recording is first made of the quiescent ambient water. This is followed by a recording of the gravity current flow. The spatially-averaged intensity profile of the gravity current is then normalised by the spatially-averaged intensity profile of the quiescent water, removing the effect of lightsheet attenuation.

Experimental studies of sediment entrainment by gravity currents, similar to those of Garcia and Parker (1993), can benefit from the PIV-S technology. Measurement of the near-bed Reynolds fluxes can be used to improve empirical sediment entrainment relationships. Winslow (2001) noted that numerical turbidity current models are very sensitive to the sediment entrainment relationship.

Further numerical research can be undertaken to improve the closure for the Reynolds fluxes. The present research used the flux-gradient hypothesis to estimate the cross-stream Reynolds flux. This hypothesis produced reasonable results, since the gravity current resembled a boundary-layer type flow. The flux-gradient hypothesis will probably not work for more complex flows. Improvements might be made by replacing the isotropic turbulent diffusivity scalar γ_t with an anisotropic turbulent diffusivity tensor $\bar{\bar{\gamma}}_t$. Other improvements might be made by using a variable turbulent Schmidt number (Hossain and Rodi). Although the RNG $k-\epsilon$ model has the option of using a variable turbulent Schmidt number, the present research found its accuracy to be poorer than that of the standard $k-\epsilon$ model with constant $\sigma_t = 1.3$. The Reynolds flux closure could also be improved by using transport equations for each Reynolds flux component (Hossain and Rodi, 1977). However, the introduction of more transport equations would be likely to have a negative impact on the computational effort and convergence rate of the solution.

One-dimensional numerical models are computationally efficient tools by which to do sensitivity analyses on field scale problems (for example, inlet boundary

conditions). Development and calibration of these models will also be of great value to industry.

List of References

Ahlman, D. (2006). A study of turbulence and scalar mixing in a wall-jet using direct numerical simulation. Tech. Rep., Royal Institute of Tecnology, Department of Mechanics, Stockholm, Sweden.

Alavian, V., Jirka, G., Denton, R., Johnson, M. and Stefan, H. (1992). Density currents entering lakes and reservoirs. *Journal of Hydraulic Engineering.*

Benedict, L. and Gould, R. (1996). Towards better uncertainty estimates for turbulence statistics. *Experiments in fluids.*

Bird, R., Stewart, W. and Lightfoot, E. (2002). *Transport Phenomena.* John Wiley & Sons Inc.

B.Kneller and Buckee, C. (2000). The structure and fluid mechanics of turbidity currents: a review of some recent studies and their geological implications. *Sedimentology.*

Bournet, P., Dartus, D., Tassin, B. and Vincon-Leite, B. (1999). Numerical investigation of plunging density current. *ASCE, Journal of Hydraulic Engineering.*

Bradshaw, P. (1971). *An introduction to turbulence and its measurement.* Pergamon Press.

Brørs, B. and Eidsvik, K. (1992). Dynamic reynolds modeling of turbidity currents. *Journal of Geophysical Research.*

Buckee, C., Kneller, B. and Peakall, J. (2001). Turbulence structure in steady, solute-driven gravity currents. *Spec. Publs. int. Ass. Sediment.*

Choi, S. and Garcia, M.H. (2002). k-ϵ turbulence model of density currents developing two-dimensionally on a slope. *Journal of Hydraulic Engineering.*

Choux, C., Baas, J., McCaffrey, W. and Haughton, P. (2005). Comparison of spatio-temporal evolution of experimental particulate gravity flows at two different initial concentrations, based on velocity, grain size and density data. *Sedimentary Geology.*

Cowen, E., Chang, K. and Liao, Q. (2001). A single-camera ptv-lif technique. *Experiments in fluids*.

Craft, T., Gerasimov, A., Iacovides, H., Kidger, J. and Launder, B. (2004). The negatively buoyant turbulent wall jet: performance of alternative options in rans modelling. *Heat and Fluid Flow*.

CRC handbook of chemistry and physics (1997-1998). CRC Press, ISBN 0-8493-0478-4.

Dallimore, C., Imberger, J. and Ishikawa, T. (2001). Entrainment and turbulence in saline underflow in lake ogawara. *Journal of Hydraulic Engineering*.

Daviero, G., Roberts, P. and Maile, K. (2001). Refractive index matching in large-scale stratified experiments. *Experiments in fluids*.

Ellison, T. and Turner, J. (1959). Turbulent entrainment in stratified flows. *Journal of Fluid Mechanics*.

Eriksson, J., Karlsson, R. and Persson, J. (1998). An experimental study of a two-dimensional plane turbulent wall jet. *Experiments in fluids*.

Fajardo, C., Smith, J. and Sick, V. (2006). Sustained simultaneous high-speed imaging of scalar and velocity fields using a single laser. *Applied Physics B - Lasers and Optics*.

Farrell, G. and Stefan, H. (1988). Mathematical modeling of plunging reservoir flows. *Journal of Hydraulic Research*.

Fernandez, R. and Imberger, J. (2006). Bed roughness induced entrainment in a high richardson number underflow. *Journal of Hydraulic Research*.

FLUENT 6.3 (2006). *User's Guide*. Fluent Inc.

Garcia, M. (1993). Hydraulic jumps in sediment-driven bottom currents. *J. Hydraul. Res.*

Garcia, M. and Parker, G. (1993). Experiments on the entrainment of sediment into suspension by a dense bottom current. *Journal of Geophysical Research*.

George, W., Abrahamsson, H., Eriksson, J., Karlsson, R., Lofdahl, L. and Wosnik, M. (2000). A similarity theory for the turbulent plane wall jet without external stream. *Journal of Fluid Mechanics*.

Guillard, F., Fritzon, R., Revstedt, J., Tragardh, C., Alden, M. and Fuchs, L. (1998). Mixing in a confined turbulent impinging jet using planar laser-induced fluorescence. *Experiments in fluids*.

Hartel, C., Meiburg, E. and Necker, F. (2000). Analysis and direct numerical simulation of the flow at a gravity-current head. part 1. flow topology and front speed for slip and no-slip boundaries. *J. Fluid Mech.*

Hossain, M. and Rodi, W. (). In: *Second international symposium on stratified flows*. The Norwegian Institute of Technology.

Hossain, M. and Rodi, W. (1977). Influence of buoyancy on the turbulence intensities in horizontal and vertical jets. In: Spalding, D.B. and Afgan, N. (eds.), *Heat transfer and turbulent buoyant convection*. McGraw-Hill.

Huang, H., Imran, J. and Pirmez, C. (2005). Numerical modeling of turbidity currents with a deforming bottom boundary. *Journal of Hydraulic Engineering*.

Kim, S. and Choudhury, D. (1995). A near-wall treatment using wall functions sensitized to pressure gradient. *ASME FED, Seperated and Comples flows*.

Kneller, B., Bennett, S. and McCaffrey, W. (1997). Velocity and turbulence structure of density currents and internal solitary waves: potential sediment transport and the formation of wave ripples in deep water. *Sedimentary Geology*.

Kneller, B., Bennett, S. and McCaffrey, W. (1999). Velocity structure, turbulence and fluid stresses in experimental gravity currents. *Journal of Geophysical Research*.

Launder, B. and Spalding, D. (1974). The numerical computation of turbulent flows. *Computer methods in applied mechanics and engineering*.

Lee, H. and Yu, W. (1997). Experimental study of reservoir turbidity current. *Journal of Hydraulic Engineering*.

Manninen, M. and Taivassalo, V. (1996). On the mixture model for multiphase flow. Tech. Rep., Valtion teknillinen tutkimuskeskus (VTT), Finland.

MARNET-CFD (2003). Best practice guidelines for marine applications of computational fluid dynamics. Available at: `https://pronet.wsatkins.co.uk/marnet/publications/bpg.pdf`.

Matlab (2006). *Signal Processing Toolbox User's Guide*. The Mathworks Inc.

McCaffrey, W., Choux, C., Baas, J. and Haughton, P. (2003). Spatio-temporal evolution of velocity structure, concentration and grain-size stratification within experimental particulate gravity currents. *Marine and Petroleum Geology*.

Nezu, I. and Nakagawa, H. (). In: *Turbulence in open-channel flows*. IAHR - Monograph Series.

Parker, G., Fukushima, Y. and Pantin, H. (1986). Self-accelerating turbidity currents. *Journal of Fluid Mechanics*.

Parker, G., Garcia, M., Fukushima, Y. and Yu, W. (1987). Experiments on turbidity currents over an erodible bed. *Journal of Hydraulic Research*.

Phillips, C. and Parr, J. (1999). *Signals, systems and transforms*. Prentice Hall.

Poelma, C. (2004). *PhD Dissertation: Experiments in particle-laden turbulence - simultaneous particle/fluid measurements in grid-generated turbulence using particle image velocimetry.*

Pope, S. (2001). *Turbulent Flows.* Cambridge University Press.

Raffel, M., Willert, C. and Kompenhans, J. (1998). *Particle Image Velocimetry: A practical guide.* Springer.

Ramaprabhu, P. and Andrews, M. (2003). Simultaneous measurements of velocity and density in buoyancy-driven mixing. *Experiments in fluids.*

Ramaprabhu, P. and Andrews, M. (2004). Experimental investigation of rayleigh-taylor mixing at small atwood numbers. *Journal of Fluid Mechanics.*

Reynolds, O. (1894). On the dynamical theory of incompressible viscous flows and the determination of the criterion. *Philos. Trans. R. Soc. London Series A.*

Rhie, C. and Chow, W. (1983). Numerical study of the turbulent flow past an airfoil with trailing edge seperation. *AIAA Journal.*

Rodi, W. (1980). *Turbulence Models and their Application in Hydraulics - A State of the Art Review.* IAHR.

Rodi, W. (1987). Examples of calculation methods for flow and mixing in stratified fluids. *Journal of Geophysical Research.*

Simpson, J. (1997). *Gravity currents in the environment and the laboratory.* Cambridge University Press.

Tennekes, H. and Lumley, J. (1973). *A First Course in Turbulence.* The MIT Press.

Thomas, L., Dalziel, S. and Marino, B. (2003). The structure of the head of an inertial gravity current determined by particle-tracking velocimetry. *Experiments in fluids.*

Turner, J. (1973). *Buoyancy effects in fluids.* Cambridge University Press.

van der Graaf, G. (2007). Gpiv manual. Available at: `http://gpiv.sourceforge.net/gpiv_doc/index.html`.

Versteeg, H. and Malalasekera, W. (1995). *An introduction to Computational Fluid Dynamics - The Finite Volume Method.* Pearson Prentice Hall.

Wernersson, E. and Tragardh, C. (2000). Measurements and analysis of high-intensity turbulent characteristics in a turbine-agitated tank. *Experiments in fluids.*

Westerweel, J. and Scarano, F. (2005). Universal outlier detection. *Experiments in fluids.*

Winslow, K. (2001). *PhD Dissertation: Sediment transport by turbidity currents.* UMI Dissertation Services.

Wörner, M. (2003). A compact introduction to the numerical modeling of multiphase flows. Tech. Rep., Institut fr Reaktorsicherheit, Programm Nukleare Sicherheitsforschung, Karlsruhe.

Yakhot, V., Orszag, S., Thangam, S., Gatski, T. and Speziale, C. (1992). Development of turbulence models for shear flows by a double expansion technique. *Phys. Fluids A*.

Yang, T. and Shy, S. (2005). Two-way interaction between solid particles and homogeneous air turbulence: particle settling rate and turbulence modification measurements. *Journal of Fluid Mechanics*.

Appendices

Appendix A

Tables of depth-averaged differences and errors

Alternative	Profiles at 0,9 m	Profiles at 2,4 m
$\epsilon = 1{,}38 \times 10^{-5}$	0	0
$\epsilon = 1{,}38 \times 10^{-4}$	0,3	0,4
$\epsilon = 1{,}38 \times 10^{-3}$	0,7	0,8

Table A.1: Depth-averaged differences: $\delta_d[U, \epsilon = 1{,}38 \times 10^{-5}, \textbf{alternative}]$

Alternative	Profiles at 0,9 m	Profiles at 2,4 m
$\epsilon = 1{,}38 \times 10^{-5}$	0	0
$\epsilon = 1{,}38 \times 10^{-4}$	0,6	0,5
$\epsilon = 1{,}38 \times 10^{-3}$	1,5	0,9

Table A.2: Depth-averaged differences: $\delta_d[\langle \Delta\rho \rangle, \epsilon = 1{,}38 \times 10^{-5}, \textbf{alternative}]$

Alternative	Profiles at 0,9 m	Profiles at 2,4 m
5x330	3,9	5,7
10x330	2,0	1,7
16x660	0,0	0,0
25x1320	0,9	0,5

Table A.3: Depth-averaged differences: $\delta_d[U, \textbf{16x660}, \textbf{alternative}]$

Alternative	Profiles at 0,9 m	Profiles at 2,4 m
5x330	10,7	5,1
10x330	3,7	2,0
16x660	0,0	0,0
25x1320	0,6	0,5

Table A.4: Depth-averaged differences: $\delta_d[\langle\Delta\rho\rangle, \textbf{16x660}, \textbf{alternative}]$

Alternative	Profiles at 0,9 m	Profiles at 2,4 m
$R^\phi = 10^{-2}$	7,2	12,7
$R^\phi = 10^{-3}$	1,9	2,8
$R^\phi = 10^{-4}$	0,0	0,0
$R^\phi = 10^{-5}$	0,0	0,0

Table A.5: Depth-averaged differences: $\delta_d[U, R^\phi = 10^{-4}, \textbf{alternative}]$

Alternative	Profiles at 0,9 m	Profiles at 2,4 m
$R^\phi = 10^{-2}$	19,6	22,7
$R^\phi = 10^{-3}$	2,9	3,5
$R^\phi = 10^{-4}$	0,0	0,0
$R^\phi = 10^{-5}$	0,0	0,0

Table A.6: Depth-averaged differences: $\delta_d[\langle\Delta\rho\rangle, R^\phi = 10^{-4}, \textbf{alternative}]$

Alternative	Profiles at 0,9 m	Profiles at 2,4 m
20% decrease in reference U	5,4	9,2
20% increase in reference U	7,7	12,4

Table A.7: Depth-averaged differences: $\delta_d[U, U = 0{,}079, \textbf{alternative}]$

Alternative	Profiles at 0,9 m	Profiles at 2,4 m
20% decrease in reference U	6,0	5,9
20% increase in reference U	6,7	8,7

Table A.8: Depth-averaged differences: $\delta_d[\langle\Delta\rho\rangle, U = 0{,}079, \textbf{alternative}]$

Alternative	Profiles at 0,9 m	Profiles at 2,4 m
$\langle\omega\rangle = 0$	8,2	33,2
20% increase in reference $\langle\omega\rangle$	2,0	3,8
80% increase in reference $\langle\omega\rangle$	5,9	10,1

Table A.9: Depth-averaged differences: $\delta_d[U, \langle\omega\rangle = 0{,}002\,81, \textbf{alternative}]$

Alternative	Profiles at 0,9 m	Profiles at 2,4 m
$\langle\omega\rangle = 0$	25,9	26,6
20% increase in reference $\langle\omega\rangle$	7,6	5,5
80% increase in reference $\langle\omega\rangle$	23,2	17,7

Table A.10: Depth-averaged differences: $\delta_d[\langle\Delta\rho\rangle, \langle\omega\rangle = 0{,}002\,81, \textbf{alternative}]$

Alternative	Profiles at 0,9 m	Profiles at 2,4 m
20% decrease in reference k	0,1	0,0
20% increase in reference k	0,1	0,1

Table A.11: Depth-averaged differences: $\delta_d[U, k = 6{,}875 \times 10^{-5}, \textbf{alternative}]$

Alternative	Profiles at 0,9 m	Profiles at 2,4 m
20% decrease in reference k	0,1	0,1
20% increase in reference k	0,0	0,1

Table A.12: Depth-averaged differences: $\delta_d[\langle\Delta\rho\rangle, k = 6{,}875 \times 10^{-5}, \textbf{alternative}]$

Alternative	Profiles at 0,9 m	Profiles at 2,4 m
20% decrease in reference ϵ	0,1	0,1
20% increase in reference ϵ	0,1	0,1

Table A.13: Depth-averaged differences: $\delta_d[U, \epsilon = 1{,}38 \times 10^{-5}, \textbf{alternative}]$

Alternative	Profiles at 0,9 m	Profiles at 2,4 m
20% decrease in reference ϵ	0,1	0,2
20% increase in reference ϵ	0,2	0,2

Table A.14: Depth-averaged differences: $\delta_d[\langle\Delta\rho\rangle, \epsilon = 1{,}38 \times 10^{-5}, \textbf{alternative}]$

Alternative	Profiles at 0,9 m	Profiles at 2,4 m
$k-\epsilon$ ($\sigma_t = 0.7$)	12,45	21,46
$k-\epsilon$ ($\sigma_t = 1.3$)	10,36	20,3
RNG $k-\epsilon$	14,58	23,5

Table A.15: Depth-averaged errors: $\varepsilon_d[U, \textbf{PIV-S}, \textbf{alternative}]$

Alternative	Profiles at 0,9 m	Profiles at 2,4 m
$k-\epsilon$ ($\sigma_t = 0.7$)	19,12	11,8
$k-\epsilon$ ($\sigma_t = 1.3$)	10,46	10,1
RNG $k-\epsilon$	6,29	11,3

Table A.16: Depth-averaged errors: $\varepsilon_d[\langle\Delta\rho\rangle, \textbf{PIV-S}, \textbf{alternative}]$

Alternative	Profiles at 0,9 m	Profiles at 2,4 m
$k-\epsilon$ ($\sigma_t = 0.7$)	58,4	20,6
$k-\epsilon$ ($\sigma_t = 1.3$)	21,5	15,5

Table A.17: Depth-averaged errors: $\varepsilon_d[\nu_t/\nu, \textbf{PIV-S}, \textbf{alternative}]$

Alternative	Profiles at 0,9 m	Profiles at 2,4 m
$k-\epsilon$ ($\sigma_t = 0.7$)	23,1	25,6
$k-\epsilon$ ($\sigma_t = 1.3$)	14,9	15,3

Table A.18: Depth-averaged errors: $\varepsilon_d[\langle\Delta\rho' v'\rangle, \textbf{PIV-S}, \textbf{alternative}]$

Alternative	Profiles at 0,9 m	Profiles at 2,4 m
$k-\epsilon$ ($\sigma_t = 0.7$)	6,3	5,2
$k-\epsilon$ ($\sigma_t = 1.3$)	6,0	3,7

Table A.19: Depth-averaged errors: $\varepsilon_d[\mathcal{P}, \textbf{PIV-S}, \textbf{alternative}]$

Appendix B

FLUENT User Defined Functions

B.1 Mixture density

The density for an aqueous solution of $NaCl$ is given by equation 2.4.1. The source code implementation is given below:

```
#include "udf.h"

/************************************************************************
   UDF that computes the species mixture density (NaCl and water).
    P.S. for a density difference of 2kg/m3 use massfrac=0.00281
    (calculated from least-squares)
************************************************************************/
DEFINE_PROPERTY(rho_mix,c,t)
{
    real rho_m;
    real Massfrac_0;
    /*Massfrac_i = C_YI(c,t,i)*/
    Massfrac_0 = C_YI(c,t,0);
    /*Least-squares fit from "CRC handbook of chemistry and physics"
    78th edition p.8-73*/
    rho_m = 711.81818*Massfrac_0 + 998.2364; /* [kg/m3] */
    return rho_m;
}
```

B.2 Molecular mixture viscosity

The dynamic viscosity for an aqueous solution of $NaCl$ is given by equation 4.2.63. The source code implementation is given below:

```
#include "udf.h"

/************************************************************************
   UDF that computes the species mixture viscosity (NaCl and water).
************************************************************************/
DEFINE_PROPERTY(visc_mix,c,t)
{
    real visc;
    real Massfrac_0;
    /*Massfrac_i = C_YI(c,t,i)*/
    Massfrac_0 = C_YI(c,t,0);
    /*Least-squares fit from "CRC handbook of chemistry and physics"
    78th edition p.8-73*/
    visc = 0.0016848*Massfrac_0 + 0.00100261; /* [kg/m.s] */
    return visc;
}
```

B.3 Effective diffusivity of $NaCl$ species

The effective diffusivity for $NaCl$ species is given by equation 4.3.4. The source code implementation is given below:

```
/************************************************************************
   UDF that computes diffusivity for specie alpha
************************************************************************/
DEFINE_DIFFUSIVITY(diff_eff,c,t,i)
{
    real schmidt;
    schmidt = 1.3;
    return 1.61e-09 + C_MU_EFF(c,t) / (C_R(c,t)*schmidt);
}
```

Appendix C

Tensor integral theorems

C.1 Gauss divergence theorem

The Gauss divergence theorem is given by (Bird *et al.*, 2002, pg. 824)

$$\int_V \bar{\nabla} \cdot \bar{\phi} dV = \int_A \bar{n} \cdot \bar{\phi} dA \tag{C.1.1}$$

where A is the surface of the control volume and $\bar{n}$ is the normal vector of this surface.

C.2 Integration by parts

The product rule is given by

$$\bar{\nabla} \cdot (\bar{u}\bar{v}) = \bar{v}\left(\bar{\nabla} \cdot \bar{u}\right) + \bar{u} \cdot \bar{\nabla}\bar{v} \tag{C.2.1}$$

Integration over a control volume gives

$$\int_V \bar{\nabla} \cdot (\bar{u}\bar{v})\, dV = \int_V \bar{v}\left(\bar{\nabla} \cdot \bar{u}\right) dV + \int_V \bar{u} \cdot \bar{\nabla}\bar{v} dV \tag{C.2.2}$$

Applying the Gauss divergence rule gives the generalization of integration by parts

$$\int_V \bar{u} \cdot \bar{\nabla}\bar{v} dV = -\int_V \bar{v}\left(\bar{\nabla} \cdot \bar{u}\right) dV + \int_A \bar{n} \cdot (\bar{u}\bar{v})\, dA \tag{C.2.3}$$

C.3 Differentiation of a volume integral (Leibniz formula)

The Leibniz formula is given by (Bird *et al.*, 2002, pg. 824)

$$\frac{d}{dt}\int_{V(t)}\phi dV = \int_{V(t)}\frac{\partial\phi}{\partial t}dV + \int_{A(t)}\phi\bar{n}\cdot\bar{v}_b dA \tag{C.3.1}$$

where $V(t)$ is the volume of the control volume, which can vary with time; $A(t)$ is the boundary of the control volume, which can vary with time; $\bar{n}$ is the normal vector of the control volume boundary and $\bar{v}_b$ is the velocity at which the boundary of the control volume is moving.

The first term represents the rate at which the volume integral is changing. The second term is the volume integral of the Eulerian time derivative (An Eulerian control volume has boundaries which are fixed in space). The last term represents the rate of change of the volume integral, due to movement of the control volume's boundaries.

Governing equations often describe rates of change of volume integrals (e.g. rates of change of mass or momentum). The Leibniz formula is useful in this regard, since it can be applied to such terms irrespective whether the Eulerian or Lagrangean viewpoint is used (A Lagrangean material volume moves with the flow, always containing the same fluid particles).

From a Eulerian viewpoint ($\bar{v}_b = 0$) the Leibniz formula reduces to

$$\frac{d}{dt}\int_{V}\phi dV = \int_{V}\frac{\partial\phi}{\partial t}dV \tag{C.3.2}$$

From a Lagrangean viewpoint ($\bar{v}_b = \bar{v}$) the Leibniz formula becomes

$$\frac{d}{dt}\int_{V(t)}\phi dV = \int_{V(t)}\frac{\partial\phi}{\partial t}dV + \int_{A(t)}\phi\bar{n}\cdot\bar{v}dA \tag{C.3.3}$$

where $\bar{v}$ is the velocity of the fluid.

Appendix D

Original contributions

D.1 Contributions by George Gerber

All the experiments and numerical simulations were conducted entirely by George Gerber. The dissertation was also written entirely by George Gerber.

D.1.1 Experimental contributions

Reynolds flux profiles (figs. 3.12a, 3.12b, 3.27a and 3.27b), buoyancy production profiles (figs. 3.15a, 3.15b, 3.30a and 3.30b) and turbulent diffusivity profiles (figs. 3.16b and 3.32a) were measured for the first time for a negatively buoyant gravity current:

1. The Reynolds flux measurements showed that turbulent mass transport was anisotropic due to gravity damping the vertical flux component (figs. 3.12a, 3.12b, 3.27a and 3.27b).
2. The shear and buoyancy production profiles (figs. 3.15a and 3.15b) showed that shear production dominated buoyancy production when the gravity current had a supercritical bulk Richardson number. The buoyancy production profile showed a single outer peak, while shear production profile showed an inner and outer peak due to shearing at the bed and interface.

3. It was found that the outer Reynolds flux peaks (fig 3.27a), outer shear production peak and outer buoyancy production peak (fig. 3.30a) disappeared when the gravity current had a near-critical bulk Richardson number. This disappearance of the outer peaks was due to the stable density gradient continuously damping the turbulence intensities until the turbulence collapsed (fig 3.31a).

4. The turbulent diffusivity ratio profile showed a single outer peak when the gravity current had a supercritical bulk Richardson number (fig 3.16b). This indicated that turbulent mass transport occurred primarily in the outer region. The turbulent diffusivity ratio profile became negligible when the gravity current had a near-critical bulk Richardson number (3.32a). This indicated that turbulent mass transport became negligible when turbulence collapsed.

Although previous Reynolds stress measurements have been conducted on gravity currents (figs. 3.11 and 3.26b), this dissertation provided measurements at a much higher resolution (figs 3.9a, 3.9b, 3.24a and 3.24b). This allowed the location of inner and outer Reynolds stress peaks to be determined with greater certainty. This also allowed the location of the shear production peaks (figs 3.15a, 3.15b, 3.30a and 3.30b) and turbulent viscosity ratio peaks (figs 3.16a and 3.31a) to be determined with greater certainty:

1. It was observed that the outer Reynolds stress peaks disappeared when the gravity current had a near-critical bulk Richardson number (figs. 3.25a, 3.25b and 3.26a). This disappearance was also attributed to the damping effect of the stable density gradient.

2. In contrast to the observations of Buckee *et al.* (2001), which used low resolution data, no regions of negative shear production were observed.

3. The turbulent viscosity ratio profile showed a single outer peak when the gravity current had a supercritical bulk Richardson number (fig 3.16a). This indicated that shearing at the interface made a significant contribution to turbulence production. When the gravity current had a near-critical bulk Richardson number the outer peak disappeared, but an inner peak remained (fig 3.31b). This indicated that shearing at the bed was the only significant contribution to turbulence production.

The high resolution density measurements also allowed the location of excess density intensity peaks to be determined with greater certainty (fig 3.29a). This is

an improvement over low resolution, historical measurements (fig 3.29b). The high resolution measurements showed that greatest mixing occurred in the outer region when the bulk Richardson number was supercritical. When the bulk Richardson number was near-critical the outer region was no longer the primary region of turbulent mixing.

D.1.2 PIV-S technology contribution

The application field of the PIV-S technology was extended to steady, continuously stratified flows with a seven step methodology (section 2.5.4). This methodology produced an empirical relationship between spatially-averaged intensity and mixture density (eqs 2.5.1, 2.5.3 and 2.5.4). This relationship can then be used to compute a mixture density signal from a spatially-averaged intensity signal in a steady, continuously stratified flow.

The PIV-S technology was applied for the first time to a negatively buoyant gravity current moving along a bed. Hence simultaneous velocity and mixture density measurements were conducted for the first time on a gravity current.

D.1.3 Numerical contributions

A depth-averaged difference (eq. 4.4.28) was defined by George Gerber with which to quantify the difference in profiles of various model scenarios. A depth-averaged error (eq. 4.8.1) was also defined by George Gerber with which to quantify the difference between simulated profiles and measured PIV-S profiles.

It was found that the RNG k-epsilon turbulence model predicted the occurrence of transverse vortices due to the Kelvin-Helmholtz instability (fig 4.14). These vortices have been observed experimentally (B.Kneller and Buckee, 2000). The standard k-epsilon turbulence model did not predict any vortices (fig. 4.13). Even though the standard k-epsilon model incorrectly predicted their absence it was found that this model produced similar or marginally smaller depth-averaged errors compared to the RNG model (tables A.15 and A.16). A standard k-epsilon model with a turbulent Schmidt number of 1,3 produced the smallest depth-averaged errors in the region of 10% for excess density and $10\% - 20\%$ for mean velocity (tables A.15 and A.16).

The numerical results confirmed the observations made by Winslow (2001) that

the turbulence boundary conditions at the inlet does not have a significant influence on the downstream evolution of the gravity current (section 4.7).

D.1.4 Measurement advice

The measured integral timescale showed that lag times between velocity samples need to be large > 1 s for the samples to be uncorrelated and independent for a saline gravity current (section 2.6.3). Independent samples are required to compute stable Reynolds stresses and Reynolds fluxes (i.e. means, variances and covariances). The measurements of Buckee *et al.* (2001), Kneller *et al.* (1999) and Choux *et al.* (2005) might be unreliable due to the short lag times between samples.

D.2 Contributions not by George Gerber

Contributions made by other researchers are indicated throughout the text of this dissertation. However, the following major elements were not contributed by George Gerber:

1. PIV cross-correlation equation (eq. 2.3.1)
2. PIV-S equation (eq. 2.5.2)
3. Definition of inner, outer and depth-averaged scales (fig. 3.3, eqs. 3.2.2, 3.2.3, 3.2.4, 3.2.5 and 3.2.6)
4. Terms, definitions and conventions appearing in the glossary of this dissertation

D.3 Location where research was conducted

All the experimental work was conducted in the hydraulics laboratory of Stellenbosch University. All the numerical simulations were conducted on the desktop of George Gerber in room S413, Stellenbosch University.